

Radiative Effects of Clouds in the Arctic

Der Fakultät für Physik und Geowissenschaften

der Universität Leipzig

eingereichte

DISSERTATION

zur Erlangung des akademischen Grades

Doctor rerum naturalium

(Dr. rer. nat.)

vorgelegt

von M.Sc. Carola Barrientos-Velasco

geboren am 15.11.1989

in La Paz Bolivien

Gutachter: Prof. Dr. Andreas Macke

Prof. Dr. Susanne Crewell

Tag der Verleihung: 24 Oktober 2022

Bibliographische Beschreibung:

Barrientos-Velasco, Carola

Strahlungseffekte von Wolken in der Arktis

Universität Leipzig, Dissertation

107 S., 231 Lit., 59 Abb., 17 Tab.

Zusammenfassung:

In dieser Arbeit wird der Strahlungseffekt von arktischen Wolken im Frühsommer anhand von Messungen während der Expedition PS106 des Forschungsschiffs Polarstern sowie passiven Satellitenbeobachtungen untersucht. Die Wechselwirkung von Wolken mit Strahlung wird dabei unter Berücksichtigung des Einflusses von verschiedenen Wolken- und Oberflächeneigenschaften im Detail charakterisiert.

Die kleinskaligen Variabilität der Solarstrahlung auf einer Eisscholle wird auf Basis eines Pyranometernetzwerks analysiert, das ein Gebiet von 0.83 km x 1.59 km für die Zeit vom 4. bis 16. Juni 2017 abdeckte. Es werden fünf charakteristische Himmelszustände inklusive zugehöriger Mittelwerte und Variabilität der Globalstrahlung identifiziert. Ein Vergleich zwischen Punktmessungen und Flächenmitteln mittels einer Wavelet-basierten Multi-Skalen-Analyse zeigt, dass die Amplitude und Skalenabhängigkeit der Variabilität charakteristische Merkmale für diese Himmelszustände aufweisen. Bei bewölktem Himmel werden ausgeprägte Muster im Tagesgang und in der räumlichen Verteilung der Beobachtungen sichtbar, die vermutlich auf mehrfache Reflexion von Strahlung zwischen Boden und Wolkenbasis sowie die inhomogenen Bodenbedingungen zurückzuführen sind.

Eine Sensitivitätsanalyse der Strahlungsflüsse für wolkenfreie und bewölkte Bedingungen mit einem 1D-Strahlungsmodell wird präsentiert und als Grundlage verwendet, um zu untersuchen, wie gut aktuelle schiffsgestützte und passive satellitengestützte Fernerkundungsbeobachtungen den Strahlungseffekt von Wolken und die arktische Strahlungsbilanz wiedergeben können.

Aus den schiffsgestützten Fernerkundungsbeobachtungen mit dem Cloudnet-Algorithmus abgeleitete Wolkeneigenschaften werden als Eingangsdaten für Strahlungstransportsimulationen verwendet. Die Ergebnisse werden mit Schiffsmessungen der abwärtsgerichteten terrestrischen und solaren Strahlungsflüsse sowie mit Satellitenprodukten von CERES (Clouds and the Earth's Radiant Energy System, SYN1Deg, Ed. 4.1) verglichen, um die Übereinstimmung von simulierten und beobachteten Strahlungsflüssen zu testen und den Wolkenstrahlungseffekt zu charakterisieren. Für unbewölkte Situationen wird eine Schließung der Strahlungsflüsse erzielt. Die größten Abweichungen sind für tiefliegenden Niederschlags, Stratus- und Eiswolken festzustellen. Darüber hinaus wird der Wolkenstrahlungseffekt entlang der PS106-Fahrtroute mit dem der gesamten Arktis verglichen, um den räumlichen Kontext zu erweitern, unter Verwendung der großräumigen Abdeckung der CERES-Produkte. Die Ergebnisse belegen für den Untersuchungszeitraum einen dominanten Einfluss der solaren Strahlung auf den Strahlungshaushalt. Aufgrund der Reduktion der Solarstrahlung durch Wolken ergibt sich entlang der PS106-Fahrtroute und für die zentrale Arktis eine wolkenbedingte Abkühlung von -8.8 W m^{-2} und -9.3 W m^{-2} . Die CERES-basierte Analyse belegt, dass die PS106-Wolkenbeobachtungen als repräsentativ für arktische Bewölkung während des Frühsommers 2017 betrachtet werden können.

Bibliographic Description:

Barrientos-Velasco, Carola

Radiative Effects of Clouds Arctic

Universität Leipzig, Dissertation

107 p., 231 ref., 59 fig., 17 tab.

Abstract:

In this thesis, the radiative effect of Arctic clouds during early summer is investigated based on observations collected aboard the research vessel Polarstern during the expedition PS106 conducted in 2017 in combination with passive satellite observations. The interactions of clouds with radiation, and the relevance of several macro- and microphysical properties of clouds and surface conditions are analyzed. An investigation of the small-scale variability of solar radiation on an ice floe based on a network of autonomous pyranometers covering an area of 0.83 km x 1.59 km, and the period from 4-16 June 2017 is given. Five distinct sky conditions are identified, and the mean and variance of atmospheric transmittance of global radiation are determined. Using a wavelet-based multi-resolution analysis, a comparison of individual station records and spatially averaged observations indicates that the absolute magnitude and scale-dependence of variability contain characteristic features for different sky conditions. For overcast conditions, distinctive patterns are identified in the diurnal variability and spatial distribution of the network observations, presumably caused by multiple reflection radiation between surface and cloud base in combination with the inhomogeneous surface conditions.

A sensitivity analysis of radiative fluxes is performed for clear-sky and cloudy conditions using a 1-dimensional radiative transfer model, and is used as a basis to investigate how well state-of-the-art shipborne and passive satellite remote sensing observations can constrain the radiative effect of clouds and can serve to quantify the Arctic radiation budget.

Cloud properties derived from the shipborne remote sensing observations with the Cloudnet algorithm are used as input for radiative transfer simulations. Simulated fluxes are compared to shipborne observations of the downward-terrestrial and solar fluxes as well as satellite products from CERES (Clouds and the Earth's Radiant Energy System, SYN1deg Ed. 4.1) to test closure of simulated and observed radiative fluxes, and to analyse the cloud radiative effect. Closure is achieved for clear-sky conditions. Based on selected case studies and an analysis for the entire PS106 period, the largest discrepancies are identified for low-level stratus, precipitation and ice clouds. Moreover, the cloud radiative effect inferred along the cruise track is compared to the entire Arctic to expand the regional context, making use of the wide spatial coverage of the CERES products. The results indicate a strong contribution of the solar flux to the radiation budget for the study period. Due to the reduction of solar radiation by clouds, a cooling effect of -8.8 W m^{-2} and -9.3 W m^{-2} is found at the surface for the PS106 cruise and the central Arctic, respectively. The similarity of local and regional CRE suggests that the PS106 cloud observations can be considered as representative of Arctic cloud conditions during the early summer of 2017.

Contents

1	Introduction	1
1.1	Motivation	1
1.2	Characteristics of Arctic Clouds	3
1.3	Effect of Arctic Clouds on the Radiation Budget	5
1.4	Link Between Arctic Clouds and Surface Conditions	7
1.5	Objectives of (AC) ³ and this Thesis	8
1.6	Outline	9
2	Theoretical Background	11
2.1	Radiative Quantities	11
2.2	Radiative Interactions	12
2.2.1	Absorption	13
2.2.2	Scattering and Extinction	14
2.3	Radiative Transfer Equation	16
2.4	Radiative Transfer in the Arctic	17
2.4.1	Surface Reflection and Transmission	17
2.4.2	Clear-sky Conditions	18
2.4.3	Optical Properties of Clouds	18
2.5	Radiative Transfer Modelling	22
2.5.1	Two-stream Approximation	22
2.5.2	Correlated k -distribution	22
2.5.3	RRTMG	23
2.6	Energy Budget and Cloud Radiative Effect	24
3	PS106 Expedition, Instrumentation, Data sets, and Methods	25
3.1	Instrumentation	25
3.1.1	Pyranometer Network	25
3.1.2	Ship-borne Instrumentation	29
3.2	Data sets	30
3.2.1	Cloudnet	30
3.2.2	CERES data set	32
3.2.3	Ancillary data set	33
3.3	General Conditions During PS106	33
3.3.1	Synoptic and Surface Conditions	33
3.3.2	Atmospheric Temperature and Humidity Conditions	35
3.3.3	Statistical Analysis of Cloud Properties	36
3.4	Radiative Transfer Simulation Setup	41

4	Sensitivity Analysis of Arctic Fluxes	44
4.1	Clear-sky Perturbations	44
4.1.1	Atmosphere	44
4.1.2	Surface	45
4.2	Clear-sky Radiative Flux Uncertainty	49
4.3	Cloud Perturbations	50
4.3.1	Cloud Water Path	52
4.3.2	Cloud Particle Effective Radius	53
4.3.3	Liquid Fraction and Surface Albedo	55
4.3.4	Cloud Base Height	57
4.3.5	Cloud Geometrical Thickness	58
4.4	Synopsis	59
5	Cloud Induced Spatiotemporal Variability of Solar Radiation	62
5.1	Data Analysis	62
5.1.1	Data Processing	62
5.1.2	Sky Classification	63
5.2	Case Studies	64
5.2.1	Clear-sky Case	64
5.2.2	Overcast Case	65
5.2.3	Thin Cloud Case	67
5.2.4	Multilayer Case	68
5.2.5	Broken Cloud Case	69
5.3	Wavelet-based Multiresolution Analysis	72
5.4	Synopsis and Discussion	74
6	Radiation Closure	77
6.1	Radiative Flux Comparison Between CERES and T-CARS	77
6.2	Radiative Closure for Clear-sky Atmosphere	78
6.3	Radiative Closure for Cloudy Atmosphere	80
6.4	Synopsis and Discussion	82
7	Case Studies	84
7.1	Clear-sky Case	84
7.2	Single and Multilayer Ice Cloud Case	86
7.3	Mixed Phase Cloud Case	87
7.4	Synopsis	90
8	Radiation Budget and Cloud Radiative Effects	91
8.1	Cloud Radiative Effect (CRE) Analysis	91
8.2	Radiation Budget	98
8.3	Synopsis	102
9	Summary, Conclusions and Outlook	103
9.1	Summary and Conclusions	103
9.2	Outlook	107
	Appendix	108

A Cloud Microphysical Properties During PS106	109
B CRE of Sensitivity Analysis	111
C CERES Aerosol Products	114
D Additional Observations	115
Literature	118
List of Abbreviations	139
List of Symbols	141
List of Figures	144
List of Tables	153
Acknowledgements	155

Chapter 1

Introduction

1.1 Motivation

The response of the Earth’s climate system to anthropogenic or natural perturbations is strongly influenced by a number of feedbacks. The climate system is controlled by the interactions between radiative and non-radiative processes in connection with the atmosphere, ocean, sea ice, and land surfaces. Cloud feedbacks play a key role in the interactions with other feedbacks by influencing the radiation budget by affecting the solar and terrestrial radiative fluxes. Furthermore, cloud feedbacks constitute the largest inter-model spread uncertainty in climate sensitivity [Bony et al. 2006; Zelinka et al. 2012; Vial et al. 2013; Pithan and Mauritsen 2014; Block et al. 2020; Previdi et al. 2021].

Polar regions are the most sensitive regions of the Earth’s climate system [Bony et al. 2006; Meredith et al. 2019; IPCC 2021]. They are characterized by complex processes and yet not fully understood feedbacks mechanisms which are linked to a contrasting and variable surface, extreme weather conditions, and contrasting change in the annual solar insolation [Goosse et al. 2018; Block et al. 2020].

The Arctic is a focal point for studying the response of the climate system to anthropogenic forcing [Manabe and Wetherald 1975; Manabe and Stouffer 1980; Johannessen et al. 2004; Pithan and Mauritsen 2014; Stuecker et al. 2018; Wendisch et al. 2019]. This region has warmed at more than twice the global mean rate on the past decades [Ballinger et al. 2021]. This phenomenon, also referred to as Arctic amplification, has been observed in measurements and reproduced by general circulation models [Winton 2006; Serreze and Barry 2011; Kay et al. 2011; Johannessen et al. 2004; Pithan and Mauritsen 2014; Goosse et al. 2018; Block et al. 2020]. In contrast to the Arctic, the Antarctic presents a weaker polar amplification that can be attributed to the interhemispheric asymmetry in the ocean heat uptake [Bitz et al. 2006; Salzmänn 2017; Stuecker et al. 2018].

The warming in the Arctic is affecting its ecosystems by reducing the polar ice cap [Polyakov et al. 2010], reducing the habitat of marine mammals [Burek et al. 2008], affecting biological processes such as the metabolic balance of Arctic zooplankton [Alcaraz et al. 2013] and modifying the assimilation of nutrients by plants and microbes [Schmidt et al. 2002]. A warmer Arctic modifies the environment and presents challenges to the subsistence of indigenous people [Hansell et al. 1998; Olsen et al. 2011]. Moreover, the impacts of the warmer Arctic are not confined locally. They

can affect the rest of the Earth by increasing the sea level [Proshutinsky et al. 2001; Box et al. 2018], influencing global weather patterns [Overland et al. 2015; Francis et al. 2009; Cohen et al. 2014; Francis and Skific 2015], and accelerating the release of greenhouse gases by the thawing of the permafrost and, thus, intensifying climate change [Miller et al. 2010; Shakhova et al. 2014; Schuur et al. 2015; Turetsky et al. 2019].

Several studies have found the lapse-rate feedback to be the local positive feedback dominating Arctic amplification [Pithan and Mauritsen 2014; Stuecker et al. 2018; Block et al. 2020]. This feedback is positive, especially in winter, due to the suppression of vertical mixing leading to a stable stratification that increases the warming in the thin near-surface layer [Pithan and Mauritsen 2014; Goosse et al. 2018]. In summer, however, the surface albedo feedback is positive and of high relevance in the Arctic climate system [Arrhenius 1896; Curry et al. 1995; Winton 2006; Screen and Simmonds 2010; Taylor et al. 2013; Kashiwase et al. 2017]. This feedback describes the cycle of the decrease of sea ice extent and snow cover that exposes more absorbent surfaces like the open ocean, vegetation, or land. Darker surfaces lead to further absorption of solar radiation, increasing the warming of the Arctic.

Contrary to the lapse rate and surface albedo feedbacks, the cloud radiative effect can be positive or negative depending on which radiative flux dominates more. Clouds influence the radiative budget by affecting the solar and terrestrial radiative fluxes. In a warm Arctic scenario with a reduced sea ice extent, cloud cover increases resulting in an increase of the downward terrestrial radiation at the surface yielding to further warming [Kay et al. 2016; Morrison et al. 2018]. Also, the fraction of liquid in mixed-phase clouds increases, leading to a higher cloud albedo which causes further reflection of the solar radiation to the top-of-the atmosphere reducing the warming at the surface [Bodas-Salcedo et al. 2016; Jahangir et al. 2021]. Cloud feedbacks are involved in other feedbacks [e.g., water vapour, surface albedo], and their complex interactions with surface process play an important role in the Arctic energy budget [Morrison et al. 2012; He et al. 2019].

To further analyse the effect of clouds on the radiation budget, this thesis presents the analysis carried out of the radiative effects of Arctic clouds based on radiative flux observations, remote sensing observations of clouds, and radiative transfer simulations for the research expedition PS106. This investigation was done within the scope of the research project **ArctiC Amplification: Climate Relevant Atmospheric and SurfaCe Processes and Feedback Mechanisms ((AC)³** phase 1.

This introduction, which is based on Barrientos-Velasco et al. 2020 [hereafter Barrientos-Velasco et al. 2020] and Barrientos-Velasco et al. 2022 [hereafter Barrientos-Velasco et al. 2022], provides an overview of the characteristics of Arctic clouds [Section 1.2], the effects of clouds on the Arctic radiation budget [Section 1.3], and their interaction with Arctic surface conditions [Section 1.4]. Moreover, section 1.5 presents the general description of project A01 in the framework of the research program (AC)³ and introduces the main research objectives of this Thesis. This chapter concludes by presenting the outline of this work (Section 1.6).

1.2 Characteristics of Arctic Clouds

Throughout this thesis, the Arctic is defined as the region covering $70^\circ - 90^\circ\text{N}$. It will be clarified whenever subsequent studies may consider otherwise.

Cloud Fraction

Based on ground-based, satellite and reanalyses data, the frequency of occurrence of Arctic clouds presents a seasonal cycle showing the largest cloud fraction during September-October [Eastman and Warren 2010; Dong et al. 2010; Huang et al. 2017]. Ground-based observations in sites like Barrow-Alaska, now renamed to Utqiagvik [$71^\circ 19'\text{N}$, $156^\circ 37'$], and during the Surface Heat Energy Budget of the Arctic (SHEBA) campaign can corroborate these findings as illustrated in Figure 1.1 [Shupe et al. 2011]. However, at the Eureka observatory in Canada [$80^\circ 00'\text{N}$, $85^\circ 57'$], the cloud fraction indicates a unique local annual cloudiness cycle that does not follow the other sites.

The study of Eastman and Warren 2010 shows that the annual cycle of cloud fraction is more pronounced for higher Arctic latitudes [$70^\circ - 90^\circ\text{N}$]. The occurrence of clouds is mainly dominated by stratus, stratocumulus, and fog. Additionally, this study also separates the average amount of cloud cover by land and ocean, concluding that over the Arctic region [$60^\circ - 90^\circ\text{N}$], the ocean is cloudier with an annual mean of 75 % cloud fraction. In contrast, over land, the cloud cover is 66 %. A similar contrasting difference of cloud fraction over land and ocean is confirmed with the data sets from the Climate Monitoring Satellite Application Facility (CMSAF) in the study of Boccolari and Parmiggiani 2018 [see their Fig. 4].

Cloud Vertical Structure and Type

Stratiform Arctic clouds (stratus + stratocumulus + fog) are the most frequent type of clouds during the entire annual cycle, especially from May to September [Eastman and Warren 2010]. Considering all types of clouds observed at the different Arctic sites [e.g., Barrow-Alaska, Eureka-Canada], the mean annual cloud base height is about 1 km and a mean cloud geometrical thickness of about 2 km. The maximum cloud top height observed ranges up to 9 km [see Fig. 12 in Shupe et al. 2011]. Single-layer stratiform Arctic clouds have a mean cloud geometrical thickness between 200 and 700 metres with the lowest mean value of about 300 metres from March to May and the highest mean value of 400 metres from September to November [see Fig. 5 in de Boer et al. 2009].

Single-layer and multilayer clouds comprise a large part of the annual cloud occurrence in the Arctic and are present throughout the entire annual cycle [Intrieri et al. 2002b; Vassel et al. 2019; Nomokonova et al. 2019]. For instance, at Ny-Ålesund Norway, multilayer clouds occur about 44.8 % of the time, whereas single-layer clouds are present for 36 % of the year [Nomokonova et al. 2019]. During June and July, multilayer clouds occur more frequently, reaching up to 9 km in height and can persist at temperatures between -34 and 0°C [Intrieri et al. 2002b; Shupe 2011].

Cloud Phase and Persistence

Accurately determining the cloud phase is particularly important since it provides information about how clouds interact with the radiation budget and how associ-

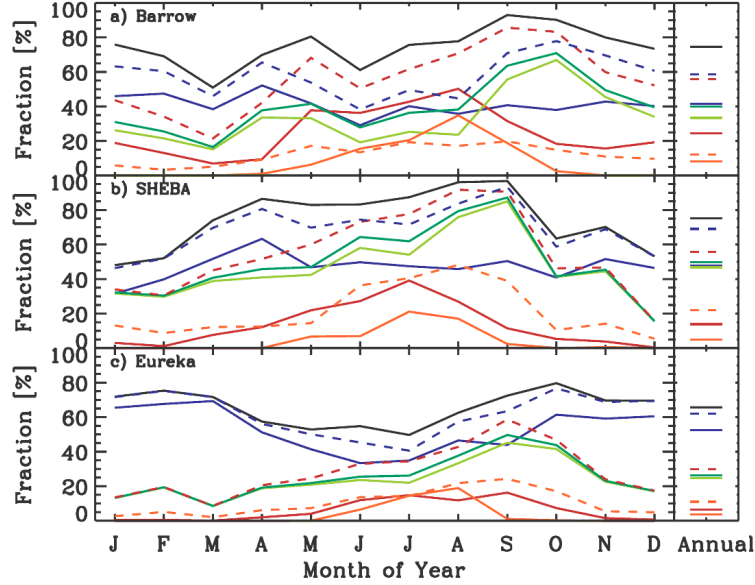


Figure 1.1: Monthly mean cloud fraction for different cloud types at **(a)** Barrow also known as Utqiagvik, **(b)** SHEBA, and **(c)** Eureka. The solid black line indicates cloud fraction, ice-only (solid blue), liquid-only (solid red), liquid precipitation including drizzle and rain (solid orange), mixed-phase cloud fraction (solid light green), and mixed-phase column fraction (solid dark green). Also included are the occurrence fractions of ice in any type of cloud (dashed blue), liquid in any type of cloud (dashed red), and multiple, distinct layers of liquid water in any type of cloud (dashed orange). Annual average occurrence fractions for each phase type are indicated at the right. Figure obtained from Shupe et al. 2011.

ated they are through different processes in the climate system [Shupe 2011; Morrison et al. 2012; Cesana and Storelvmo 2017]. For instance, for a given amount of water path, the optical depth of a liquid cloud is larger than an ice cloud [Cesana and Storelvmo 2017]. Furthermore, the coexistence of liquid and ice phase within a cloud, also defined as mixed-phase, will be dependent on processes such as Wegener-Bergeron-Findeisen (WBF), where ice crystals grow at the expense of the surrounding droplets because of the higher saturation vapour pressure of water than ice particles [Bergeron 1935; Findeisen et al. 2015; Morrison et al. 2012; Cesana and Storelvmo 2017].

Arctic single-phase liquid clouds occur more frequently during summer [Shupe 2011; Nomokonova et al. 2019; Achtert et al. 2020; Griesche et al. 2020]. At Ny-Ålesund, liquid clouds have a higher frequency of occurrence from September to November [Nomokonova et al. 2019]. This characteristic is not representative for the entire Arctic, as high occurrences were found in Utqiagvik for May and August, in Eureka site during August, and in July during the SHEBA project as shown in Figure 1.1 [Uttal et al. 2002; Shupe 2011].

During the summer and fall months, cloud liquid water is more persistent, surpassing a mean of 10 hours per case observed at Utqiagvik and SHEBA. In contrast to the sites mentioned before, liquid clouds are relatively infrequent in Eureka, and their mean persistence time lasts about 5 hours per case observed [see Fig. 1.1c].

Ice clouds are present in the Arctic during the entire year [Shupe 2011; Nomokonova

et al. 2019]. Arctic ice clouds can be observed at low altitudes and up to 8 km [e.g., at Ny-Ålesund, [Nomokonova et al. 2019] or up to 10 km as observed at Utqiagvik. In contrast to liquid clouds, their residence time last longer during winter, especially at the Eureka site [Shupe 2011]. In contrast to lower latitudes, mixed-phase clouds are present in the Arctic region throughout the entire year [Shupe et al. 2006; de Boer et al. 2009; Shupe 2011; Nomokonova et al. 2019; Tjernström and Graversen 2009], and they often persist for several days [Curry et al. 1996; Shupe et al. 2006; de Boer et al. 2009; Morrison et al. 2012]. The frequent geometrical thickness of mixed-phase clouds is about 1 km. However, they can also extend up to 3.5 km, as has been observed at Ny-Ålesund [Nomokonova et al. 2019]. As observed at Utqiagvik and Eureka, mixed-phase clouds can persist at temperatures ranging from about 243 K to 276 K.

1.3 Effect of Arctic Clouds on the Radiation Budget

This section summarizes the principal characteristics of the radiative effects of clouds on the radiation budget based on the literature. Note that a more detailed description of the relevant optical properties of clouds and the radiation budget is presented in Section 2.4.3 and 2.6, respectively. This thesis considers a broadband spectral range for the Solar (SOL) flux of 0.2-5 μm and for the Thermal Infrared (TIR) flux of 5-50 μm .

Clouds strongly modulate the Earth's radiation budget. A change in their radiative effect in response to a global temperature change may produce a considerable feedback on the Earth's temperature [Bony et al. 2006]. Thus, having accurate observations is necessary to monitor any imbalance caused by global warming [Christensen et al. 2016]. An example of the quantification of the radiation budget in the Arctic enclosing satellite, reanalysis and ground-based data sets is given by Christensen et al. 2016 within the Arctic Observation and Reanalysis Integrated System (ArORIS). Based on the ArORIS data set, the Arctic energy budget has been calculated for the period 2007-2010 [see Fig. 1.2].

At the surface (SFC), the energy budget is composed by the radiation budget [enclosing the SOL and TIR flux], plus the Sensible Heat (SH) and Latent Heat (LH) heat fluxes. Through the atmosphere, the components are the radiation fluxes and the heat transport, and at the Top Of the Atmosphere (TOA) the radiative fluxes. Figure 1.2 shows that the radiation budget and heat transport are the largest components of the energy budget. Both SH and LH play a less significant role in the annual mean. At the TOA, the radiative fluxes are well observed. At the SFC, the thermal infrared flux dominates the annual energy budget [see Fig. 5 in Christensen et al. 2016].

The complexity of Arctic clouds is enhanced by their involvement in several processes and feedback mechanisms [Curry et al. 1996; Bony et al. 2006; Morrison et al. 2012; Goosse et al. 2018]. For instance, the cloud cooling or warming effect at the surface interact with the non-radiative feedback by enhancing or diminishing the snow and sea ice melting processes and ice growth-thickness [Bitz and Roe 2004; Perovich 2018]. The reduction of the surface albedo will enlarge the absorption of SOL

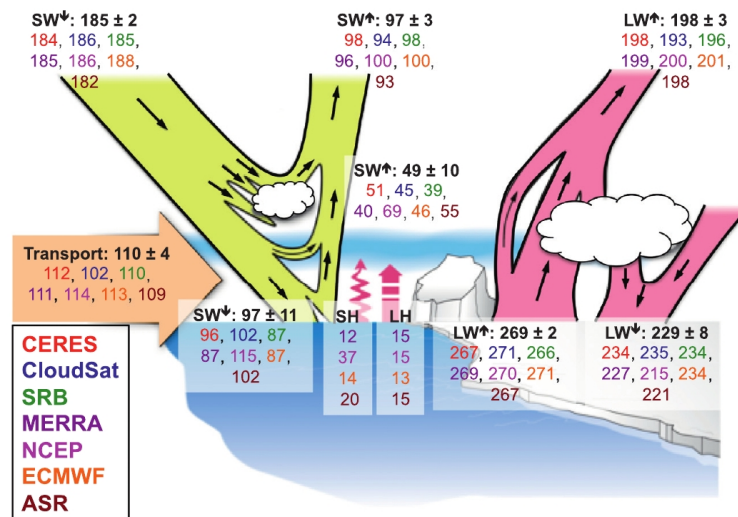


Figure 1.2: Diagram of the annual energy budget for the Arctic ($70\text{--}82^\circ\text{N}$). The solar (SW) and thermal infrared (LW) flux are shown in yellow and pink, respectively. The orange arrow indicates the heat transport to the Arctic. The Squiggly and broken upward arrows denote the sensible heat (SH; H_s) and latent heat (LH; H_l), correspondingly. All fluxes are expressed in W m^{-2} . The Figure is obtained from Christensen et al. 2016.

radiation, but at the same time, will enhance the emission of TIR at the TOA interacting with the Planck and the Lapse rate feedbacks [Crook et al. 2011].

In the Arctic region, several studies have given attention to the Cloud Radiative Effect (CRE) at the surface due to the influence of clouds on surface processes [see Section 2.6]. During the winter months, the downward TIR radiation increases the warming at the surface leading to further sea ice melt. During this season, the net CRE ranges from about 5 to 60 W m^{-2} . During spring and autumn the CRE is dominated by the TIR flux with a net CRE ranging from about 10 to 55 W m^{-2} , and 2 to 60 W m^{-2} , respectively [Intrieri et al. 2002a; Ebell et al. 2020].

During summer, at SHEBA and Ny-Ålesund it was reported values of net CRE in the range of -2 to 0 W m^{-2} and -150 to -5 W m^{-2} , respectively [Intrieri et al. 2002a; Ebell et al. 2020]. Furthermore, the study of Dong et al. 2010 presents a 10-year analysis of the CRE and has reported a summer seasonal mean CRE of -26.2 W m^{-2} , denoting once more an important contribution of CRE_{SOL} during summer. The SOL CRE is substantially sensitive to the surface conditions, solar zenith angle, and cloud properties.

The studies mentioned are time- and site-dependent, and there is still significant uncertainty on the cloud conditions and their role in the Arctic radiation budget. This is even more evident over the Arctic Ocean, where observations are infrequent or non-existent. Thus, extending surface observations is imperative to understand small scale processes further and validate model results and satellite observations for long term, large scale analyses.

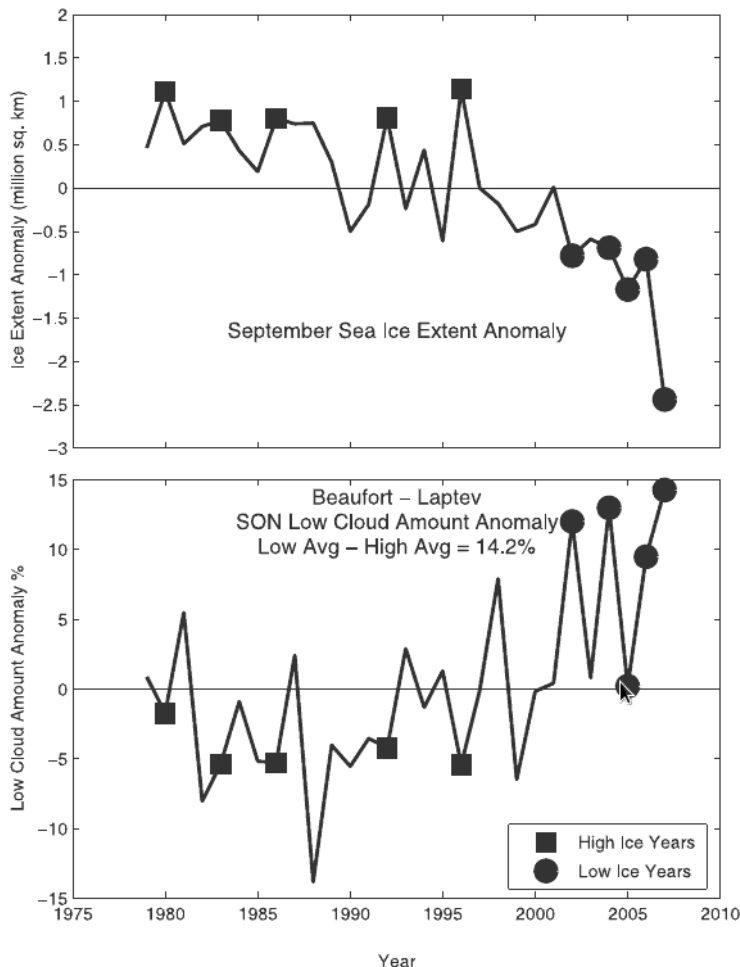


Figure 1.3: Series of September Arctic sea ice extent anomaly with high- and low-ice years shown (top), and the time series of autumn low cloud cover anomaly showing cloud anomalies during high- and low-ice years (bottom). Figure obtained from Eastman and Warren 2010

1.4 Link Between Arctic Clouds and Surface Conditions

The surface conditions are a key parameter affecting the formation, persistence and morphological conditions of clouds. Simultaneously, clouds contribute to the surface characteristics by regulating the heat transmitted from the atmosphere to the surface. Arctic clouds reduce the amount of SOL radiation absorbed by reduced sea ice, and at the same time, enhance the warming by means of enhanced TIR radiation. Therefore, it is critical to understand the relation between clouds and the surface-albedo feedback. Several studies have focused on the influence of clouds on the seasonal variability of Arctic sea ice loss and how the latter is connected to the surface-albedo feedback [Francis et al. 2005; Kay et al. 2008; Kay et al. 2011; Schweiger et al. 2008; Eastman and Warren 2010; Palm et al. 2010; He et al. 2019; Choi et al. 2020].

The studies of Eastman and Warren 2010 and He et al. 2019 found an evident correlation between the reduction of sea-ice concentration and low-level cloud fraction

over the Beaufort and Laptev Sea. Figure 1.3 shows the autumn time series of sea ice extent anomaly (top) and the low cloud amount anomaly over the Beaufort and Laptev Sea (bottom). Figure 1.3 suggests a clear relation between the increase of low cloud cover and the sea ice extent, with a larger correlation for the sea ice minima observed in 2007.

Passive microwave satellite observations show downward trends of sea ice extent since 1979. While the minimum sea ice extent has an inter-annual variability, in 2007 the minimum extent reached a dramatic low-value [Stroeve et al. 2008]. Focusing on this year, several studies demonstrated that an anti-cyclonic pattern of the summer atmospheric circulation in the Western Arctic leads to reduced cloudiness that enhances the absorption of downward solar radiation at the surface. The increase in absorption of solar radiation leads to warmer temperatures causing a decrease in sea ice extent [Kay et al. 2008; Zhang et al. 2008; Dong et al. 2013].

1.5 Objectives of (AC)³ and this Thesis

The Collaborative Research Center/Transregio (CRC/TR172) (AC)³ during its first phase aimed to further investigate key atmospheric processes contributing to Arctic Amplification based on satellite observations, collected observations obtained during field campaigns, and modelling activities that were in close collaboration with the field campaigns [Wendisch et al. 2019].

The (AC)³ phase 1 research project was organized into 5 scientific clusters. Cluster A focused on energy fluxes in the Arctic boundary layer, B studied clouds, aerosols and water vapour, C analysed surface processes and atmospheric trace gases, D investigated atmospheric circulation and transport, and E was the cluster that integrated and synthesized clusters A-D. Within cluster A, project A01 was dedicated to studying Arctic aerosol, cloud, and radiation characteristics from ship-based observations during the summer of 2017.

In project (AC)³ phase 1, two campaigns were held in 2017, performing in-situ and remote sensing observations of atmospheric parameters over the Arctic Ocean. The **A**rctic **C**loud **O**bservations **U**sing **A**irborne **M**easurements during **P**olar **D**ay (ACLOUD) aircraft campaign took place from 23 May to 6 June [Wendisch et al. 2019; Ehrlich et al. 2019]. The PS106 campaign was integrated by the **P**hysical **F**eedbacks of **A**rctic **B**oundary **L**ayer, **S**ea **I**ce, **C**loud and **A**erosol (PASCAL) expedition that took place aboard the German Research Vessel (R/V) Polarstern from 24 May to 21 June, with several remote sensing observations continuing during the second leg with **S**urvival of **P**olar **C**od in a **C**hanging **A**rctic **O**cean (SiPCA) cruise from 23 June to 20 July [Macke and Flores 2018] [see Fig. 1.4].

Project A01 aimed to explore the role of clouds and aerosols in the radiation budget by focusing on the observations obtained during the PS106 expedition. The atmospheric observations were obtained with the mobile remote sensing platform OCEANET, which was set up aboard Polarstern [Macke 2009; Kalisch and Macke 2012; Hanschmann et al. 2012; Kanitz et al. 2013]. Furthermore, in situ observations of downward solar and terrestrial radiation were collected on the top of the OCEANET container and a network of pyranometers was set up over an ice floe to investigate the spatiotemporal variability of solar radiation from 4 to 16 June

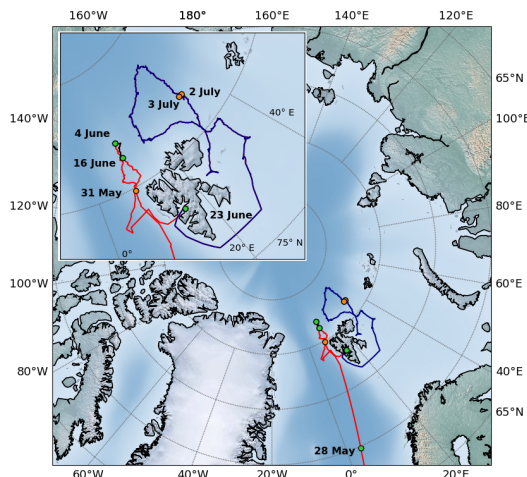


Figure 1.4: Cruise track of the PS106 Polarstern expedition is shown on a polar stereographic map of the Arctic. The red line shows the track for the first leg (PS106/1, also denoted as PASCAL), the black line indicates the position for the ice floe camp during PASCAL, and the blue line shows the cruise track for the second leg (PS106/2, also denoted as SiPCA). The upper left box zooms in the ice floe camp drift. Green dots indicate the start of PASCAL and SiPCA legs, and the beginning and end of the ice floe camp. Orange dots depict the location of several case studies discussed in chapter 7. Figure adapted from Barrientos-Velasco et al. 2022.

2017. For PS106, the remote sensing observations collected aboard Polarstern were subsequently utilized to derive cloud macro and micro physics properties of clouds based on the Cloudnet algorithm [Illingworth et al. 2007; Griesche et al. 2020].

As part of project A01 in (AC)³ phase 1, this thesis aims to improve the understanding of the radiation budget by investigating the interaction between clouds and surface parameters based on the comprehensive measurements obtained during the PS106 cruise and by determining the CRE by carrying out radiative transfer simulations for the entire cruise. Furthermore, the analysis is extended by including satellite remote sensing products with the aim to provide a spatial and potential climatological context. The scope of this thesis is motivated by the following research questions:

1. Do we understand cloud radiation interactions in the Arctic?
2. Under which conditions can state-of-the-art shipborne and passive satellite remote sensing observations constrain the radiative effects of clouds?
3. Can we quantify the effects of clouds on the surface radiation budget, and how representative are the PS106 results for the entire Arctic?

1.6 Outline

The thesis is structured as follows: chapter 2 introduces the theoretical background for the present thesis. chapter 3 presents the instrumentation, the main data sets analysed in the thesis and describes the main meteorological conditions during the

PS106 cruise. This chapter is followed by a sensitivity analysis of a standard clear-sky and cloudy atmosphere in chapter 4. The investigation of small scale variability of solar radiation variability is presented in chapter 5. chapter 6 describes the radiative closure for the entire PS106 cruise. This chapter is followed by the description of selected cases studies that present the radiative closure and the cloud radiative effects in chapter 7. The analysis of the cloud radiative effect is extended for the PS106 cruise and the Arctic region by considering satellite products in chapter 8. Finally, in chapter 9, the thesis closes with conclusions and gives an outlook for future research.

Chapter 2

Theoretical Background

This chapter introduces the theoretical background on atmospheric radiative theory based on the textbooks of Wendisch and Yang 2012, Yung 2003, and Petty 2006. The radiative quantities are introduced in section 2.1. The definitions of radiative interactions are presented in section 2.2. This section is followed by the description of the radiative transfer equation (section 2.3). Relevant radiative transfer interactions in the Arctic are presented in section 2.4. This is followed by the description of the radiative transfer modelling used in this thesis in section 2.5. This chapter ends with an explanation of the energy budget and cloud radiative effect (subsection 2.6).

The most relevant process responsible for the energy transfer in the atmosphere is the electromagnetic (EM) radiation. The EM radiation transports energy in the form of waves, which are often described in terms of their wavelength (λ) [see Eq. 2.1].

$$\lambda = \frac{c}{\tilde{\nu}}. \quad (2.1)$$

In Equation 2.1, $\tilde{\nu}$ represents the frequency and c is the speed of light in a vacuum [$2.998 \times 10^8 \text{ ms}^{-1}$]. Throughout his work, the analysis focusses on the solar [SOL; 0.2-5 μm] and thermal infrared [TIR; 5-50 μm] broadband spectral range, also referred to as shortwave and longwave radiation.

2.1 Radiative Quantities

To describe the transfer of radiation several definitions should be introduced. The spectral radiant energy flux Φ_λ describes the power of the EM radiation at a certain position and time. In other words, it describes the relation of the radiant energy E_{rad} in a time t ($t + dt$) and a wavelength (λ) range ($\lambda + d\lambda$), as indicated by equation 2.2.

$$\Phi_\lambda = \frac{d^2 E_{rad}}{dt d\lambda}. \quad (2.2)$$

In equation 2.2, the term Φ_λ is expressed in units of W nm^{-1} . The energy flux density or spectral radiance [F_λ] can be determined by normalizing Φ_λ to the corresponding area element $d^2 A$ [see Eq. 2.3 and Fig. 2.1].

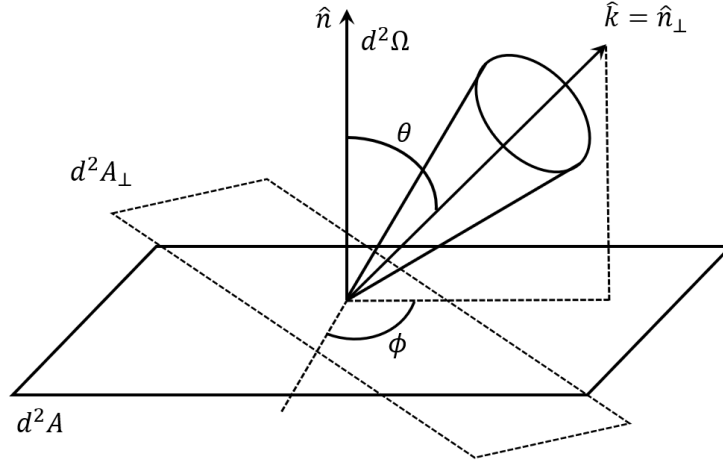


Figure 2.1: Geometry of the definition of radiance.

$$F_\lambda = \frac{d^2 \Phi_\lambda}{d^2 A} = \frac{d^4 E_{rad}}{d^2 A dt d\lambda}. \quad (2.3)$$

where F_λ is expressed in $\text{W m}^{-2} \text{nm}^{-1}$ and quantifies the spectral radiant energy flux through the unit area from the complete hemisphere. The spectral radiance or intensity $I_\lambda \hat{k}$ (in units of $\text{Wm}^2 \text{nm}^{-1} \text{sr}^{-1}$), within a solid angle $d^2\Omega$, in a specific direction \hat{k} is given by:

$$I_\lambda(\hat{k}) = \frac{d^4 \Phi_\lambda}{\cos \theta d^2 A d^2 \Omega} = \frac{d^6 E_{rad}}{dt d\lambda \cos \theta d^2 A d^2 \Omega}. \quad (2.4)$$

where θ is the angle of incidence. In other words, it is the angle between the normal unit vector of the area element, \hat{n} , and \hat{k} (see Figure 2.1). The expression $\cos \theta d^2 A = d^2 A_\perp$ indicates the propagation of the spectral radiant energy flux. Thus, in polar coordinates, the spectral radiance can be obtained by integrating the spectral radiance over the solid angle, as indicated in Equation 2.5.

$$F_\lambda = \iint_{2\pi} I_\lambda(\hat{k}) \cdot \cos \theta d^2 \Omega = \int_0^{2\pi} \int_0^\pi I_\lambda(\theta, \phi) \cdot \cos \theta \cdot \sin \theta d\theta d\phi, \quad (2.5)$$

The atmospheric transmission or transmittance (AT_g) is a term that characterizes the fraction of radiation that passes through the atmosphere at different solar zenith angles [SZA; θ] and sky conditions. The AT_g can be derived with Equation 2.6, where μ_o is the cosine of θ , F_o is the solar constant with a value of 1360.8 W m^{-2} [Kopp and Lean 2011], ϵ is the actual Earth-Sun distance in astronomical units (AU).

$$AT_g = \left[\frac{F_\lambda^\downarrow}{\epsilon^2 \cdot F_o \cdot \mu_o} \right]. \quad (2.6)$$

2.2 Radiative Interactions

A pencil of radiation that traverse a medium will be weakened by its interaction with matter. In the atmosphere, gas molecules, aerosols, cloud droplets, and ice crystals contribute to the extinction of solar and emission of terrestrial radiation.

Each of the contributions is dependent on the radiation, the concentration of the mentioned particles, and their absorbance or scattering properties.

The intensity of radiation I_λ becomes $I_\lambda + dI_\lambda$ after passing through a thickness ds in the direction of its propagation as indicated by

$$dI_\lambda = -k_\lambda \rho I_\lambda ds, \quad (2.7)$$

where ρ is the density of the material, k_λ denotes the mass extinction cross-section for a specific wavelength.

In the following subsections, relevant definitions related to absorption, scattering, and extinction are summarized considering that the atmosphere is highly stratified. This approximation, also referred to as the plane-parallel approximation, is used since the properties such as pressure, temperature, density, composition vary more vertically than horizontally.

2.2.1 Absorption

The absorption describes how matter takes up the energy of a photon and transforms the EM energy into thermal or chemical energy. A pencil of radiation traversing an absorbing and emitting medium will be weakened due to its interaction with matter through absorption or strengthened by thermal emission from the medium.

The absorption of different molecules in the atmosphere occurs differently along the EM spectrum. The absorption in the visible [$0.4 \mu m < \lambda < 0.7 \mu m$] and near Infrared (IR) [$0.7 \mu m < \lambda < 4 \mu m$] are dominated by the oxygen [0.76, 0.69, 0.63 μm], ozone [visible, UV, 1.58, 1.27, 1.06 μm bands], water vapour [0.94, 0.82, 0.72, Visible, 4.3, and 2.7 μm bands], carbon dioxide [2.0, 1.6, 1.4, 4.74, 3.3 μm bands], and other minor gases like nitrous oxide [4.06, 3.9, 2.97, 2.87, 3.83, 3.53, 3.31, 3.26 μm bands], carbon monoxide [4.67 and 2.34 μm bands], methane [2.2 and 1.66 μm bands], and nitrogen dioxide [visible bands]. The description of the absorption in the TIR and SOL radiation is summarized in the following subsections.

Absorption in the TIR radiation

The general equation for the radiative transfer in an absorbing and emitting medium is given in Equation 2.8 in terms of the differential change in the radiance.

$$\frac{1}{k_\lambda \rho_a} \frac{dI_\lambda}{ds} = -I_\lambda + J_\lambda. \quad (2.8)$$

In Equation 2.8, the k_λ is the absorption coefficient, ρ_a is the density of absorbing gases, s is the slant path, and J_λ is the source function for the absorbing and emitting medium¹. It is commonly assumed that the radiance is independent of time, the atmosphere is in thermodynamic equilibrium, and that the variation of radiance and atmospheric parameters [e.g., temperature and gas profiles] vary vertically². Under these conditions, the absorption and emission process is considered to be symmetrical with respect to the azimuthal angle [ϕ]. Under these assumptions, the basic equation that describes the TIR radiation in height coordinate may be written as

¹The source function is given by the Planck function and can be expressed as $B_\lambda(T)$

²This term is also referred to as plane-parallel assumption

$$\mu \frac{dI_\lambda(z, \mu)}{k_\lambda \rho_a dz} = I_\lambda(z, \mu) - B_\lambda(T(z)). \quad (2.9)$$

where $B_\lambda(T)$ is the Planck intensity.

The absorption of energy by molecules and particles leads to emission, which is associated with blackbody radiation. The blackbody concept is used to describe a material where the absorption is complete.

The intensity of radiation emitted by a blackbody is described by the Planck's Function, which relates the emitted monochromatic intensity to the frequency and temperature of the emitting material as described by Equation 2.10 [$W m^{-2} \mu m^{-1} sr^{-1}$].

$$B_\lambda(T) = \frac{2hc}{\lambda^5 (e^{hc/k_B \lambda T} - 1)}, \quad (2.10)$$

where h is the Planck's constant [6.626×10^{-34} J s] and k_B is the Boltzmann's constant [1.3806×10^{-23} J/K].

The Stefan Boltzmann law gives the broadband flux emitted by a blackbody and is calculated by integrating Plank's function over all wavelengths and over the 2π steradians of solid angle of one hemisphere [Petty 2006; see Equation 2.11].

$$F(T) = \sigma T^4. \quad (2.11)$$

Equation 2.11 states that the flux density emitted by a blackbody is proportional to the fourth power of the absolute temperature, where σ is 5.67×10^{-8} $W m^{-2} K^{-4}$.

Absorption in the SOL radiation

Assuming a plane-parallel and non-scattering atmosphere, the absorption of the SOL radiation defined as normal absorption optical depth ($\tau(z)$) for a monochromatic wavelength and for a specific absorber is given by:

$$\tau(z) = \int_z^\infty n(z) \sigma_a dz, \quad (2.12)$$

where σ_a is the absorption cross-section [cm^2], and $n(z)$ is the number density [cm^{-3}] for a specific absorber. The number density can be calculated with Equation 2.13

$$\tau(z) = n_0 e^{-z/H}, \quad (2.13)$$

where n_0 is the value of n at some arbitrary level at which z is taken to be zero, H is the scale height.

2.2.2 Scattering and Extinction

The scattering occurs when the beam of radiation changed of direction out of the original direction. The extinction is the result of the absorption plus the scattering. A way to characterize the contribution of each parameter is by determining their coefficients β [see Eq. 2.14].

$$\beta_{ext} = \beta_{abs} + \beta_{sca}. \quad (2.14)$$

The relative importance of the scattering versus the absorption in a medium can be determined by the single scattering albedo $\tilde{\omega}$. This parameter indicates how much incident radiation is scattered or absorbed. A $\tilde{\omega}$ equal to 1 indicates a conservative scattering where there is no absorption, a $\tilde{\omega}$ equal to zero means only absorption.

$$\tilde{\omega} = \frac{\beta_{sca}}{\beta_{ext}}. \quad (2.15)$$

In terms of the geometric cross-sectional area of a particle, A [$A = \pi r^2$], it is possible to define the extinction, absorption and scattering cross-sections C in m^2 , which relates to the incident irradiance F_{inc} in $W m^{-2}$ and the radiant energy flux Φ in W [see Equation 2.16].

$$C_{ext} = \frac{\Phi_{ext}}{F_{inc}}, \quad C_{abs} = \frac{\Phi_{abs}}{F_{inc}}, \quad C_{sca} = \frac{\Phi_{sca}}{F_{inc}}. \quad (2.16)$$

For volumetric properties it is assumed a population of suspended particles in a confined volume. These properties are weighted by the size distribution ($dN/d\log D$) and are obtained by integrating the single-scattering optical properties.

The extinction $\langle \beta_{ext}(\lambda) \rangle$, and scattering $\langle \beta_{sca}(\lambda) \rangle$ coefficients are calculated with Equation 2.17 and 2.18, respectively expressed in m^{-1} .

$$\langle \beta_{ext}(\lambda) \rangle = \int_0^\infty C_{ext}(\lambda, D') \cdot \frac{dN}{dD'}(D') dD'. \quad (2.17)$$

$$\langle \beta_{sca}(\lambda) \rangle = \int_0^\infty C_{sca}(\lambda, D) \cdot \frac{dN}{dD'}(D') dD'. \quad (2.18)$$

$$\begin{aligned} \langle \beta_{abs}(\lambda) \rangle &= \int_0^\infty C_{abs}(\lambda, D) \cdot \frac{dN}{dD'}(D') dD' \\ &= \langle \beta_{ext}(\lambda) \rangle - \langle \beta_{sca}(\lambda) \rangle. \end{aligned} \quad (2.19)$$

with C_{ext} , C_{sca} , and C_{abs} in m^2 , dN/dD' in m^{-3} .

The ratio of the size of a particle to the wavelength is of crucial importance to determine the scattering. The effect of particle size on scattering is given by the size parameter (x). For spherical particles, it is defined as:

$$x = \frac{2\pi \cdot r}{\lambda}, \quad (2.20)$$

where r is the radius of a spherical particle and λ is the incident wavelength. For particles whose sizes are $x \ll 1$, the scattering is referred to as Rayleigh scattering. If the particles are similar or larger than the wavelength ($x \gtrsim 1$) the scattering is named Lorenz-Mie scattering (see Fig. 2.2).

Non-spherical particles like dry aerosol particles, ice crystals, large precipitation droplets can be described with Lorenz-Mie theory by use of a simplified assumption that the volume or surface is considered equivalent to a sphere. Non-spherical scattering can be studied using analytical methods, numerical techniques or approximate methods [Wendisch and Yang 2012; Macke et al. 1998].

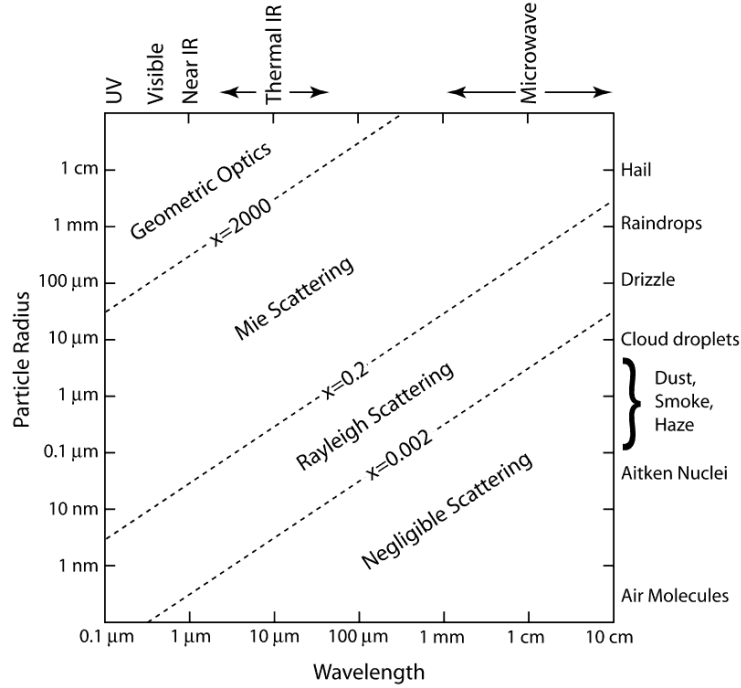


Figure 2.2: Scattering regimes for atmospheric particles, where $x = \alpha = 2\pi \cdot r / \lambda$. Figure obtained from Petty 2006.

2.3 Radiative Transfer Equation

The Radiative Transfer Equation (RTE) describes the propagation of the electromagnetic radiation in the atmosphere, and the interaction with matter (e.g., cloud particles, aerosol particles, molecules). The RTE is determined by the single scattering albedo ($\tilde{\omega}$), scattering phase function (p), extinction coefficient (β_{ext}).

In a scenario where the scattering is not important β_e is equal β_a . Under these conditions, the equation of Schwarzschild [Eq. 2.21] describes that the radiance along a particular medium is able to increase or decrease with the distance travelled depending on whether the radiant intensity at a point s ($I(s)$) is less than or greater than the Planck's Function [Eq. 2.10].

$$\frac{dI}{ds} = \beta_a(B - I). \quad (2.21)$$

The inclusion of scattering needs the consideration of the radiation passing through an infinitesimal volume from any direction $\hat{\Omega}'$ that can potentially contribute to the scattered radiation in the direction of interest $\hat{\Omega}$. This relation is expressed in equation 2.22:

$$dI_{sca} = \frac{\beta_s}{4\pi} \int_{4\pi} p(\hat{\Omega}', \hat{\Omega}) I(\hat{\Omega}') dw' ds, \quad (2.22)$$

where the integral is over the 4π steradians of the solid angle, and the scattering phase function $\mathcal{P}(\hat{\Omega}', \hat{\Omega})$.

The complete differential form of the radiative transfer equation is given in Equation 2.23.

$$dI = -\beta_e I ds + \beta_a B ds + \frac{\beta_s}{4\pi} \int_{4\pi} p(\hat{\Omega}', \hat{\Omega}) I(\hat{\Omega}') dw' ds. \quad (2.23)$$

The second and last term of Equation 2.23 represent the thermal emission and scattering, respectively. The sum of both terms divided by $d\tau$ [$d\tau = -\beta_e ds$] represents the source function $J(\hat{\Omega})$. Note that if \tilde{w} is zero the scattering term vanishes, and if \tilde{w} is equal to one, the thermal emission vanishes.

In a plane parallel atmosphere, the RTE is adapted to specify the direction of the propagation of the radiation from the zenith. Considering the Equation 2.23 and the relation with $d\tau$, the RTE for a plane parallel atmosphere is expressed as:

$$\frac{dI(\hat{\Omega})}{d\tau} = I(\hat{\Omega}) - (1 - \tilde{w})B - \frac{\tilde{w}}{4\pi} \int_0^{2\pi} \int_{-1}^1 p(\mu, \phi; \mu', \phi') I(\mu', \phi') d\mu' d\phi'. \quad (2.24)$$

The RTE presented in Equation 2.40 indicates that in order to determine $I(\mu, \phi)$ at any particular level τ in the atmosphere, one must simultaneously determine $I(\mu', \phi')$ for all values of μ' and ϕ' and for all the other values of τ , which suggests that the solution is impossible unless one considers restrictive assumptions. Therefore, several alternative methods have been developed in the field of radiative transfer throughout the years. Several numerical solutions have been created to solve the RTE. One of the most straightforward possible analytical solutions is the two-stream approximation method which is presented in the following section.

2.4 Radiative Transfer in the Arctic

The study of atmospheric radiative transfer in the Arctic relates to the evident interaction between the state of the atmosphere and the surface conditions. This is particularly complex in the Arctic due to the contrasting and variable surface conditions and characteristic annual insolation. The following subsections provide a general description of relevant parameters affecting the radiative transfer.

2.4.1 Surface Reflection and Transmission

The reflection (R) or transmission (T) function of SOL radiation depend on the solar flux density in the direction of the incident beam [F_\odot] and their relation with the solar zenith and azimuth angle. The physical definitions of local albedo or reflection (r) and transmission (t) are given as:

$$r(\mu_0) = \frac{F_{dif}^\uparrow(0)}{\mu_0 F_\odot} = \frac{1}{\pi} \int_0^{2\pi} \int_0^1 R(\mu, \phi; \mu_0, \phi_0) \mu d\mu d\phi, \quad (2.25)$$

$$t(\mu_0) = \frac{F_{dif}^\downarrow(\tau_1)}{\mu_0 F_\odot} = \frac{1}{\pi} \int_0^{2\pi} \int_0^1 T(\mu, \phi; \mu_0, \phi_0) \mu d\mu d\phi. \quad (2.26)$$

For clarification, the direct transmission is defined as $e^{-\tau_1/\mu_0}$. Similarly, the absorption between the optical depths of 0 and τ_1 can be obtained from the net flux density

divergence that considers the direct transmission components at levels 0 and τ_1 and normalized by $\mu_0 F_\odot$.

In the TIR, the upward surface flux is determined by the emission from the surface [ϵ_s] and, in a cloudy atmosphere, the reflection of the flux emitted from the cloud base [F_c^\downarrow].

$$F_s^\uparrow = \epsilon_s \sigma T_s^4 + (1 - \epsilon_s) F_c^\downarrow. \quad (2.27)$$

2.4.2 Clear-sky Conditions

During clear-sky conditions, the absorption of atmospheric gases [see section 2.2.1] and radiative interaction with aerosols are relevant for the radiation transfer. In the Arctic, however, the radiative interactions with aerosols are less significant as in mid-latitudes or the tropics [Yu et al. 2006].

Under clear-sky conditions, the radiative interactions between the atmosphere and the surface are different during polar day and night. In the scenario of a clear-sky atmosphere during the polar day, there is more absorption of the solar radiation at the surface, leading to an increase of surface temperature yielding to a reduction of sea ice [Kay et al. 2008; Sedlar and Devasthale 2012]. During the polar night, a warmer atmospheric scenario can lead to weaker static stability leading to larger upwards surface turbulent fluxes, which in turn increase the warming and moisture processes increasing the downward thermal infrared fluxes. These processes can enhance the formation of clouds and, therefore, increase the warming of the surface [see the following subsection for physical explanation].

2.4.3 Optical Properties of Clouds

The presence of clouds contribute to the increase of solar flux reflected back to space. This effect, referred to as the solar albedo effect, reduces the solar flux available in the atmosphere leading to a cooling of the Earth's system. Clouds reduce the thermal radiation emitted to space by absorbing the thermal flux from the surface and the atmosphere below the cloud layer, and also by emitting thermal radiation at generally colder cloud-top temperatures. This process leads to a greenhouse effect. The intensity by which both processes interact in the Earth's system depends on the geometric space and position, thermodynamic phase, and particle size distribution [dN/dD']³.

Clouds reflect and absorb both solar and terrestrial radiation. The intensity of the absorption and reflectance depends on their optical depth⁴ [τ ; Eq. 2.28], their single scatter albedo [$\langle\tilde{\omega}(\lambda)\rangle$, Eq. 2.29] and scattering phase function [$\langle p(\lambda, \vartheta)\rangle$; Eq. 2.30]. These properties depend on the size parameter x and the complex index of refraction m for the constituent particles of the cloud, which depend on the wavelength λ , and x also depends on the droplet or ice crystal radius. The index of refraction m depends on composition and material phase, which can be liquid or ice, or in more complex conditions mixed-phase.

³D is the geometrical particle diameter.

⁴Also known as optical thickness.

The dimensionless (τ) is the integral of the extinction coefficient ($\langle\beta_{ext}(\lambda)\rangle$) of a cloud between cloud base (z_{base}) and cloud top (z_{top}).

$$\tau = \int_{z_{base}}^{z_{top}} \langle\beta_{ext}(\lambda)\rangle(z') dz'. \quad (2.28)$$

$$\langle\tilde{\omega}(\lambda)\rangle = \frac{1}{\langle\beta_{ext}(\lambda)\rangle} \int_0^\infty \tilde{\omega}(\lambda, D') \cdot C_{ext}(\lambda, D') \cdot \frac{dN}{dD'}(D') dD'. \quad (2.29)$$

$$\langle p(\lambda, \vartheta)\rangle = \frac{1}{\langle\beta_{sca}(\lambda)\rangle} \int_0^\infty p(\lambda, \vartheta, D') \cdot C_{sca}(D') \cdot \frac{dN}{dD'}(D') dD'. \quad (2.30)$$

Equation 2.28 and 2.29 give dimensionless values, and in Equation 2.30 the values are expressed in sr^{-1} . The dimensionless scattering phase function, ($\mathcal{P}(\vartheta)$), represents the relative angular distribution of the scattered radiation by a particle where ϑ is the cosine of the scattering angle Θ . The relationship between the dimensionless scattering phase function and phase function $p(\vartheta)$ is given by Equation 2.31.

$$\mathcal{P}(\vartheta) = 4\pi sr \cdot p(\vartheta). \quad (2.31)$$

The term referred to as the asymmetry factor denotes the relative strength of the forward scattering and is related to the first moment of the phase function [see Eq. 2.32]. When g is equal to zero, the scattering is isotropic as it is in the case of the Rayleigh scattering if g is greater than zero, the photons are preferentially scattered into the forward hemisphere in relation to the original direction of travel, and if g is lower than zero, it indicates that the photons have a backward scattering. If g is equal to 1 indicates that the scattering into exactly the same direction as the photon was already travelling. A g equal to -1 indicates an unlikely scenario with every scattering event possible.

$$g = \frac{1}{2} \int_{-1}^1 p(\cos\Theta) \cos\Theta d \cos\Theta. \quad (2.32)$$

Microphysical Properties of Clouds

The microphysical properties of clouds are given by the cloud droplet size distribution. The mean droplet radius in an ensemble of cloud droplets, weighted by dN/dD' is characterized by the effective cloud droplet radius (r_E). The liquid effective radius ($r_{E,L}$) can be expressed as:

$$r_{E,L} = \frac{1}{2} \frac{\int D'^3 \frac{dN}{dD'}(D') dD'}{\int D'^2 \frac{dN}{dD'}(D') dD'}. \quad (2.33)$$

The r_E is defined as the ratio of the third to the second moment of the particle size distribution, which represents the ratio of volume of a cloud particle to its cross-sectional area. In case of ice crystals, r_E can be calculated with Equation 2.34. Grenfell and Warren 1999 represented each ice particle by a collection of spheres with the same ratio of volume to surface area as individual ice particles.

$$r_{E,I} = \frac{3}{4} \frac{\int V_D(D') \cdot \frac{dN}{dD'}(D') dD'}{\int A_D(D') \cdot \frac{dN}{dD'}(D') dD'}. \quad (2.34)$$

In Equation 2.34, V is the volume and A is the surface A by a collection of spheres.

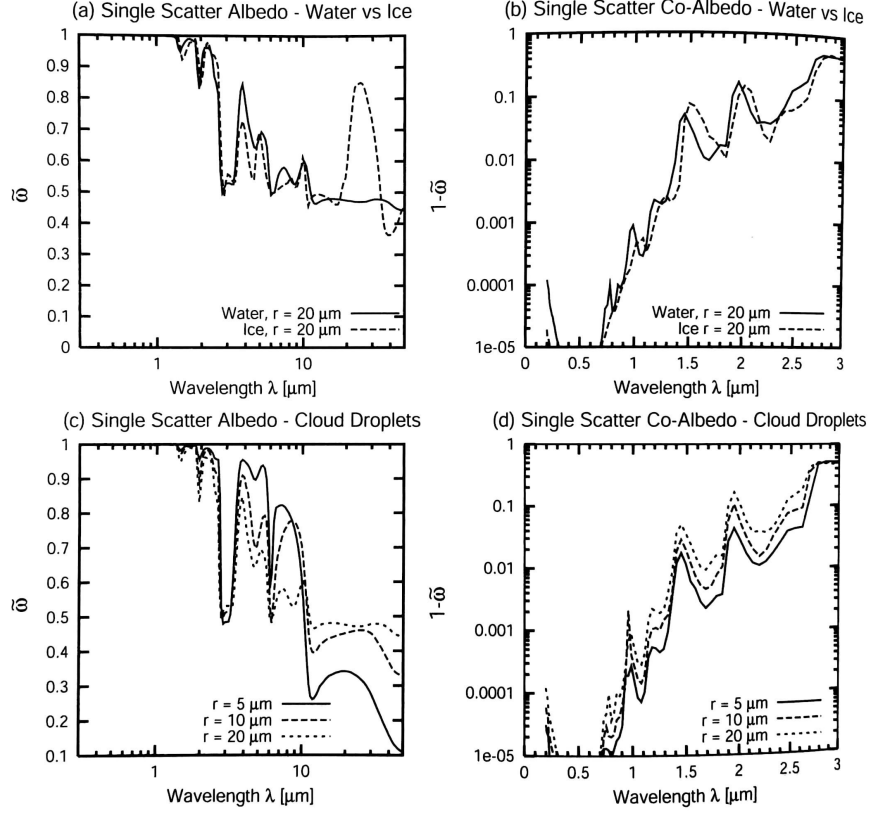


Figure 2.3: Single scattering albedo ($\tilde{\omega}$) and co-albedo (defined as $1-\tilde{\omega}$) as a function of wavelength for water and ice particles of several sizes. Panels (a) and (c) depicts the $\tilde{\omega}$ over the visible [$0.4 \mu\text{m} < \lambda < 0.7 \mu\text{m}$], near IR [$0.7 \mu\text{m} < \lambda < 4 \mu\text{m}$] and TIR range [$4 \mu < \lambda < 50 \mu\text{m}$]. Panels (b) and (d) shows the scattering co-albedo for the solar band. Figure obtained from Petty 2006.

The liquid water content (q_L), expressed in gm^{-3} , refers to the mass of liquid water in a cloud volume of 1 m^3 .

$$q_L = \frac{4\pi}{3} \cdot \rho_w \int \left(\frac{D'}{2}\right)^3 \cdot \frac{dN}{dD'}(D')dD', \quad (2.35)$$

where ρ_w is the density of liquid water. The q_L can also be expressed using τ and r_E for a vertically homogeneous cloud from cloud base (z_{base}) to cloud top (z_{top} ; see Eq. 2.36).

$$q_L = \frac{2\rho_w}{3} \int_{z_{base}}^{z_{top}} \frac{r_E \cdot \tau}{z'} dz'. \quad (2.36)$$

The q_L for an adiabatic cloud can be obtained by replacing $\frac{2}{3}$ with $\frac{5}{9}$ [Wood and Hartmann 2006]. The vertical integration of q_L derives the liquid water path (Q_L) expressed in gm^{-2} units.

$$Q_L = \int_{z_{base}}^{z_{top}} q_L(z') dz'. \quad (2.37)$$

Similarly to the liquid phase, q and Q can be determined for the ice phase as indicated in Equation 2.38 and 2.39, respectively.

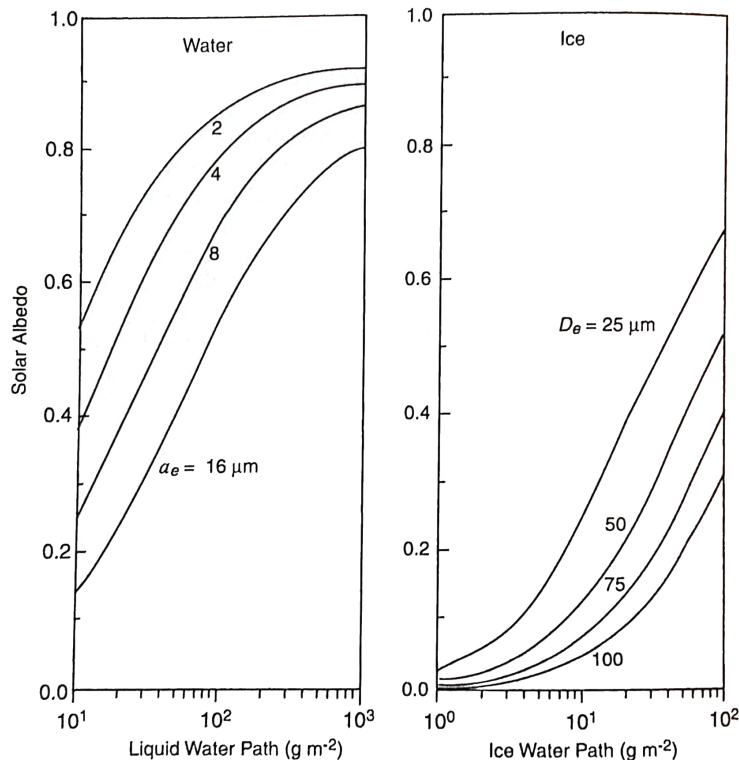


Figure 2.4: Broadband solar albedo of water and ice water clouds as a function of the liquid (Q_L) and ice water path (Q_I) and the mean effective water droplet radius (a_e ; here referred as $r_{E,L}$) and hexagonal ice crystals size (D_e ; here referred as $r_{E,I}$) for the solar spectrum $[0.2-5 \mu m]$. Figure obtained from Yung 2003

$$q_I = \rho_i \int V_D(D') \cdot \frac{dN}{dD'}(D') dD'. \quad (2.38)$$

$$Q_I = \int_{z_{base}}^{z_{top}} q_I(z') dz'. \quad (2.39)$$

where ρ_i is the mass density for ice particles.

The $\tilde{\omega}$ has large influence on how cloud reflectivity/absorptivity varies with at different λ . This is illustrated in Figure 2.3. The top panel of Figure 2.3 illustrates the complexity of the absorption regarding the particle phase. There is a significant difference in the single scatter albedo at several wavelengths between spherical ice and water particle of the same size. For some wavelengths, water droplets are less absorptive than the ice particles and vice versa. Moreover, for most of the wavelengths there is a clear dependence of the $\tilde{\omega}$ on the droplet radius in liquid clouds suggesting that, in general, the larger droplets are more absorptive than smaller droplets at the same wavelengths. For the solar band the absorption is rather weak, therefore the absorption of liquid and ice particle and the comparison of various water droplets sizes are represented with the scattering co-albedo.

Another way to understand the relation between cloud properties and radiation is by contrasting different values of r_E and Q with the solar albedo. Both, r_E and Q , have a direct relation with the cloud optical depth τ [see Eq. 2.37 and Eq. 2.39].

For a liquid and ice cloud, the solar albedo increases as the Q_L or Q_I increases. This effect is enhanced by smaller particles since smaller particles reflect more solar radiation due to its larger effective optical depth [see Fig. 2.4].

2.5 Radiative Transfer Modelling

This section describes the method used to solve the RTE [section 2.5.1] and also the method used to derive spectral radiances in the atmosphere [section 2.5.2]. Based on this theoretical background, the 1D radiative transfer model used in this thesis is described in more detail in section 2.5.3.

2.5.1 Two-stream Approximation

The two-stream is a discrete ordinate approximation that solves multiple scattering contribution by considering the upward and downward intensities weighted by the fraction of the forward and backward phase functions [Schuster 1905]. This methodology transforms the RTE into two first-order inhomogeneous differential equations. Considering that the contribution of a beam of radiation to the horizontal flux is dependent on the cosine of the zenith angle and not on the azimuthal angle, the RTE can be simplified as:

$$\mu \frac{dI(\mu)}{d\tau} = I(\mu) - \frac{\tilde{\omega}}{2} \int_{-1}^1 p(\mu, \mu') I(\mu') d\mu'. \quad (2.40)$$

Developing Equation 2.40 separately for each hemisphere yields the following equation:

$$\mu \frac{dI^\uparrow}{d\tau} = I^\uparrow - \frac{\tilde{\omega}}{2} \left[\int_0^1 p(\mu, \mu') d\mu' \right] I^\uparrow - \frac{\tilde{\omega}}{2} \left[\int_{-1}^0 p(\mu, \mu') d\mu' \right] I^\downarrow. \quad (2.41)$$

Considering the backscattered fraction b quantity into Equation 2.41 and sustaining the assumption that I is independent of μ in each hemisphere, it is obtained the two-stream equations for diffuse incidence.

$$\frac{1}{2} \frac{dI^\uparrow}{d\tau} = (1 - \tilde{\omega}) I^\uparrow + \tilde{\omega} \bar{b} (I^\uparrow - I^\downarrow). \quad (2.42)$$

$$-\frac{1}{2} \frac{dI^\downarrow}{d\tau} = (1 - \tilde{\omega}) I^\downarrow - \tilde{\omega} \bar{b} (I^\uparrow - I^\downarrow). \quad (2.43)$$

where \bar{b} is the mean backscatter fraction expressed as:

$$\bar{b} = \int_0^1 b(\mu) d\mu. \quad (2.44)$$

2.5.2 Correlated k -distribution

The correlated k distribution method uses the method of grouping gaseous spectral transmittances according to the absorption coefficient k_λ [see Eq. 2.8]. In a homogeneous atmosphere, the spectral transmittance $T_\lambda(u)$ is independent of the ordering

of k for a given spectral interval. Therefore, the integration over wavelength regions are replaced by the integration over the k space, as described by Equation 2.45.

$$T_{\bar{\lambda}}(u) = \int_{\Delta\lambda} e^{-k_{\lambda}u} \frac{d\lambda}{\Delta\lambda} = \int_0^{\infty} e^{ku} f(k) dk. \quad (2.45)$$

The probability distribution function of Equation is the inverse of the Laplace transform L^{-1} of the spectral transmittance such that

$$f(k) = L^{-1}(T_{\bar{\lambda}}(u)). \quad (2.46)$$

Furthermore, a cumulative probability function may be defined in the form

$$g(k) = \int_0^k f(k) dk, \quad (2.47)$$

where $g(0) = 0$, $g(k \rightarrow \infty) = 1$ and $dg(k) = f(k)dk$. Thus, by definition $g(k)$ is a monotonically increasing and smooth function in k space. By using the g function, the spectral transmittance can be defined as

$$T_{\bar{\lambda}}(u) = \int_0^1 e^{-k(g)u} dg \cong \sum_{j=1}^M e^{-k(g_j)u} \Delta g_j. \quad (2.48)$$

Consequently, the integration in g space replaces the wavelength integration and can be evaluated by a finite sum of exponential terms.

For nonhomogeneous atmosphere, the k -distribution can be extended with the correlated k -distribution method. In this method, the vertical nonhomogeneity of the atmosphere is considered by assuming a simple k -distribution at different temperature and pressures in a way that the spectral transmittance can be represented [see Eq. 2.49].

$$T_{\bar{\lambda}}(u) \cong \int_0^1 \exp\left[-\sum_j k_j(g) \Delta u_j\right] dg. \quad (2.49)$$

2.5.3 RRTMG

The present study uses the widely used rapid radiative transfer model (RRTM) for GCM applications (RRTMG; Mlawer et al. 1997; Barker et al. 2003; Clough et al. 2005). rapid radiative transfer model for general circulations application (RRTMG) is a Line-by-Line Radiative Transfer Model (LBLRTM) that utilizes the correlated-K approach to accurately calculate the SOL [0.2-12.20 μm] and TIR [3.08-1000 μm] fluxes and heating rates.

For the TIR and SOL, the RRTMG parameterization for ice and liquid optical properties are based on the radiative transfer model Streamer [Key 1996] and Hu and Stamnes 1993, respectively. In the model, ice crystals are assumed to be spherical with $r_{E,I}$ values between 5.0 and 131.0 μm . In the case of $r_{E,L}$, the model accepts values in the range from 2.5 to 60 μm .

Note that chapter 3.4 provides the specifications of the setup and input parameters used for the radiative transfer calculations considered in this thesis.

2.6 Energy Budget and Cloud Radiative Effect

The energy budget (E) is a fundamental property of the climate system that quantifies the energy fluxes between various interfaces of different compartments of the Earth's climate system [Loeb and Wielicki 2015]. At the TOA the energy budget is equivalent to the radiation budget and can be determined with Equation 2.50. At the surface the energy budget considers the net solar and terrestrial fluxes, turbulent sensible (H_s), and latent heat fluxes (H_l), and the conduction of heat to the surface (C) as indicated in Equation 2.51 where all compartments are expressed in W m^{-2} [Sedlar et al. 2010].

$$E^{TOA} = F^{TOA} = F_{SOL}^{\downarrow,TOA} - F_{SOL}^{\uparrow,TOA} - F_{TIR}^{\uparrow,TOA}. \quad (2.50)$$

$$E^{SFC} = (F_{SOL}^{\downarrow,SFC} - F_{SOL}^{\uparrow,SFC}) + (F_{TIR}^{\downarrow,SFC} - F_{TIR}^{\uparrow,SFC}) - H_s - H_l + C. \quad (2.51)$$

The energy budget can be calculated based on best estimates of global climate models constrained by surface and satellite observations [Wild et al. 2013]. Considering the focus of study, Figure 1.2 shows the magnitudes of the Arctic's averaged energy budget components.

The influence of clouds on the radiation budget is measured by determining the CRE. It is defined as the difference between the all-sky and clear-sky net fluxes in W m^{-2} at the SFC, ATM, and TOA [Mace et al. 2006]. The CRE can be calculated with equation 2.52, where x can be replaced with (SOL, TOA), (TIR, TOA), (SOL, SFC), (TIR, SFC). The estimation throughout the ATM is calculated by the difference between the TOA and the SFC. The CRE_{NET} , at the SFC, ATM, or TOA, is given by the sum of the CRE_{SOL} and CRE_{TIR} .

$$CRE_x = (F_x \downarrow - F_x \uparrow)_{all-sky} - (F_x \downarrow - F_x \uparrow)_{clear-sky}. \quad (2.52)$$

Chapter 3

PS106 Expedition, Instrumentation, Data sets, and Methods

This chapter embeds the description of different instrumentation used to observe several atmospheric and near-surface properties. It also presents different shipborne, ice-floe based and satellite-based data sets that are considered to describe the atmospheric and surface conditions during PS106 cruise and to use as the basis for the analysis carried out along this thesis. Finally, it is described the methods followed along with this thesis.

3.1 Instrumentation

During the PS106 ice floe camp (4 to 16 June 2017), 15 pyranometers stations were deployed to investigate the spatiotemporal variability of the downward solar radiation at the surface. Furthermore, the OCEANET facility and a cloud radar were installed aboard Polarstern to collect remote sensing observations of the atmosphere during the entire PS106 expedition. As part of OCEANET, meteorological observations and downward solar and terrestrial radiative fluxes were also measured.

3.1.1 Pyranometer Network

The Pyranometer Network (Pyrnet) was used in PS106 as a subset of 99 autonomous stations that were developed at the Leibniz Institute for Tropospheric Research (TROPOS) to investigate the spatiotemporal variability of global radiation induced by clouds. A detailed description of the 99 stations is given in Madhavan et al. 2016, and the description focused on the PS106 experiment is given in Barrientos-Velasco et al. 2020.

The pyranometer network was first deployed as part of the 'High Definition Clouds and Precipitation for advancing Climate Prediction' ($HD(CP)^2$) Observational Prototype Experiment (HOPE) field campaigns [Macke et al. 2017]. Besides the description provided in Madhavan et al. 2016, a detailed multi-resolution analysis of the spatiotemporal variability of solar irradiance for HOPE is given in Madhavan et al. 2017.

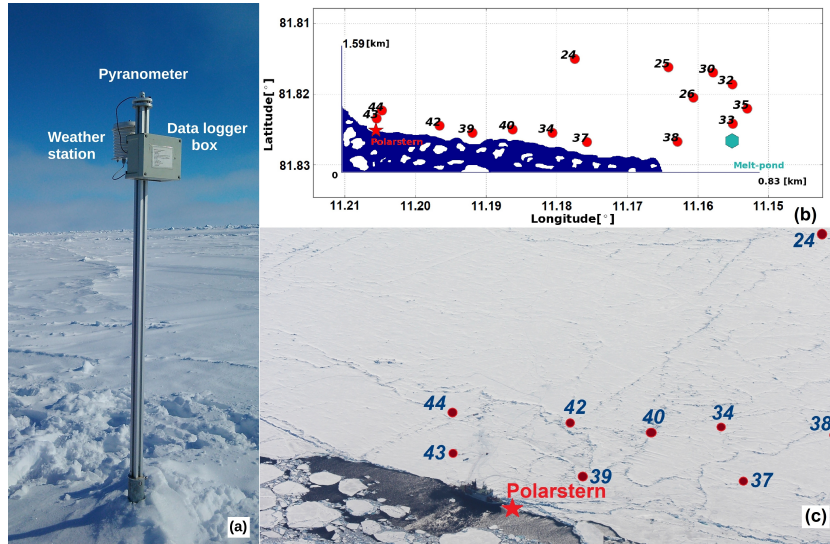


Figure 3.1: Characteristics of Pynnet set up in the Arctic. Panel (a) shows a photograph of a pyranometer station on the ice floe. Panel (b) shows the map of the pyranometer stations. Red circles show the location on 11 June 2017, at 14:50Z, while the red star marks the position of Polarstern, and the turquoise hexagon marks the approximate position of a melt-pond. Note that the latitude and longitude axes have been inverted for easier comparison with panel (c). Panel (c) edited photograph of the ice floe showing the approximate location of several stations (red circles) and Polarstern (red star). Photographed by Svenja Kohnemann. Figure adapted from Barrientos-Velasco et al. 2020.

The pyranometer network installed on an ice floe covered an approximate area of 0.83 km x 1.59 km, with individual stations separated by several decametres [see Fig. 3.1b and c]. The location of each station was limited by other observations that took place on the ice floe, as well as the maximum allowed safe distance from the ship of 1 nautical mile (1.8 km). From 4 June to 16 June, Polarstern drifted from 81.7 to 81.95 degrees northern latitude and from 9.86 to 11.58 degrees eastern longitude.

Each pyranometer station was mounted on an aluminium rod of 1.8 m height (Fig. 3.1a). The top of each station was equipped with a data logger containing a Global Positioning System (GPS) antenna module (model: Fastrax UP501), a meteorological station measuring relative humidity (RH) and air temperature (T_a), and an EKO Instruments silicon photodiode pyranometer with a spectral range of 0.3-1.1 μm (model: ML-020VM) at 1 Hz frequency. The spectral range of the photodiode pyranometer does not consider the spectral irradiance beyond 1.1 μm , which comprises about 22 % of the incoming solar energy [Nann and Riordan 1991]. Nevertheless, previous studies have demonstrated that the spectral range where higher cloud transmittance occurs between 0.3-0.7 μm [Wiscombe et al. 1984; Bartlett et al. 1998]. Therefore, the experimental setup considered is still expected to capture the main variability effects of atmospheric cloud transmittance.

The photodiode pyranometers used have an accuracy of about 5 %, which is substantially larger than measurement uncertainty achieved by state-of-the-art secondary standard thermopile pyranometers. It is worth mentioning that additional venti-

Table 3.1: Main components and specifications of a pyranometer station

1. Photodiode pyranometer sensor	Type (ML-0.20VM)
Response time	10ms
Zero offset - thermal radiation (200 Wm^{-2})	0 Wm^{-2}
Zero offset - temperature change (5 Kh^{-1})	0 Wm^{-2}
Non-stability ^a	$\pm 2 \%$
Non-linearity ^b	$\pm 0.2\%$
Temperature response ^c	$\pm 0.5 \%$
Spectral error (during the day)	$\pm 2\text{-}5 \%$
2.ADC data logger	Type (Driesen+Kern DKRF 4001-P)
Analog power supply output	3.3 V
Temperature range	-40 to $85 \text{ }^\circ\text{C}$
Differential linearity error (resolution)	± 1 Least significant bit (LSB)
Gain error	$\pm 5 \%$
3. Amplifier	Type (INA 333)
Operational temperature range	-40 to $+ 150 \text{ }^\circ\text{C}$
Power supply voltage range	1.8 - 5.5 V
Range of gain	1 to 1000
Gain error	$\pm 0.3 \%$ (Gain = 300)
4. GPS	Type (FasTrax UP501)
Position accuracy	1.8 m (CEP95)
Velocity accuracy	0.1ms^{-1}
Time accuracy	$\pm 50 \text{ ns(RMS)}$

^a % change in responsivity per year

^b % deviation from responsivity at 1000 Wm^{-2} due to change in irradiance %

^c % deviation due to change in ambient temperature from -10 to $50 \text{ }^\circ\text{C}$

lation and heating improve the data quality, in particular regarding dew, rain and frost on the pyranometers. However, such a set-up demands additional power that makes unfeasible an adaptation given the current version of a pyranometer station. Thus, the pyranometer network set-up is best suited for the investigation of spatial and temporal variability. The main components and specifications of a pyranometer station are presented in Table 3.1.

Sublimation occurring on the probe of the relative humidity sensor compromised the observations. Therefore, the values of this parameter are not recommended for use and are not considered in this study. The accuracy of the T_a measurements are $\pm 1.5 \text{ }^\circ\text{C}$ at $-40 \text{ }^\circ\text{C}$, increases linearly to $\pm 0.5 \text{ }^\circ\text{C}$ at $0 \text{ }^\circ\text{C}$ and remains stable up to $40 \text{ }^\circ\text{C}$. Finally, power for the system was supplied by a 6 V/19 Ah Zinc carbon VARTA 4R25-2 battery, allowing the system to work continuously for about 7 days.

Update of calibration coefficients

The pyranometers were calibrated in 2013 with a standard spectrum solar simulator by Eko Instruments after their production [Madhavan et al. 2016]. The stability of the calibration coefficients is specified to be better than 2 % per year. Note that additional uncertainties are introduced in the measurement system by the data logger and the gain of the instrument amplifier, as explained by Madhavan et al. 2016.

To update the calibration of the sensors and account for the spectral difference between a broadband pyranometer and the pyranometer network, an inter-comparison experiment was conducted in May 2018. The stations were set up in close vicinity to each other for 20 days on the roof of the main building at TROPOS in Leipzig, Germany. Out of this period, 2 hours of observations were chosen on a clear-sky day (10:30-12:30Z). These observations were compared to a recently calibrated secondary standard broadband thermopile pyranometer with a spectral range from 0.3 to 2.8 μm (model: Kipp & Zonen CMP21). After the comparison, the calibration coefficients were determined to minimize the difference between the network stations and the Kipp & Zonen pyranometer.

The mean of the original calibration coefficients was $7.38 \mu\text{VW}^{-1}\text{m}^2$, while the updated calibration coefficients had a mean value of $7.19 \mu\text{VW}^{-1}\text{m}^2$. This suggests that, on average, the sensitivity of the instruments decreased slightly by 2.5 % over time. Note that by updating the calibration, the root-mean-square error (RMSE) between the pyranometer stations and the reference pyranometer was reduced from 15.3 W m^{-2} to 4.5 W m^{-2} , thus showing a significant improvement.

Quality assurance

The quality of the observations consisted of checking the state of the cleanliness of the sensor's glass dome and the alignment of the levelling of the sensor. The quality control was performed daily, recording the status of the levelling and cleanliness to guarantee the accuracy of the global horizontal irradiance (GHI) observations.

Each station contains a levelling spirit ring that indicates the alignment. The levelling flag criterion is based on the bubble position of the spirit level of the pyranometer. When the bubble is located inside the inner ring, it is considered well-levelled when the bubble is in between the two rings, partially levelled, and outside the ring is not levelled. During the campaign, the complete misalignment occurred when the rod's base was no longer properly supported by the snow due to melting, leading to a tilt of the sensor and systematic errors, particularly for direct sunlight. The icing of the radiation sensor dome occurred when moist air masses with supercooled water droplets were present, which froze upon impact with the dome [Broeke et al. 2004]. This condition will generally lead to an underestimation of GHI.

The general status of the stations is presented in Figure 3.2. Every station is shown on the Y-axis, while the date is given on the X-axis. Each square is divided into two triangles, indicating the levelling status in the upper triangle and the cleanliness status in the lower one. The green colour represents a well-levelled and clean station, yellow shows a partially levelled station or a dome with liquid droplets, and red indicates completely not levelled stations or an iced dome. The analysis of the observations does not consider iced domes or completely not levelled stations (red flags). The presence of liquid droplets is considered in the study due to their likely short residence time around the dome and the fact that we have found observations to be still useful for our analysis. Furthermore, it is worth mentioning that during this likely short period, the presence of droplets is expected to cause a moderate underestimation of irradiance and more noisy observations, as it is later discussed in chapter 5.

During the study period, it is still possible that the domes were contaminated by droplets or ice before or after the daily quality assurance checks. Such events can be

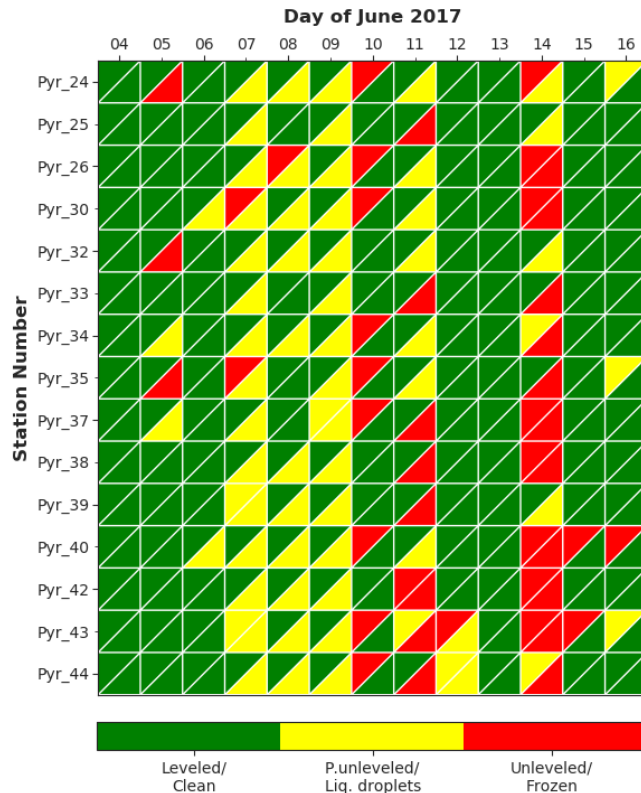


Figure 3.2: Quality flags for the pyranometer sensors. The pyranometer station number is shown on the y-axis and the date on the x-axis. Each square is divided into two triangles: the upper one shows the levelling flag, and the lower triangle the cleanliness status. Green is used for well-levelled and clean stations, while yellow denotes partially levelled stations or the presence of liquid droplets on the domes, while red is used for not levelled stations or iced domes. Figure from Barrientos-Velasco et al. 2020.

identified when significant fluctuations of atmospheric global transmittance (ATg) were observed. A deeper analysis of these cases was verified with the all-sky camera observations operated on Polarstern.

3.1.2 Ship-borne Instrumentation

The OCEANET facility was established to provide continuous ship-borne atmospheric observations. It aims to provide continuous observations for the investigation of the transfer of energy and material between the ocean and the atmosphere [Macke 2009; Kalisch and Macke 2012; Hanschmann et al. 2012; Kanitz et al. 2013]. OCEANET has been operated aboard Polarstern since 2009 during transfer cruises between the hemispheres, crossing the Atlantic Ocean from Bremerhaven in Germany to Punta Arena in Chile and Stellenbosh or Cape Town in South Africa. In 2017, OCEANET was operated for the first time in the Arctic Ocean during two legs of the PS106 expedition named PASCAL (Physical feedbacks of Arctic planetary boundary layer, Sea ice, Cloud and Aerosol; PS106/1) and SiPCA (Survival of Polar Cod in a Changing Arctic Ocean; PS106/2), respectively [see Figure 1.4; Macke and Flores 2018].

The OCEANET container is equipped with a multi-wavelength Raman polarization lidar Polly^{XT}, a 14-channel microwave radiometer (MWR) HATPRO (Humidity And Temperature PROfiler), and a fish-eye sky camera. Complementing the standard OCEANET observations, a Doppler cloud radar of type Mira-35 was installed about 10 meters above the container. The cloud radar can profile optically thick clouds and measure Doppler spectra produced by vertical cloud motions. These remote sensing instrumentation are combined with observations by an Optical Disdrometer of type OM470, and Vaisala RS92-SGP radiosondes launched every 6 hours as input to the Cloudnet processing [Griesche et al. 2020].

Additionally, on top of the OCEANET container, a CGR4 Kipp & Zonen broadband pyrgeometer (4.5 - 42 μm) and a CMP21 broadband pyranometer (0.285-2.8 μm) both manufactured by Kipp & Zonen were installed. The accuracy of these instruments in polar regions is expected to be within $\pm 10 \text{ W m}^{-2}$ and $\pm 20 \text{ W m}^{-2}$ for pyrgeometers and pyranometers, respectively [Lanconelli et al. 2011]. In the case of the pyrgeometer, additional uncertainties due to variation in the vertically integrated water vapour column need to be considered. At values below 10 mm, the atmospheric window produces spectral heterogeneities that distort the pyrgeometer measurements [Gröbner et al. 2014]. Gröbner and Wacker 2015 compared the performance of a calibrated World Infrared Standard Group (WISG) and a CGR4 pyrgeometer and found that for specific periods of time, the deviations can reach up to 3 W m^{-2} . Therefore, the total instrumental uncertainty for the pyrgeometer is inferred to be $\pm 13 \text{ W m}^{-2}$. Operating these instruments aboard Polarstern introduces additional uncertainties due to the ship's exhaust plume and the ship's superstructures interfering with the terrestrial and solar irradiances.

In addition, a meteorological station was installed at about 10 meters above sea level (m.a.s.l) next to the OCEANET container to measure atmospheric pressure, temperature, and relative humidity with a sensor of type Series EE33 from E+E elektronik33.

3.2 Data sets

This section describes the main data sets used throughout this thesis.

3.2.1 Cloudnet

Cloudnet is the project that targets a systematic evaluation of the representation of clouds in forecast and climate models [Illingworth et al. 2007]. Within the scope of Cloudnet, a robust series of algorithms has been developed for retrieving vertical profiles of the macro and microphysical properties of clouds from a synergistic combination of cloud radar, lidar, and microwave radiometer observations. The details of the adaptation of the Cloudnet algorithm for the observations during PS106 is described in Griesche et al. 2020.

This section gives a summary of the methodology applied by Griesche et al. 2020 to obtain vertical profiles of liquid water content (q_L), liquid particle effective radius ($r_{E,L}$), ice water content (q_I), ice crystal effective radius ($r_{E,I}$), and the additional information of the identification of low-level stratus (LLS) clouds [see Table 3.2].

Summary of Cloud Properties Retrievals from Cloudnet				
Cloud parameter	Instruments	Assumption	Limit.	Reference
q_L	MWR and radar	log-normal CDD	PPT	Frisch et al. 1998
q_I	Radar	Exp. IPSD	PPT	Hogan et al. 2006
$r_{E,L}$	MWR and radar	log-normal CDD	PPT	Frisch et al. 2002
$r_{E,I}$	Radar	Spherical shape	PPT	Delanoë et al. 2007 Griesche et al. 2020

Table 3.2: The table summarizes the instruments, main assumptions, limitations (Limit.) and references used in Cloudnet to derive the liquid and ice water content (q), and ice and liquid effective radius (r_E). The abbreviation MWR stands for microwave radiometer, CDD for cloud-droplet distribution, IPSD for ice-particle size distribution, PPT for precipitation, and Exp for exponential.

As a first step, the measurements are averaged onto a common pixel grid with a vertical and temporal resolution of 31.18 m and 30 s, respectively [Griesche et al. 2020]. Then, each pixel is categorized into seven distinct classes, following a bit-wise diagnosis described by Hogan and Connor 2004. The final target classification provides 11 different pixel categories: clear sky, cloud droplets only, drizzle or rain, drizzle or rain and cloud droplets, ice, ice and super-cooled droplets, melting ice, melting ice and cloud droplets, aerosols, insects, and aerosols and insects.

The cloud thermodynamic phase is implemented following Griesche et al. 2020 based on the lidar and radar measurements. Liquid phase is assigned to pixels when the lidar backscatter signal exceeds a threshold of $2e-5 \text{ Mm}^{-1}\text{s}^{-1}$ and is reduced at least by a factor of 10 within 250 m due to the strong signal attenuation in liquid clouds. When the radar signal indicates falling particles at a dew point temperature below 0°C , the pixel is considered as ice. If both criteria are full-filled simultaneously, the pixel is classified as mixed-phase.

The liquid water path (Q_L) is obtained applying the measurements from the MWR HATPRO to the Löhnert and Crewell 2003 retrieval method. This method is based on the analysis of a long-term radiosonde data set, which in this case is based on a long-term data set from Ny-Ålesund - Norway (78.9°N , 11.85°E , WMO Code 6260). Once Q_L is known, the liquid water content (q_L) and $r_{E,L}$ are determined. The retrieval of q_L is obtained by distributing Q_L among the identified liquid and mixed-phase cloud pixels defined by the Cloudnet algorithm. This method assumes a log-normal spherical cloud-droplet distribution, which is constant with height. The uncertainties of q_L are propagated from the typical uncertainty of 20-25 g m^{-2} from the Q_L [Löhnert and Crewell 2003].

The ice water content (q_I) is obtained based on measurements from the cloud radar for the pixels flagged as ice or mixed-phase [Hogan et al. 2006]. This parameter depends on temperature (T ; $^\circ\text{C}$) and cloud radar reflectivity (Z_e ; dBZ). Based on the values of q_L and q_I , vertical profiles of cloud fraction (CF) are estimated at one-hour resolution. The $r_{E,I}$ is derived based on empirical relationships between the visible extinction coefficient, cloud radar reflectivity, model temperature and assumes a spherical shape [Griesche et al. 2020].

The Cloudnet products also contain quality flags that indicate when the pixels have

a reliable retrieval, contain a mixture of drops and ice, instances where large ice crystals, drizzle, or rain can bias the radar reflectivity. The latter might also affect the reliability of Q_L retrievals from the MWR. The use of these flags is considered later on in chapter 6 and 7 for the interpretation of the results.

3.2.2 CERES data set

The CERES SYN1deg, Ed.4.1. product (hereinafter CERES) provides global solar and terrestrial radiative fluxes at the TOA, at four pressure levels, and at the SFC interpolated to a spatial resolution of 1° latitude by 1° longitude and at 1-hour resolution [Young et al. 1998]. While TOA fluxes are based on radiance observations by the Clouds and the Earth’s Radiant Energy System (CERES) instruments which are converted into irradiance [Loeb et al. 2018], in-atmosphere and surface fluxes are calculated based on the Fu-Liou radiative transfer model [Fu and Liou 1992] and are adjusted for consistency with the TOA observations [Gupta et al. 2010; Rose et al. 2013; Rutan et al. 2015; Kato et al. 2018; Minnis et al. 2020]. For this purpose, CERES uses cloud properties from geostationary and polar satellites observations, particularly from the Moderate Resolution Imaging Spectroradiometer (MODIS). In addition to radiative fluxes, various surface, cloud and aerosol parameters are included to enable the exploration of the relationships among clouds, aerosols, and radiation [Minnis et al. 2020]. As ancillary input, CERES relies on re-analysis data from the Global Modeling Assimilation Office Global Earth Observing System (GEOS-5) in its version 5.4.

The relevant cloud properties used in this study include the CF, Q_L , Q_I , $r_{E,L}$, $r_{E,I}$, cloud base (P_b) and top pressure (P_t). It is worth mentioning that the cloud properties mentioned are estimated based on MODIS cloud retrieval algorithm for cloud emissivity, cloud effective temperature, cloud particle effective radius, and cloud optical depth. The complete description of the retrievals and changes made between Edition 2 and Edition 4 algorithms are presented in Minnis et al. 2020.

Additionally, throughout this work, the surface parameters like skin temperature (Skt), surface albedo (α), and snow/ice coverage are also relevant for analysing the results and conditions during PS106. In contrast to previous versions, the surface albedo is determined considering the $1.24 \mu\text{m}$ channel instead of the $2.13 \mu\text{m}$ over snow surfaces. This change brings the advantage to maximize the range of retrieving cloud optical depth over snow-covered areas [Sun-Mack et al. 2006]. However, this modification increases the uncertainty of surface albedo due to variable snow surface albedo and bidirectional reflectance [Minnis et al. 2020].

Besides the general description of CERES given in Minnis et al. 2020, additional information of data quality, accuracy, and validation of CERES is provided in CERES-Guide 2021a and CERES-Guide 2021b. A comparison of CERES downward fluxes products with observations at the Summit observatory in Greenland indicates a mean bias (Standard Deviation (SD)) of 4.64 (5.35) W m^{-2} and 10.85 (12.77) W m^{-2} for the downward solar flux (SOL-D) and downward thermal infrared flux (TIR-D) fluxes, respectively. During the polar night, the surface TIR fluxes face major challenges due to the degradation of Terra MODIS over the polar regions. However, since this study is focused on the early summer of 2017, no additional focus is given to the limitations during the polar night.

In summary, the CERES product used in this thesis as an input parameter for own radiative transfer simulations is the surface albedo. The CERES products used for the analysis of radiative closure and cloud radiative effects are the broadband SOL and TIR fluxes for all-sky, clear-sky, clear-sky without aerosols (also referred to as virtually pristine or just pristine for simplicity), and cloudy without aerosols atmosphere.

3.2.3 Ancillary data set

The ancillary data sets mentioned in this section are used to describe the synoptic, atmospheric, and surface conditions during PS106. Additionally, part of the ancillary data is also used as input parameters to perform radiative transfer simulations, which is later on further discussed in Section 3.4.

Hourly pressure level profiles of temperature, pressure, ozone and specific humidity from the European Centre for Medium-Range Weather Forecasts (ECMWF) Re-Analysis (ERA5) data set are used as input parameters for the simulations. ERA5 assimilates 4D-Var using polar and geostationary satellites, surface, radiosonde, dropsonde, and aircraft measurements [Hersbach et al. 2020]. The spatial resolution of ERA5 is 0.25° latitude by 0.25° longitude at 1-hour resolution.

This work considers the climatological values of trace gases for the Air Force Geophysics Laboratory (AFGL) sub-Arctic summer atmosphere from Anderson et al. 1986. The vertical profiles of trace gases are included as inputs to the radiative transfer simulations.

Finally, to provide a general description of the synoptic conditions during the PS106 expedition, the values of the Arctic oscillation index (AO) are used from the National Weather Service Climate Prediction Center at National Oceanic and Atmospheric Administration (NOAA) [NWS CPC 2021]. The AO is a large-scale index of climate variability. This index indicates the climate pattern characterized by an exchange of atmospheric mass between the Arctic Ocean and the surroundings at around 55°N latitude [Rigor et al. 2002].

3.3 General Conditions During PS106

A general synoptic-scale description focused on PASCAL (PS106/1), ACLOUD campaign and Ny-Ålesund for the early summer period of 2017 is provided in Knudsen et al. 2018. This analysis is based on near-surface and upper-air meteorological observations, operational satellite and model data. This section describes the meteorological, atmospheric, and surface conditions during PS106 based on data sets collected aboard Polarstern, CERES, and ERA5.

3.3.1 Synoptic and Surface Conditions

The PS106 cruise navigated the Arctic open ocean, marginal ice zone, and sea ice during leg one (28 June to 21 July) and two (22 July to 16 July). The 3 regions mentioned can be recognized with the snow cover and surface albedo [see Fig. 3.3a and b]. Polarstern entered the defined Arctic region (70° - 90°N), the conditions were

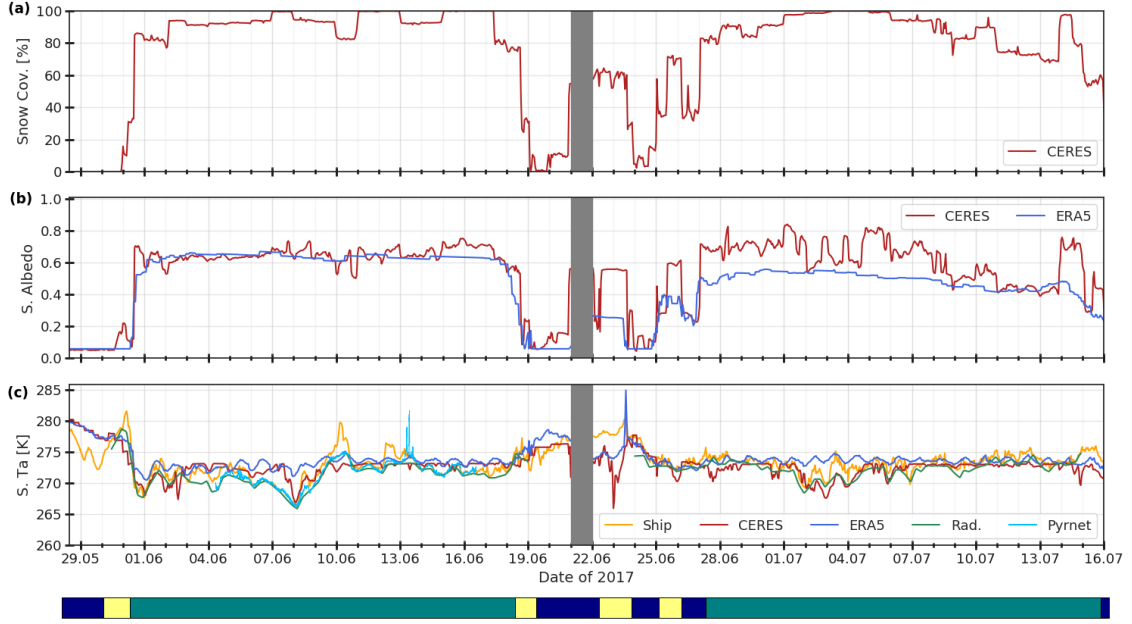


Figure 3.3: Surface conditions during PS106. Panel (a) shows one hour resolution time series of snow cover (%) obtained from CERES. Panel (b) shows time series of surface albedo based on CERES (red line) and ERA5 (blue line). Panel (c) shows time series of near-surface temperature based on Polarstern observations at 10 m.a.s.l (orange line), based on radiosondes at 10 m.a.s.l (green line), and skin temperature from ERA5 (blue line), CERES (red line) and mean values obtained from Pyrnet (light blue line). The bottom bar indicates an approximation of the surface conditions during PS106. Dark blue indicates open ocean, yellow suggests marginal sea ice zone, and mostly sea ice is shown in teal. Figure modified from Barrientos-Velasco et al. 2022.

open water until 31 May 2017; during that day, Polarstern navigated the marginal zone until reaching sea ice conditions from 1 to 18 June 2017. Between 18 and 27 June, Polarstern cruised open ocean and marginal sea ice zones until reaching sea ice surfaces. The latter condition was relatively constant along the cruise until the end of the expedition on 16 July 2017.

In Figure 3.3b, a comparison of surface albedo between CERES and ERA5 is presented. During PS106/1, there is a rather good agreement between both data sets. However, during the second leg, there is a larger difference between CERES and ERA5 from 25 June to 8 July 2017. Part of the difference might be due to a heterogeneous and variable sea ice cover that can lead to different results since the spatial coverage of both data sets is different. Another plausible cause is an overestimation of surface albedo from CERES and seasonal ablation biases from ERA5 [Trepte et al. 2019; Dutra et al. 2010].

Based on the ship-borne observations, the near-surface temperature varied more strongly during leg 1 than during leg 2 of PS106 [see Fig. 3.3c]. The variation is more evident during the two episodes. The first episode describes the entering of a colder region since it occurred during the transition from the open ocean to sea ice from 31 May to 1 June, varying the near-surface temperature from 279K to 268K. The second episode observed was on 7 June when the near-surface temperature

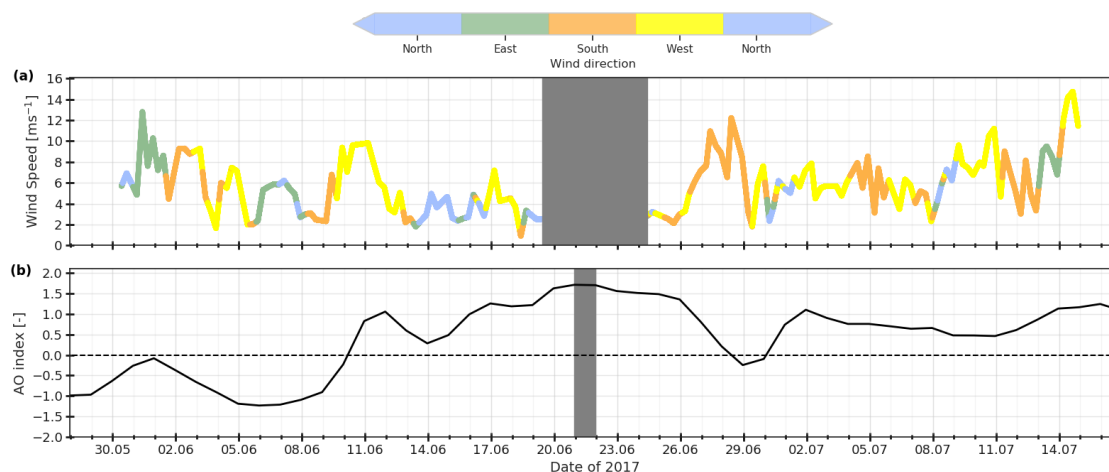


Figure 3.4: Panel (a) shows the time series of near surface wind speed (ms^{-1}) and direction obtained from Polarstern observations. Panel (b) shows the AO index reported by the NOAA.

started to decrease from about 270K to 266K, and then increased again by 10 June to about 275 K or even higher according to Polarstern observations. During both episodes, the coldest temperature periods have winds coming from East and South East, suggesting a plausible influence of advected cold air influencing the near-surface temperatures as well as local processes (Fig. 3.4).

Additionally, the influence of the large-scale Arctic circulation on the synoptic conditions during PS106 is considered. For this analysis, the AO is used. The AO is a climate index that characterizes the atmospheric circulation of the Arctic region by considering geopotential height anomalies of the 1000 mb isobar between $20^{\circ} - 90^{\circ} N$. The AO index is defined as the loading of the dominating mode obtained from an Empirical Orthogonal Function (EOF) analysis of the monthly-mean anomaly fields. The values considered for this study are obtained from the climate data centre of the NOAA [NWS CPC 2021] (source: <ftp://ftp.cpc.ncep.noaa.gov/cwlinks/>).

A positive AO index generally corresponds to strong westerly winds in the upper atmosphere, lower than usual atmospheric pressures and temperatures in the Arctic, and an opposite effect on pressure and temperature at mid-latitudes. On the other hand, a negative AO index corresponds to weaker upper-level winds, higher atmospheric pressure and warmer than usual temperatures in the Arctic, and an increase of storms in the mid-latitudes [Thompson and Wallace 1998].

For most of the PS106 cruise, the AO index was positive [see Fig. 3.4b], suggesting a high surface pressure, more persistent cyclonic circulation allowing mid-latitude jet streams to blow persistently and strongly from west to east [see Fig. 3.4a]. The latter generates a locked cold Arctic air locked in the polar region.

3.3.2 Atmospheric Temperature and Humidity Conditions

The anomalies of the vertical profiles of atmospheric temperature and specific humidity based on ERA5 are shown in Fig. 3.5 for the PS106 track, together with the mean profiles and the sub-Arctic summer standard atmosphere [Anderson et al.

1986]. Panels 3.5a and 3.5b, indicate a strong temperature and humidity inversion layers from 1 June to 9 June 2017, followed by a generally warmer atmosphere from 10 June to 14 June 2017. Additionally, relatively warm and humid conditions are observed at the end of leg 2 (11 July to 16 July 2017), caused by water vapour transport as described in Knudsen et al. 2018 and Viceto et al. 2021. Based on the ship-borne observations, the near-surface temperature varied more strongly during leg 1 than during leg 2 of PS106 [see Fig. 3.3c]. Most of the humidity intrusions observed in Fig. 3.5b have southerly and westerly origins of the advected air masses, based on the wind direction obtained from the radiosondes (not shown). The mean vertical profiles of atmospheric temperature and specific humidity indicate good agreement of radiosondes and ERA5, which are colder and dryer than the climatological values of the sub-Arctic summer standard atmosphere.

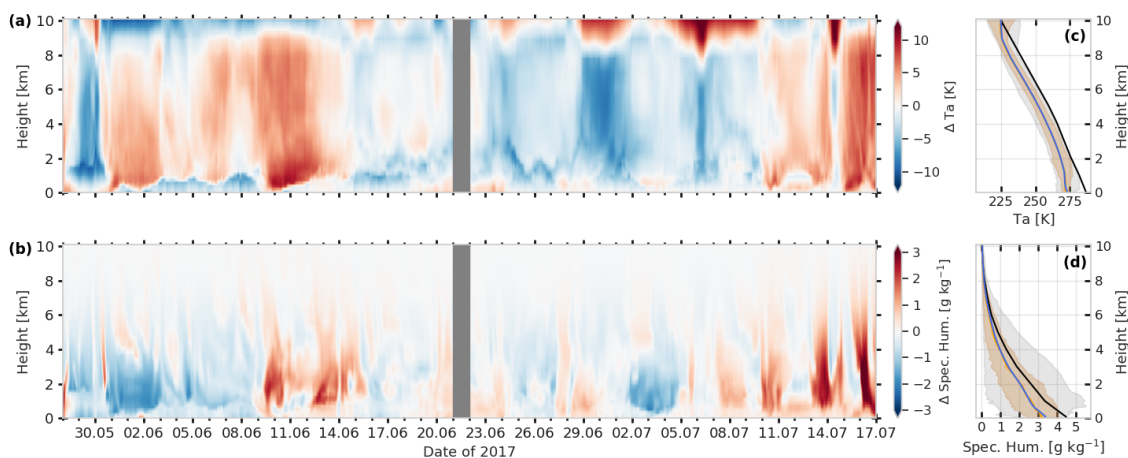


Figure 3.5: Time-height indicator plot of atmospheric profiles obtained from ERA5 along the PS106 cruise track. Panel (a) shows the atmospheric temperature anomaly (δT_a), panel (b) shows specific humidity anomalies. In (c) and (d), the mean profiles of atmospheric temperature and specific humidity, respectively, are shown. The blue and orange lines correspond to ERA5, radiosondes, and the Sub-Arctic Summer standard atmosphere [Anderson et al. 1986] is displayed in black. The grey-shaded area indicates the minimum and maximum while, while the rose-shaded area shows the interquartile range of ERA5 vertical profiles. Figure from Barrientos-Velasco et al. 2022.

3.3.3 Statistical Analysis of Cloud Properties

This section presents a classification of cloudy conditions to describe the atmospheric conditions during the PS106 cruise. This classification is based on target classification product from Cloudnet, and the identification of low-level stratus clouds (LLS) from Griesche et al. 2020. The following description is presented in the format of a flag classification of cloud conditions by structure, thermodynamic phase, and whether their conditions were optimum for radiative studies during PS106. Chapters 6 and 7 provide a broader description of the cloud conditions in the context of radiative closure and cloud radiative effects analysis during PS106.

A characterisation of cloud conditions during the PS106 expedition is given next, considering CF, vertical layer structure and thermodynamic phase. The Cloudnet

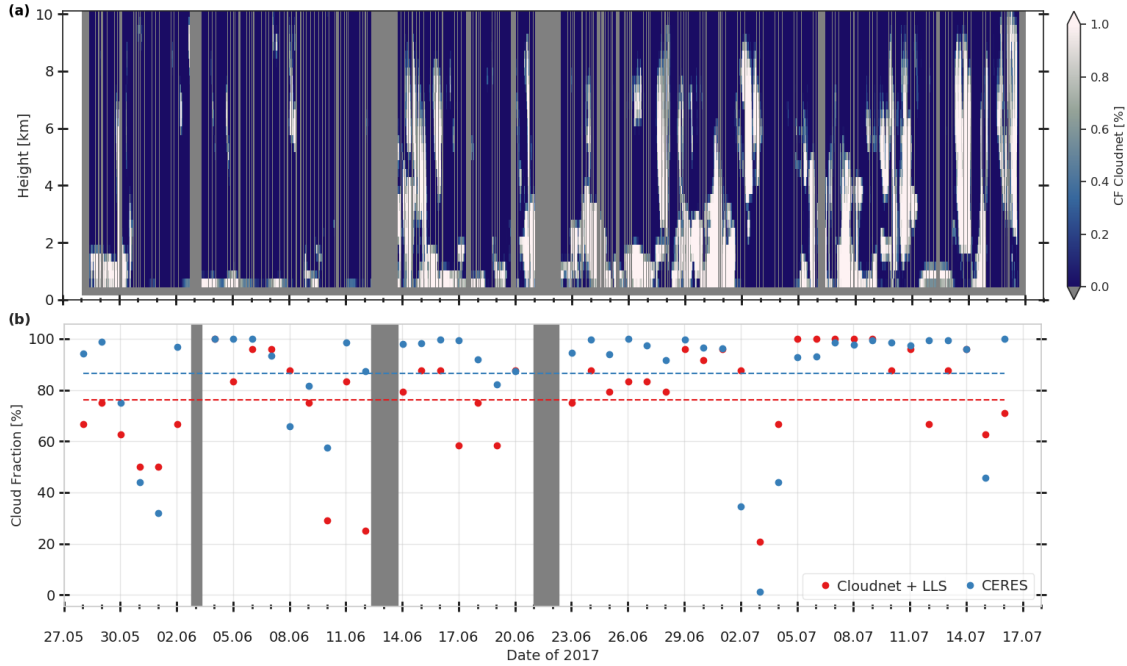


Figure 3.6: Cloud fraction (CF) observed along the PS106 cruise track. Panel (a) shows the vertically resolved mean CF based on Cloudnet observations at hourly resolution. Data gaps are indicated in grey. Panel (b) shows daily mean CF based on Cloudnet plus detection of low-level stratus clouds (LLS) introduced by Griesche et al. 2020 (red) and CERES (blue). Source: Barrientos-Velasco et al. 2022.

vertical profiles of CF are shown in Fig. 3.6a, while a comparison of daily mean CF is presented in Fig. 3.6b. For the last panel, Cloudnet and LLS clouds introduced in Griesche et al. 2020 are analysed together to compare the total CF values with CERES. Cloudnet plus LLS and CERES CF have been aggregated from hourly to daily means. Hourly values with data gaps in the Cloudnet plus LLS observations have been excluded from CERES to ensure consistent temporal sampling. It is worth mentioning that the inclusion of LLS to Cloudnet CF improved the analysis by reducing the total data gaps from 25.2 % to 6.6 % for the entire PS106 period.

The comparison aims to determine the consistency of the CERES and Cloudnet CF, despite their different instrumental data, perspectives, spatial and temporal sampling, and retrieval algorithms. It is worth noting that CERES provides a spatially averaged CF for a 1° latitude by 1° longitude region. At the same time, Cloudnet yields vertically resolved information on cloud cover as time series for the location of Polarstern, as shown in Fig. 3.6a. Mean values of CF are 86.7 % and 76.1 % for CERES and Cloudnet plus LLS, respectively. The CERES CF without exclusion of Cloudnet data gaps is higher at 86.9 %, indicating that data gaps occur more frequently in cloudy conditions.

A description of the type of clouds observed during PS106 is shown in Fig. 3.7. The classification used is based on the Cloudnet target classification and supplemented by the analysis of LLS clouds. While the cloud type classification was already presented in Fig. 18c of Griesche et al. 2020, here we additionally consider the data quality and a more detailed description of mixed-phase clouds for the PS106 cruise.

A description of the type of clouds observed during PS106 is presented in Fig. 3.7.

The classification used is based on the Cloudnet target classification and supplemented by the analysis of low-level stratus (LLS) clouds introduced in Griesche et al. 2020. While the cloud type classification was already presented in Fig. 18c of Griesche et al. 2020, here we additionally consider the data quality and a more detailed description of mixed-phase clouds for the PS106 cruise.

During PS106, 45.4 % and 35.6 % of the time, single and multilayer clouds were observed by Cloudnet, respectively (Fig. 3.7a). The remaining 12.4 % of the time, cloud-free conditions were detected, and data gaps occurred for 6.6 % of the time. While single-layer clouds are more frequent during the first leg, the frequency of multilayer clouds is higher during the second leg [see Fig. 3.7a and Fig. 18c in Griesche et al. 2020]. The frequency of single-layer and multilayer clouds are typical for early summer conditions, as previously observed in other studies [e.g., Shupe 2011; Nomokonova et al. 2019].

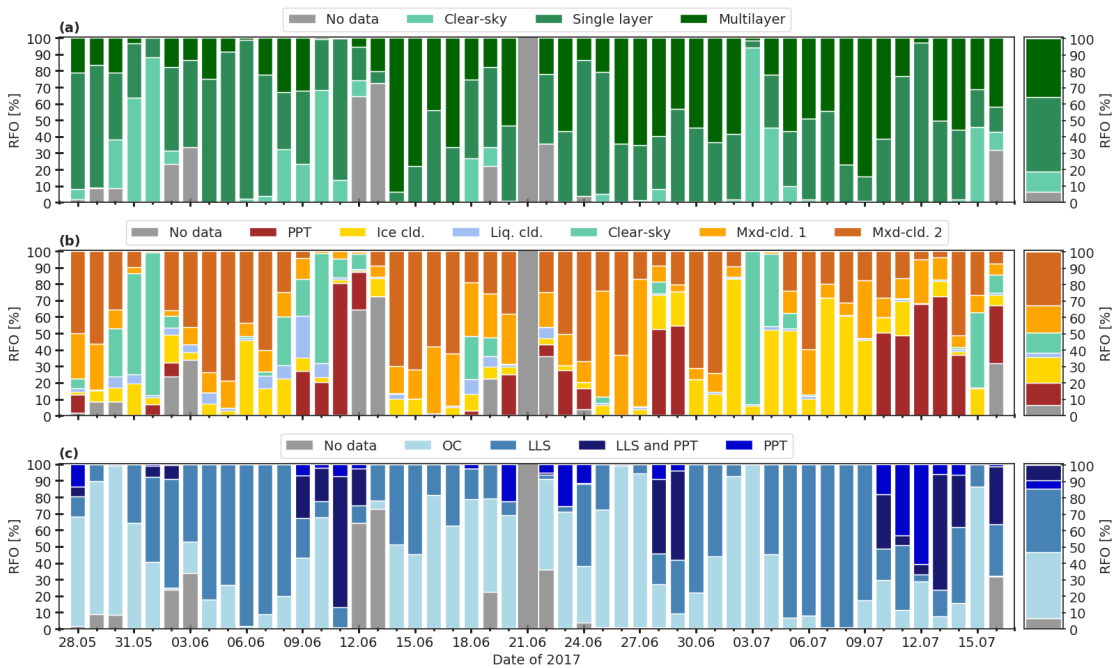


Figure 3.7: Daily and overall relative frequency of occurrence (RFO) of various cloud characteristics. Panel (a) shows the RFO of clear-sky, single-level clouds, and multilayer clouds. Panel (b) shows the RFO of the thermodynamic phase of single-layer clouds, differentiating periods of ice clouds, liquid clouds, mixed-phase clouds of type 1 or 2, precipitation (PPT), and clear-sky. Data gaps are marked in grey in all panels. Panel (c) is the RFO of various quality flags indicating optimum conditions (OC), low-level stratus (LLS), PPT and simultaneous occurrence of LLS and PPT. Figure obtained from Barrientos-Velasco et al. 2022.

The cloud phase flag to analyse the thermodynamic phase of clouds. Even though the cloud phase flag is available for the entire PS106 time series, the focus is here directed to the thermodynamic phase of single-layer clouds, since these cases are the most frequent, and the analysis is less complicated than for multilayer conditions. Fig. 3.7b indicates an occurrence frequency of 32.6 % for single-layer mixed-phase clouds of type two (ice and super-cooled droplets), 16.8 % for mixed-phase clouds of type one (well-defined ice and liquid phase), and 15.6 % for single layer ice clouds.

The remaining period is composed of single-layer clouds with precipitation (13.6 %), clear-sky periods (12.1 %), and single layer liquid clouds (2.7 %).

The quality status flag shows that only 40.1 % of the time, optimum observations conditions were identified [see Fig. 3.7c]. For about 39.0 % of the time, low-level stratus (LLS) with a cloud base below 155 m prevailed, implying that during these periods, the cloud base height lay below the altitude detection limit of 155 m of the cloud radar [see Fig. 18a in Griesche et al. 2020]. Precipitation (PPT) alone and moments with LLS and PPT occurred for about 5.1 % and 9.2 % of the time, respectively. Under LLS and PPT conditions, the observations of cloud macro- and microphysical parameters have a degraded quality and reduced accuracy. Thus, for only about 40.1 % of the time, observations are of sufficient quality, e.g., for radiative transfer simulations.

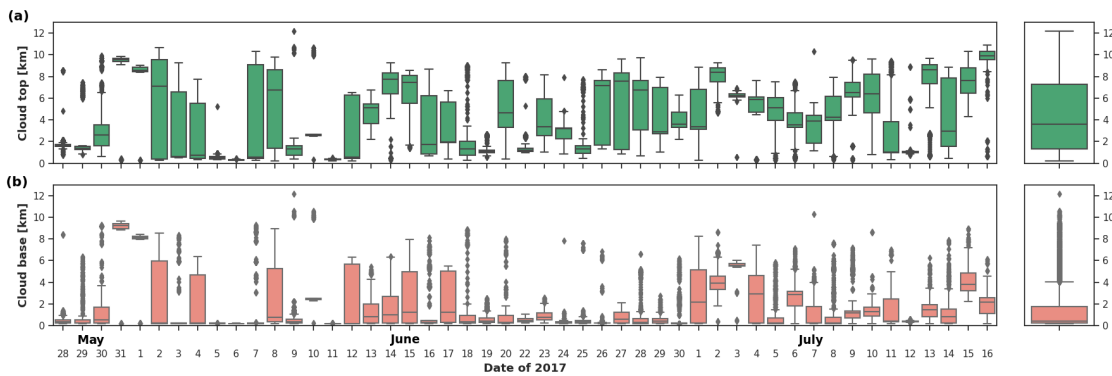


Figure 3.8: Macrophysical properties of clouds during PS106. Panel (a) shows box plot time series of cloud top. Panel (b) similar to (a), but for the cloud base. At the end of each panel is shown the box plot for the entire time series. The limits of the box indicate the 25th and 75th percentile of the interquartile range, the line inside the box denotes the median, minimum and maximum values are given by the vertical line of each box. The outliers are presented as diamonds.

The macrophysical properties of clouds during PS106 are shown in Figure 3.8. While during PS106/1, most of the days, clouds were relatively low at heights below 2 km, PS106/2 indicated a rather larger variance of cloud tops and cloud bases heights. The latter is more evident for the period between 29 June until the end of the PS106 cruise. Considering just Cloudnet data, the mean (median) cloud base height is 1.4 (0.4) km, and cloud top is 4.3 (3.6) km. By including the identification of LLS, the cloud base height reduces to 69 (71) m. The mean (median) cloud geometrical thickness calculated is 2.9 (1.7) m with minimum and maximum values of 31 m and 10.5 km, respectively.

Based on Cloudnet products, the statistical distributions of cloud microphysical properties are shown in Figure 3.9. The values of $r_{E,L}$ indicate a monomodal distribution with a larger occurrence around $7.5 \mu\text{m}$. The mean (median) calculated is $8.7 \mu\text{m}$ ($7.6 \mu\text{m}$) with a minimum and maximum of $1.8 \mu\text{m}$ and $43.0 \mu\text{m}$, respectively. Given that the minimum valid size of $r_{E,L}$ of the cloud optical property parameterization used by RRTMG [i.e., Streamer method; Key 1996; Hu and Stamnes 1993] is $2.5 \mu\text{m}$, all smaller retrieval results were set to this value. This correction did not modify the results significantly, as can be observed in Figure 3.9a. In the case

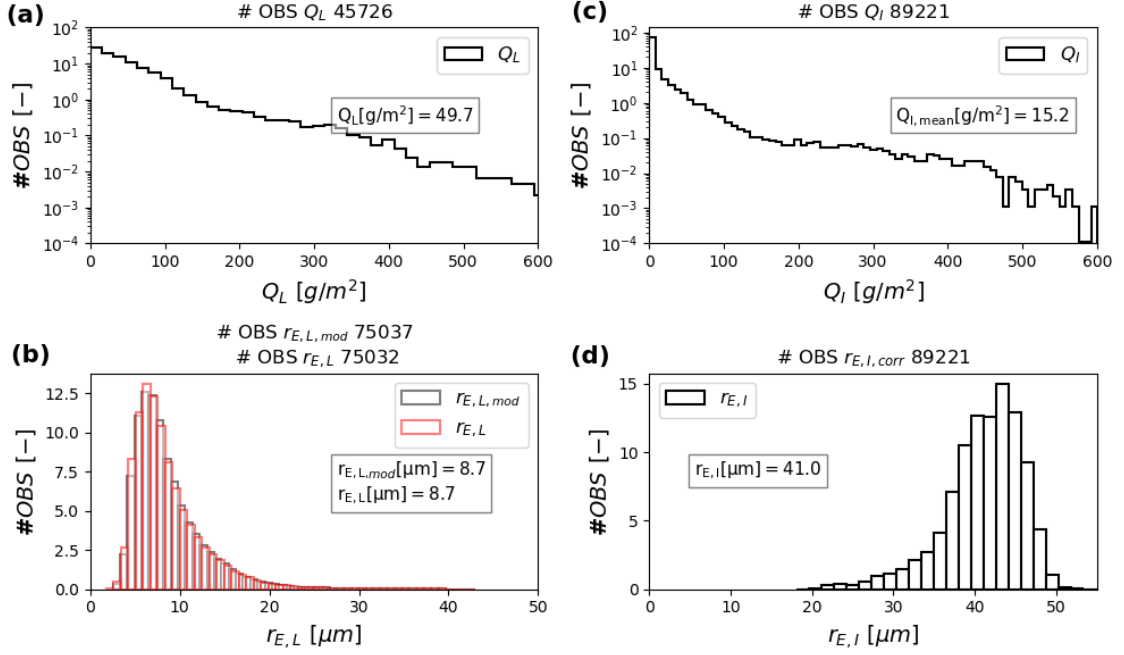


Figure 3.9: Cloud microphysics during PS106 based on Cloudnet data. Panel (a) shows the frequency of occurrence of liquid water path (Q_L), (b) shows the distribution of the liquid effective radius ($r_{E,L}$) based on Cloudnet (in black) and a modified ($r_{E,L,mod}$) version where all values lower than $2.5 \mu\text{m}$ are changed to $2.5 \mu\text{m}$ (in red). Panel (c) shows the frequency of occurrence of the ice water path (Q_I), and panel (d) shows the distribution of ice effective radius ($r_{E,I}$). On the top of each panel the total number of observations are indicated.

of $r_{E,I}$, the distribution is also monomodal with a larger occurrence around $43 \mu\text{m}$. In this case, the mean (median) calculated is $41.0 \mu\text{m}$ ($41.8 \mu\text{m}$). The lowest value derived is $18.1 \mu\text{m}$, and the maximum is $56.3 \mu\text{m}$. The distributions of Q_L and Q_I show a larger distribution to values below 50 g m^{-2} in both cases. The mean Q_L is 49.7 g m^{-2} , and the mean Q_I calculated is 15.2 g m^{-2} .

The analysis of the microphysical properties of clouds considering the flags introduced in Figure 3.7 indicates that the distribution of Q_L and $r_{E,L}$ do not vary much between single and multiple layer clouds [see Fig. A.1a and b]. On the other hand, the distribution of Q_I indicate higher values for multilayer clouds with a mean of 13.7 g m^{-2} than single layer cases with a mean of 7.1 g m^{-2} . While the distribution of $r_{E,I}$ show a monomodal distribution for large size $r_{E,I}$ for single-layer clouds with a mean $42.8 \mu\text{m}$, the monomodal distribution for multilayer presents a larger frequency for lower mean value of $39.1 \mu\text{m}$ [see Fig. A.1d].

There is also a distinct difference in the analysis of the cloud phase for single-layer clouds. The Q_L values indicate more frequent larger values for mixed-phase clouds type 2 than type 1 and single-phase liquid clouds. The mean values registered for mixed-phase type 2, type 1 and liquid clouds are 48.7 g m^{-2} , 31.6 g m^{-2} and 29.4 g m^{-2} , respectively. In the case of Q_I the largest values registered are for ice clouds with a mean 9.4 g m^{-2} , then mixed-phase type 2 with a mean of 8.9 g m^{-2} , and a very low mean value of 1.7 g m^{-2} for mixed-phase type 1 [see Fig. A.1a and c]. For $r_{E,L}$ and $r_{E,I}$ the values are larger for mixed-phase 2 than mixed-phase type

1 and single-phase clouds. The mean values of $r_{E,L}$ ($r_{E,I}$) for mixed-phase type 2, type one and single-phase clouds are $11.2 \mu\text{m}$ ($46.9 \mu\text{m}$), $7.4 \mu\text{m}$ ($41.9 \mu\text{m}$) and $6.9 \mu\text{m}$ ($42.3 \mu\text{m}$), respectively [see Fig. A.1b and d].

The cloud macrophysical properties described in this section (i.e., cloud top and cloud base height, cloud geometrical thickness) for most of the cases follow the typical characteristics of low-level persistent clouds [Shupe et al. 2011; Nomokonova et al. 2019; Achtert et al. 2020; Sedlar et al. 2010; Sotiropoulou et al. 2016]. During PS106, nonetheless, low-level stratus clouds are observed. To retrieve their cloud base height and microphysical properties are challenging from the ship-borne remote sensing instrumentation Griesche et al. 2020. These situations are considered to be frequent over the Arctic Ocean, as described in other studies [e.g., Sedlar et al. 2010; Tjernström et al. 2014; Achtert et al. 2020].

At Ny-Ålesund similar values of Q_L have been reported. The mean values of 30 and 66 g m^{-2} have been quantified for single layer liquid and mixed-phase. In the case Q_I , mean values have been observed for single-layer ice and mixed-phase clouds of 273 and 164 g m^{-2} , respectively [Nomokonova et al. 2019]. These values are higher in magnitude than the values observed in PS106. This variation might be due to different characteristics of the local observations. However, the analysis of Nomokonova et al. 2019 comprises a 14-month data set, and no specific values are given for the summer season.

Cloud macro and microphysical properties were derived using the Cloudnet algorithm during the Arctic Clouds in Summer Experiment (ACSE) conducted in 2014. The ACSE covered the Barents Sea, Kara Sea, Laptev Sea, East Siberian Sea, and Barrow [see Fig. 1 in Achtert et al. 2020]. Considering only reliable data observations for ACSE, the mean(median) Q_L during summer was 37 ± 59 (13) g m^{-2} with a peak on the distribution around 10 g m^{-2} . This value is within a similar magnitude to what was observed during PS106. In the case of Q_I , the mean(median) value reported was 34 (7) g m^{-2} , which is double than the value shown in Figure 3.9.

The statistical analysis of cloud properties presented in this subsection describes local observations collected for the central Arctic for early summer 2017. In general, the observations are consistent with the values presented in the literature [Shupe et al. 2015; Nomokonova et al. 2019; Achtert et al. 2020]. However, it is worth noting that the PS106 cruise was characterized by a dominant presence of low-level clouds [see Fig. 7 in Wendisch et al. 2019] and low values of Q in contrast to other regions. The analysis described is used as the basis for the sensitivity analysis of cloudy conditions detailed in chapter 4.2. The results obtained in chapter 4.2 are used as a reference for the interpretation of results in chapter 6 and 7.

3.4 Radiative Transfer Simulation Setup

The radiative transfer simulations were performed with the TROPOS Cloud and Aerosol Radiative effect Simulator (henceforward T-CARS) [Barrientos-Velasco et al. 2022], which is a Python-based framework to investigate aerosol and cloud radiative effects. T-CARS uses the radiative transfer model RRTMG and the input data sources such as atmospheric profiles of trace gases, temperature, humidity, properties of clouds, aerosols, and surface parameters. This framework was implemented in Barlakas et al. 2020, Witthuhn et al. 2021 and Barrientos-Velasco et al. 2022.

In this thesis, the T-CARS output files have an atmospheric grid that consists of 197 atmospheric levels from the surface up to 20 km height at 1-minute resolution. The first 10 km of the atmosphere is divided into 160 levels with a grid layer thickness of 62.4 m. The following 5 km of the atmosphere have a layer thickness of 250 m, and the last 5 km of the atmosphere a layer thickness of 193.8 m.

Hourly pressure level profiles of temperature, pressure, ozone mass mixing ratio and specific humidity from ERA5 data set are used as input parameters for the simulations. ERA5 assimilates 4D-Var using polar and geostationary satellites, surface, radiosonde, dropsonde, and aircraft measurements [Hersbach et al. 2020]. In the case of PS106, the Vaisala Radiosonde RS92-SGP launched every 6 hours were also assimilated.

The atmospheric temperature and pressure measured at 10 m.a.s.l aboard Polarstern are used in T-CARS as skin temperature and surface pressure, respectively. We opted for this set-up since these parameters are the closest to the surface and are the only available measurement for the entire cruise. For comparison purposes, the surface temperature from ERA5 and CERES are also considered.

The surface albedo for our radiative transfer simulations is based on CERES. Additionally, the hourly surface albedo from ERA5 is considered for comparison. Both data sets are collocated every minute to the Polarstern location for the entire PS106 expedition.

The input data sets mentioned previously are linearly interpolated to the simulation grid. Moreover, the climatological values of trace gases for the Air Force Geophysics Laboratory (AFGL) sub-Arctic summer atmosphere from Anderson et al. 1986 are considered. The pressure level ERA5 data set is used in the model by interpolating atmospheric pressure, temperature, specific humidity, and ozone mass mixing ratio. Additionally, $r_{E,L}$ and $r_{E,I}$ are linearly interpolated to match the grid of the simulations. The values of q_L and q_I are introduced into the model as Q_L and Q_I . This step is done by multiplying each interpolated ice and water content value to the grid layer thickness.

Note that parameterization of liquid and ice cloud properties used in RRTMG are based on the parameterization developed by Hu and Stamnes 1993 and Key 1996, respectively. In the case of Cloudnet, the parameterizations used to retrieve cloud properties rely on different algorithms [see Table 3.2]. While it is important to consider the consistency of cloud properties retrievals between the radiative transfer model and Cloudnet products, it is outside the scope of the present work the adaptation of Cloudnet retrievals into the radiative transfer model.

The surface input parameters, such as ship-borne measured pressure, temperature, and albedo from CERES, are interpolated at 1-minute resolution and applied to the model. The surface emissivity is assigned with a constant value based on the amount of sea ice encountered at the vicinity of Polarstern. The values of sea ice fraction are obtained from CERES as reference. When values of sea ice fraction are larger than 50 %, a constant surface emissivity of 0.9999 is used in the model. If the sea ice fraction is lower than 50 %, a constant of 0.9907 is considered. The constant values mentioned are obtained from Wilber et al. 1999.

The T-CARS output provides vertical profiles of broadband upward and downward, TIR and SOL fluxes, and heating rates for cloudy and clear-sky conditions. Addi-

Parameter	Data source	Units
Atmospheric parameters		
Atmospheric temperature	ERA5	K
Atmospheric Pressure	ERA5	hPa
Specific humidity	ERA5	g kg^{-1}
O ₃ mixed ratio	ERA5	[-]
CO ₂ mixed ratio	Anderson et al. 1986	[-]
N ₂ O mixed ratio	Anderson et al. 1986	[-]
CO mixed ratio	Anderson et al. 1986	[-]
CH ₄ mixed ratio	Anderson et al. 1986	[-]
O ₂ mixed ratio	Anderson et al. 1986	[-]
Surface parameters		
Skin temperature	Ship-borne	K
Surface pressure	Ship-borne	hPa
Surface albedo	CERES	[-]
Surface emissivity	Wilber et al. 1999	[-]
Cloud properties		
Q_L	Cloudnet	gm^{-2}
Q_i	Cloudnet	gm^{-2}
$r_{E,L}$	Cloudnet	μm
$r_{E,I}$	Cloudnet	μm

Table 3.3: T-CARS input parameters

tionally, it is included in the output files latitude, longitude coordinates, the quality flags mentioned in chapter 3.3.3, temperature and pressure levels, and the cloud top and cloud base obtained from the Cloudnet data set and the cloud boundaries from the analysis of LLS described in Griesche et al. 2020.

It is important to mention that the simulations obtained from T-CARS do not consider aerosols since the input parameters needed for the radiative transfer model were not measured continuously [e.g., aerosol optical thickness, aerosol scattering albedo, aerosol asymmetry parameter]. Thus, T-CARS simulations depicts fluxes for a virtual pristine atmosphere or an atmosphere with clouds and no aerosols.

The T-CARS output files provide the vertical profiles of broadband upward and downward, TIR and SOL fluxes, heating rates for cloudy and clear-sky conditions and the flag classification introduced in subsection 3.3.3 [see Fig. 3.7].

Chapter 4

Sensitivity Analysis of Arctic Fluxes

This chapter presents a series of sensitivity analyses to quantify the response of radiative fluxes to the perturbation of various atmospheric and surface parameters focused on PS106. The research aims to better understand the flux variations due to uncertainties or variability of relevant parameters. The values found in this analysis are used as the uncertainty range for the study of radiative closure in Chapter 6. The sensitivity analysis for clear-sky conditions is based on the results presented in [Barrientos-Velasco et al. 2022].

4.1 Clear-sky Perturbations

The creation of a clear-sky Arctic atmosphere is based on the 3 July 2017 at 81.9° latitude and 32.51° longitude. This day was chosen because it is the day with the longest clear-sky period of PS106 [see Fig. 3.7]. To avoid differences in the analysis due to surface albedo fluctuations [see Fig. 3.3], a daily constant mean value of 0.65 was used for the entire day. During this day, the CERES ice fraction was above 0.5; therefore, the surface emissivity was kept constant at 0.9999. The 3 July covers the solar zenith angle from 59° to 75°. This range does not cover fully the solar zenith angle (SZA) range experienced during the PS106 expedition, where the values ranged from 47.6° to 80.1°, from 31 May to 16 July 2017. Nevertheless, this analysis serves as a reference to quantify the flux difference due to perturbations. The atmosphere and surface conditions created are considered the base for the clear-sky and cloudy perturbations. The following two subsections describe the atmospheric and surface perturbations for clear-sky conditions.

4.1.1 Atmosphere

Parameters such as temperature, specific humidity and ozone mixing ratio influence the TIR and SOL radiation budget. The following experiment considers the variation of these parameters to quantify the radiative flux variance at the SFC and TOA.

The perturbation of atmospheric temperature is based on the instrumental uncertainty of ± 0.5 K of the radiosonde's temperature sensor, as well as the observed range of atmospheric temperature anomalies of about ± 7 K during PS106 [see Fig. 3.5c]. The variation of ± 0.5 K has the strongest effect on the TIR-D flux at

the surface, resulting in a variation of $\pm 1 \text{ W m}^{-2}$. Notice that 3 July 2017 is a day with slightly colder than average temperatures for the first 8 km of the atmosphere, and warmer than average temperatures at about 10 km [see Fig. 3.5a]. Considering the larger temperature perturbation of $\pm 7 \text{ K}$ results in a variation of up to $\pm 14.9 \text{ W m}^{-2}$ for the TIR-D. At the TOA, the variations of ± 0.5 and $\pm 7 \text{ K}$ yield daily mean differences of $\pm 1.1 \text{ W m}^{-2}$ and $\pm 15.4 \text{ W m}^{-2}$, respectively.

The second parameter analysed is ozone. Ozone reduces the SOL flux in the atmosphere by absorption at ultraviolet ($\lambda \lesssim 0.35 \mu\text{m}$) and visible wavelengths ($0.5 \mu\text{m} \lesssim \lambda \lesssim 0.7 \mu\text{m}$). Variations of ozone concentration are significant in the stratosphere, where reduced ozone causes colder temperatures, enhancing the decrease of ozone [Randel and Wu 1999]. The ozone concentration is linked to synoptic mechanisms through interactions with atmospheric dynamics and photochemistry, as described in Anstey and Shepherd 2014. Bahramvash Shams et al. 2019 investigated the variation of the vertical profiles of ozone at four Arctic sites from 2005 to 2017. These findings are used as a basis to quantify the sensitivity of ozone for a perturbation by $\pm 12.5 \%$ and $\pm 25 \%$. The former value is used to approximate the monthly variation of ozone during summer months [see Fig. 5 in Bahramvash Shams et al. 2019], which is similar to the uncertainty of $\pm 10 \%$ ozonesondes [Deshler et al. 2017]. The smaller variation leads to a decrease of $\pm 0.7 \text{ W m}^{-2}$ and $\pm 0.3 \text{ W m}^{-2}$ at the SFC and TOA for the SOL flux, respectively, and $\pm 0.3 \text{ W m}^{-2}$ both at the SFC and the TOA for the TIR.

The last atmospheric parameter investigating the radiative perturbations is water vapour. Water vapour is the dominant absorber throughout most of the TIR [Delamere et al. 2010] and has strong absorption bands in the SOL ($\lambda > 900 \text{ nm}$). The strength of SOL absorption also depends on the SZA [Wyser et al. 2008]. Our sensitivity analysis considers a variation of 5% , which is used to represent the instrumental uncertainty of radiosondes, and 15% , which approximates the range between the minimum and maximum column amounts. The variation of 5% leads to differences of $\pm 1 \text{ W m}^{-2}$ and $\pm 0.9 \text{ W m}^{-2}$ for the SOL-D and TIR-D, respectively, at the surface. At the TOA, this perturbation yields differences of $\pm 0.5 \text{ W m}^{-2}$ and $\pm 0.7 \text{ W m}^{-2}$ for the upward thermal infrared flux (TIR-U) and upward solar flux (SOL-U), respectively [see Table 4.1]. The column amount of water vapour is largest in July, and a positive trend in water vapour since the 1990s has been reported, especially during summer [Di Biagio et al. 2012; Rinke et al. 2019]. In addition, recurrent episodes of humidity intrusions can increase the water vapour column by about 8 times above the background level and increase the TIR-D flux at the surface by up to 16 W m^{-2} [Doyle et al. 2011].

4.1.2 Surface

The surface perturbations are focused on the sea surface temperature (SST), surface albedo from CERES (α), and surface emissivity. During PS106, the temperature measurement onboard Polarstern closest to the surface was located at 10 m above sea level. While the SST is a relevant parameter, especially for the thermal emission, it was opted to use the 10 m as a reference since SST was not directly measured during the entire cruise. The accuracy of the ship-borne temperature sensor is of $\pm 0.3 \text{ }^\circ\text{C}$ is used for the sensitivity study, together with a perturbation of $\pm 5 \text{ }^\circ\text{C}$,

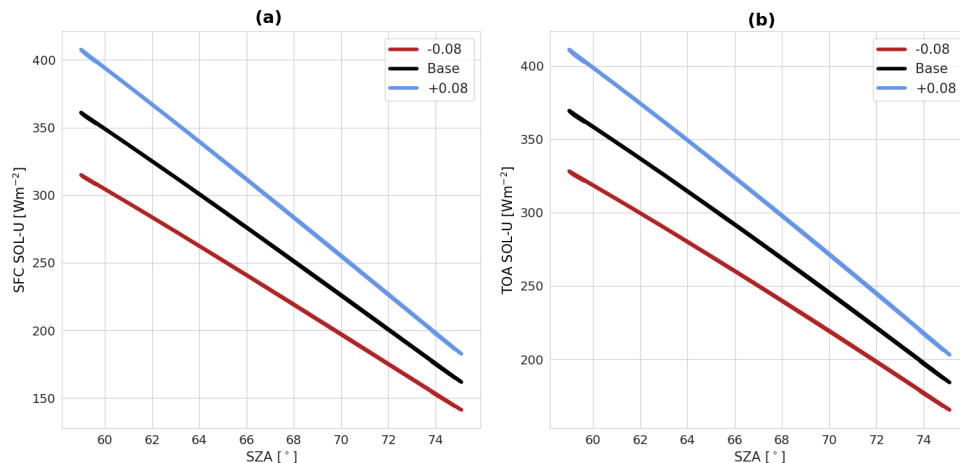


Figure 4.1: Comparison between the upward solar (SOL-U) flux and the SZA at the surface (SFC; panel **a**), and at the top-of-the-atmosphere (TOA; panel **b**) of the base simulation (black) and the variation of ± 0.08 surface albedo of the base simulation.

which corresponds to the largest difference between ship measurements and skin temperature obtained from ERA5 and CERES [see Fig. 3.3c].

The variation of SST only influences the TIR fluxes, causing changes of $\pm 0.3 \text{ W m}^{-2}$ and $\pm 1.4 \text{ W m}^{-2}$ for the TIR-D and TIR-U, respectively, at the SFC. At the TOA, a difference of $\pm 0.5 \text{ W m}^{-2}$ in the TIR-U. Naturally, more considerable variation in skin temperature yields to larger flux differences as indicated in Table 4.1 and Table 4.3, which is particularly relevant for days when these differences are more pronounced [e.g., 6 to 8 June, 22 to 23 June, 2 to 5 July 2017; see Fig. 3.3c.]

Surface albedo is an extremely important parameter for the SOL radiative fluxes [Shupe et al. 2005; Sedlar et al. 2010; Ebell et al. 2020; Stapf et al. 2020]. The retrieval of this parameter from satellites in the Arctic is particularly challenging due to the difficult cloud detection over snow- and ice-covered surfaces and rapid temporal changes induced by melting. Ground-based observations often have limited spatial representativeness. Figure 3.3b shows the time series of hourly surface albedo from CERES and ERA5. However, the difference is more noticeable from 27 June to 8 July 2017. For the PS106 cruise, the mean surface albedo difference between CERES and ERA5 is 0.08. For this study, the daily mean surface albedo of 0.65 is kept constant, and then it is varied ± 0.08 to investigate the radiative effect of these perturbations. Additionally, the minimum (0.05), mean (0.53), maximum (0.84) values of the CERES surface albedo for PS106 are considered to evaluate the sensitivity of SOL fluxes to surface albedo variability during the expedition.

The following results are presented in daily means to provide a general value of the flux difference. However, it is worth noting that fluxes depend strongly on the SZA as shown by Figure 4.1. For instance, at a SZA of 75° the flux difference between the base simulation and ± 0.08 is about $\pm 21.5 \text{ W m}^{-2}$, whereas at a SZA of 58° the flux difference is $\pm 45.3 \text{ W m}^{-2}$.

A variation of the surface albedo by ± 0.08 yields a mean flux difference of $\pm 2.1 \text{ W m}^{-2}$ and $\pm 33.6 \text{ W m}^{-2}$ at the SFC for the clear-sky SOL-D and SOL-U, respectively. This difference also depends strongly on the SZA. For instance, a SZA of

59° leads to a flux difference of the SOL-U at the SFC of $\pm 46.6 \text{ W m}^{-2}$, whereas at a SZA of 75° this difference is $\pm 20.8 \text{ W m}^{-2}$ (not shown). The values presented in Table 4.1 and 4.3 for the surface albedo also indicate the large contrast between the additional values studied (0.84, 0.53, 0.3, and 0.05) minus the constant surface albedo of 0.65. At the SFC, open ocean [e.g., a surface albedo equal to 0.05] causes a large reduction of the SOL-D and SOL-U by 13.9 W m^{-2} and 241.1 W m^{-2} , respectively. On the other hand, the highest surface albedo observed during PS106 (0.84) results in an increase of the clear-sky SOL-D and SOL-U of 5.1 W m^{-2} and 8.4 W m^{-2} , respectively. At the TOA, the daily mean values indicate a reduction by 217.6 W m^{-2} and an increase by 72 W m^{-2} for surface albedos of 0.05 and 0.84, respectively. The importance of surface albedo under clear-sky Arctic conditions has also been analysed in other studies [Wyser et al. 2008; Di Biagio et al. 2012; Sedlar and Devasthale 2012]. Nevertheless, the analysis of the SOL-U flux was not further investigated individually.

The last parameter considered in the analysis is the surface emissivity. A value of 0.9999 is used for surfaces covered by ice, while a value of 0.9907 is used for water surfaces [Wilber et al. 1999]. Additionally, the constant value of 0.988 used by Riihelä et al. 2017 is considered, who used this value for a wider Arctic area, based on Hori et al. 2006. The variation of this parameter only affects the TIR-U. Contrasting the surface emissivity over sea ice and open-ocean, a mean flux difference found is 0.8 W m^{-2} and 0.7 W m^{-2} at the SFC, and TOA, respectively. The comparison with the value used in Riihelä et al. 2017 yields a smaller difference of 0.2 W m^{-2} at the SFC and 0.1 W m^{-2} at the TOA.

Comparison at the SFC

Atmospheric parameters									
Parameter	Variation	TIR-D	TIR-U	Net TIR	SOL-D	SOL-U	Net SOL	NET	
Temperature	± 7 [K]	± 14.9	-	± 14.9	± 0.2	± 0.1	± 0.1	± 14.8	
	± 0.5 [K]	± 1.0	-	± 1.0	± 0.0	± 0.0	± 0.0	± 1.0	
Ozone	± 25 [%]	± 0.6	-	± 0.6	± 1.4	± 0.9	± 0.5	± 0.0	
	± 12.5 [%]	± 0.3	-	± 0.3	± 0.7	± 0.5	± 0.3	± 0.0	
Water vapour	± 15 [%]	± 3.3	-	± 3.3	± 2.7	± 1.8	± 0.9	± 2.4	
	± 5 [%]	± 1.0	-	± 1.0	± 0.9	± 0.6	± 0.3	± 0.7	
Surface parameters									
Parameter	Variation	TIR-D	TIR-U	Net TIR	SOL-D	SOL-U	Net SOL	NET	
Skin temperature	± 5 [K]	± 5.3	± 23.6	± 18.3	-	-	-	± 18.3	
	± 0.3 [K]	± 0.3	± 1.4	± 1.1	-	-	-	± 1.1	
Albedo[0.65]	0.05 [-]	-	-	-	-13.9	-241.1	227.2	227.2	
	0.30 [-]	-	-	-	-8.5	-142.8	134.3	134.3	
	0.53 [-]	-	-	-	-3.0	-49.7	46.7	46.7	
	0.84 [-]	-	-	-	5.1	8.4	-75.3	-75.3	
	± 0.08 [-]	-	-	-	± 2.1	± 33.6	± 31.5	± 32.0	
Emissivity [0.9999]	0.9980 [-]	-	-0.2	0.2	-	-	-	0.2	
	0.9907 [-]	-	-0.8	0.8	-	-	-	0.8	

Table 4.1: Variation of several atmospheric and surface parameters for clear-sky simulations. The table indicates the mean upward and downward SOL and TIR flux differences between the perturbed simulations minus the idealized base atmosphere simulation. All values indicate surface fluxes in $W m^{-2}$.

Comparison at the TOA				
Atmospheric parameters				
Parameter	Variation	TIR-U	SOL-U	NET
Temperature	± 7 [K]	± 15.4	± 0.1	± 15.3
	± 0.5 [K]	$\pm \mathbf{1.1}$	± 0.0	± 1.1
Ozone	± 25 [%]	± 0.6	± 1.7	± 2.3
	± 12.5 [%]	$\pm \mathbf{0.3}$	$\pm \mathbf{0.8}$	± 1.1
Water vapour	± 15 [%]	± 1.5	± 2.2	± 3.7
	± 5 [%]	$\pm \mathbf{0.5}$	$\pm \mathbf{0.7}$	± 1.2

Table 4.2: Variation of several atmospheric parameters. The table indicates the mean upward SOL, TIR, and net flux differences at the top-of-the-atmosphere (TOA) of clear-sky perturbed simulations minus the simulated idealized atmosphere. Values in W m^{-2} .

Comparison at the TOA				
Surface parameters				
Parameter	Variation	TIR-U	SOL-U	NET
Skin temperature	± 5 [K]	± 8.1	-	± 8.1
	± 0.3 [K]	$\pm \mathbf{0.5}$	-	± 0.5
Albedo [0.65]	0.05 [-]	-	-217.6	-217.6
	0.30 [-]	-	-128.7	-128.7
	0.53 [-]	-	-44.7	-44.7
	0.84 [-]	-	72.2	72.2
	± 0.08 [-]	-	$\pm \mathbf{30.2}$	± 30.2
Surface emissivity [0.9999]	0.9980 [-]	-0.1	-	-0.1
	0.9907 [-]	-0.7	-	-0.7

Table 4.3: The table indicates the mean upward SOL, TIR, and net flux differences at the top-of-the-atmosphere (TOA) of clear-sky perturbed simulations minus idealized atmosphere simulation. Values in W m^{-2} .

4.2 Clear-sky Radiative Flux Uncertainty

The clear-sky uncertainty range is used as a limit test closure of simulated and observed radiative fluxes. The closure limit values quantify the uncertainty propagated from the input parameters introduced to the radiative transfer model and consider the instrumental uncertainties of the observations.

This analysis is focused on the downward TIR, and SOL fluxes at the SFC since the radiative closure is based on the observations carried out during the PS106 cruise. A similar comparison for the upward fluxes was not possible due to the logistic challenges that such a setup requires in a ship. Based on the results presented in Section 4.1 and the values given in Table 4.1 and Table 4.2 the total daily mean flux uncertainty propagated from the input parameters is round $\pm 3 \text{ W m}^{-2}$ for the TIR-D

and $\pm 4 \text{ W m}^{-2}$ for SOL-D at the SFC. Note that this refers to daily mean values; however, for the SOL fluxes, the actual values can increase or reduce depending on the SZA. Thus, values should be considered as a guide more than absolute values.

Additionally, it should also be considered the instrumental uncertainties of the pyrgeometer and pyranometer operating aboard Polarstern. As discussed in section 3.1.2 the uncertainty of the pyrgeometer and pyranometer is $\pm 13 \text{ W m}^{-2}$ and $\pm 20 \text{ W m}^{-2}$, respectively. Thus, the total uncertainty range value from the uncertainties of the input data sets for the radiative closure analysis is $\pm 16 \text{ W m}^{-2}$ and $\pm 24 \text{ W m}^{-2}$ for the TIR-D and SOL-D, respectively.

4.3 Cloud Perturbations

The analysis considers the variation of cloud microphysical properties such as the total amount of water path, effective radius (r_E), and cloud phase over different surface albedo (α). Furthermore, macrophysical properties like cloud base height (CBH), cloud geometrical thickness (CGT) were also varied to investigate the flux differences due to their variation. In this case, a persistent single-layer cloud was created with cloud macro and micro-physical parameters that are based on the description of cloud properties given in Chapter 3.3.3. Note that the following sensitivity analysis keeps the cloud optical depth constant.

The following subsections describe the results obtained from the sensitivity study for each of the variations considered by presenting first the flux comparisons and then the comparison of CRE calculated for each perturbation. Table 4.3 shows the constant and variable parameters considered for each sensitivity case.

Table 4.4: Description of constant and variable parameters for the sensitivity analysis of a single-layer cloudy sky.

Parameter	Cloud type	Constant Parameters	Variation
Q	Liquid	$r_{E,L}=8.7 \mu\text{m}$, CGT = 250 m, CBH = 250 m, $\alpha = 0.65$	$Q_L = 10, 25, 50, 75, 100$ and 125 gm^{-2}
	Ice	$r_{E,I}=41 \mu\text{m}$, CGT = 250 m, CBH = 250 m, $\alpha = 0.65$	$Q_I = 10, 25, 50, 75, 100$ and 125 gm^{-2}
r_E	Liquid	$Q_L = 50 \text{ gm}^{-2}$, CGT = 250 m, CBH = 250 m, $\alpha = 0.65$	$r_{E,L} = 2.5, 5, 8.7$, and $10 \mu\text{m}$
	Ice	$Q_I = 50 \text{ gm}^{-2}$, CGT = 250 m, CBH = 250 m, $\alpha = 0.65$	$r_{E,I} = 20, 30, 41$ and $45 \mu\text{m}$
LF	Mixed-phase	$Q = 50 \text{ gm}^{-2}$, CGT = 250 m, $r_{E,L}=8.7 \mu\text{m}$, $r_{E,I}=41 \mu\text{m}$ CBH = 250 m, $\alpha = 0.65$	LF = 0.9, 0.8, 0.5, 0.2, 0.1 [-]
Albedo (α)	Liquid	$Q_L = 50 \text{ gm}^{-2}$, $r_{E,L}=8.7 \mu\text{m}$, CGT = 250 m, CBH = 250 m	$\alpha = 0.2, 0.4, 0.6, 0.65, 0.8$ [-]
	Ice	$Q_I = 50 \text{ gm}^{-2}$, $r_{E,I}=41 \mu\text{m}$, CGT = 250 m, CBH = 250 m	$\alpha = 0.2, 0.4, 0.6, 0.65, 0.8$ [-]
	Mixed-phase	$Q = 50 \text{ gm}^{-2}$, CGT = 250 m, CBH = 250 m $r_{E,L}=8.7 \mu\text{m}$, $r_{E,I}=41 \mu\text{m}$	$\alpha = 0.2, 0.4, 0.6, 0.65, 0.8$ [-] LF = 0.9, 0.8, 0.5, 0.2, 0.1 [-]
CBH	Liquid	$Q_L = 100 \text{ gm}^{-2}$, H = 112 m, $r_{E,L}=8.7 \mu\text{m}$	CBH = 62.4, 124.9, 250, 560, 2062 m
	Ice	$Q_I = 100 \text{ gm}^{-2}$, H = 112 m, $r_{E,I}=41 \mu\text{m}$	
CGT	Liquid	$Q_L = 50 \text{ gm}^{-2}$, CBH = 250, $r_{E,L}=8.7 \mu\text{m}$	
	Ice	$Q_I = 50 \text{ gm}^{-2}$, CBH = 250, $r_{E,I}=41 \mu\text{m}$	CGT = 0.125, 0.250, 1, 2, 3 km

Q variation								
Q [g m ⁻²]	Liquid cloud				Ice cloud			
	TIR-D	TIR-U	SOL-D	SOL-U	TIR-D	TIR-U	SOL-D	SOL-U
10	287.4	239.4	324.3	296.1	251.4	239.3	378.4	278.9
25	308.9	239.6	279.0	307.6	279.0	239.4	353.0	282.4
50	313.2	239.7	236.1	318.3	300.5	239.5	323.6	286.9
75	313.5	239.8	205.4	326.3	308.5	239.6	303.4	290.2
100	313.6	239.8	181.6	332.7	311.5	239.6	288.3	292.8
125	313.7	239.8	162.6	338.0	312.7	239.7	276.1	294.9

Table 4.5: Mean TIR and SOL flux results from the sensitivity analysis of water path (Q) for a single-layer liquid and ice clouds. The downward and upward mean fluxes are calculated at the surface (SFC) and top-of-the-atmosphere (TOA), respectively.

4.3.1 Cloud Water Path

The cloud water path (Q) perturbations consider a variation of 10, 25, 50, 75, and 125 g m⁻² for a single-phase liquid and ice cloud. For all the liquid and ice cloud variation, cloud base height and cloud geometrical thickness are set to 250 metres. For the liquid cloud, a constant $r_{E,L}$ of 8.7 μm and for the ice cloud, a $r_{E,I}$ of 41.0 μm are considered [see Table 4.3].

For PS106, the mean observed values of Q_L and Q_I were 49.7 and 15.2 g m⁻², respectively [see description in Chapter 3.3.3 and Fig. 3.9]. The uncertainty in the retrieval is considered to be at least 25 g m⁻² [Crewell and Löhnert 2003; Marchand et al. 2003], therefore focus is given to the difference of ± 25 g m⁻² of the mean value. However, additional values are also provided to deepen the comparison to other observed values.

Table 4.5 shows the mean SOL and TIR irradiances for the perturbed Q simulations for single-layer liquid- and ice-containing clouds. For the liquid cloud, the TIR-D flux at the SFC varies strongest at a Q_L lower than 50 g m⁻². This is due to the saturation of the downward infrared radiance occurring at values lower than approximately 60 g m⁻² as the cloud radiates as a nearly-ideal black body [see Fig. 1 in Turner 2007, Fig. 3 in Garrett et al. 2002].

The variation of Q affects the SOL flux stronger than the TIR. As the values of Q increases, the cloud albedo increases leading to a reduction (increment) of the SOL flux at the SFC (TOA) [see section 2.4]. The SOL flux is extremely dependent on the position of the sun and the surface conditions. At low SZA the differences are larger as shown in Figure 4.2. For example, at a SZA of 59° the flux difference of the SOL-D between 10 and 25 g m⁻² is 63.3 and 25.2 W m⁻² for a liquid and ice cloud, respectively. The same comparison, but for a SZA of 75° leads to a flux difference of 25.0 W m⁻² for a liquid cloud and 23.5 W m⁻² for an ice cloud [see Fig. 4.2a and c].

At the TOA the variation of Q does not affect significantly the TIR-U. As seen in Table 4.5 the values for a liquid and ice cloud remain near 239 W m⁻². For the SOL-U flux, the difference is larger and dependent on the SZA [see Fig. 4.2b and Fig. 4.2d]. For instance, for a liquid cloud the mean SOL-U flux difference between 10 and 25 g m⁻² at a SZA of 59° is 15.2 W m⁻², while at a SZA of 75° is 6.7 W m⁻².

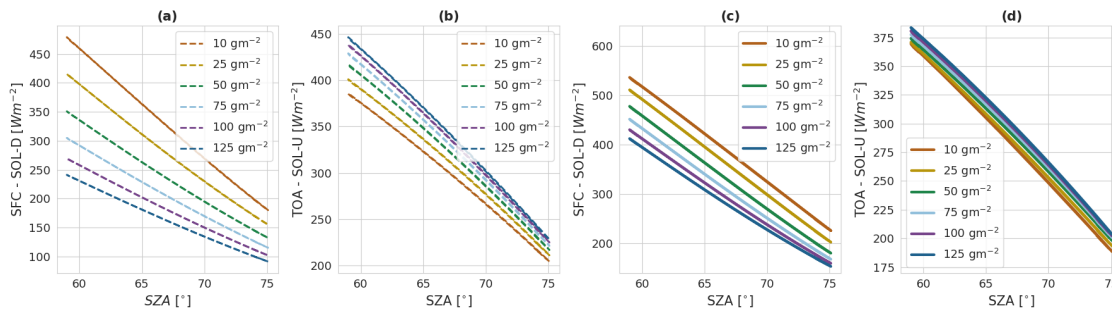


Figure 4.2: Comparison of solar (SOL) flux and the solar zenith angle (SZA) for different values of liquid (Q_L ; dashed line) and ice water path (Q_I ; solid line). Panels (a) and (c) show the downward flux at the surface (SFC), and panels (b) and (d) show the upward flux at the top-of-the-atmosphere (TOA).

The same comparison for an ice cloud leads to a SOL-U flux difference of 1.4 W m^{-2} and 4.9 W m^{-2} , for a SZA of 59° and 75° , respectively.

The Q has an important effect on the CRE. Figure B.1 shows the daily mean variation of the CRE in function of Q at the SFC and TOA. At the SFC and TOA, there is a warming and cooling effect of clouds, respectively regardless of the cloud phase. The TIR CRE is directly proportional to Q ; however, its increase with the increment of Q does not surpass the effect of the SOL flux in the CRE. At the SFC, the CRE for a liquid cloud decreases as the Q increases; this is due to a more optically thick cloud that reduces the SOL-D flux warming reaching the SFC. At the TOA, the effect is reversed since as the Q increases, the larger is the amount of SOL-U flux reflected back at the TOA. In the case of an ice cloud, there is not such a large variation of CRE as in the liquid case at the SFC or TOA. The large variation of the net CRE for liquid clouds indicates that liquid clouds are more susceptible to radiative changes mostly attributed to the SOL flux.

4.3.2 Cloud Particle Effective Radius

The r_E is an important parameter affecting both TIR and SOL fluxes. Comparing clouds with the same Q , as it is considered in all the simulations in this section, the cloud with the largest cloud optical depth would be the one with the smallest r_E leading to a larger reflection of SOL flux and a stronger emission of TIR flux. The cloud phase plays an important role since, in general, liquid clouds contains smaller r_E than ice clouds leading to a larger optical depth and higher reflection of the SOL radiation to space for the same water path [Cesana and Storelvmo 2017].

For this experiment, the r_E is varied for an ice and liquid cloud, keeping constant the other macro- and microphysical parameters, as shown in Table 4.3. In the case of the liquid cloud, the values were varied to 2.5, 5.0, 8.7, and $10 \mu\text{m}$. Liquid clouds can also present larger $r_{E,L}$ of up to $41 \mu\text{m}$ [see Fig. 3.9a], especially during precipitation. However, such cases are outside the scope of the sensitivity analysis. In the case of single-layer ice cloud, the values were varied to 20, 30, 41, and $45 \mu\text{m}$ [see Fig. 3.9c].

The variation of $r_{E,L}$ does not affect the TIR-D significantly, since the mean flux value of 313 W m^{-2} changes less than 0.4 W m^{-2} by varying the $r_{E,L}$ from 2.5 to

r_E variation							
TIR-D				TIR-U			
Liquid		Ice		Liquid		Ice	
$[\mu\text{m}]$	$[\text{W m}^{-2}]$	$[\mu\text{m}]$	$[\text{W m}^{-2}]$	$[\mu\text{m}]$	$[\text{W m}^{-2}]$	$[\mu\text{m}]$	$[\text{W m}^{-2}]$
2.5	313.1	20	311.0	2.5	239.8	20	239.6
5.0	313.3	30	306.7	5.0	239.8	30	239.5
8.7	313.2	41	300.5	8.7	239.7	41	239.5
10	313.0	45	298.1	10	239.7	45	239.4
SOL-D				SOL-U			
Liquid		Ice		Liquid		Ice	
$[\mu\text{m}]$	$[\text{W m}^{-2}]$	$[\mu\text{m}]$	$[\text{W m}^{-2}]$	$[\mu\text{m}]$	$[\text{W m}^{-2}]$	$[\mu\text{m}]$	$[\text{W m}^{-2}]$
2.5	113.6	20	286.4	2.5	365.2	20	297.3
5.0	185.3	30	307.9	5.0	337.7	30	291.0
8.7	236.1	41	323.6	8.7	318.3	41	286.9
10	246.5	45	327.9	10	314.3	45	285.9

Table 4.6: Mean TIR and SOL flux values of the sensitivity analysis of effective radii (r_E) for liquid and ice clouds. The downward and upward mean fluxes are calculated at the surface (SFC) and top-of-the-atmosphere (TOA), respectively.

$10\mu\text{m}$ [see Table 4.6]. In the case of ice clouds, however, the same variation of $r_{E,L}$ can affect the TIR-D flux up to 12.9 W m^{-2} . At the TOA, the variation of $r_{E,L}$ has a weak impact on the TIR-U flux. Both for liquid and ice, the flux remains around 239 W m^{-2} as the cloud radiates as a blackbody.

The r_E parameter is extremely important for the SOL and therefore sensitive to the SZA. For a liquid cloud, the comparison between 2.5 to $5.0\mu\text{m}$ can lead to a mean flux difference of up to 71.7 W m^{-2} . The variation between 2.5 and $5\mu\text{m}$ at a SZA of 75° yields to a flux difference of 40.2 W m^{-2} , whereas at a SZA of 59° the difference is 106.6 W m^{-2} . In the case of an ice cloud, the comparison between a $r_{E,I}$ of 30 and $41\mu\text{m}$ leads to a flux difference of 9.7 W m^{-2} and 20 W m^{-2} for a SZA of 75° and 59° , respectively.

At the TOA, the variation of r_E affects the SOL-U in a less intense magnitude than at the SFC. For instance, comparing a $r_{E,L}$ between 2.5 and $5\mu\text{m}$ can lead to important flux differences larger than 15 W m^{-2} at high SZA angles [e.g., 75°]. The same comparison for a SZA of 59° yields a flux difference of 40.6 W m^{-2} . The flux difference between a $r_{E,L}$ of 2.5 and $5\mu\text{m}$ at a SZA of 75° yields to a flux difference of 15.5 W m^{-2} , and at a SZA of 59° the difference is 40.6 W m^{-2} . For an ice cloud, the flux difference between 30 and $41\mu\text{m}$ for a SZA of 75° is 3.0 W m^{-2} and for a SZA of 59° is 4.5 W m^{-2} .

The variation of r_E affects the magnitude of the CRE significantly. Figure B.2 shows the mean values of CRE for the variation of liquid and ice r_E . Interestingly, for the given single-layer liquid cloud case study, the only condition that can lead to a cloud cooling effect occurs when the $r_{E,L}$ is small enough that the net CRE is dominated by the SOL flux. This is because smaller droplets could lead to larger optical depth and therefore reflect more of the SOL flux [see section 2.4].

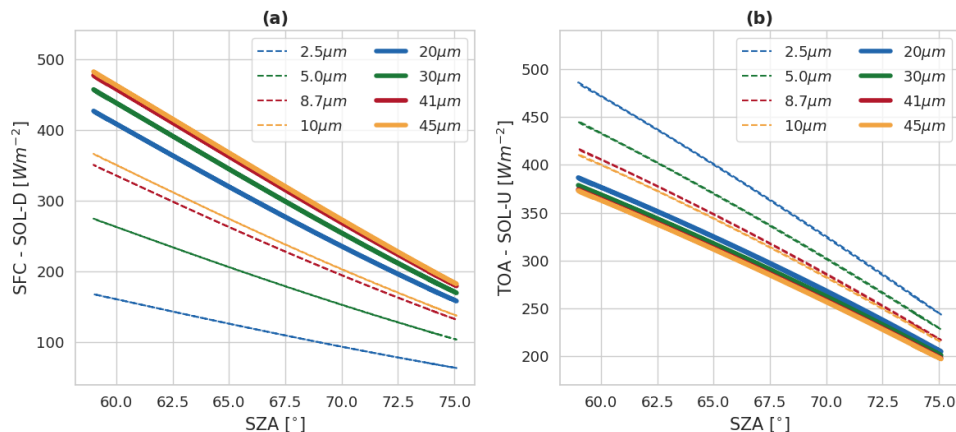


Figure 4.3: Comparison between the solar flux (SOL) and the solar zenith angle (SZA) for different values of liquid ($r_{E,L}$; dashed line) and ice effective radius ($r_{E,I}$; solid line). Panel (a) shows the downward flux SOL-D at the surface (SFC), and panel (b) shows the upward flux (SOL-U) at the top-of-the-atmosphere TOA.

4.3.3 Liquid Fraction and Surface Albedo

The radiative relevance of the amount of liquid in a single-layer mixed-phase cloud is investigated in this section. Furthermore, the interaction between the cloud liquid fraction and the surface conditions is evaluated. The variation of liquid fraction (LF) was varied from 1.0 (entirely liquid) to 0.0 (entirely ice). The simulated cloud cases are composed of a mixture of ice crystals and liquid droplets, all equally distributed within the cloud boundaries. The variation of the cloud phase has a stronger effect on the SOL flux than the TIR fluxes. Therefore, main emphasis is given to the SOL flux, its dependency with the SZA, and its interaction with the surface albedo [see Fig. 4.4].

The solar heating at the surface is linearly dependent on the surface albedo. In the contrasting Arctic with open ocean and ice with snow areas, the effect of a mixed-phase cloud with the same macro and microphysical properties can vary the amount of SOL flux reaching the SFC and the TOA.

The larger the amount of Q_L of a mixed-phase cloud with otherwise constant total water path, the larger is the decrease (increase) of the SOL at the SFC (TOA). As explained in section 2.4 and 4.3.1, this is due to the increase of the cloud albedo. Therefore, identifying the correct cloud phase is as important as determining the surface albedo since this parameter depends on the ratio of direct to diffuse SOL downward flux.

The Figure 4.4 shows the variation of the SOL-D for different LF over different surface albedos. Over snow or ice surfaces (albedo = 0.8) the largest SOL-D flux difference between a mostly liquid (LF = 0.9) and high ice cloud (LF = 0.1) occurring at a SZA of 59° is 74.9 W m^{-2} . This difference at a SZA of 75° is of 25.9 W m^{-2} . In contrast, over ocean (albedo = 0.2) these differences are larger. For instance, comparing LF of 0.9 and 0.1 for a SZA of 59° and 75° the SOL-D flux difference are 132.0 W m^{-2} and 47.7 W m^{-2} , respectively.

At the TOA a variation of LF of 0.9 and 0.1 at a SZA of 59° over a high reflective surface is 14.5 W m^{-2} , whereas over ocean this comparison leads to a difference of

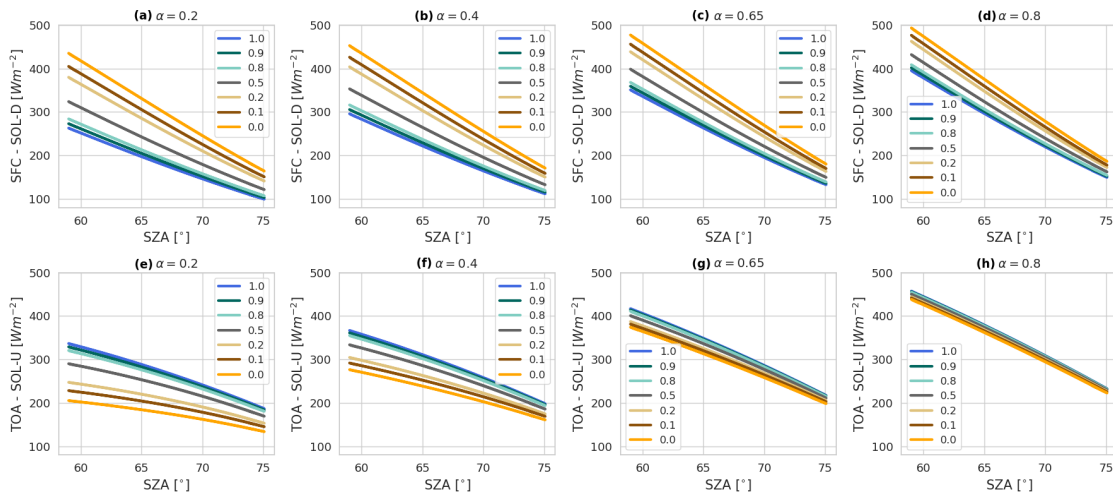


Figure 4.4: Comparison between the solar flux (SOL) and the solar zenith angle (SZA) for several single-layer mixed-phase clouds with different liquid fractions. The upper row shows the downward flux at the surface (SFC) and the lower row shows the upward flux at the top-of-the-atmosphere (TOA). Panels (a) and (e) show the comparison for a surface albedo (α) of 0.2, panels (b) and (f) for a α of 0.4, panels (c) and (g) for a α of 0.65, and (d) and (h) for a α of 0.8.

100.8 W m^{-2} . These results not only upholds the importance of the right identification of the cloud phase for the SOL fluxes but also reveals the sensitivity of its identification at low SZA in function of the surface albedo [see Fig. 4.4].

The variation of LF affects the TIR flux in a considerable lower magnitude than the SOL flux because this parameter does not change the cloud height and temperature. The variation of a LF of 0.9 and 0.1 can lead to a mean daily flux difference of about and 4 W m^{-2} and 0.2 W m^{-2} of the TIR-D at the SFC and TIR-U at the TOA, respectively. While the surface albedo influences only the SOL flux, the SST influences the TIR flux.

The quantification of the daily mean CRE at the SFC comparing different LF and surface albedo is presented in Figure 4.5. Over ice/snow surfaces, there is a clear dominance of a warming effect with relatively similar values ranging around 65 W m^{-2} . Over a surface albedo of 0.65, the warming effect is still persistent but in a larger magnitude as the cloud tends to have a higher fraction of ice. For lower albedos of 0.4 and 0.2, there is a cooler CRE as more liquid the cloud has. Similarly, at the TOA the CRE is very dependent on the surface albedo. For a surface albedo of 0.65 and 0.8, the cooling effect increases as the liquid fraction increases. On the other hand for the simulated cases of a surface albedo of 0.4 and 0.2 there is a clear warming effect that can go above 100 W m^{-2} [see Fig. B.3]. This sensitivity analysis does not only confirm the importance of the liquid phase in mixed-phase clouds in the radiation budget as discussed in other studies [Shupe and Intrieri 2004; de Boer et al. 2009; Sedlar and Devasthale 2012; Morrison et al. 2012], but also highlights its intrinsic dependency on the surface albedo and the SZA.

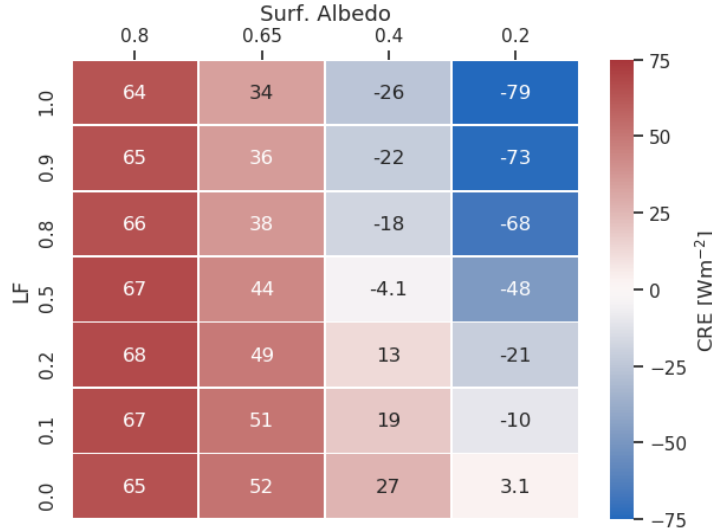


Figure 4.5: Mean values of the net cloud radiative effect (CRE) for a single-layer cloud at the surface (SFC) for several surface albedo and the liquid fraction (LF) values.

4.3.4 Cloud Base Height

The sensitivity study presented in this section keeps constant the CGT of 250 m, Q of 50 g m^{-2} and r_E of $8.7 \mu\text{m}$ and $41 \mu\text{m}$ for the liquid and ice cloud phase, respectively. During PS106, the cloud base detection limit of the Mira-35 cloud radar was 165 m above sea level [Griesche et al. 2020], hence the cloud base heights of 62.4 m, 124.9 m were considered to quantify the effect on the SOL and TIR fluxes of a lower cloud base. Moreover, additional CBH of 560 m, and 2062 m were considered for the sensitivity analysis. A CBH higher than 2000 m were not considered since most of the CBH observed in the Arctic are below this height [see Fig. 3.8b; Shupe et al. 2011; Maturilli and Ebell 2018; Achtert et al. 2020; Nomokonova et al. 2020; Griesche et al. 2020].

The mean downward (at the SFC) and upward (at the TOA) fluxes of the SOL and TIR are given in Table 4.7. The variation of the CBH yields particular interest to the TIR-D at the SFC, especially in the atmospheric window [$7.19\text{-}12.2 \mu\text{m}$] where the atmosphere is relatively transparent [Yung 2003]. The CBH determines the emission temperature and the air layers contributing to the TIR-D flux reaching the surface [Viúdez-Mora et al. 2015]. However, part of this radiation can be reduced due to the TIR scattering effect that causes a cooling below the cloud [Zhao et al. 2018]. The results of the simulations performed indicate that a variation of 187.6 m in the CBH yields to a flux difference of 1.6 W m^{-2} and 1.2 W m^{-2} for a liquid and ice cloud, respectively. The second flux affected the most by this perturbation is the SOL-U flux at the TOA with a flux difference of 1.2 W m^{-2} and 0.5 W m^{-2} for a liquid and ice cloud, respectively.

At the TOA the TIR-U flux increases as the cloud base is closer to the surface. The somewhat contrary value calculated at a CBH of 124.9 m for liquid and ice might be attributed to a temperature inversion that could have contributed to a lower value than expected in the radiative calculation.

CBH variation								
CBH [m]	Liquid cloud				Ice cloud			
	TIR-D	TIR-U	SOL-D	SOL-U	TIR-D	TIR-U	SOL-D	SOL-U
62.4	314.8	238.9	236.5	317.1	301.7	239.3	323.6	286.4
124.9	314.6	239.1	236.3	317.5	301.2	239.2	323.6	286.6
250	313.2	239.7	236.1	318.3	300.5	239.5	323.6	286.9
560	313.7	238.2	235.8	319.8	300.5	238.7	323.6	287.6
2062	300.7	225.9	235.1	325.8	289.4	228.2	323.7	290.2

Table 4.7: Mean TIR and SOL flux values of the sensitivity analysis of cloud base height (CBH) for liquid and ice clouds. The downward and upward mean fluxes are calculated at the surface (SFC) and top-of-the-atmosphere (TOA), respectively.

The CBH is a relevant parameter and challenging to determine by satellite passive remote sensing observations [Chan and Comiso 2011], especially during night. Based on CERES products and GEOPROF-Lidar observations, the study of Yost et al. 2020 quantified the CBH biases of -0.47 km (0.17 km) and 1.82 km (0.46 km) for ice (liquid) clouds during day and nighttime, respectively [see Fig. 14, Fig. 15, and Fig. 22 in their study]. Such biases affect on the TIR and SOL fluxes specially when the differences on CBH are larger than 1 km.

The daily mean CRE was calculated and illustrated in Figure B.4. The CRE decreases as the CBH increases. An underestimation of about 62 m in the CBH can lead to an overestimation of the CRE of 0.2 W m^{-2} . While this value is rather low in comparison to the previous sensitivity analysis, the difference is more pronounced when the CBH surpasses 1000 m. Nevertheless, the most frequent cloud base heights are below 300 m suggesting that other parameters have a larger influence on the CRE as it is also discussed in Viúdez-Mora et al. 2015 [see their section 5.4].

4.3.5 Cloud Geometrical Thickness

The last variation considered in this chapter is the CGT. While active remote sensing instruments can identify the boundary of clouds relatively well, it is more challenging for passive remote sensing observations [Chan and Comiso 2011; Chan and Comiso 2013]. The aim of this comparison is to quantify the difference on SOL, TIR fluxes and the CRE by varying the CGT while keeping constant the values of Q , r_E , CBH, and surface conditions [see Table 4.3].

The CGT is a parameter of particular interest in the TIR wavelengths since the brightness temperature is indirectly sensitive to the cloud geometric height thickness linked to the corresponding cloud temperature. The brightness temperature depends on the effective temperature, which in turn also depends on the cloud geometric height and thickness [see Fig. 2 in Garrett et al. 2009]. The CGT was varied for a liquid and ice single-layer cloud. This parameter has larger effects at the TOA. The results for the downward fluxes at the SFC and upward fluxes at the TOA for the SOL and TIR fluxes are shown in Table 4.8.

The comparison of a CGT of 0.125 km and 3 km has an effect on the TIR-U (TIR-D) for a liquid and ice cloud of 11.7 W m^{-2} (1.9 W m^{-2}) and 6.9 W m^{-2} (3.3 W m^{-2}), respectively. In the case of the SOL flux the variation is dependent on the SZA

(not shown). For a SZA of 59° the SOL-U (SOL-D) flux difference between a CGT of 0.125 km and 3 km for a liquid and ice cloud are 12.4 W m^{-2} (3.9 W m^{-2}) and 3.4 W m^{-2} (1.2 W m^{-2}), accordingly. In the case of a SZA of 75° , the SOL-U (SOL-D) for a liquid is 10.2 W m^{-2} (0.9 W m^{-2}) and for an ice cloud is 4.7 W m^{-2} (1.4 W m^{-2}).

The CGT has been investigated in Yost et al. 2020 by comparing remote sensing observations from CERES Ed.4 and CALIOP/CPR Cloud thickness and quantified a bias of -0.25 km and -0.42 km for liquid clouds during day and night, respectively. The comparison considered opaque and non-opaque ice clouds observed during day and night. The largest biases encountered were for opaque ice clouds during the night of -2.74 km [see Fig. 13d in their paper]. Such a large bias can lead to important TIR-U fluxes differences at the TOA that is of relevance at the moment of investigating the radiative effect of clouds or determining radiative closure at the TOA.

The net CRE was calculated for all the simulations performed, and as in the sensitivity analysis of the variation of the CBH, and Q there is a warming effect at the SFC and cooling effect of clouds at the TOA [see Fig. B.5]. At the SFC, as is to be expected, the variation of the CGT does not play a significant role in the CRE for liquid and ice clouds. Nevertheless, at the TOA, there is a clear decrease in the cooling of the CRE as the CGT increases in magnitude. It is worth mentioning that the simulations performed greatly depend on cloud-top height temperature assumption. For the simulations, the vertical profiles of temperature and humidity were kept constant regardless of the variation of CGT.

CGT variation								
CGT [m]	Liquid cloud				Ice cloud			
	TIR-D	TIR-U	SOL-D	SOL-U	TIR-D	TIR-U	SOL-D	SOL-U
125	313.2	239.1	236.2	317.8	300.4	239.1	323.6	286.8
250	313.2	239.7	236.1	318.3	300.5	239.5	323.6	286.9
1000	313.1	236.0	235.8	320.7	299.9	237.5	323.6	287.8
2000	312.5	228.8	235.5	323.5	297.9	233.0	323.7	288.8
3000	311.5	221.6	235.3	326.6	295.5	228.3	323.7	289.9

Table 4.8: Mean TIR and SOL fluxes of the sensitivity analysis of cloud geometrical thickness (CGT) for liquid and ice clouds. The downward and upward mean fluxes are calculated at the surface (SFC) and top-of-the-atmosphere (TOA), respectively.

4.4 Synopsis

In this chapter, the TIR and SOL flux changes due to the perturbations of several atmospheric and surface properties in a clear-sky and cloudy atmosphere were investigated. This analysis was based on the mean values presented and discussed in Chapter 3.3 for 3 July 2017 at 81.9° latitude and 32.51° longitude. The daily mean results of the variation of a clear-sky atmosphere are presented in Table 4.1, Table 4.2, Table 4.3, and summarized in Table 4.9. In the case of a cloudy atmosphere, the description of constant and variable parameters are detailed in Table 4.4 and

Summary of the most important parameters affecting SOL and TIR fluxes							
Clear-sky conditions							
Parameters		Ta	Ozone	Water Vapour	Skt	α	S. Emis.
TOA	TIR-U	1	5	3	2	-	4
	SOL-U	4	3	2	-	1	-
SFC	TIR-D	1	4	2	3	-	-
	SOL-D	4	3	2	-	1	-

Table 4.9: Ranking of parameters that affect the SOL and TIR fluxes at the SFC and TOA for clear-sky conditions. The value of 1 is given to the parameter that affects the most, and 5 to the parameter that affects the least each flux. In bold are marked the parameters that need the most attention. Symbol ‘-’ indicates no effect.

Summary of the most important parameters affecting SOL and TIR fluxes						
Cloudy conditions						
Parameters		Q	r_E	LF and α	CBH	CGT
TOA	TIR-U	1	4	5	3	2
	SOL-U	2	2	1	4	3
	CRE	3	2	1	4	5
SFC	TIR-D	1	4	2	3	5
	SOL-D	2	2	1	3	4
	CRE	3	2	1	4	5

Table 4.10: Ranking of parameters that affect the SOL and TIR fluxes at the SFC and TOA for cloudy conditions. The value of 1 is given to the parameter that affects the most, and 5 to the parameter that affects the least each flux. In bold are marked the parameters that need the most attention.

results are illustrated in several figures and tables in section 4.3, appendix B, and summarized in Table 4.10.

Clear-sky perturbations of atmospheric and surface parameters indicated that at the SFC the most dominant parameters for the TIR flux are the atmospheric temperature, water vapour, and skin temperature [see Table 4.1]. In the case of the SOL flux, the parameters that are more sensitive to the variation of the surface albedo (α), water vapour, and ozone. The magnitude of the variation of the surface albedo is the highest among all and can lead to a variance larger than 30 W m^{-2} for the SOL-U at the TOA.

The results of a clear-sky atmosphere were used to set the uncertainty range based on the input parameters of T-CARS and propagate their uncertainties in radiative flux terms. The values obtained together with the instrumental accuracy are $\pm 16 \text{ W m}^{-2}$ for the TIR-D and $\pm 24 \text{ W m}^{-2}$ for the SOL-D. These values are used for the analysis and radiative flux comparison between observations and simulations at the SFC in chapter 6 and 7.

For a cloudy atmosphere, several micro and macrophysical parameters of a single-layer cloud were modified. Additionally, several simulations of mixed-phase clouds over different surface conditions were performed. The analysis was focused on the variation of Q , r_E , LF and surface albedo, CBH, and CGT. The comparison consisted on focusing the individual downward (at the SFC) and upward SOL and TIR fluxes (at the TOA) and to quantify the net CRE at both the SFC and TOA.

The interaction between cloud-phase and the surface conditions can play a decisive role in whether a cloud has a warming or cooling effect [see Fig. 4.5, and Fig. B.3]. While the LF has an effect on both SOL and TIR fluxes, the surface albedo has a direct effect on the SOL flux being at the same time susceptible to the changes in the SZA [see Fig. 4.4].

Among the microphysical parameters of clouds, the Q has the largest relevance on the TIR [see Table 4.5]. The SOL flux is sensitive to large variations of Q , and r_E which are in turn dependent on the SZA [see Fig. 4.2 and Fig. 4.3]. The results presented in Table 4.7, Table 4.8, Figure B.4, and Figure B.5 indicate that the perturbation of cloud macrophysical properties do not have a strong influence on the CRE or the variation of the fluxes in general [see Table 4.10]. However, the accurate determination of the CGT is of importance for the TIR-U flux at the TOA due to the relation with the effective temperature and brightness temperature [Garrett et al. 2009].

Chapter 5

Cloud Induced Spatiotemporal Variability of Solar Radiation

5.1 Data Analysis

This chapter presents the results, analysis, and discussion of the experiment conducted with a set of 15 pyranometer stations on the ice-floe camp period during PS106. While an introduction to the characteristics of the pyranometer network was given in subsection 3.1.1, here, a more detailed description is given to the data processing and data analysis for the entire period as well as for selected cases studies. This chapter is based on the data published on Barrientos-Velasco et al. 2018 and the work presented in Barrientos-Velasco et al. 2020.

5.1.1 Data Processing

The raw data of each pyranometer station are stored in ASCII files in counts of 10 bits on a SD card. The recorded data was subsequently converted to GHI (W m^{-2}), air temperature (T_a in K) and relative humidity (RH in %) using the equations given in Madhavan et al. 2016. The values of GHI, T_a and RH were averaged to 1Hz sampling frequency according to the GPS time reference. The data set was processed into NetCDF files following the latest 1.7 version of the Climate and Forecast Conventions Unidata 2012. Daily files containing all 15 pyranometer stations including GHI, T_a , RH, latitude, longitude, levelling and cleanliness flags, station number, and corrected calibration coefficient were prepared. Earth Sun distance (in AU), solar constant and solar zenith (θ in degrees) and azimuth angles (α in degrees) were added to the data set based on the algorithms given in the World Meteorological Organization (WMO) Guide to Meteorological Instruments and Methods of Observations for practical application WMO 2008.

In this analysis, AT_g is calculated from the GHI measurements following equation 2.6. AT_g is hence defined as the fraction of radiation that is transmitted through the atmosphere [e.g., Yung 2003]. While at the TOA, AT_g is 1, the value is reduced at the SFC due to absorption and scattering processes occurring in the atmosphere. At the SFC, the highest values are generally observed during cloudless conditions, while clouds generally cause a reduction of AT_g . Under certain situations, however, the presence of broken clouds can amplify AT_g to reach values larger than 1 due

to horizontal photon transport and 3D radiative effects. Such enhancements can exceed 400 W m^{-2} and persist up to 20 seconds [Schade et al. 2007].

5.1.2 Sky Classification

An overview of cloud conditions was introduced in subsection 3.3.3. In this section, a similar classification is made based on the visual inspection of all-sky camera observations recorded aboard Polarstern. These images provide a complete impression of the horizontal variability of clouds which is important for the characterization of inhomogeneities of the atmospheric transmittance. As a first step, overcast, cloudless and broken cloud conditions were classified from the all-sky camera observations on Polarstern. Due to the availability of observations with a cloud radar of type Mira-35 and multi-wavelength polarization Raman lidar Polly^{XT} [Engelmann et al. 2016] during PS106 [Wendisch et al. 2019; Macke and Flores 2018], these were used in addition to identify the presence of multilayer clouds, a separation which has not been considered in previous studies [Madhavan et al. 2016; Madhavan et al. 2017; Lohmann et al. 2016; Lohmann and Monahan 2018]. Cirrus clouds and low, geometrically thin stratus clouds were also observed and considered together as thin clouds due to their low occurrence frequency to study their effects on ATg.

The ultimate classification was made considering the daily quick looks of the range-corrected signal at 532 and 1064 nm wavelength from the lidar, daily plots of the radar reflectivity, and images from the all-sky camera. Whenever the lidar signal was attenuated, the information of the cloud radar was used to identify the presence of single or multiple layers of clouds. For apparently clear-sky moments as identified by the lidar and radar quick looks, images from the sky camera were used to confirm the absence of clouds or to identify thin cloud layers or broken cloud situations. In this study, conditions were only considered cloudless when the images from the all-sky camera did not show any clouds within its fisheye field of view. The transition from one type of sky condition to another was only recorded when this class lasted for longer than 15 minutes. When the change was observed for less than 15 minutes, cases were assumed to belong to the previous sky condition. Thin clouds were defined as clouds with a geometrical thickness below 450 m. The result of this classification is shown by the background colour-coding in Figure 5.1.

It is worth mentioning that Cloudnet data sets were not processed at the time this classification was made. Thus, this classification was made manually for the period of the ice-floe camp, and then the results were published in Barrientos-Velasco et al. 2020.

The most frequent conditions observed during the ice-floe camp were overcast (39.6 %), then multilayer (32.4 %), broken clouds (22.1 %), thin clouds (3.5 %), and as the least frequent cloudless conditions (2.4 %). The time series of Figure 5.1 indicates a rather stable behaviour of ATg for overcast conditions and cloudless conditions, with a mean ATg of 0.5 and 0.78, respectively. Thin clouds show a relatively stable fluctuation of ATg with a mean of 0.72. Multilayer clouds show abrupt changes of ATg, with a mean value of 0.46. In contrast, during broken cloud conditions, the values vary not only in time but also in space since the standard deviation is the highest during these conditions (see Fig. 5.1b). A summary of the distribution of ATg is presented in Figure 5.2.

In addition, the ice floe camp was classified into warm and cold period based on the near-surface temperature measured aboard Polarstern (see Fig. 3.3c). The days from 4 to 10 of June were categorized as cold conditions, and from 10 to 16 of June, the conditions were classified as warm.

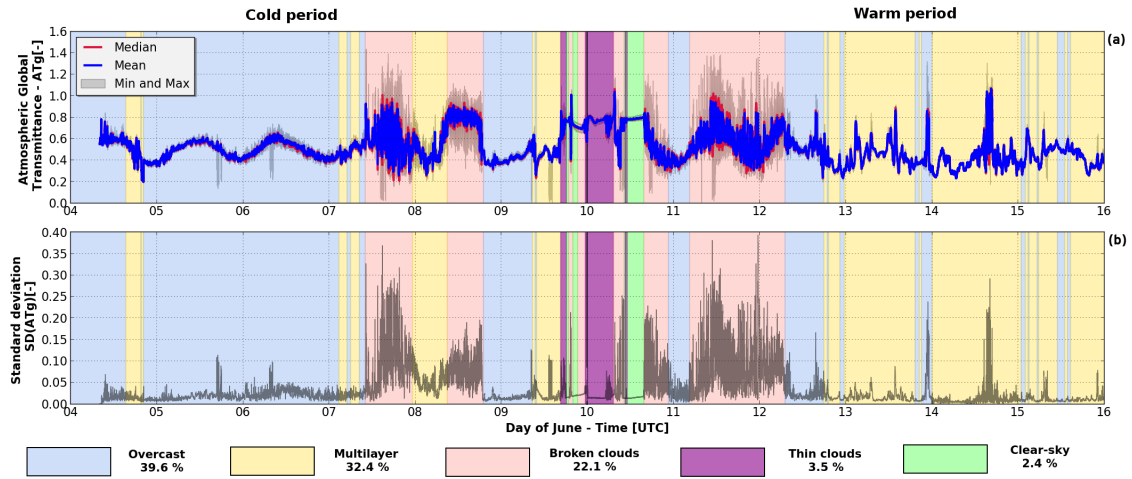


Figure 5.1: (a) Time series of atmospheric global transmittance (ATg) derived from pyranometer network. In blue is shown the mean and in red the median. (b) Time series of the inter-station standard deviation of ATg. Shaded grey area indicate minimum and maximum values in (a) and (b). Source: Barrientos-Velasco et al. 2020.

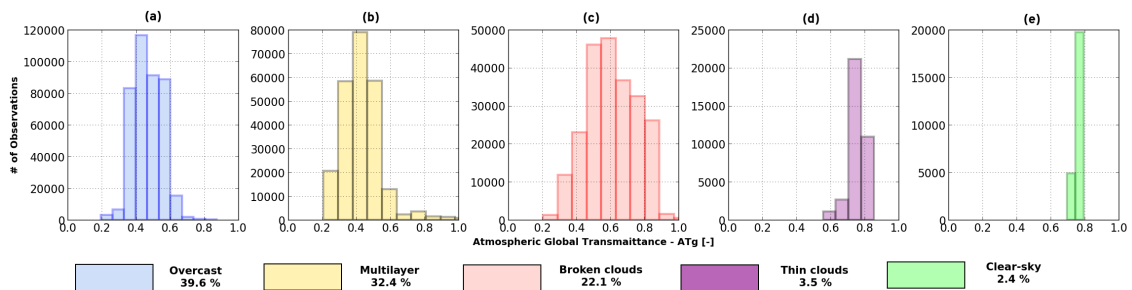


Figure 5.2: Histograms of atmospheric global transmittance (ATg) for (a) overcast, (b) multilayer, (c) broken cloud, (d) thin cloud and (e) cloudless sky conditions. Source: Barrientos-Velasco et al. 2020.

5.2 Case Studies

Several case studies were selected based on the time series shown in Figure 5.1. Each of the case studies corresponds to each of the five atmospheric conditions defined.

5.2.1 Clear-sky Case

The clear-sky case chosen correspond to 10 June 2017 (11:10Z - 15:43Z). This day was the longest clear-sky period during the ice floe period. This case study also coincides

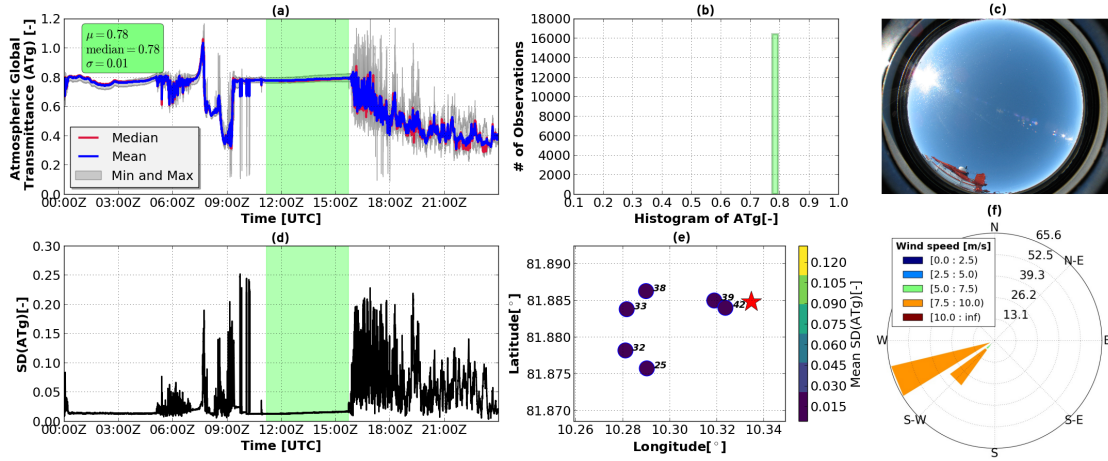


Figure 5.3: Overview of the cloudless case: (a) shows the time series of atmospheric global transmittance (ATg), and the green-shaded background marks the cloudless period (June 10, 2017, 11:10Z - 15:43Z). (b) Histogram of global transmittance for cloudless conditions. (c) Photograph from the all-sky camera at 13:51:44Z. (d) Time series of the inter-station standard deviation (SD) of ATg based on all functional stations. (e) Map of the stations showing the temporal SD for individual stations, while the red star marks the position of Polarstern. Panel (f) shows the wind rose for the selected period. Source: Barrientos-Velasco et al. 2020.

with the beginning of the warm period, with a mean ambient temperature of 274 K. This day was also characterized by the warmest air in the upper atmospheric layers during the ice floe period, and a relatively low boundary layer of about 200 m height [Knudsen et al. 2018; see Fig. 3.5a].

The positive AO index (see Fig. 3.5) suggests relatively dry conditions associated with an anti-cyclonic circulation [Knudsen et al. 2018], leading to reduced cloudiness and enhanced downward solar radiation. The time series of ATg is shown in 5.3a, and the green background highlights the cloudless period. The narrow distribution of ATg with values just below 0.8 is shown in Figure 5.3b. The comparable small reduction of transmittance is mainly due to scattering and absorption by atmospheric gases and, to a lesser degree, due to aerosols. In early spring or autumn, lower values of ATg are found due to the lower sun and the resulting longer optical path through the atmosphere [Zhao and Garrett 2015]. The temporal standard deviation of the operational pyranometers is shown in Figure 5.3d, having a mean value of 0.014 for the period of interest. Variability in the observed global transmittance is mainly noticed for stations 39 and 42, with a standard deviation of 0.0090 and 0.0092, respectively. This variability can likely be attributed to undetected deficiencies such as an unlevelled instrument due to melting.

5.2.2 Overcast Case

The day chosen to study overcast conditions is 6 June (00:00Z and 23:59Z). During this day, the boundary layer increased in height from 300 m to about 430 m. This day was characterized by the presence of a LLS cloud type with a cloud base below 100 m and a cloud top of about 490 m [see Fig. 3.7 and 3.9]. The wind speed measured aboard Polarstern increased from 2.5 m/s to almost 10 m/s in the evening

with easterly origin [see Fig. 5.4 e and 5.4f]. The mean surface temperature recorded by the pyranometer network during this period was 270.1 K, with an inter-station SD of 0.38 K.

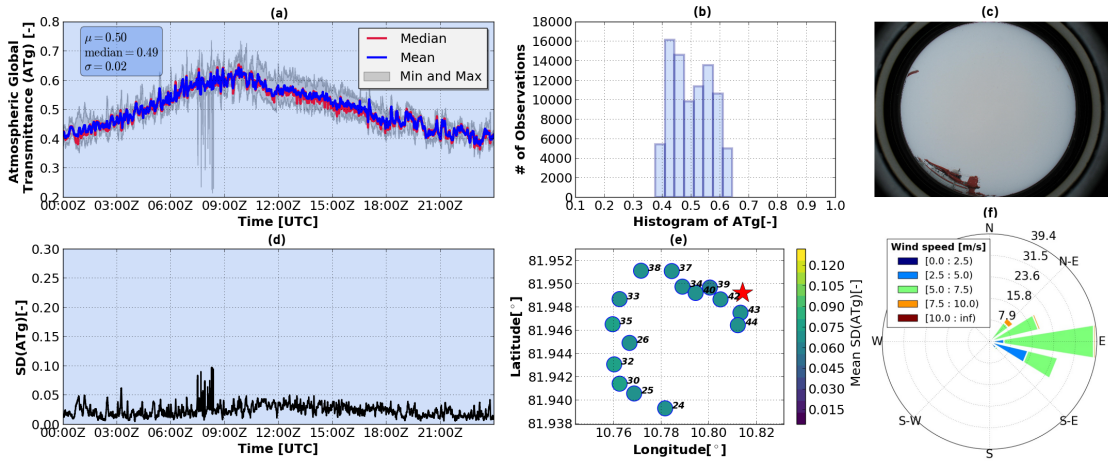


Figure 5.4: Overview of overcast case: Same as Fig. 5.3, but for 6 June 2017, 00:00Z - 23:59Z. All-sky camera photograph taken at 13:41:54Z. Source: Barrientos-Velasco et al. 2020.

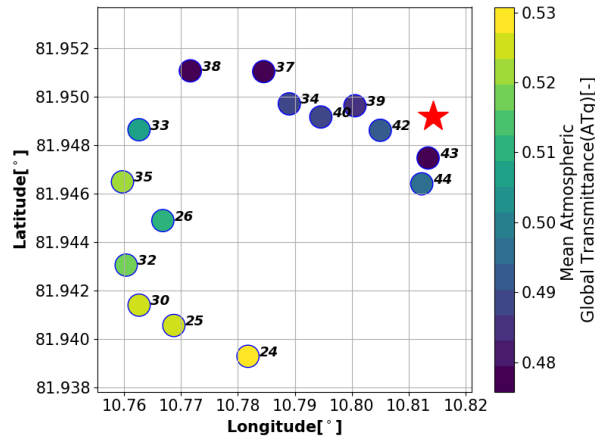


Figure 5.5: Station map showing the average atmospheric global transmittance for the overcast case (June 6, 2017, 00:00Z - 23:59Z). The red star marks the position of Polarstern. Source: Barrientos-Velasco et al. 2020.

The distribution of ATg during this period was monomodal [Fig. 5.4b], with a mean value of 0.50. The time series of the standard deviation presented values lower than 0.1 (mean SD = 0.023), as well as high values from 7:29Z to 8:27Z, when the dome of the instruments might have experienced momentary icing [Fig. 5.4d]. The stations showing this behaviour were 26, 30, 34, 35, 38, 40 and 43. The spatial distribution of the SD shows slightly higher values in the southwest of the ice floe region [Fig. 5.4e]. This effect can be most likely attributed to a more snowy surrounded area, whereas pyranometers 37, 34, 40, 39, 42, 43 and 44 were closer to the ice edge [Fig. 3.1b]. Snow-covered surfaces reflect more SOL radiation to the atmosphere than the open ocean. Once this reflected energy reaches a cloud, a part of it is reflected back to the surface, increasing the total amount of downward SOL radiation. Thus, for homogeneous single-layer clouds, the stations closer to the ice

edge show lower variation [i.e. around 0.48] because the darker surface absorbs more energy.

Complementary, Figure 5.5 shows the spatial distribution of the mean ATg. It clearly shows how stations near Polarstern [red star] and the edge of the ice floe observe lower transmittance values than the stations farther away from the ice edge, with absolute differences ranging up to 0.06. A similar plot was made for June 5, where the sky conditions were also overcast. A similar but less pronounced pattern was observed, with a smaller difference of up to 0.03 [not shown].

5.2.3 Thin Cloud Case

Thin clouds were not frequent during the ice floe camp period. The only cases where these types of clouds were observed were on 9 and 10 June. The thin-cloud case selected for the case study was observed between 16:36Z and 18:08Z on 9 June. The overall cloud conditions during this period were complex because the clouds varied in both height and depth. From 16:30Z to 17:00Z, a single cloud layer with a base height of 1.1 km and top height of 1.5 km was observed. During this period, drizzle was observed at the cloud base. Following this period, a very shallow cloud was observed with a cloud top of about 0.45 km from 17:00 to 18:05Z.

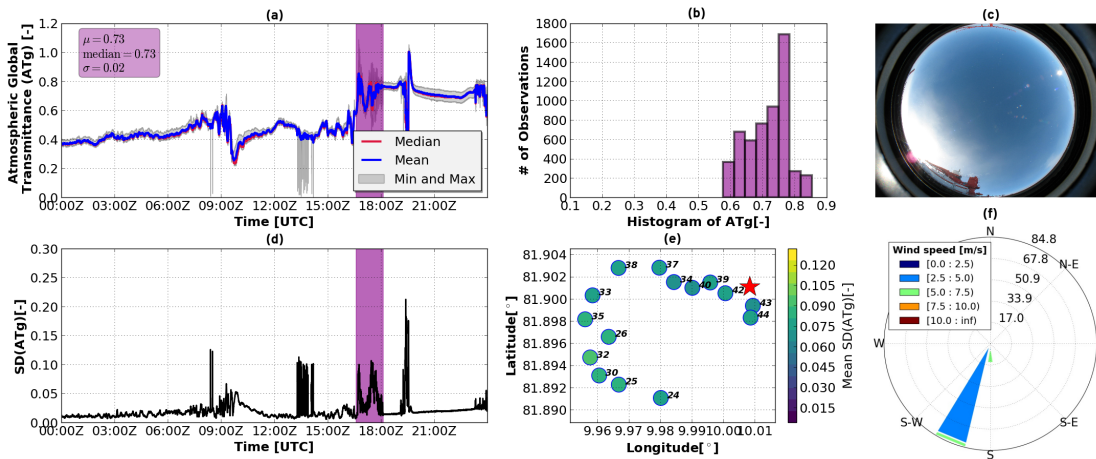


Figure 5.6: Overview of thin cloud case: the same as Fig. 5.3 but for 9 June 2017, 16:36-18:08Z. (c) Photograph taken at 17:29:28Z. Source: Barrientos-Velasco et al. 2020.

The mean ambient temperature during this period was 273.9 K with an SD of 0.35 K. During this condition; the cloud-base height was at 450 m, the temperature increased steadily from 273.15 to 274.11 K. The winds came mainly from the south, following an anticyclonic circulation with mean wind speeds of 5.2 m/s [Knudsen et al. 2018, Fig. 3.4, Fig. 5.6f]. The variance of height and composition had an impact on the ATg and temperature measured by the pyranometer network, as can be seen in the shaded purple background in Figure 5.6a. The highest values of inter-station SD occurred when the optical thickness of the cloud decreased at 17:30Z. The mean ATg during this period was 0.72, with a left-skewed distribution [see Fig. 5.6b]. The spatial distribution of the SD shows a similar trend as in the overcast case. This suggests that during these conditions, the highest variability occurred

in the region away from the ice floe edge and melt pond [Fig.3.1b]. The spatial distribution of mean transmittance shows a less evident pattern, suggesting that part of this variability is caused by variable cloud structures more than due to the particular location of the stations. The highest difference in the mean transmittance between all operational stations is 0.08.

5.2.4 Multilayer Case

Multilayer cases were more frequent during the warm period of the ice floe camp. The case selected is 13 June from 00:00Z to 19:15Z. This day had a positive AO index, implying that the episode was dominated by an anticyclonic circulation when the air was advected over the open ocean, favouring high temperature and humidity (Knudsen et al. 2018, Fig. 3.5a). Wind speeds were below 5 ms^{-1} coming from the south-west and north-east (see Fig.3.4a and Fig. 5.7f).

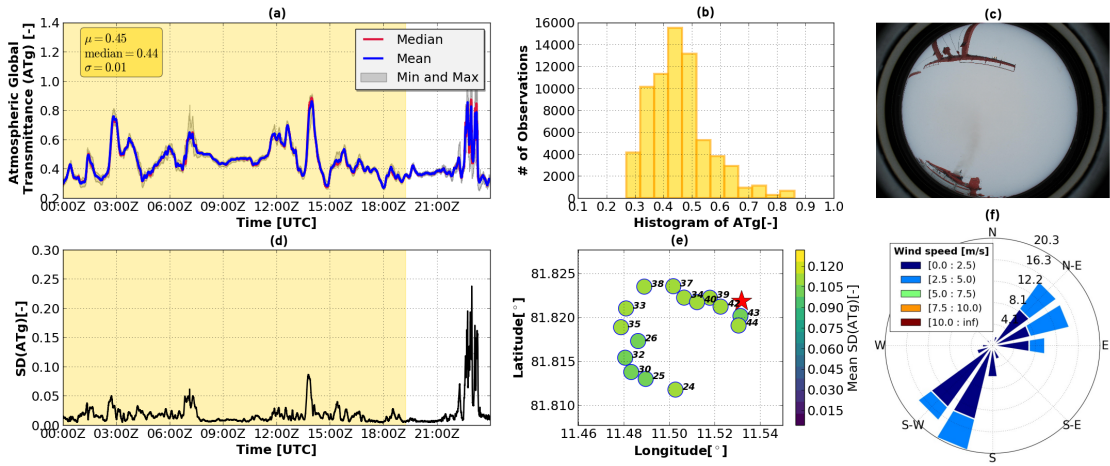


Figure 5.7: Overview of multilayer case: Same as Fig. 5.3, but for June 13, 2017, 00:00Z - 19:15Z. All-sky camera photograph taken at 10:09:35Z. Source: Barrientos-Velasco et al. 2020.

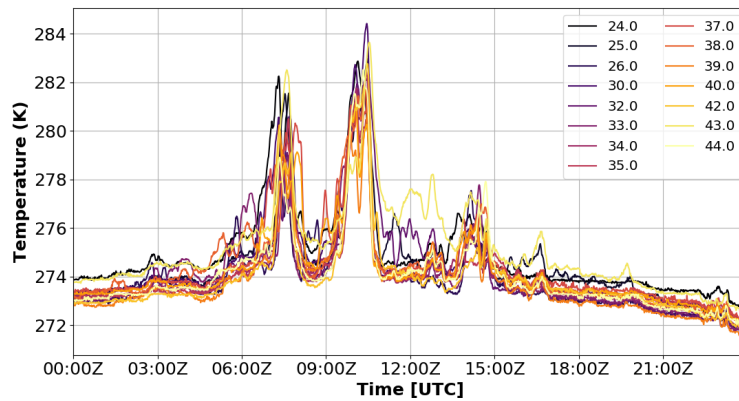


Figure 5.8: Time series of 1-minute averaged temperature for all stations on June 13, 2017. Source: Barrientos-Velasco et al. 2020.

Considering the near-surface temperature recorded with the pyranometer network, 13 June 2017 was the warmest day of the ice floe camp (see Fig. 3.3c). At around 7:30Z and 10:15Z, the highest temperatures of 279.03 K and 281.1 K were recorded

(see Fig. 5.8). The Polarstern temperature sensor did not record this increase in temperature. The observed fluctuations suggest that the near-surface air temperature over the ice floe experienced significant variability, likely due to turbulent mixing of warmer elevated air masses. A spatial comparison among the sensors of SD and mean near-surface temperature did not indicate a particular pattern. Still, it showed relatively high differences of the mean temperature of up to 1.4 K.

From 00:00Z to 02:24Z, three layers of clouds were identified with tops at 0.9, 4.8 and 7.8 km. The remaining time of the period was characterized mainly by complex structures of two cloud layers showing low values and a right-skewed distribution with an ATg of 0.45. The variation observed is mainly due to the different vertical structure of the multiple cloud layers (See. Fig. 5.7b). The time series of ATg and inter-station SD indicated no significant variation among the stations (Fig. 5.7a and d). Furthermore, the values of temporal SD found for the individual stations do not show a prominent spatial variation as, for example, observed for the overcast and thin cloud cases (Fig. 5.7e). Considering that the difference between the lowest and the highest value of SD is low (0.007).

5.2.5 Broken Cloud Case

The case study chosen for broken cloud conditions is 8 June 2017 between 8:30Z and 18:59Z. This period was characterized by fluctuating occurrences of stratus fractus (Fig. 5.10b at 11:02Z) and cumulus fractus clouds (Fig. 5.9c). During this period, south-easterly winds with a mean speed of 2.6 ms^{-1} dominated (Fig. c and Fig. 5.9f). Near-surface air temperatures observed with the pyranometer network increased by 2 K from 267 to 269 K. This behaviour was also recorded by the Polarstern sensor (Fig. b). Before the broken cloud conditions began, the temperatures recorded were the lowest registered during the entire campaign.

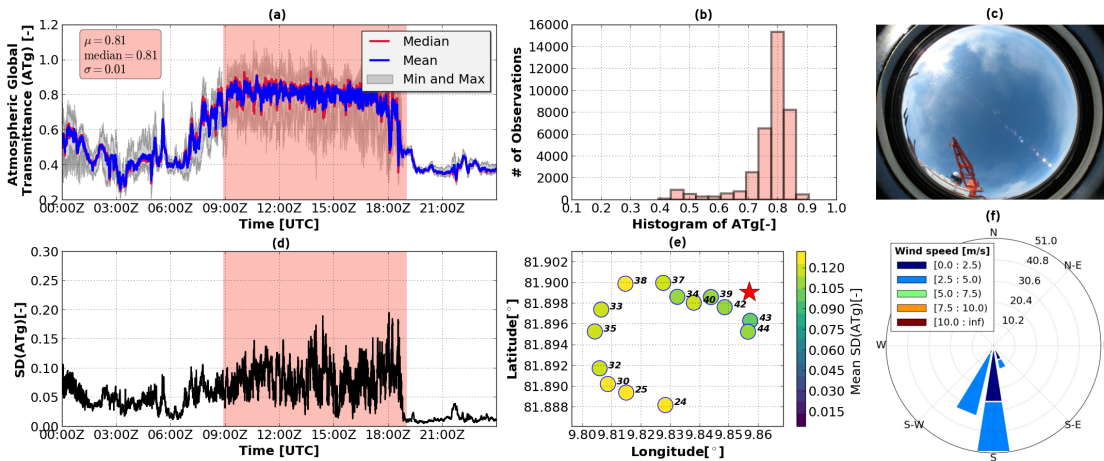


Figure 5.9: Overview of broken cloud case: Same as Fig. 5.3, but for June 8, 2017, 08:55Z - 19:00Z. All-sky camera photograph taken at 12:41:14Z. Source: Barrientos-Velasco et al. 2020.

The broken cloud period is indicated by the pink-shaded background in Figure 5.9a and c. The mean and median ATg is represented in Figure 5.9a in blue and red, respectively. For this case study, the increase of diffuse solar radiation is not only

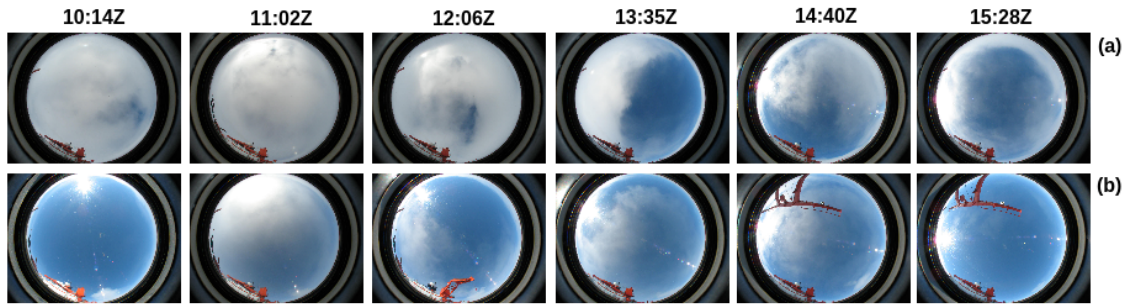


Figure 5.10: All-sky camera photographs for (a) June 7, and (b) June 8, taken at different times throughout the day. Source: Barrientos-Velasco et al. 2020.

due to the broken cloud conditions, but also to the multiple reflections between surface and heterogeneous cloud fields. Under these conditions, the plane-parallel cloud approximation cannot satisfactorily describe radiative transfer [Wendler et al. 2004; Schade et al. 2007]. In particular, it is well-known that horizontal photon transport can lead to periods with enhanced solar radiation, where values of the global transmittance can exceed the clear-sky values or even unity for some moments [Schade et al. 2007]. In addition, Byrne et al. 1996 demonstrated that in broken clouds fields, the average photon path-length is greater than that predicted by homogeneous radiative transfer calculations, also leading to enhanced absorption.

The distribution of ATg for this case study shows a left-skewed distribution and a mean value of 0.81, with a mean, standard deviation of 0.01 (see Fig. 5.9b). The time series shown in Figure 5.9d indicate evident spikes before and after the selected period. Furthermore, the spatial variability, shown in Figure 5.9e, indicates higher values of temporal standard deviation for the stations further away from the ice floe edge. However, the mean ATg does not show the same pattern as in Figure 5.5. The latter may indicate that the variability observed is dominated by the cloud organization and not by the contrast between the open ocean and highly reflective surfaces.

A summary of the results given is presented in Table 5.1. This table provides the mean values of temperature, ATg, and the SD of ATg for all the cases studies and the periods defined in the analysis.

Table 5.1: Mean values of: Ambient temperature T_a [K], atmospheric global transmittance ATg [-] for case studies (C) and all period (P). All based on the pyranometer network. Source: Barrientos-Velasco et al. 2020.

Case/Period	Overcast		Broken clouds		Thin clouds		Cloudless		Multilayer	
	C	P	C	P	C	P	C	P	C	P
Date	6 June	-	8 June	-	9 June	-	10 June	-	13 June	-
Time	00:00-23:59	-	8:55-19:00	-	16:36-18:08	-	11:10-15:43	-	00:00-19:15	-
T_a [K]	270.2	271.1	269.0	271.1	273.9	274.2	274.3	274.3	274.6	271.93
ATg [-]	0.50	0.46	0.77	0.61	0.72	0.76	0.78	0.76	0.46	0.43
$SD(ATg)$ [-]	0.071	0.084	0.118	0.146	0.080	0.043	0.015	0.028	0.107	0.114

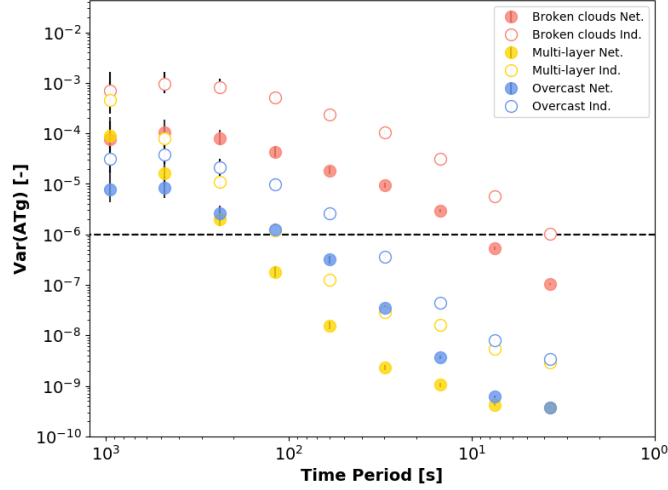


Figure 5.11: Wavelet-based power spectral density (WSD) of the station-averaged ATg (filled circles) and averaged WSD from the individual stations (empty circles), for 3-hour periods (15:00Z-18:00Z) with broken clouds (8 June 2017), multilayer (13 June 2017) and overcast (6 June 2017) conditions. The dashed horizontal line denotes the measurement uncertainty of the pyranometer. Source: Barrientos-Velasco et al. 2020.

5.3 Wavelet-based Multiresolution Analysis

This section aims to investigate the timescale dependence of variability in global irradiance, the time series of ATg obtained from the pyranometer network have been subjected to a wavelet-based multiresolution analysis using the Haar wavelet, following the methodology introduced in Deneke et al. 2009 and Madhavan et al. 2017. In summary, low-pass-filtered versions of the time series are calculated first, using a running mean of length $L = 2^J$ as a filter. In wavelet analysis, these running means are referred to as the wavelet smooths. The difference between two wavelet smooths of scale J and $J + 1$ correspond to the result of a bandpass filter and are called wavelet details. The wavelet details are then used to obtain time-localized estimates of the time-scale-dependent variance of the time series [Percival 1995], which is denoted as the wavelet power spectral density Wavelet power Spectral Density (WSD).

The results of this analysis are presented in Figure 5.11. This figure shows the WSD obtained from the observations for a period of three hours of broken clouds, multilayer clouds, and overcast conditions from 15:00Z to 18:00Z for the case days presented previously, in a double-logarithmic plot, and includes estimates of its uncertainty. Figure 5.11 compares the WSD calculated in two different ways. Filled circles correspond to the WSD, which has been calculated based on the average ATg of all functional stations, which approximates the WSD of ATg averaged across the spatial domain of the network, with a characteristic length scale of about 1 km. Empty circles correspond to the averaged WSD of individual stations, and thus a point-like measurement. Due to the 3-hour length of the time series, the WSD for periods at and above 1000 s cannot be reliably obtained, as it can be observed from the increasing uncertainty.

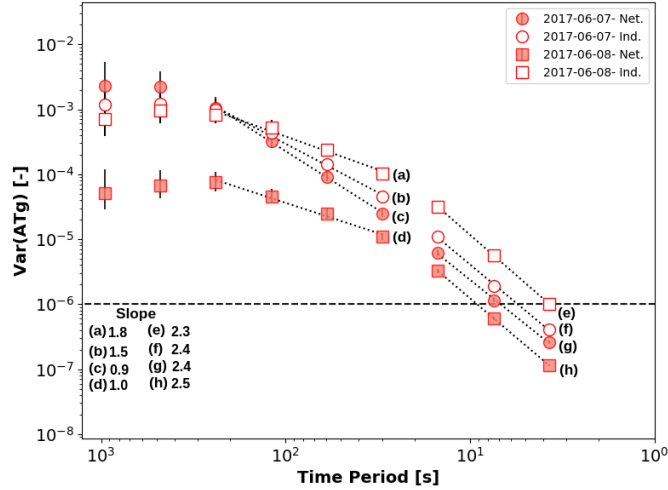


Figure 5.12: Wavelet-based power spectral density (WSD) of the station-averaged ATg (filled circles) and average WSD from the individual stations (empty circles) for 3-hour periods (15:00Z-18:00Z) of broken clouds on June 7 (circles) and June 8 (squares). Solid lines indicate the linear regression for the time period selected, and the dashed horizontal line corresponds to the measurement uncertainty of the pyranometer. Source: Barrientos-Velasco et al. 2020.

A characteristic decrease of variance with increasing temporal frequency (or equivalently, a decreasing time period) for the different sky conditions is observed. In particular, strongly differing slopes of the WSD are observed for the different conditions and frequency ranges, which suggests that the WSD is sensitive to structural differences of the clouds. As noted already by Madhavan et al. 2017, variability is significantly reduced when considering the spatially averaged atmospheric transmittance, irrespective of the considered cloud type. Broken clouds exhibit the largest variability, while the multilayer cloud situations show the smallest variability across all time scales.

Additionally, the WSD for two different periods of broken clouds is compared (see Fig. 5.12). As noted before, on 7 June, stratus fractus was observed, with stronger winds likely responsible for stronger fluctuations and longer periods of cloud-free sky, while the broken clouds observed on 8 June were characterized by a mixture of cumulus fractus, stratus fractus and stratocumulus. These conditions introduced fewer fluctuations in ATg. The lower variability can already be seen in Figure 5.1b. It is noteworthy that spatial averaging has a much stronger effect on the magnitude of variability for the June 8 case, which indicates that the relevant variations in cloud properties occurred on length scales smaller than the extent of the pyranometer network, while a much smaller reduction is observed for June 7. This indicates that cloud scales larger than the extent of the pyranometer network dominated the variability in transmittance during this period.

A stronger scale-dependency can be recognized in the WSD for the broken clouds observed on 8 June compared to 7 June. Estimating the slope of the WSD from the 4 points above and below a period of 100s, slopes of the WSD of 1.5 and 1.7 are obtained for June 7, while much lower values of 0.9 and 1.0 are found for June 8, for spatially averaged and point observations, respectively. Here, the values for

June 7 are close to the theoretical value of $5/3$ expected from turbulence theory for the dissipation of energy expected from homogeneous isotropic turbulence, while the lower values are in better agreement with the values reported by Madhavan et al. 2017 for broken cloud observations.

Comparing Figure 5.11 and 5.12, differences of the WSD for the average of all functional stations (filled circles) and the individual point-like measurements (empty circles) can be seen, indicating that the variability is reduced by about 0.1 as the spatial averaging cancels out part of the small-scale spatial variability. Hence, spatial averaging of stations allows resolving temporal changes better, while the magnitude of the difference provides information on the small-scale spatial structure of clouds. The results obtained here also suggest that future measurements of GHI in similar highly reflective surface conditions should be done with a temporal resolution of at least 10 seconds to capture the variability under broken cloud conditions fully. This conclusion corroborates the findings of Lohmann and Monahan 2018 that, based on the HOPE-Jülich campaign, suggest increasing the current recording of solar irradiance from one-minute resolution as recommended by the Baseline Surface Radiation Network (BSRN) [McArthur 2005] to a much higher temporal resolution.

5.4 Synopsis and Discussion

Over the past years, the Arctic has been experiencing an unprecedented increase in surface temperature and an associated decrease in sea ice extent, exceeding model-based climate projections by far. Scientific efforts to identify and understand the mechanisms that contribute most to this Arctic warming are still ongoing [Serreze and Francis 2006; Serreze and Barry 2011; Vihma 2014; Wendisch et al. 2017]. After the two extreme events with very low sea ice in 2007 and 2012, the debate to explain these events was divided into two sides. Several studies suggest that meridional heat transport is the main contributor to Arctic warming [Nussbaumer and Pinker 2012; Graversen et al. 2011]. On the other hand, several studies propose that anomalies in the solar radiation budget and clouds contribute to sea ice loss during summer [Kay et al. 2008; Pinker et al. 2014].

As one specific aspect of the solar radiation budget, the present study focuses on the analysis of the spatiotemporal variability of the solar atmospheric transmissivity at the surface as it is introduced by clouds. Despite the fact the silicon photodiode pyranometers used in this study operate with a limited spectral range of $0.3\text{-}1.1\ \mu\text{m}$ and thus do not cover the entire solar spectral range like a conventional broadband thermopile pyranometer, they do capture the main changes of the solar spectral transmission induced by clouds [Bartlett et al. 1998]. Therefore, it is worth stressing that the analysis of the spatiotemporal variability induced by clouds in the shortwave infrared region [e.g., in the atmospheric windows at 1.6 or $2.2\ \mu\text{m}$ commonly used for satellite remote sensing] is outside of the scope of this study, and might be a valuable investigation for future research.

To deepen the analysis, the characterization of synoptic conditions given by Knudsen et al. 2018 is used as a basis. Based on the near-surface air temperature, a cold period was identified from 4-9 June 2017 and a warm period from 10-16 June 2017. Although the classification labels the first period as cold, the AO index indicates that atmospheric conditions were warmer than average. In contrast, atmospheric

circulation over the Arctic for the warm period featured stronger westerlies at sub-polar latitudes and lower sea level pressure over the Arctic [Thompson and Wallace 1998; Rigor et al. 2002].

For the period of study, it has been demonstrated that the ATg differs significantly for different cloud types. During the cold period, overcast single-layer clouds were more frequent. The mean ATg during overcast conditions was relatively low (0.48). The warm period was mainly dominated by multilayer clouds, with a mean ATg of 0.41 and winds mainly coming from west and north. The distribution and temporal variability of ATg for overcast and multilayer clouds were similar. However, the distinction is important since overcast conditions represent more clearly the daily variability and the spatial distribution of the stations showing a specific pattern. Broken clouds were observed during both periods and for wind speeds higher than 4 m/s, and air masses coming from the north and east for the cold period and from the west during the warm period. The mean ATg for broken clouds observed was 0.61 and showed the highest temporal variability.

In addition, wavelet-based power spectra showed pronounced differences for different sky conditions, with the highest variances for low broken clouds. Different scaling properties were observed in two different periods of broken clouds, likely reflecting different typical scales of cloud structures. The variances observed during broken cloud conditions, however, seem to be smaller than the ones reported during a field campaign in Germany in 2013 by Madhavan et al. 2017. This difference is likely due to less convective cloud development taking place in the Arctic. Furthermore, we studied the differences between broken cloud conditions. The mixture of stratus fractus, cumulus fractus, and stratiformis clouds marked a higher variability computed with the WSD than just stratus fractus cases that were more recurrent during the ice floe camp. This difference is relevant to characterize the variability of solar radiation better and link it to cloud structure, for example, in radiative closure studies considering 3D radiative effects [Rozwadowska and Cahalan 2002].

For single layer clouds the location of stations showed a pattern making a division between the stations near the ship (ice floe-edge) and the ones located farther. This behaviour suggests that highly reflective surfaces enhance the spatial variability for the cases studied. It should be noted that this pattern is based on the limited data set of 2 weeks and a more solid conclusion should be made after analysing a larger period of time.

Although a comparison of ATg including its spatiotemporal variability was made for different sky conditions, its relevance for the solar radiation budget and the Arctic climate system cannot be assessed based on the present, rather short time series of observations. Specific and relevant analysis of the snow metamorphism is still needed in order to understand thermal diffusivity and consequently the effect on ice thickness evolution [Saloranta 2000]. Knowledge about the variability of the downward solar radiation is of special importance in the Arctic as the heterogeneous surface composed of snow, leads and melt ponds is warmed differently for spatially uniform and non-uniform solar irradiance. Transmission and absorption of solar radiation by the Arctic surface are equally important, not only to study sea ice sea alteration [Light et al. 2008; Nicolaus et al. 2012], but also to better understand the direct influence on bio-geochemical processes that depend on sub-ice light conditions [Slagstad et al. 2011].

The pyranometer network offers valuable information on the variability of the solar flux at the surface on small scales, making it possible to better characterize temporal and spatial fluctuations than by single station measurements. This data brings the possibility to investigate further the effects of the horizontal distribution of clouds, the solar zenith angle, cloud phase, surface reflectivity. Moreover, with information on wind direction and speed, it might be possible to separate the observed variability into components arising from advection, by cloud spatial structure, and by temporal changes of clouds. This data set can also be used as a reference for a comparison with radiative transfer simulations using a 3-D Monte Carlo radiative transfer model using large-eddy simulations as input. Such analysis can help to investigate further the link between cloud spatial structure and the resulting variability in the solar radiation field.

Chapter 6

Radiation Closure

In this chapter, the radiative closure (RC) analysis based on the simulations derived with T-CARS, CERES products and ship-borne observations of SOL and TIR fluxes is introduced. First, the analysis consists of comparing CERES products and T-CARS outputs under clear-sky conditions. This comparison determines how consistent both data sets are and quantifies the radiative difference by considering aerosols and pristine conditions. This chapter closes with a comparison of downward radiative fluxes from CERES, T-CARS and the ship-borne observations to evaluate if a radiative closure can be determined for clear-sky and cloudy conditions. This chapter is based on the results presented in Barrientos-Velasco et al. 2022.

Radiative closure is called satisfactory when the simulations agree with the observations within a predefined uncertainty range or threshold value. For clear-sky conditions, the benchmark is defined in subsection 4.2. For the downward SOL and TIR flux, the net uncertainty range is $\pm 24 \text{ W m}^{-2}$, and $\pm 16 \text{ W m}^{-2}$, respectively.

6.1 Radiative Flux Comparison Between CERES and T-CARS

In this section, T-CARS outputs and CERES products are compared under clear-sky conditions. Additionally, the effect of aerosols on the downward fluxes is investigated by quantifying the flux differences under clear-sky and pristine conditions for the PS106 cruise.

The aerosol contribution to the SOL-D and TIR-D flux during PS106 is illustrated in Figure 6.1. Figure 6.1a and 6.1b shows the flux difference of CERES products with and without aerosols for the TIR-D and SOL-D flux, respectively. Based on CERES only, the presence of aerosols affects more intensively the SOL-D radiative flux than the TIR-D because aerosol is transparent to thermal radiation except for coarse mode aerosols [e.g., dust or smoke]. Under clear-sky conditions, the presence of aerosols can lead to a mean underestimation of the SOL-D flux of -10.8 W m^{-2} [see Fig. 6.1f]. Panels 6.1a, b, c, and d show in detail the days on which the difference is larger due to an important load of aerosols in specific days affecting the computation of the mean values.

The treatment of aerosol in the CERES products is based on the aerosol optical depth (AOD) obtained from the Model of Atmospheric Transport and Chemistry

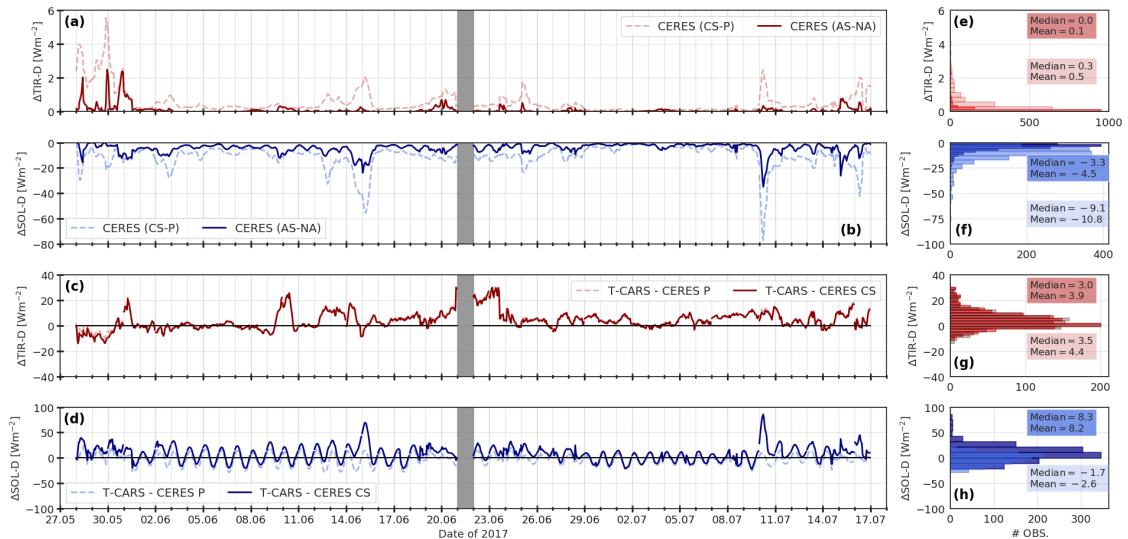


Figure 6.1: Time series of the flux difference of downward surface radiative fluxes between CERES and T-CARS for pristine (P), clear-sky conditions (CS), all-sky (AS), and cloudy without aerosols (NA). Panel (a) shows the difference of the TIR-D CERES (CS-P) and CERES (AS-NA). Panel (b) shows the same as (a), but the downward SOL (SOL-D) flux. Panel (c) shows the TIR-D differences between T-CARS and CERES P, and T-CARS minus CERES CS. Panel (d) shows the same as (c), but for the SOL-D. The histograms of each left-hand side panel are shown on the right. The TIR-D and SOL-D fluxes are shown in red and blue, respectively. Source: Barrientos-Velasco et al. 2022.

(MATCH; Collins et al. 2001). Based on MATCH outputs at 0.55 and 0.84 μm , it was observed significant peaks of AOD for 30 May, 2 June, 9 June, 12 to 13 June, 14 to 15 June, 25 June, 10 July, and 16 July 2017. The majority of these peaks presented an AOD below 0.2, except for 15 June and 10 July. During these days, the values reached an AOD at 0.55 μm of 0.61 and 0.78, respectively [see Fig. C.1].

Considering CERES products, the direct and indirect aerosol radiative effects are calculated. The direct aerosol effect is calculated by subtracting the downward and upward radiative fluxes for a clear-sky minus the simulated pristine atmosphere. Similarly, the indirect aerosol effect is derived by subtracting the downward and upward radiative fluxes of the simulated all-sky atmosphere minus a cloudy atmosphere without aerosols. The results of this analysis indicates that aerosols effects are negligible for most purposes, the values are relatively large in comparison to the direct aerosol effect of -0.4 to -2.6 W m^{-2} reported by Rastak et al. 2014.

6.2 Radiative Closure for Clear-sky Atmosphere

This section compares T-CARS outputs, CERES products of the SOL-D and TIR-D fluxes to ship-borne observations for clear-sky conditions based on the Cloudnet flag classification and the sky camera images.

The results of the flux difference of simulations minus observations are presented in Figure 6.2. Figure 6.2a illustrates in red the flux difference based on Cloudnet flag classification only. This comparison indicates a skewed left distribution with a

mean underestimation of T-CARS simulations of -24.9 W m^{-2} for the TIR-D. After applying the improved quality screening described above, a mean flux difference of -14.2 W m^{-2} is found, together with a correlation coefficient of 0.92, and a more symmetric distribution than without this quality screening. The mean flux difference below the uncertainty limit of $\pm 16 \text{ W m}^{-2}$, and the strong correlation coefficient confirms that RC can be achieved for the T-CARS simulations under clear-sky conditions.

In the case of CERES, the bias for the TIR-D flux is -4.6 W m^{-2} , with a standard deviation of 20.9 W m^{-2} , and a root-mean-square error (RMSE) of 18.5 W m^{-2} . The bias found is below the instrumental uncertainty suggesting that RC can be determined for CERES. However, the rather low correlation coefficient of 0.476 indicates that the values do not reproduce variability as well as the T-CARS simulations and might be affected by the presence of clouds within the CERES footprint [see Fig. 6.2c]. To test this hypothesis, clear-sky and pristine CERES products were also considered. For both data sets, the correlation coefficient reached values above 0.765, which confirms that the all-sky CERES correlation coefficient is reduced by the presence of clouds. With this change, the bias however increased to -19.8 W m^{-2} and -18.2 W m^{-2} for the clear-sky and pristine data sets, respectively [see Fig. 6.2d].

The negative bias found for both T-CARS and CERES fluxes might also be caused by a positive bias of the ship-borne pyrgeometer observations, e.g., due to the influence of the exhaust plume of Polarstern or variation of temperature due to the operational instruments located near the pyrgeometer. As there was only one pyrgeometer measurement aboard Polarstern, it is impossible to investigate this hypothesis further. However, for future campaigns, it is recommended to operate two pyrgeometers installed in different locations of the research vessel to exclude such influences.

The comparison for the SOL-D flux uses a stricter screening of data, which also excludes all periods when the superstructure of Polarstern obstructed the pyranometer's field of view. For T-CARS, a positive bias of 44.2 W m^{-2} and a correlation coefficient of 0.85 was found initially without this screening. With screening, a bias of 9.5 W m^{-2} and a correlation coefficient of 0.95 were obtained. In the case of CERES, the biases for all-sky, clear-sky, and pristine conditions were -27.1 W m^{-2} , 3.6 W m^{-2} , and 12.0 W m^{-2} , respectively. These values confirm that the larger negative bias for all-sky conditions is due to the presence of clouds within the CERES footprint. The biases of both T-CARS and CERES are both within the uncertainty limit of $\pm 20 \text{ W m}^{-2}$ indicating that radiative closure is achieved for both data sets.

Previous studies reported a similar magnitude of differences between simulated and observed downward fluxes for clear-sky conditions. For instance, the analysis by Ebell et al. 2020 focused at Ny-Ålesund reported a mean (median) flux difference of -5.0 (-5.5) W m^{-2} and 12.6 (-2.6) W m^{-2} for the TIR-D and SOL-D, accordingly [see Fig. 3 in Ebell et al. 2020]. The studies of Shupe et al. 2015 and Miller et al. 2015 found a median difference of simulations and observations for the TIR-D (SOL-D) flux of -6.9 (5.4) W m^{-2} and -5.5 (15.6) W m^{-2} for the Barrow and Summit-Greenland sites, respectively.

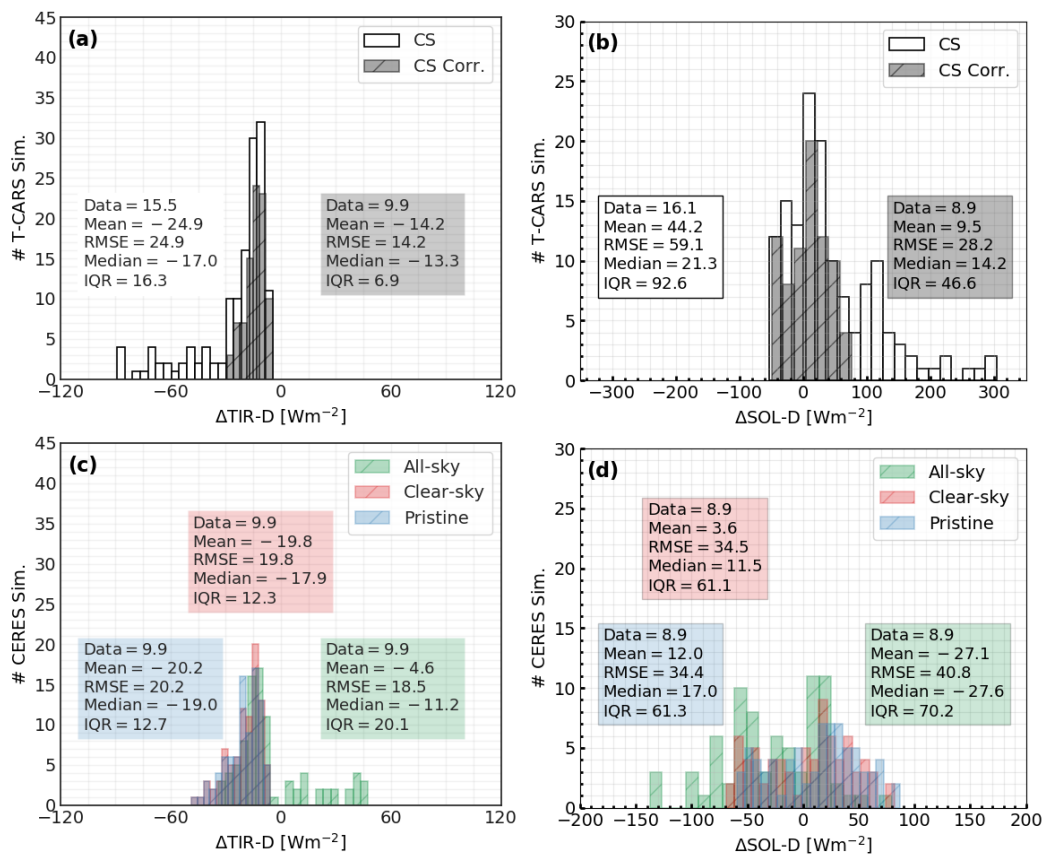


Figure 6.2: Histograms of flux difference (FD) of simulations minus observations for downward TIR (TIR-D) flux (panels a and c) and the downward SOL (SOL-D) flux (panels b and d) for clear-sky (CS) conditions. Panels a and b show T-CARS comparison, where the filled histograms show the filtered data by excluding the moments where the observations were compromised. Panels c and d show the comparison of CERES for All-sky (green), clear-sky (red) and pristine simulations (blue) for the same filtered time steps as in T-CARS. Source: Barrientos-Velasco et al. 2022.

6.3 Radiative Closure for Cloudy Atmosphere

Several detection problems from the ship-borne remote sensing instrumentation limited the quality of the microphysical cloud retrievals. In general, under LLS and PPT conditions, the observations of cloud macro and microphysical parameters have a degraded quality. Thus, for only about 40.1 % of the time, observations were of sufficient quality, for radiative transfer simulations [see Fig. 3.7]. These conditions challenge the determination of RC for cloudy conditions. The analysis focused only on optimum conditions lead to better results, and in some periods, T-CARS outputs match the observations. However, such moments were intermittent, making it difficult to provide a RC analysis for the entire PS106 cruise.

This section focuses on the CERES all-sky products and the TIR and SOL downward fluxes observed aboard Polarstern. Figure 6.3a illustrates the time series of the TIR-D observations and CERES all-sky product following the same trend and, in most of the cases, similar values are observed. Some periods can be identified with a reduced agreement. These cases occur particularly during precipitation periods,

which might affect the pyrgeometer measurements (e.g., 12 June, 20 June, 28 to 29 June, and 11 to 14 July). More significant discrepancies are also observed in the presence of multilayer clouds (e.g., 20 June, 5 to 9 July), which feature a more challenging structure and pose challenges for passive remote sensing [Minnis et al. 2019; Yost et al. 2020].

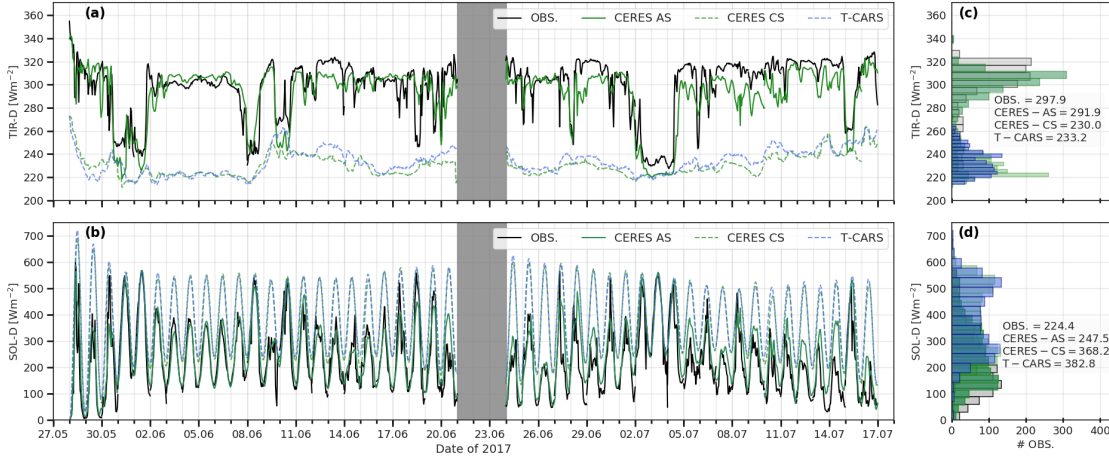


Figure 6.3: Time series of TIR-D (a) and SOL-D (b) during PS106. In panel (a) and (b), observations are shown in solid black lines, CERES all-sky (AS) products in the solid green line, and clear-sky (CS) in the dashed green line, clear-sky T-CARS simulation is shown in the dashed blue line. The distribution of the time series shown in panel (a) and (b) are shown in panel (c) and (d), respectively. Source: Barrientos-Velasco et al. 2022.

The discrepancy shown for 13 June 2017 might also be attributed to precipitation as it was also the case on 12 June. However, this cannot be confirmed by the observations due to missing data. This day was also brought to attention by Barrientos-Velasco et al. 2020 since the near-surface temperature measured on the ice-floe by several instruments reached a mean temperature of 281.1 K, about 4 K warmer than the temperature measured aboard Polarstern [Barrientos-Velasco et al. 2020], CERES and ERA5 skin temperature. This day was also characterized by a more humid than usual upper atmosphere, a cyclonic weather system, northerly winds [Barrientos-Velasco et al. 2020], strong temperature inversions, and an intense persistent fog leading to a very low horizontal visibility [see Fig. 18b in Griesche et al. 2020]. This humidity intrusion can lead to an additional energy flux to the surface, enhancing the fog to persist [Tjernström et al. 2019]. The fluctuations of atmospheric temperature and relative humidity described might be different from the atmospheric profiles used by CERES, causing the difference of up to 20 W m^{-2} (Fig. 6.3a).

The mean flux difference between observations and all-sky CERES TIR-D products is 6 W m^{-2} with a standard deviation of 14.6 W m^{-2} (Fig. 6.3c). Moreover, a linear regression between CERES and observations is illustrated in Figure 6.4a showing a correlation coefficient (R^2) of 0.69. The mean flux difference is within the instrumental uncertainty of $\pm 13 \text{ W m}^{-2}$ of the pyrgeometer. Thus, it is possible to determine a RC for CERES TIR-D radiative flux in general terms.

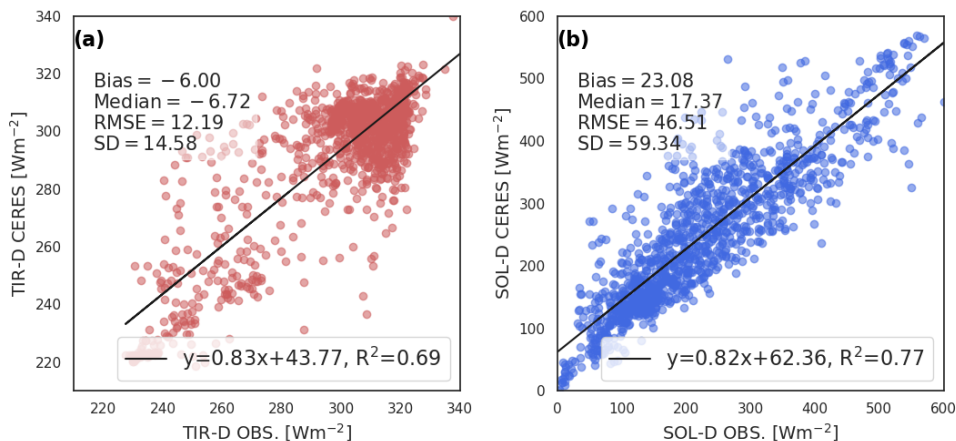


Figure 6.4: Scatter plots comparing the CERES fluxes and ship-based radiative flux observations (Obs.) for the downward TIR (a) and SOL (b) fluxes. The black line represents the best linear fit. The resulting fit equation and the square of the Pearson correlation coefficient (R^2) are shown in each panel. Source: Barrientos-Velasco et al. 2022.

There is relatively good agreement of SOL-D flux between the CERES simulations and observations for the entire PS106 [see Fig. 6.3b]. Most of the discrepancies are caused by precipitation [e.g., 13 to 14 July], broken cloud conditions, and instances when Polarstern’s superstructures compromised the pyranometer observations [see Fig. D.1]. Figure 6.3d shows the distribution of the time series of the SOL-D flux. This panel shows a similar distribution between the observations and the SOL-D flux simulated by CERES. This comparison indicates that CERES SOL-D flux is positively biased by 23.1 W m^{-2} , with a standard deviation of 59.3 W m^{-2} . This value is considered acceptable since the instrumental uncertainty is $\pm 20 \text{ W m}^{-2}$, and the moments with broken cloud conditions or obstruction of the observations are not excluded from the comparison. Nevertheless, it is important to stress that obtaining good quality ship-borne observations of downward fluxes is challenging due to recurrent obstructions of the view of the radiometer’s sensor.

6.4 Synopsis and Discussion

This chapter has presented the radiative flux comparison between CERES flux products, T-CARS outputs, and ship-borne observations for the PS106 expedition. First, a comparison of the SOL-D and TIR-D between CERES products and T-CARS outputs for clear-sky conditions were presented.

The effect of aerosols on downward fluxes has been evaluated with CERES products. This analysis has indicated that aerosols can enhance the TIR-D by 0.5 W m^{-2} and reduce the SOL-D by -10.8 W m^{-2} under clear-sky conditions. Note that under cloudy conditions, this effect is reduced to 0.1 W m^{-2} and -4.5 W m^{-2} , respectively [see Fig. 6.1a and b].

The RC for T-CARS outputs and CERES simulations have been achieved for clear-sky conditions. Under cloudy conditions, the RC was hampered by several challenges due to environmental conditions that compromised the ship-borne remote sensing

observations [e.g., precipitation, LLS conditions, periods with strong radar reflectivity]. Furthermore, promising results were identified for optimum flagged conditions [see Fig. 3.7]. However, their recurrence was irregular; therefore, it was opted to focus on specific case studies as the ones highlighted in chapter 7.

The RC for CERES products has been determined for the TIR-D flux during all-sky conditions for the entire PS106 cruise. The mean flux difference of TIR-D is within the ship-borne instrumental uncertainty of the pyrgeometer ($\pm 13 \text{ W m}^{-2}$). Also, the mean flux difference of SOL-D surpasses by 3.1 W m^{-2} the instrumental uncertainty of the pyranometer ($\pm 20 \text{ W m}^{-2}$). However, this difference is considered acceptable since the moments of broken cloud conditions or Polarstern's infrastructure compromising the observations were not excluded from the analysis. Nevertheless, it is suggested to implement an algorithm that can identify and flag the moments where the ship's structures hampered the observations for future studies.

The study of Riihelä et al. 2017 presents a comparison of radiative fluxes between the CERES edition 3 products and in-situ observations from the drifting Tara ice camp from April to September 2007. Their results are presented as daily means and indicate a RMSE of 24.5 W m^{-2} and 17.1 W m^{-2} for the SOL-D and TIR-D, respectively. In our study, results are relatively similar for the TIR-D, with a RMSE of 12.3 W m^{-2} . In the case of the SOL-D, the RMSE found for PS106 has a value of 46.5 W m^{-2} . It should be noted that our results are based on hourly means instead of the daily mean reported by Riihelä et al. 2017. Furthermore, the observations made during the Tara ice floe camp were unaffected by the interference of the ship superstructure with the observations.

The study by Dong et al. 2016 focuses on the radiative closure of SOL-D flux for single-layer overcast liquid-phase Arctic stratus clouds over the snow-free and snow-covered surface. Their analysis considers CERES edition 2 and 4 products, which are subsequently compared to radiation observations and cloud retrievals at the Atmospheric Radiation Measurement North Slope of Alaska (ARM NSA) site at Utqiagvik, Alaska. CERES edition 4 shows a mean bias against observations below 10 W m^{-2} for the SOL-D and for snow-free as well as snow conditions. Evidently, the flux difference of 23.1 W m^{-2} is larger than the value reported by Dong et al. 2016; however, the present study includes more complex cloud situations, which enlarges the differences of radiative fluxes.

Chapter 7

Case Studies

In this chapter, selected case studies that represent the main atmospheric conditions during PS106 are presented. Each case study compares ship-borne broadband radiative flux observations, T-CARS outputs, and CERES simulations. For cloudy conditions, the case studies also present the comparison between CERES and Cloudnet products of cloud macro and microphysical properties and the derivation of the CRE. The following results are presented at a 10-minute average resolution, similarly to Ebell et al. 2020 and Shupe et al. 2015.

7.1 Clear-sky Case

The 3 July is the day with the longest cloud-free period during PS106 [see Fig. 3.6, Fig. 3.7, and Fig. D.2]. An overview of cloud conditions and radiative fluxes for this day is given in Fig. 7.1 and its location is shown in Fig. 1.4. Panel (a) in Fig. 7.1 shows ice clouds, observed by Cloudnet, from 00:00Z to around 02:30Z. Later periods when CERES reported clouds while Cloudnet did not were further analysed using the all-sky camera images. They showed a thin cloud at the horizon between 21:30Z to 23:59Z, which is outside the field of view for the zenith-pointing active remote sensing instruments. In this case study, particular focus is given to the period of clear-sky conditions for both CERES and Cloudnet.

Good agreement is found for the ship-borne flux observations, the T-CARS simulations, and the CERES products for the SOL-D at the SFC. The mean difference of the simulations minus the observations lies below 8 W m^{-2} , a value that is well within the uncertainty limit of $\pm 24 \text{ W m}^{-2}$ used for the RC assessment. For the TIR-D fluxes, there is a larger difference between the ship-borne observations on the one hand and the T-CARS simulations and CERES products on the other hand. However, the mean difference remains below 14 W m^{-2} , again smaller than the uncertainty limit of $\pm 16 \text{ W m}^{-2}$ chosen as satisfactory for the RC assessment. Therefore, our results confirm that RC is reached for both the downward SOL and TIR fluxes for this clear-sky case.

To analyse the consistency of T-CARS simulations and CERES products at the TOA, the SOL-U and TIR-U fluxes are compared [see Fig. 7.1b, Fig. 7.1c]. Figure 7.1b and 7.1f shows a similar temporal behaviour of the SOL-U fluxes for the considered period. The mean difference between T-CARS and CERES is 10.0 W m^{-2} , with the largest instantaneous differences occurring after 18:40Z. Since the T-CARS

simulations use the same surface albedo as CERES as input, the reason for this difference is most likely due to the spatio-temporal interpolation of CERES [Young et al. 1998]. For the TIR-U fluxes, the mean difference is 3.7 W m^{-2} [see Fig. 7.1c and 7.1g], possibly, due to differences in the CERES skin temperature and the ship-borne measurement of near-surface temperature used by T-CARS [see Fig. 3.3c and Fig. 3.3g]. The mean differences of the radiative fluxes are sufficiently small to confirm the consistency of CERES and T-CARS fluxes, in agreement with similar studies which compared CERES with other radiative transfer simulations [e.g., Dong et al. 2016; Dolinar et al. 2016].

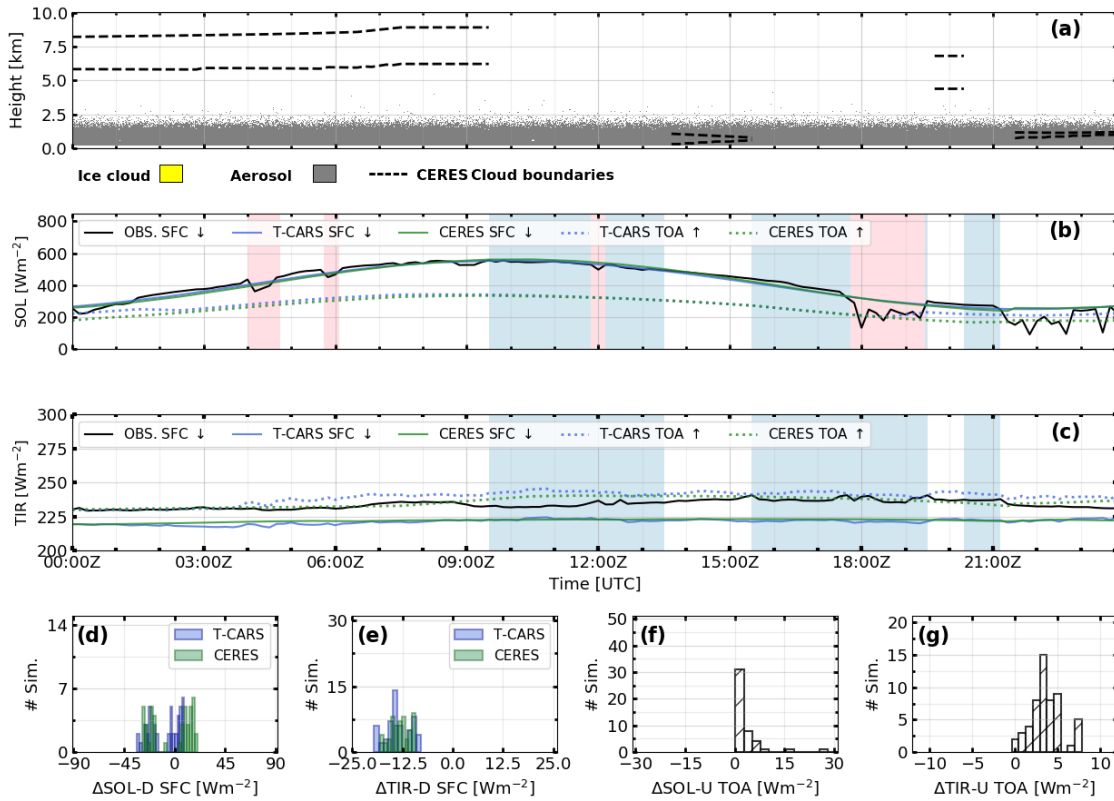


Figure 7.1: Overview of radiative fluxes for the 3 July 2017 case. Panel (a) shows the time series of the Cloudnet target classification and the CERES-based cloud boundaries (dashed black lines). Panel (b) and (c) show the time series of the SOL fluxes and TIR fluxes, respectively at 10-minutes resolution. In both panels (b and c), the down-looking arrow indicates (\downarrow) the downward fluxes at the surface (SFC), and the up-looking arrow (\uparrow) shows the upward fluxes at the top of the atmosphere (TOA). Panels (d) and (e) show histograms of the difference of T-CARS/CERES SOL-D and TIR-D fluxes and observations at the surface, respectively. Panels (f) and (g) show histograms of the difference of T-CATS and CERES SOL-U and TIR-U fluxes at the TOA, respectively. The number of 10-minute data points contributing to the histogram in panel (d) is 44, while it is 55 for panels (e)-(g). Pale-rose shading indicates periods when the ship’s superstructures obstructed the ship-borne flux observations. Light-blue background indicates the period of clear-sky considered for the analysis. Source: Barrientos-Velasco et al. 2022.

7.2 Single and Multilayer Ice Cloud Case

Single layer clouds are the most prominent atmospheric conditions during PS106 [see Fig. 3.7]. The day chosen to investigate these types of clouds under relatively stable surface conditions is 2 July 2017.

Based on the target classification of Cloudnet, this day was characterized by well-defined single and multilayer ice clouds [see Fig. 7.2a and Fig. D.3]. Middle and high-level ice clouds were observed for most of the day, with an average cloud base at about 2.6 km. An exception is observed for the period from 5:57Z to 8:35Z when a relatively thin cloud layer consisting of ice and super-cooled droplets was identified [see Fig. 7.2a]. For most of the day, the cloud top height from CERES is significantly lower than that from Cloudnet, probably because the cloud is semi-transparent in the thermal infrared, and warmer radiation from the lower altitude bias the cloud top height retrieval used in CERES. The cloud base height is relatively close to the base obtained from the Cloudnet target classification. It is well-known that the retrieval of cloud top height from passive satellite instruments is limited by large uncertainties for thin ice clouds and polar regions [e.g., Yost et al. 2020]; therefore, these discrepancies are not surprising.

The comparison of CERES and T-CARS fluxes against observations for the SOL-D and TIR-D show a good agreement [see Fig. 7.2b, 7.2c, 7.2d and 7.2e]. The values are below the clear-sky uncertainty limits established in chapter 4.2. This comparison suggests that RC is achieved for T-CARS and CERES. At the TOA, there is a more significant difference of -15.4 W m^{-2} and -15.0 W m^{-2} for the TIR-U and SOL-U, respectively [see Fig. 7.2f and 7.2g]. This difference is likely linked to the differences in cloud properties retrieved by Cloudnet and CERES that are displayed in Fig. 7.3. Discrepancies in other parameters such as the skin temperature, atmospheric profiles, cloud top height, and cloud geometrical thickness might also have had an effect on the flux differences at the TOA.

Panels a and b of Fig. 7.3 show the time series of the Q and r_E obtained from Cloudnet and CERES, respectively. Despite the difference in retrieval methods, there is, in general, a good agreement of the values of Q_I and $r_{E,I}$ from CERES and Cloudnet [see Fig. 7.3a and 7.3b]. Based on CERES, the entire day was characterized by the presence of a mixed-phase cloud. The values shown for Q_L are relatively large, especially during the period from 17:00Z to 19:00Z. It is possible that within the CERES footprint, a cloud with such a large Q_L might have been present. Nevertheless, it is worth noting that the fluxes shown in Fig. 7.2b and (c) are calculated considering the cloud fraction, which remained below 15 % from 12:30Z until the end of the day (not shown). The latter suggests that care must be taken when comparing cloud properties obtained from the ship-borne active instruments and from CERES with its coarse spatial footprint.

In Figure 7.3c is shown the 10-minute time series of the CRE at the SFC and TOA based on CERES products and T-CARS simulations. In general for this case study, the net CRE at the SFC is consistent between T-CARS and CERES, despite the noted discrepancies in cloud properties. The net CRE at the SFC has values of 1.3 W m^{-2} and 2.7 W m^{-2} for CERES and T-CARS, respectively. At the TOA, the difference is more significant due to the mentioned differences in the TIR-U flux. The net CRE at the TOA derived by T-CARS is 8.9 W m^{-2} , whereas CERES

suggests a cooling by -11.1 W m^{-2} . It is suspected that the flux differences are caused by difference in skin-temperature (see Fig. 3.3c) and near surface values between CERES and T-CARS, an overestimation of Q and misidentification of cloud top boundaries by CERES affecting the TIR CRE at the TOA. This case study is also complex due to the variable surface conditions that in combination to the different cloud properties increase the flux differences [see Fig. 3.3]. Such inconsistencies need to be clarified and further investigated in future studies.

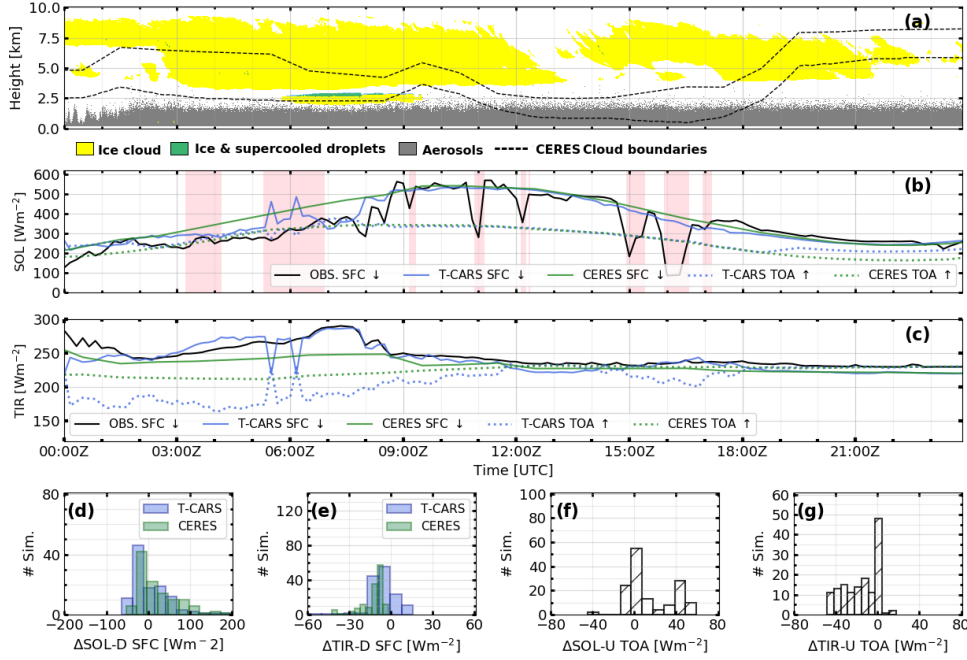


Figure 7.2: Overview of radiative fluxes for the 2 July 2017 case. Panel (a) shows the time series of the Cloudnet target classification and the CERES-based cloud boundaries (dashed black lines). Panel (b) and (c) show the time series of the SOL fluxes and TIR fluxes, respectively, at 10-minutes resolution. In both panels (b and c), the down-looking arrow indicates (\downarrow) the downward fluxes at the surface (SFC), and the up-looking arrow (\uparrow) shows the upward fluxes at the top of the atmosphere (TOA). Panels (d) and (e) show histograms of the difference of T-CARS/CERES SOL-D and TIR-D fluxes and observations at the surface, respectively. Panels (f) and (g) show histograms of the difference of T-CATS and CERES SOL-U and TIR-U fluxes at the TOA, respectively. The number of 10-minute data points contributing to the histogram in panel (d) is 44, while it is 55 for panels (e)-(g). Pale-rose shading indicates periods when the ship's superstructures obstructed the ship-borne flux observations. Light-blue background indicates the period of clear-sky considered for the analysis. Source: Barrientos-Velasco et al. 2022.

7.3 Mixed Phase Cloud Case

The selected case to study mixed-phase clouds is 26 June 2017. This day was characterized by well-defined cloud layers consisting of ice and liquid droplets, corresponding to a mixed-phase cloud of type 1. A further reason for the selection is the long period of optimum observation conditions reported by Cloudnet [Fig. 3.7c].

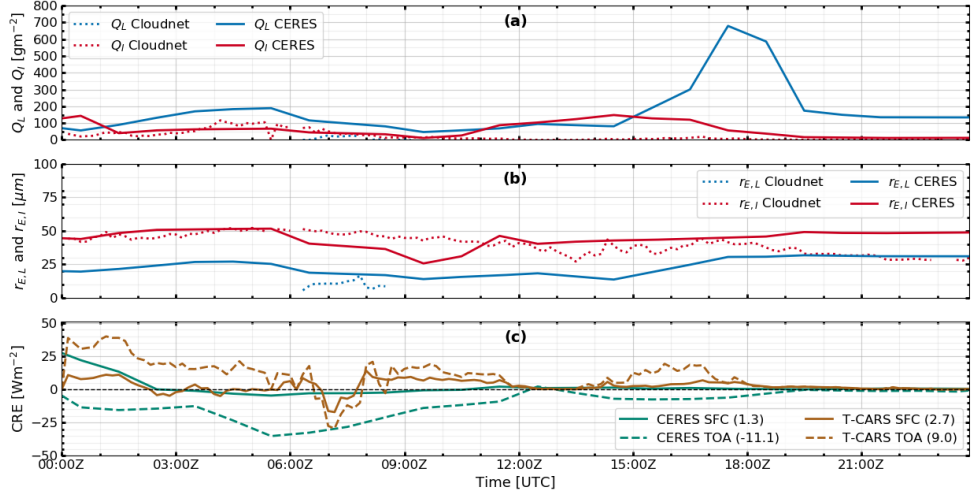


Figure 7.3: Time series of 10-minute resolution cloud microphysics properties and CRE between CERES and Cloudnet for 2 July 2017 case. Panel (a) shows the comparison between CERES and Cloudnet of liquid water path (Q_L ; blue) and ice water path (Q_I ; red). Panel (b) shows the liquid effective radii ($r_{E,L}$; blue) and the ice effective radii ($r_{E,I}$; red). Panel (c) shows the cloud radiative effect (CRE) at the surface (SFC; solid lines) and the top of the atmosphere (TOA; dashed lines) from T-CARS (brown) and CERES (green). Source: Barrientos-Velasco et al. 2022.

Moreover, this day is also of interest due to an underestimation of high-level cloud amount by CERES in comparison to Cloudnet, as is corroborated in Fig. 7.4a. This day is also characterized by changing surface conditions, as the ship crossed the sea-ice transit zone [see Fig. 3.3 and Fig. D.4].

This day was characterized by a low-level cloud located within the first 2 km of the atmosphere, and by several periods with a relatively thin ice cloud layer located between 6 and 9 km height [Fig. 7.4a]. According to Cloudnet, the well-separated liquid phase layer within the ice clouds is characterized by low radar reflectivity values, upward-directed Doppler velocity, and high lidar backscatter. There were two periods around 10:00Z and 23:00Z where, due to uncorrected attenuation, Q_L could not be derived by Cloudnet [Fig. 7.5a and b]. These two periods, marked by the pale-yellow shaded areas, are excluded from the T-CARS and CERES histogram analysis for a fair comparison shown in Figures 7.4d, (e), (f), (g).

Panel (b), (c), (d) and (e) in Fig. 7.4 indicate a good agreement between in-situ observations and CERES fluxes. The daily mean difference of fluxes is 16.1 W m^{-2} and -0.6 W m^{-2} for the SOL-D and TIR-D, respectively. For the T-CARS simulations, the mean flux difference is significantly larger, with 77.1 W m^{-2} for the SOL-D and -12.0 W m^{-2} for the TIR-D. Based on these results, RC can be confirmed for the SOL-D and TIR-D fluxes from CERES products and the TIR-D T-CARS simulations. The difference in the T-CARS SOL-D fluxes exceeds the expected uncertainty limits. An additional comparison is made considering the cloud properties to investigate the latter. At the TOA the flux difference between T-CARS and CERES is low with a mean flux difference of -0.2 W m^{-2} for the TIR-U [see Fig. 7.4f]. For the SOL-U the mean flux difference is -19 W m^{-2} [see Fig. 7.4g], which in part is mostly attributed by the two periods at 03:00Z and 09:00Z where the values of Q

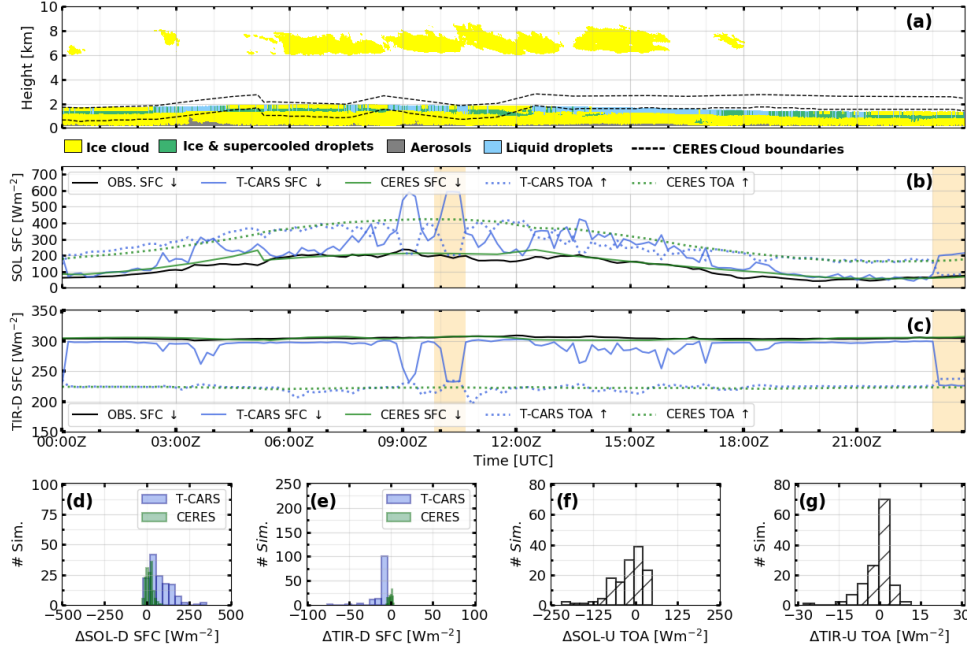


Figure 7.4: Same as Figure 7.2, but for 26 June 2017. Pale-orange shaded background indicate lidar attenuation. Source: Barrientos-Velasco et al. 2022.

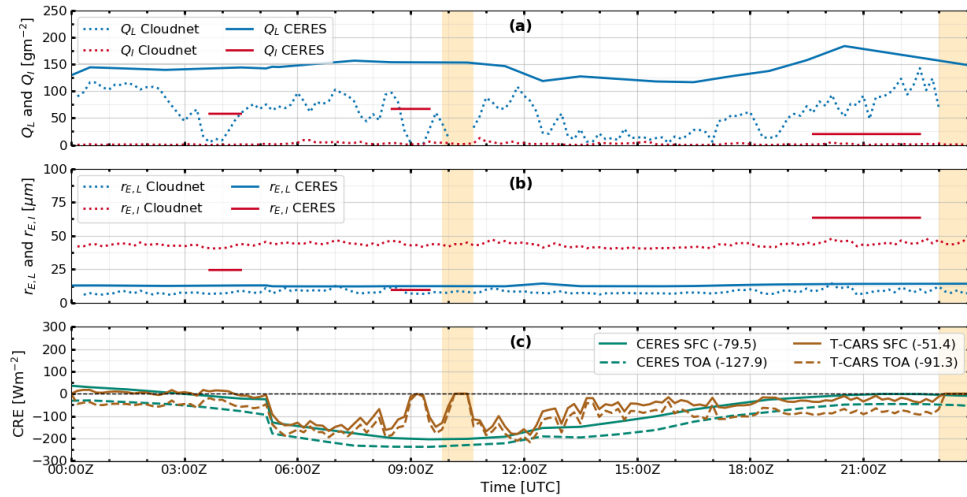


Figure 7.5: Same as Figure 7.3, but for 26 June 2017. Pale-orange shaded background indicate lidar attenuation. Source: Barrientos-Velasco et al. 2022.

reduce considerably.

Panels (a) and (b) of Fig. 7.5 show the 10-minute time series of cloud properties from the Cloudnet and CERES data sets. In contrast to Cloudnet, CERES reports only three periods with the presence of a mixed-phase cloud. The largest difference in cloud properties occurs in the cloud water path products. For Cloudnet, the mean Q_L is 56.2 g m^{-2} , and for Q_I , the mean is 1.9 g m^{-2} . In the case of CERES, these values are 119.7 g m^{-2} and 38.1 g m^{-2} for Q_L and Q_I , respectively. The variable and lower values of Q are likely responsible for the rapid changes and the positive (negative) bias of the SOL-D (TIR-D) flux visible in Fig. 7.4a and b.

This case study has a strong cloud cooling influence both at the SFC and TOA that

is enhanced by the surface albedo [see Fig. 7.5c and Fig. 3.3b]. In Fig. 7.5c an abrupt change of the CRE at the SFC and the TOA is visible at 05:00Z, due to a simultaneous rapid reduction of surface albedo from a value of 0.6 to 0.27 [see also Fig. 3.3a].

Based on CERES, a daily-mean net CRE of -79.5 W m^{-2} and -127.9 W m^{-2} is found at the SFC and TOA. The T-CARS simulations also indicate radiative cooling at the SFC and the TOA, but smaller in magnitude. As the downward SOL and TIR fluxes at the surface from CERES are more consistent with in-situ observations, the CERES values are considered to be more accurate than T-CARS outputs.

7.4 Synopsis

In this chapter, selected case studies were described depicting the most relevant and frequent sky conditions observed during the PS106 cruise. Each case study presented a comparison between simulations and observations to investigate the RC and in cloudy cases to also quantify the CRE. For most of the cases, the results indicated a good agreement between T-CARS, CERES and shipborne observations, suggesting that RC was successful. However, significant differences of CRE have been reported at the TOA despite indicating similar microphysical cloud properties between CERES and Cloudnet. These differences at the TOA might be attributed to differences in the thermodynamic atmospheric profiles, different cloud phase and macrophysical characteristics of cloud structure between both data sets.

These case studies also illustrated time periods where high-level clouds were misidentified by CERES and periods where Cloudnet missed low-level clouds. Despite not capturing the correct cloud boundaries, CERES succeeded to provide simulated surface fluxes similar to the downward fluxes observed aboard Polarstern. On the other hand, the miss-identification of clouds by Cloudnet challenged the correct cloud microphysical retrievals enlarging the flux difference (FD) between T-CARS and observations. It is suggested that future studies also consider the upward fluxes, especially for the SOL flux, due to its important sensitivity with the surface albedo.

Chapter 8

Radiation Budget and Cloud Radiative Effects

In this chapter, the analysis of the CRE and the radiation budget for PS106 cruise and the Arctic region based on CERES products are presented. The results are analysed in the context of the CF, Q , SZA, and surface albedo. The results presented in this chapter are based on Barrientos-Velasco et al. 2022.

8.1 CRE Analysis

This chapter presents the estimation of the CRE and radiation budget for the summer-time Arctic and the period of the PS106 expedition based on CERES products. It was initially planned to include the T-CARS simulations in this analysis; however, the limited satisfactory results obviated a meaningful comparison for the entire PS106 cruise. In particular, the exclusion of situations with the prevailing low-level stratus clouds, precipitation and ice clouds are expected to bias mean fluxes since the microphysical products were not of sufficient quality for radiative transfer simulations. The CERES data for the period of the first [from 16:45Z on 28 May until midnight on 20 June 2017] and the second leg of PS106 [22 June to 16 July 2017] are used for consistency with the temporal analyses given in chapter 6.2. The cruise track during this period lays entirely within the Arctic, defined here to cover the range from 70°-90°N, and consistent with the definition used by several previous studies [e.g., Walsh et al. 2009; Huang et al. 2017]. In addition to the effects of clouds on the radiation budget, the relevance of the direct aerosol radiative effect for the radiation budget is briefly discussed based on CERES products.

The CRE along the cruise track of the PS106 cruise is shown as a time series with hourly resolution in Figure 8.1 for the SOL, TIR, and net components at the SFC and the TOA. The TIR CRE at the SFC and TOA have mean values of 60.6 and 14.4 W m^{-2} , respectively. These values suggest significant warming of the surface and cooling of the atmosphere caused by clouds. Periods when the TIR CRE at the surface surpassed 80 W m^{-2} occurred mostly for persistent mixed-phase single-layer low-level clouds [e.g., 3 to 6 June, 16 to 17 June, 25 June, and 1 July 2017; see Fig. 3.7a and 3.7c]. The persistent cloud structure observed from 5 June to 7 June 2017 is studied in more detail in Egerer et al. 2021, who suggest that humidity inversions supply moisture to the cloud layer, increasing the persistence of the cloud. Time periods with the largest TIR CRE occurred mostly over sea ice or the marginal zone.

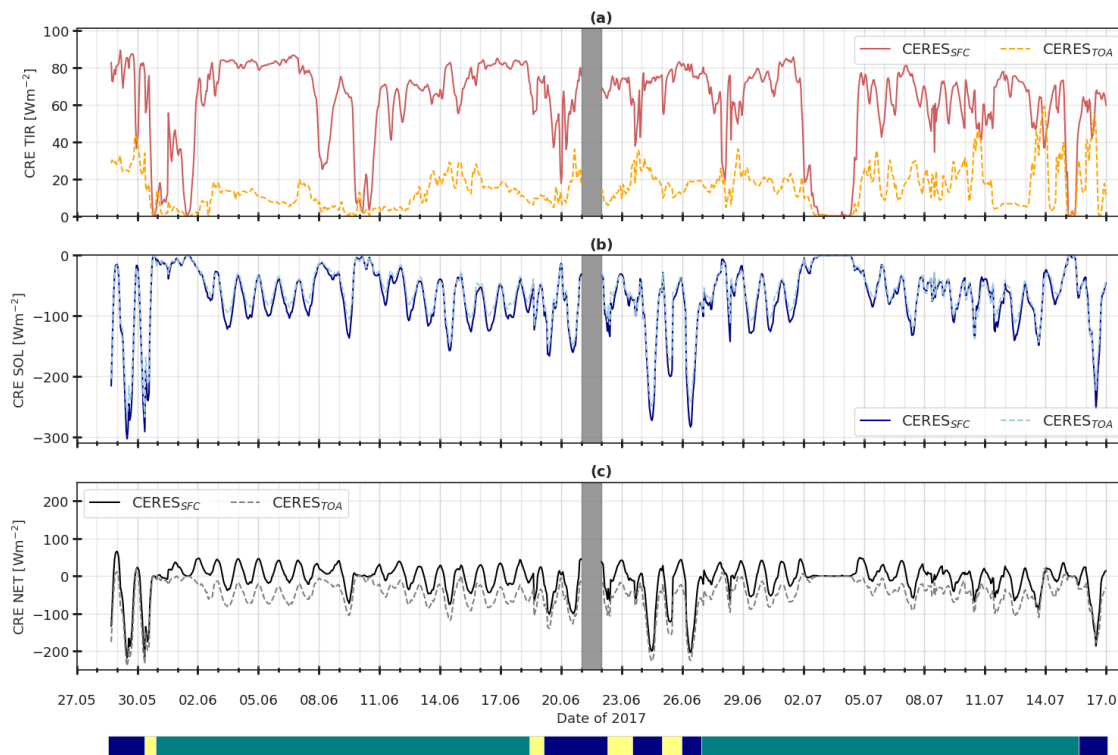


Figure 8.1: Time series of hourly TIR (a), SOL (b), and NET (c) CRE for PS106 expedition at the SFC (solid line) and at the TOA (dashed line). Source: Barrientos-Velasco et al. 2022.

The SOL CRE shows a clear dependency on the surface albedo and SZA, as shown by the oscillations visible at the SFC and the TOA in Figure 8.1b. The colour band shown at the bottom of Figure 8.1 indicates whether Polarstern was located in the open sea, the sea ice-marginal zone, or within the sea ice. The surface conditions and the SZA strongly modulate the magnitude of the SOL CRE. Thus, the highest values of SOL CRE are found for open ocean rather than for sea ice due to the high surface albedo of ice, which enhances the amount of reflected SOL radiation and reduces the SOL CRE.

The magnitude of CRE depends on several additional factors, including cloud macro and microphysics, surface conditions, and SZA [Shupe et al. 2005; Sedlar et al. 2010; Ebell et al. 2020; Stapf et al. 2020]. To investigate the interactions among these parameters, the values of CRE_{SFC} are plotted versus these parameters in a scatter plot in Figure 8.2 using colour-coding on the points based on the SZA values. Figure 8.2 clearly illustrates that neither of the considered parameters alone can explain the magnitude of the CRE. Nevertheless, it can be recognized that the SZA determines whether clouds cool (low SZA) or warm the surface (high SZA) and that an increase in CF also causes an increase in the CRE.

In panel 8.2b, the CF is compared with the CRE_{SFC} to investigate the dependence of the net CRE on this parameter. The dependence on surface albedo shown in Figure 8.2b indicates that larger surface cooling by clouds occurs over the open ocean than over ice. Displaying cases with a surface albedo lower (higher) than 0.4 in separate panels [see Fig. 8.2c and Fig. 8.2d, respectively]. The role of Q_L as reported by CERES is investigated for different surface types. Over open ocean, the

Table 8.1: Cloud radiative effect (CRE) based on CERES for PS106 cruise and Arctic region. Source: Barrientos-Velasco et al. 2022.

CRE [W m^{-2}]	PS106			Arctic R.			
	TIR	SOL	Net	TIR	SOL	Net	
TOA	Mean	14.5	-62.8	-48.4	14.3	-55.8	-40.1
	SD	10.2	45.8	42.4	4.0	30.1	27.5
	Median	13.2	-54.9	-39.6	14.3	-46.9	-21.9
	IQR	13.2	47.3	45.3	3.6	25.6	22.8
SFC	Mean	60.8	-69.6	-8.8	51.3	-60.6	-9.3
	SD	68.2	-60.2	0.6	51.0	-51.8	2.2
	Median	23.0	51.9	44.2	9.5	32.1	28.1
	IQR	22.3	57.9	37	11.7	27.4	26.7

CRE_{SFC} depends more strongly on SZA than on Q_L . Over highly reflective surfaces, in contrast, larger values of Q_L more often cause a warming than a cooling effect at the SFC [see Fig. 8.2d].

The CRE_{SFC} has also been compared to the surface albedo to determine how this parameter influences the CRE. Figure 8.2b shows a strong relation among the CRE_{SFC} , the surface albedo and the SZA. While the correlation between SZA and the CRE_{SFC} is evident, the surface albedo importantly indicates that the largest cooling CRE_{SFC} occur over the open ocean than over ice and that most of the warming of the CRE_{SFC} occurred over highly reflective surfaces. Moreover, Figure 8.2b shows a subdivision in two by separating the data points with a surface albedo higher or equal than 0.4 [Fig. 8.2d], and lower than 0.4 [Fig. 8.2c]. This subdivision aims to investigate the role of Q_L derived by CERES, which largely contribute to the CRE [Shupe and Intrieri 2004; Ebell et al. 2020] on both types of surface albedo. This analysis indicates that over the open ocean, the CRE_{SFC} is more dependent on the SZA than the magnitude of Q_L . Over high reflective surfaces, the dependence of SZA over the CRE_{SFC} is also evident; however, in this case, larger values of Q_L caused warming more frequently than a cooling effect at the surface [see Fig. 8.2d].

For the PS106 cruise, the SOL cooling by clouds dominates over the TIR warming, leading to a net cooling of -8.8 W m^{-2} at the surface [see Table 8.1]. For a similar time period but over other locations in the Arctic, the net CRE at the surface was also investigated by two other studies. For Ny-Ålesund, NO, Ebell et al. 2020 find values within a range of about -20 W m^{-2} to -40 W m^{-2} [see Fig. 6c in Ebell et al. 2020]. Considering the SOL CRE, the study of Stapf et al. 2020 focused on the ACLOUD airborne campaign, calculated a mean SOL CRE at the surface of -32 W m^{-2} ; however, by considering a proposed cloud-free retrieval of surface albedo taking into account spectral effects, this value increases to -62 W m^{-2} , which is similar to our result of -68.8 W m^{-2} [see Table 8.1]. It is worth noting that Ebell et al. 2020 consider a surface albedo that is not affected by diffuse downward radiation, and values obtained by CRE represent a cloud-free albedo [Chen et al. 2006]. Due to the strong sensitivity of the SOL CRE to surface albedo, a critical assessment of the accuracy of surface albedo used by CERES, including spectral and directionality effects, e.g., with in situ observations, is recommended.

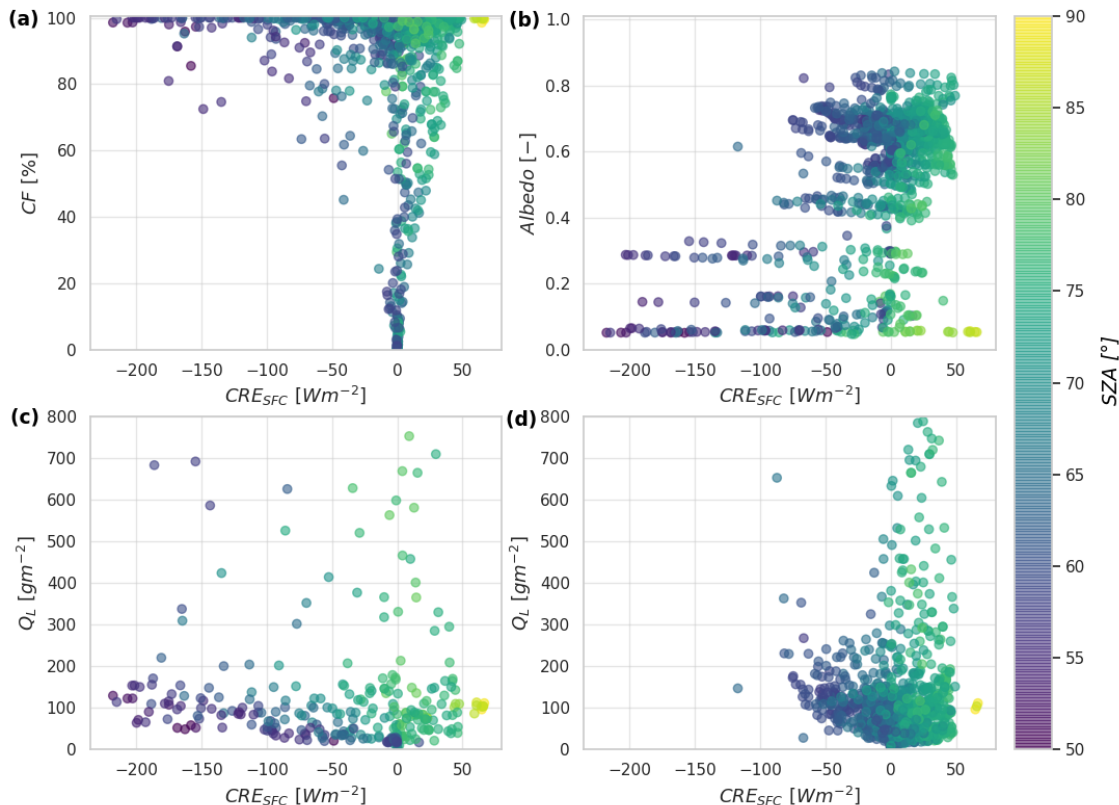


Figure 8.2: Scatter plots comparing the CRE_{SFC} with several parameters. Panel (a) shows the comparison with cloud fraction (CF). Panel (b) shows the comparison of surface albedo (α). Panels (c) and (d) show the comparison between the liquid water path (Q_L) at low surface albedo (< 0.4) and high surface albedo (> 0.4). All scatter plots are colour coded with the values of the solar zenith angle (SZA). Source: Barrientos-Velasco et al. 2022.

A similar analysis has been applied to the Arctic region to embed the results obtained for PS106 in a wider context. Panels (f) and (i) of Figure 8.3 show the mean CRE at the SFC and TOA for the entire time period of PS106, respectively. Additionally, the mean surface albedo, the TOA albedo, and the cloud fraction are shown in panels (a), (b), and (c), respectively.

For the considered period and the Arctic region, a larger cloud fraction is found over the open ocean than over land. This might be attributable to an increase of lower-tropospheric stability over land, which inhibits the mixing between the free troposphere and cloud layer, thus reducing cloud fraction [Morrison et al. 2012]. The latter effect is most evident over the Barents Sea, central Arctic, Baffin Bay, and Siberian Sea [Fig. 8.3c]. Over sea-ice, the cloud fraction is also large, with a particularly high occurrence of low and mid-low level clouds (not shown).

Based on CERES, low-level clouds are frequently found over the entire Arctic Ocean, with enhanced occurrence frequencies over the Barents Sea, Kara Sea, Laptev Sea, and the central Arctic. Mid-level clouds are mainly present over Greenland, East Arctic-Russia, Ellesmere Island and the central Arctic Ocean. High-level clouds occur more frequently over land, specifically over the Arctic-Russia, near Iqaluit in Canada, North of Sweden, Finland, and Norway (not shown). The spatial distribu-

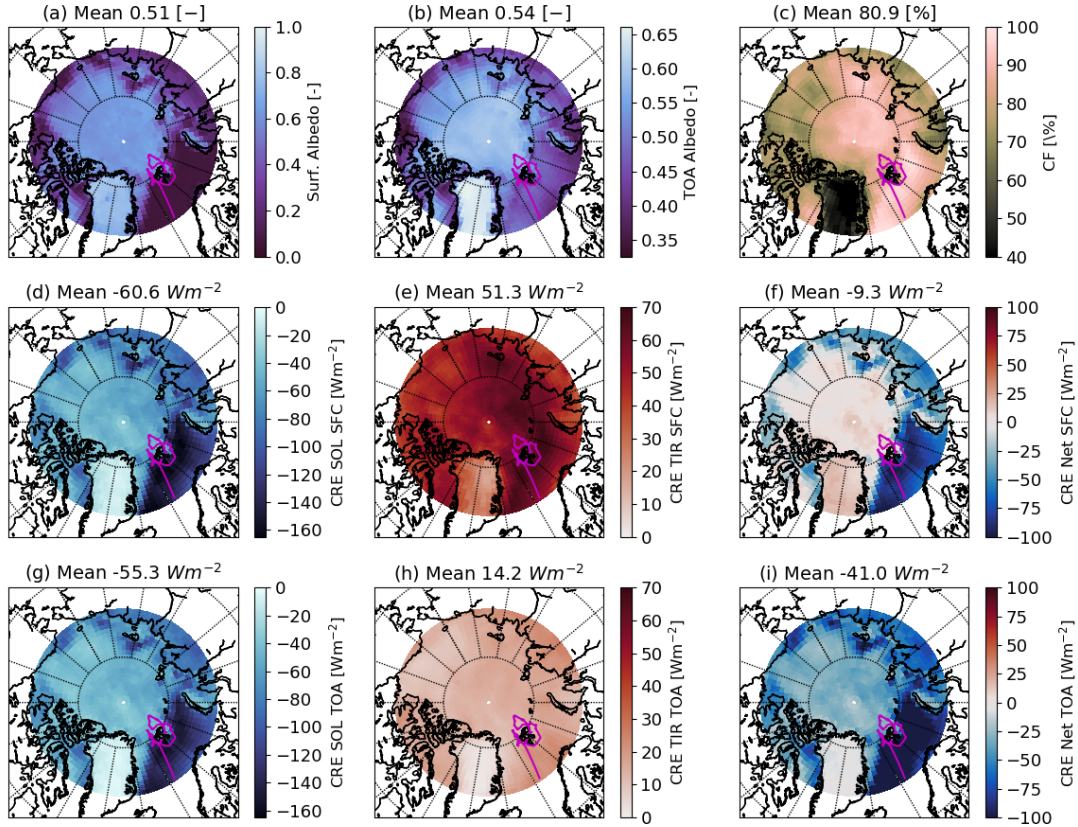


Figure 8.3: Maps of several time-averaged CERES data sets for the Arctic (70° to 90° N) and the time period of the PS106 expedition. Panel (a) shows the mean surface albedo, (b) the top of the atmosphere (TOA) albedo, and (c) the mean cloud fraction (CF). Panels (d), (e), and (f) show the CRE for the SOL, TIR, and net spectral regions, respectively, at the surface (SFC), while panels (g), (h), and (i) present the same at the TOA. An orthographic projection is used, and the PS106 cruise track is indicated in magenta. Source: Barrientos-Velasco et al. 2022.

tion of cloud fraction as visible in Figure 8.3c is consistent with the results of Palm et al. 2010 who report about an anticorrelation between sea ice extent and cloud fraction based on satellite-based lidar measurements from the CALIOP mission for a 5-year period.

Differences in the spatial distribution of cloud fraction yield differences in CRE values both at the SFC and the TOA. As indicated by Figure 8.3f, the surface CRE is highly dependent on surface albedo, suggesting a warming effect of clouds by up to 20.5 W m^{-2} over highly reflective regions covered with snow/sea ice [Fig. 8.3a]. At the TOA, the CRE shows a similar dependence on surface albedo but with a stronger cooling effect. The mean CRE for the considered period is -9.3 W m^{-2} at the surface, while it is -40.1 W m^{-2} at the TOA [see Table 8.1]. The TOA albedo depends on cloud fraction and surface albedo. Low values are only expected for clear-sky conditions over ocean, while high values correspond to either snow-covered or opaque clouds. This effect is, in particular, visible for the Barents Sea area, which corresponds to open ocean with a low surface albedo [Fig. 8.3a]; thus, the relatively high values found in Figure 8.3b are caused by the frequent occurrence of clouds, as indicated in Figure 8.3c. This region is of particular interest because mean values

of CRE at the TOA and SFC are larger than for the rest of the Arctic.

Previous studies have also investigated the CRE at the surface in the Arctic; see Table 8.3 for a list. The SHEBA expedition carried out observations in the Beaufort and Chuchki Sea, and its observations were used to estimate the CRE_{SFC} for an entire annual cycle. Based on SHEBA, Intrieri et al. 2002a concluded that clouds warm the surface for most of the year. During early July, however, a cooling effect of the surface by about -4 W m^{-2} was found. Based on the Arctic Summer Cloud Ocean Study (ASCOS) ship-borne campaign, the CRE_{SFC} was also calculated, finding a warming effect, with values ranging from 5 to about 75 W m^{-2} [see Fig. 8 in Sedlar et al. 2010]. Long-term observations can be used to resolve details of the annual cycle. Based on 10-years of observations at the North Slope Alaska (NSA) and NOAA Barrow Observatory (BRW) sites, the analysis of Dong et al. 2010 found a surface CRE ranging from -15 to -35 W m^{-2} for the period from the end of May to the middle of July [see Fig. 3 in Dong et al. 2010]. In contrast, the mixed-phase Arctic Clouds Experiment (M-PACE) conducted at the NSA site found a CRE_{SFC} ranging from 40 to 80 W m^{-2} for the months from September to December [de Boer et al. 2011], which is significantly larger than values reported by Dong et al. 2010.

In contrast to the rest of the Arctic, Greenland is covered by ice and snow during the entire year. Clouds have a warming effect during the entire annual cycle, with the highest values of CRE found from July to October [see Fig. 5 in Miller et al. 2015]. From May to July, Miller et al. 2015 report mean values of net CRE within a range of about 15 to 40 W m^{-2} , which is in the same range as the mean values reported in Figure 8.3.

Table 8.2: Summary of literature comparison of range CRE_{SFC} from different studies. Values in parenthesis indicate the mean for the entire study. Source: Barrientos-Velasco et al. 2022.

Site/Project	Type	Reference	Period	Region	CRE_{SFC} [$W m^{-2}$]
SHEBA	Ship-based	Intrieri et al. 2002a	Nov. 1997 to Oct. 1998	Beaufort and Chuchki Sea	$CRE_{SOL} = 0$ to 118 (-10) $CRE_{TIR} = 5$ to 65 (38)
ASCOS	Ship-based	Sedlar et al. 2010	Aug.-Sept. of 2008	Svalvard and Central Arctic	$CRE_{SOL} = 0$ to -50 $CRE_{TIR} = 65$ to 85
M-PACE	Observatory	de Boer et al. 2011	Sep.-Nov. of 2004	North Slope Alaska (NSA)	$CRE_{SOL} = 0$ to -55 $CRE_{TIR} = 30$ to 85
Summit Station	Observatory	Miller et al. 2015	Jan. 2011 to Oct. 2013	Greenland	$CRE_{SOL} = (0$ to -20) $CRE_{TIR} = (30$ to 60)
Greenland	Sat., Reanalysis Model and in situ,	Wang et al. 2019	May 2008 to Aug. 2013	Greenland	$CRE_{SOL} = 0$ to -70 $CRE_{TIR} = 30$ to 70
AWIPEV	Observatory	Ebell et al. 2020	June 2016 to Sep. 2018	Ny-Alesund Svalvard	$CRE_{SOL} = 0$ to -150 $CRE_{TIR} = 20$ to 60
ACLOUD	Airborne	Stapf et al. 2020	May-June 2017	Svalvard	$CRE_{SOL} = (-32), (-62)$
AFLUX	Airborne	Stapf et al. 2021	March-April 2019	Svalvard	$CRE_{TIR} = 75$
Barrow Alaska	Observatory	Dong et al. 2010	June 1998 to May 2008	BRW and NSA	$CRE_{SOL} = 0$ to -90 $CRE_{TIR} = 5$ to 65
Arctic Region	Satellite	Kay and L'Ecuver 2013	March 2000 to Feb. 2011	Arctic	$CRE_{SOL} = 0$ to -75 (-32) $CRE_{TIR} = 35$ to 70 (42)

The study from Kay and L'Ecuyer 2013 shows the CRE based on a combination of active and passive satellite-based remote sensing observations over the Arctic Ocean and report a mean CRE_{SFC} of about -30 to -40 $W m^{-2}$ at the surface for the period from the end of May to mid of July. These values are evidently larger than the mean value of -9.3 $W m^{-2}$ found in the present study. However, the results of Kay and L'Ecuyer 2013 focus mostly on the Arctic Ocean and exclude Greenland.

The comparison and discussion of the results with previous studies provide valuable context on the CRE across the Arctic for different seasons and locations. This analysis contributes to bringing ship-borne and satellite-based products together to validate and preliminarily investigate the causes of the main discrepancies. Nevertheless, it is worth noting that such a comparison cannot fully account for all factors affecting the results, including the consideration of particular sites, regions, cloud conditions, seasons, data sets, methods to obtain surface albedo, and different temporal averaging.

8.2 Radiation Budget

An overview of the most important components of the radiation budget is given in Figure 8.4. This figure shows the mean values along the PS106 cruise track in parentheses and for the entire Arctic. A full list of the different flux components can be found in Table 8.3. Along the PS106 cruise track and under all-sky conditions, the radiation budget at the SFC indicates a strong warming influence by the SOL net flux with 110.9 $W m^{-2}$, while the TIR fluxes cool the surface by -22.1 $W m^{-2}$. The presence of clouds enhances the TIR-D flux at the SFC by about 62.1 $W m^{-2}$, while reducing the SOL-D and SOL-U by 121.0 $W m^{-2}$ and 51.5 $W m^{-2}$, respectively. For the period of interest, the net radiation budget at the SFC has a value of 88.8 $W m^{-2}$ for PS106, and a value of 94.4 $W m^{-2}$ for the entire Arctic. The difference in the net radiation budget for the PS106 track and the entire Arctic is relatively small with a value of 5.6 $W m^{-2}$, and can be attributed to differences in the mean incoming SOL radiation at the TOA, downward TIR radiation, the transmission of SOL radiation through the atmosphere, and the surface albedo.

At the TOA and for the PS106 cruise, the mean net radiation budget is 0.2 $W m^{-2}$, while for clear-sky conditions, the net radiation budget would be 48.6 $W m^{-2}$. At the TOA, the presence of clouds increases the reflected solar radiation by 62.9 $W m^{-2}$ and reduces outgoing TIR flux by 14.5 $W m^{-2}$. For the Arctic, the net radiation budget under all-sky conditions has a value of 7.8 $W m^{-2}$, versus a value of 47.9 $W m^{-2}$ for clear-sky conditions. This indicates that the cooling by the cloud radiative effect is smaller for the entire Arctic than for PS106. This difference is mainly attributed to an increased reflection of solar radiation due to a larger cloud fraction and higher surface albedo along the PS106 track compared to the Arctic.

To consider the radiation budget of the atmosphere, the flux divergence has been calculated as the difference between the mean values at the TOA and the SFC. The net values found for the entire Arctic (-86.6 $W m^{-2}$) and PS106 (-88.6 $W m^{-2}$) show a significant cooling, and are once more relatively similar in magnitude. Since the net radiation budget for PS106 and the Arctic are relatively similar at the SFC, TOA and within the atmosphere, the PS106 expedition can be considered representative for the entire Arctic (see Table 8.3).

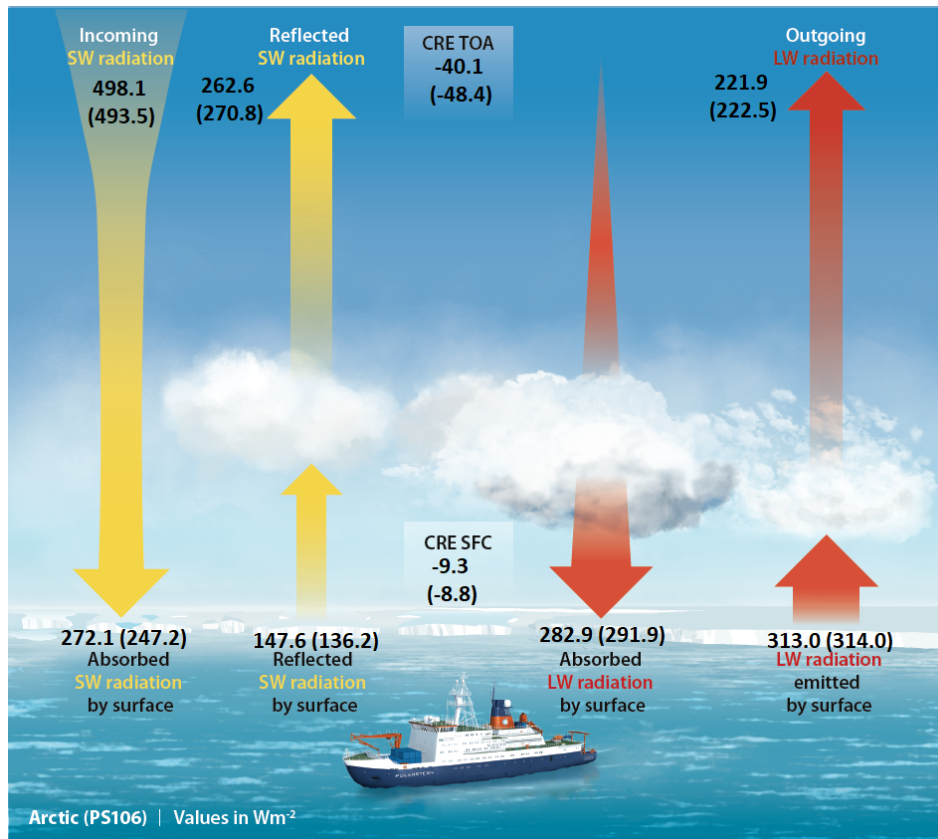


Figure 8.4: Radiation budget for PS106 cruise (a) and the entire Arctic region for the PS196 period (b). Mean values for the SW (SOL, yellow) and LW (TIR, red) are shown in $W m^{-2}$. Values in parentheses show the radiation budget during cloudless conditions. Source: Barrientos-Velasco et al. 2022

Considering net fluxes for pristine and clear-sky conditions, the direct aerosol radiative effect at the surface along the PS106 track and the entire Arctic are $-4.2 W m^{-2}$ and $-5.9 W m^{-2}$, respectively. At the TOA, the radiative effect of aerosols causes a minor cooling by $-0.1 W m^{-2}$ for both the PS106 track and the Arctic for clear-sky conditions, which changes to a small warming effect of $2.2 W m^{-2}$ and $1.9 W m^{-2}$ for PS106 and the Arctic, respectively in the presence of clouds. These values are consistent with the study of Markowicz et al. 2021, who determined the aerosol radiative effect based on radiative transfer simulations and the long-term aerosol reanalysis provided by the Navy Aerosol Analysis and Prediction System from 2003 to 2015. Focusing on the Arctic, they report an annual mean net direct (indirect) aerosol radiative effect of $-3.01 (-1.88) W m^{-2}$ and $-0.73 (0.31) W m^{-2}$, at the surface and TOA, respectively [see their Table 5]. While the values calculated in this study are larger than their annual mean, the magnitude is consistent with the early summer values reported for the months from May to July [see their Fig. 12a and Fig. 13a].

It is worth pointing out that the values of aerosol radiative effects reported here critically depend on an accurate representation of aerosol properties in the radiative transfer calculations underlying the CERES products. As aerosol properties are represented based on the assimilation of MODIS products into the MATCH aerosol transport model, its accuracy in the Arctic determines the accuracy of our findings,

and the use of reanalysis properties can have significant biases [e.g., Witthuhn et al. 2021].

Table 8.3: Radiation budget for PS106 for all-sky (AS) and a cloudless-sky (CS) based on CERES. Values represent mean and standard deviation (in parentheses) from 28 May to 20 June, 22 June to 16 July 2017. Source: Barrientos-Velasco et al. 2022.

Radiative Flux	TIR			SOL			Net	
	↓	↑	Net	↓	↑	Net		
PS106 CS	TOA	-	237.0(4.1)	-237.0(4.1)	493.5(150.0)	207.9(80.9)	285.6(121.6)	48.6(120.5)
	ATM	-229.8(9.2)	-75.7(7.3)	-154.1(9.6)	125.3(24.0)	20.2(14.9)	105.1(24.2)	-49.0(25.0)
	SFC	229.8(9.2)	312.7(9.9)	-82.9(10.0)	368.2(132.9)	187.7(94.2)	180.5(104.9)	97.6(101.9)
PS106 AS	TOA	-	222.5(10.8)	-222.5(10.8)	493.5(150.0)	270.8(87.1)	222.8(94.0)	0.2(91.9)
	ATM	-291.9(24.5)	-91.5(15.3)	-200.4(22.0)	246.4(82.9)	134.5(64.2)	111.8(30.1)	-88.6(33.7)
	SFC	291.9(24.5)	314.0(10.0)	-22.1(22.0)	247.2(116.6)	136.2(85.8)	110.9(75.1)	88.8(67.1)
Arctic R. CS	TOA	-	236.2(8.9)	-236.2(8.9)	498.1(179.8)	207.3(95.0)	290.8(147.8)	47.9(150.5)
	ATM	-230.4(23.1)	-75.6(14.0)	-154.8(11.1)	126.7(34.6)	21.0(18.1)	105.7(31.1)	-55.8(47.0)
	SFC	230.4(23.1)	311.8(21.9)	-81.4(11.1)	371.4(156.3)	186.4(110.2)	185.1(123.7)	103.7(122.4)
Arctic R. AS	TOA	-	221.9(13.3)	-221.9(13.3)	498.1(179.8)	262.6(99.4)	235.5(117.7)	7.8(113.6)
	ATM	-282.9(34.0)	-91.0(21.9)	-191.8(23.8)	226.0(99.5)	115.0(76.4)	111.0(36.7)	-86.6(45.3)
	SFC	282.9(34.0)	313.0(22.0)	-30.1(23.8)	272.1(142.8)	147.6(104.4)	124.5(91.0)	94.4(85.1)

8.3 Synopsis

In this chapter, the CRE based on CERES products along the PS106 cruise track and the Arctic region have been analysed and quantified. The analysis of the CRE was extended to the entire cruise based on CERES due to its good agreement with downward fluxes observations as discussed in chapter 6.3. The analysis of the CRE indicated a cooling effect at the SFC and at the TOA of 8.8 W m^{-2} and 48.4 W m^{-2} , respectively. The CRE at the SFC was further studied by comparing their connection with parameters like CF, surface albedo, Q_L , and SZA. This analysis indicated that the SZA modulates the intensity of the CRE more than the other parameters mentioned. Furthermore, the intricate link between the surface albedo and the SZA confirms that at low surface albedo (open ocean), the SOL CRE can reach the highest cooling values. In contrast, over high surface albedo (snow and sea ice), the values are lower since part of the SOL flux is reflected to the TOA.

Besides studying the CRE for the PS106 cruise track, the analysis was extended for the Arctic region for the period of the expedition. This analysis revealed a clear dependence of the CRE with the surface conditions indicating a warming effect over high reflective surfaces and cooling effect over the ocean over the time period under consideration, especially over the Barents Sea. The mean values for the Arctic region were relatively similar to during PS106, suggesting that the PS106 can be considered representative for the Arctic region.

The results presented in this chapter were also compared to the literature [see Table 8.2], which are based on other campaigns, periods, regions of focus and types of observations. Based on the PS106 expedition and region of focus, the results presented are congruent to the findings published in Ebell et al. 2020, and Stapf et al. 2020; Stapf et al. 2021. Based on the results presented in this chapter, it is emphasized the need to compare and validate ground-based and satellite observations for an extended analysis of small scale processes into more robust and long-term observations.

The radiation budget was quantified for cloudy and clear-sky conditions [see Fig. 8.4 and Table 8.3]. While this analysis can quantify the CRE, it also puts in evidence the dominance of the SOL flux during summer. For instance, for PS106 at the TOA, the mean SOL and TIR flux vary about 62.9 W m^{-2} and 14.5 W m^{-2} , respectively between cloudy and cloudless conditions. At the SFC, the variation for the downward (upward) SOL flux is 121.0 (51.5) W m^{-2} , and for the TIR is 62.1 (1.3) W m^{-2} . Similar values were found for the Arctic region.

Chapter 9

Summary, Conclusions and Outlook

In this last chapter, the main results of this thesis are summarized and discussed. The research questions proposed in Chapter 1.5 are answered in the context of the findings of this thesis which are partially presented in Barrientos-Velasco et al. 2020 and Barrientos-Velasco et al. 2022. This chapter also raises several open questions that should be investigated in future work.

9.1 Summary and Conclusions

Arctic amplification is considered a robust feature of climate change [Serreze et al. 2007; England et al. 2021; IPCC 2021]. However, the underlying processes and feedback mechanisms are still not fully understood. Clouds play a significant role in modifying the thermodynamic state of the atmosphere and the radiation budget. They are also involved in several processes that play a key role in understanding Arctic amplification. Moreover, cloud feedbacks constitute the largest inter-model uncertainty in general circulation models [Bony et al. 2006; Block et al. 2020].

The research project (AC)³ in its first phase aimed to understand key atmospheric processes better and collect valuable in-situ and remote sensing observations in the central Arctic with two major field campaigns [Wendisch et al. 2019]. Within this framework, project A01 aimed to improve the availability of detailed atmospheric observations in the central Arctic from shipborne remote sensing observations aboard the German Research Vessel Polarstern with the PS106 cruise [Griesche et al. 2020]. Furthermore, fine-scale modelling with large-eddy simulations of low-level stratus (LLS) Arctic clouds was carried out to investigate mixed-phase clouds [Neggers et al. 2019]. As part of project A01, this thesis aimed to better understand the surface radiation budget in the Arctic by evaluating and analysing the data collected during PS106 and using them to quantify the radiative effects of clouds. Moreover, the analysis was expanded by intercomparing the local results to satellite observations to provide a broader spatial context.

In this thesis, sets of radiative transfer simulations under clear-sky and cloudy conditions were performed to investigate and quantify the radiative effects of several perturbations [Chapter 4]. Moreover, the accuracy of the observations was evaluated and analysed to determine the radiative variation on the broadband downward

SOL and TIR radiation under different sky conditions [Chapter 5, 6, 7]. Finally, the radiation budget and the radiative effects of clouds have been quantified for the PS106 period [Chapters 7 and 8].

Do we understand cloud radiation interactions in the Arctic?

On the one hand, Arctic clouds lead to an increase of TIR radiation at the surface, resulting in an increase of snow and ice melting. On the other hand, clouds reduce the amount of the SOL radiation reaching the surface by reflecting the SOL radiation and thus reducing the warming. The strength of the effects mentioned are particularly dependent on the season and also the microphysical properties of clouds, which in turn are sensitive to atmospheric [e.g., variation of temperature and humidity; Curry et al. 1996; Cox et al. 2015], surface conditions [e.g., snow/ice cover and surface albedo; Francis et al. 2005; Kay et al. 2008; Schweiger et al. 2008; Eastman and Warren 2010; He et al. 2019; Choi et al. 2020] and the elevation of the sun. During summer, the parameters that have the most significant impact on the radiation budget at the surface are the surface albedo, cloud type, and the SZA [Minnett 1999; Dong et al. 2001; Shupe and Intrieri 2004; Sedlar et al. 2010; Stapf et al. 2019; Ebell et al. 2020].

In this thesis, sets of several sensitivity analyses were conducted to understand the cloud radiation interactions better and quantify the response of radiative fluxes to variability and uncertainties of several atmospheric and surface parameters during the PS106 cruise. Under cloudy conditions, the parameter that affects the most the TIR flux is the water path [Q]. At the surface the effect is quite evident for liquid and ice clouds, especially for values lower than around 60 g m^{-2} given that the cloud radiates as a nearly-ideal black body [see Fig. 1 in Turner 2007, Fig. 3 in Garrett et al. 2002]. At the TOA, the TIR-U flux is also affected by Q ; however, for cases with a large uncertainty of cloud geometrical thickness (CGT), the TIR-U flux can significantly change. This is due to the dependence of CGT with the cloud effective temperature and brightness temperature [Garrett et al. 2009].

It has been shown that under cloudy conditions, the parameters that affect the most the SOL flux at the SFC and TOA are the surface albedo and the cloud phase. For a given amount of cloud water path, the optical depth of a liquid cloud is larger than an ice cloud, since liquid clouds contain more particles that are smaller in size than in the case of an ice cloud. This physical characteristic leads to a larger reflection of the SOL flux at the TOA [Cesana and Storelvmo 2017]. This effect is triggered by the interaction with the surface conditions [see Fig. 4.5 and Fig. B.3], where the SOL flux may be absorbed or reflected in larger magnitude by the surface. The interaction between cloud properties and the surface conditions is susceptible to significant changes due to the SZA. At lower a SZA, the differences are enhanced since the SOL radiation must travel through more atmosphere.

Additionally, the small-scale variability of the SOL flux was investigated at high spatiotemporal resolution [Barrientos-Velasco et al. 2020]. The observations obtained from a network of 15 pyranometer stations deployed over an ice-floe for 13 days enabled the analysis of SOL flux variability under different atmospheric conditions. The spatiotemporal variability of SOL radiation was analysed in terms of atmospheric transmittance (ATg). The analysis of the published data set obtained during this experiment led to the identification of five typical sky conditions [i.e.,

overcast, multilayer, broken clouds, thin clouds and clear-sky conditions; Barrientos-Velasco et al. 2018]. Furthermore, the time series of ATg revealed a higher spatial variability during broken-cloud conditions than for another type of sky conditions [see Fig. 5.1 and Fig. 5.2].

In addition, the observations of the pyranometer network captured a spatial pattern of mean ATg where the stations near the ice floe edge showed lower values than the ones further away during overcast conditions [see Fig. 5.5]. This feature is likely explained by an increase in solar absorption by open water. In contrast, the stations located further away possibly experienced an increase in multiple reflections between a high albedo of snow and ice surfaces and the cloud base. It should be considered that this pattern is based on the limited data set of 2 weeks, and a more solid conclusion should be made after analysing a longer period of time.

The results found in this study were compared to those of a field campaign held in Germany in 2013 [Madhavan et al. 2017]. The results presented in this thesis indicate a relatively lower variability than the ones reported by Madhavan et al. 2017, which is likely due to more convective cloud development taking place in Germany than the stratiform Arctic clouds.

Under which conditions can state-of-the-art shipborne and passive satellite remote sensing observations constrain the radiative effects of clouds?

The in-situ and Cloudnet products created based on the observations collected during the PS106 cruise [Macke and Flores 2018; Griesche et al. 2020; Wendisch et al. 2019] were used as input parameters into a 1D radiative transfer model to simulate SOL and TIR broadband fluxes [Barrientos-Velasco et al. 2021; Barrientos-Velasco et al. 2022]. The simulations generated and collocated satellite simulations from CERES [Minnis et al. 2020] were compared to broadband downward radiative flux observations to evaluate whether radiative closure could be determined [see Chapter 6 and Chapter 7].

First, it is important to determine if satellite and shipborne products observed relatively similar atmospheric conditions. During the PS106 cruise, the cloud fraction observed from satellite and shipborne remote sensing were 86.7 % and 76.1 %, respectively. It is plausible that the difference in cloud fraction might be due to the spatial coverage of CERES of 1° by 1° in contrast to point shipborne base measurements. Nevertheless, there is, in general, a good agreement between Cloudnet and CERES capturing the fluctuations in cloud fraction for the cruise period. Moreover, it was found that standard Cloudnet and the supplementary determination of LLS clouds developed by [Griesche et al. 2020] improved the identification of clouds by about 18.6 % in contrast to the standard Cloudnet products [see Fig. 3.6].

Before attempting to constrain the radiative effects of clouds from remote sensing observations, it is necessary to verify the baseline by analysing clear-sky conditions. An evaluation for clear-sky conditions was done by identifying all the cloudless periods based on Cloudnet products and sky-camera images. The comparison among CERES fluxes products, radiative transfer simulations and broadband downward SOL and TIR shipborne observations indicated that, in general, the CERES and own simulations were within the instrumental uncertainties of the radiometers establishing trust under these conditions [see Chapter 6.2]. Nevertheless, it is worth

mentioning that several observations challenges were encountered with the radiometers due to the obstruction from the ship's superstructures, exhaustion, and plausible temperature fluctuation near the vicinity of the instruments tampering with the quality of the radiometers.

Under cloudy conditions, the comparisons between simulations and observations were analysed for the entire PS106 cruise [see Chapter 6] and further investigated in selected cases studies [see Chapter 7]. The radiative closure could not be achieved for the own simulations for the entire PS106 cruise due to several detection problems from the remote sensing instrumentation, which limited the quality of the microphysical cloud retrievals. Significant discrepancies between simulations and observations were found during LLS and precipitation (PPT) conditions. In general, under LLS and PPT conditions, the observations of cloud macro and microphysical parameters have a degraded quality. Thus, for only about 40.1 % of the time, observations are of sufficient quality to determine radiative closure [see Fig. 3.7 and Chapter 6.3]. The analysis only considering optimum conditions led to better results, and in some periods, the performed simulations matched the observations. Nevertheless, such periods were intermittent, making it difficult to provide a radiative closure analysis for the entire PS106 cruise. Therefore, the current work focused on selected case studies to depict the periods with good agreement with the observations and illustrate part of the challenges encountered

For all-sky conditions, CERES surface radiative fluxes and observations agreed well during PS106, with a mean flux difference of 6.0 W m^{-2} and 23.1 W m^{-2} for the SOL-D and TIR-D flux, respectively. The comparison yielded a correlation coefficient of 0.69 (0.77) and RMSE of 12.2 W m^{-2} (46.5 W m^{-2}) for the TIR-D (SOL-D). The results for the TIR-D flux lay within the instrumental uncertainties. For the SOL-D flux, the value is considered acceptable since the entire time series is considered, including periods when the superstructure of Polarstern obstructed the pyranometer. However, it is worth mentioning that these values should be interpreted with caution, and further investigation is needed. These results are consistent with the findings by Dong et al. 2016, and Riihelä et al. 2017, who also performed comparisons between in-situ radiative fluxes and CERES products at the ARM NSA site, as well as the Tara ice camp and on the Greenland Ice Sheet, respectively.

Can we quantify the effects of clouds on the surface radiation budget, and how representative are the PS106 results for the entire Arctic?

Considering the acceptable agreement found between CERES and the broadband SOL-D and TIR-D flux observations, the mean radiation budget and cloud radiative effects have been estimated along the cruise track and for the entire period of PS106 cruise. The most dominating contribution of the surface radiation budget was the SOL radiation. The SOL flux lead to a net surface flux of 88.8 W m^{-2} , and 94.4 W m^{-2} for PS106 and the entire Arctic, respectively. Additionally, the effect of clouds on the radiation budget has been quantified. The mean net CRE during PS106 along the cruise track is -8.8 W m^{-2} at the SFC and -48.4 W m^{-2} at the TOA, which suggests an atmospheric cooling of 39.6 W m^{-2} [see Chapter 8]. For the entire Arctic, the net CRE is similar to PS106, with values of -9.3 W m^{-2} , and -40.1 W m^{-2} , at the SFC and TOA, respectively [see Fig. 8.4].

The similarity between the local and regional CRE suggests that the PS106 cloud observations along the cruise track are representative of the cloud conditions found over the Arctic during this scenario. The results are also consistent with the summer results obtained from Ebell et al. 2020, who calculated the CRE during 2017 at Ny-Ålesund - Norway [see their Fig. 6].

The effect of clouds in the surface radiation budget were also investigated considering the reaction with other parameters such as the SZA and the surface albedo. It was shown that while the cloud microphysical properties play an important role in quantifying the CRE, the magnitude of CRE can be critically modulated by the surface conditions and the SZA [see Fig. 7.5c, Fig. 8.2, and Fig. 8.3a and c]. This is corroborated by the sensitivity analysis presented in Chapter 4.3.3. It was demonstrated that, especially under an extreme surface albedo [very low near 0.2 or very high above 0.8], the warming or cooling radiative effect of clouds at the surface depends less on their microphysical properties to determine whether they warm or cool the surface [see Fig. 4.5]. Moreover, it was also demonstrated that during the PS106, the strongest warming effect of clouds was observed at high SZA, when the relative importance of the SOL flux for the radiation budget is lower.

In summary, the work presented in this thesis has enhanced the understanding of relevant cloud radiative interactions by analysing the observations collected during the PS106 cruise and satellite observations. State-of-the-art remote sensing shipborne observations and satellite products were compared and evaluated through a radiative closure analysis, which provided additional information on how well-retrieved cloud properties and radiative transfer modelling represented the observations in order to physically explain the radiative effects of clouds and the radiation budget.

9.2 Outlook

The work presented in this thesis is entirely focused on the early summer PS106 research cruise. It is planned to extend the same analysis by intercomparing local and satellite observations for the Multidisciplinary drifting Observatory for the Study of Arctic Climate (MOSAiC) expedition [Shupe et al. 2022]. Analysing a longer period will allow research on potential methods to improve the accuracy of the observations to investigate the radiative effect of clouds for the entire annual cycle. An extension of the analysis will potentially improve our understanding of Arctic amplification [Taylor et al. 2022]. Particular focus will be dedicated to overcoming the limitations encountered with Cloudnet products, especially over LLS conditions in summer. For MOSAiC, also cloud products based on the Shupe-Turner [Shupe et al. 2015] algorithms will be available, allowing a comparison of Cloudnet and ARM products accuracies concerning the microphysical properties of Arctic clouds. In addition, particular attention will be given to instances where TIR radiative properties are highly sensitive to small changes in Q [lower than 60 g m^{-2} ; Garrett et al. 2002; Turner 2007; Tjernström et al. 2015; Achtert et al. 2020], which are poorly captured in this study. Furthermore, given the importance of the surface albedo and skin temperature to the interpretation of the cloud radiative effect and radiation budget, it is planned to evaluate the local observations during MOSAiC to the values used in this study.

Future results are intended to complement and support the (AC)³ phase 2 objectives

and infer the analysis in a climatological aspect by deriving radiative kernels to elucidate the role of cloud radiative feedbacks and their interactions with other radiative feedbacks [Soden et al. 2008; Zelinka et al. 2012; Tan and Storelvmo 2019; Zelinka et al. 2020]. Also, there is particular interest in exploiting the enhanced information captured by the hyperspectral observations of Infrared Atmospheric Sounding Interferometer (IASI) in contrast to broadband observations which can allow identifying atmospheric characteristics, especially during the winter. Besides the use of a 1D broadband radiative transfer model, it is planned to perform radiative transfer simulations in the same IASI spectra with a particular focus at the TOA. Bringing together the CERES and IASI attributes, it is planned to widen the analysis for a period of 23 and 16 years, respectively.

An important aspect of improvement relates to the adaptation of a 1D radiative transfer model to the cloud microphysical parameterizations used in Cloudnet. This thesis did not investigate the consistency between radiative transfer models and remote sensing observations retrievals; however, such analysis can potentially help determine how well radiative transfer modelling can physically explain the radiative effect of clouds.

There is still room to further investigate the effect of clouds in the Arctic at different scales. Adopting a small scale and high temporal resolution perspective, the analysis of solar radiation variability can be extended, including observations of the surface albedo at the same spatial and temporal resolution as the pyranometer network. Such an experimental setup could quantify the spatial variability induced by multiple reflections between the highly reflective surface and clouds and the effects of inhomogeneities in surface albedo. This type of experiment can provide additional information to elucidate cloud and surface interactions like the one shown in Figure 5.5 or in more complex scenarios with broken clouds conditions. Additionally, in the future, experiments including one or several spectrometers can provide information to quantify changes in the spectral distribution of solar radiation under different sky and surface conditions. Furthermore, with observations extending into the shortwave infrared range, a similar analysis could help to understand better cloud effects on atmospheric transmissivity at wavelengths above $1.1 \mu\text{m}$.

To better understand the complexity of radiative transfer in the Arctic due to cloud variability and surface albedo heterogeneity, it is recommended to utilize 3D radiative transfer models in the future [Scheirer and Macke 2003; Marshak and Davis 2005]. This recommendation can potentially help interpret the observations obtained with the pyranometer network. In addition, such studies can potentially deepen the understanding of plane-parallel biases of broken clouds over sea ice surfaces [Rozwadowska and Cahalan 2002; Wendler et al. 2004].

Appendix A

Cloud Microphysical Properties During PS106

Microphysical properties of clouds based on Cloudnet for different atmospheric conditions. The classification considers the method described in Chapter 3.3.3.

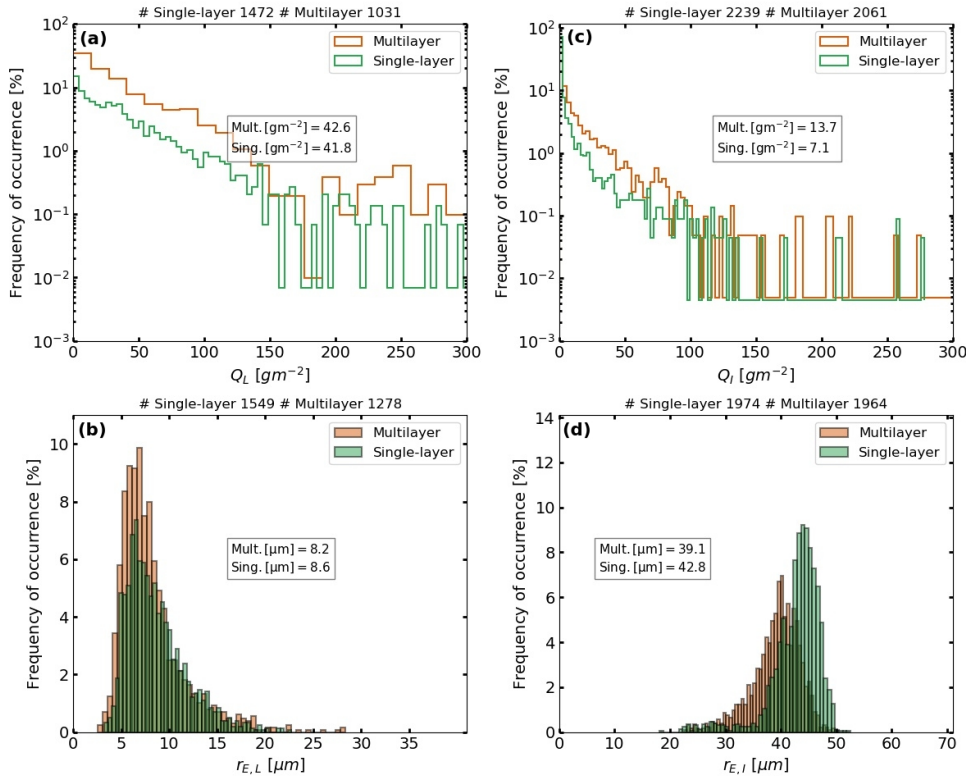


Figure A.1: Microphysical properties of single-layer and multilayer cloud conditions during PS106. Panels (a) and (c) show the frequency of occurrence of liquid (Q_L) and ice (Q_I) water path, respectively. Panels (b) and (d) show the distribution of the frequency of occurrence of ice and liquid effective radius. In orange is depicted all single-layer cases, and in green the multilayer cases.

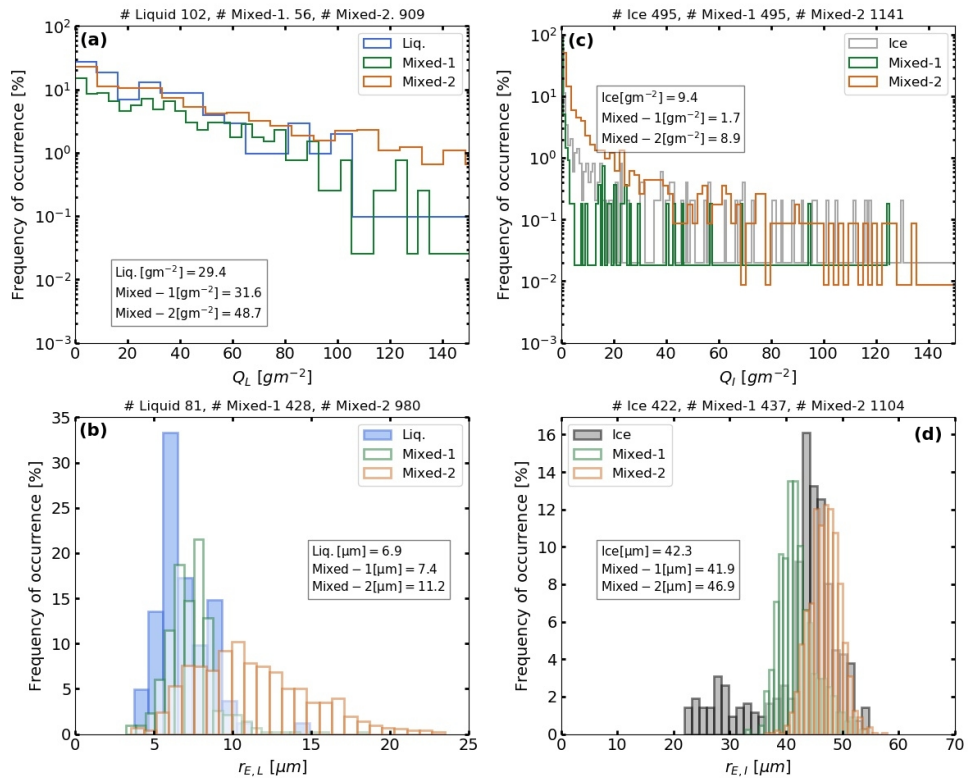


Figure A.2: Same as Fig. A.1, but for single-layer liquid (in blue), ice (in grey), mixed-phase type 1 (in green), type 2 (in orange) cloud conditions.

Appendix B

CRE of Sensitivity Analysis

This appendix shows complementary results to chapter 4. The following figures represent the daily mean net CRE for the different simulations performed varying cloud micro- and macrophysical properties of clouds and surface conditions.

Variation of microphysical properties of clouds

In this section is shown the mean results of the net CRE of the variation of Q and r_E for simulated single-layer liquid and ice cloud.

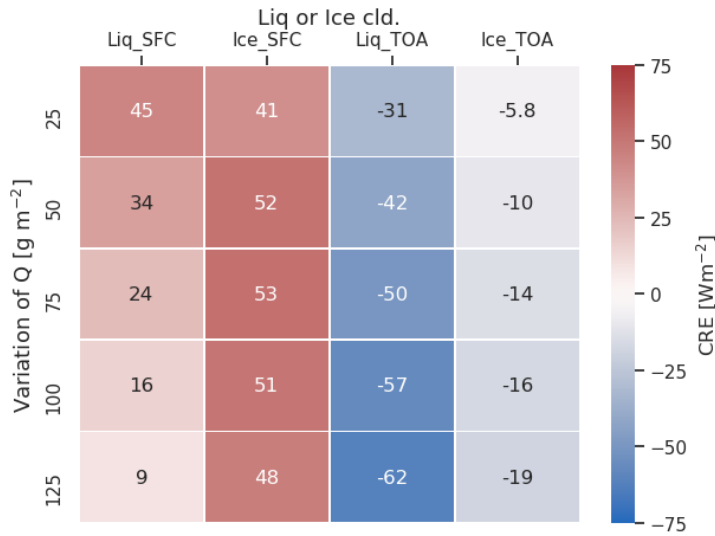


Figure B.1: Mean values of the net cloud radiative effect (CRE) for a single-layer liquid and ice cloud at the surface (SFC) and at the top of the atmosphere (TOA) for several values of cloud water path (Q).

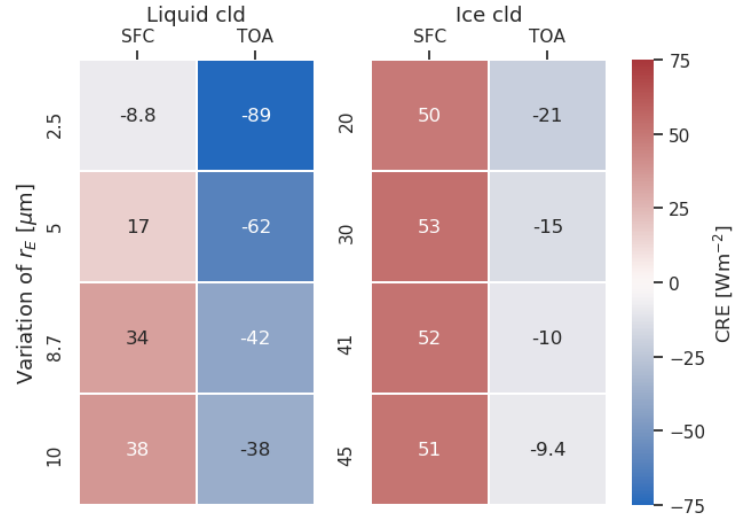


Figure B.2: Mean values of the net cloud radiative effect (CRE) for a single-layer liquid and ice cloud at the surface (SFC) and at the top of the atmosphere (TOA) for several values of effective radius (r_E).

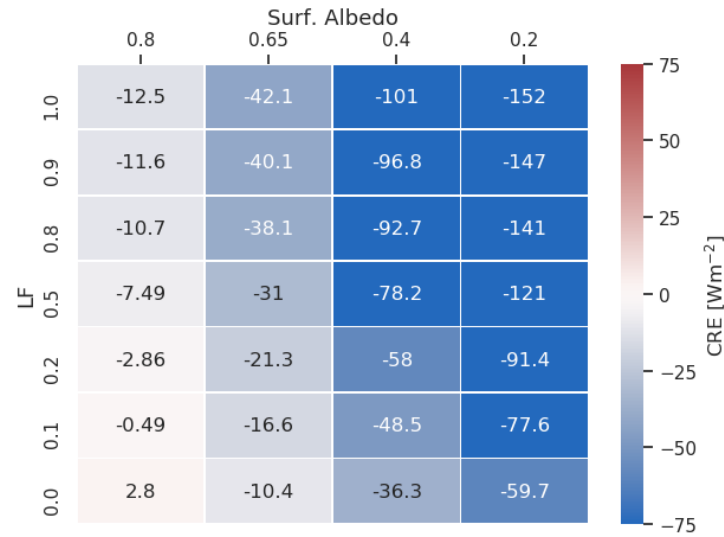


Figure B.3: Mean values of the net cloud radiative effect (CRE) for single-layer mixed-phase clouds at the top of the atmosphere (TOA) for several values of surface albedo.

Variation of macrophysical properties of clouds

In this section is shown the mean results of the net CRE of the variation of cloud base height (CBH) and cloud geometrical thickness (CGT) for simulated single-layer liquid and ice cloud.

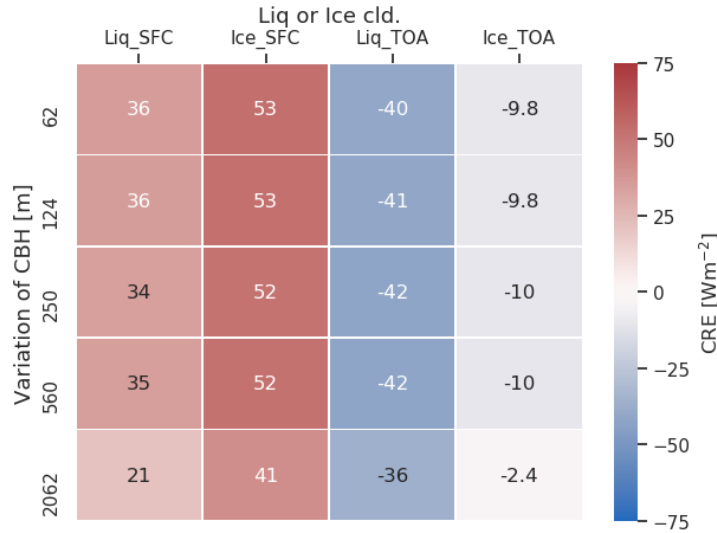


Figure B.4: Mean values of the net cloud radiative effect (CRE) for a single-layer liquid and ice cloud at the surface (SFC) and at the top of the atmosphere (TOA) for several values of cloud base height (CBH).

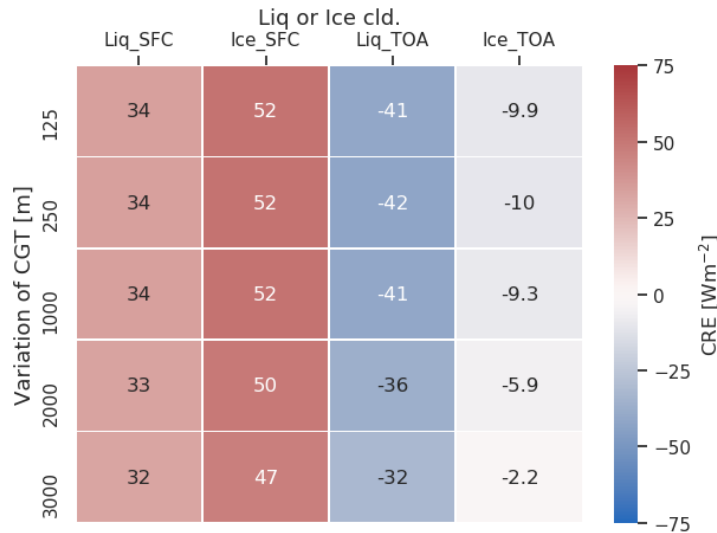


Figure B.5: Mean values of the net cloud radiative effect (CRE) for a single-layer liquid and ice cloud at the surface (SFC) and at the top of the atmosphere (TOA) for several values of cloud geometrical thickness (CGT).

Appendix C

CERES Aerosol Products

CERES AOD inputs come from the Model of Atmospheric Transport and Chemistry (MATCH) as described in Collins et al. 2001.

Based on the values from MATCH the time series of aerosols concentration is given at $55 \mu\text{m}$ and $84 \mu\text{m}$ (see Fig. C.1).

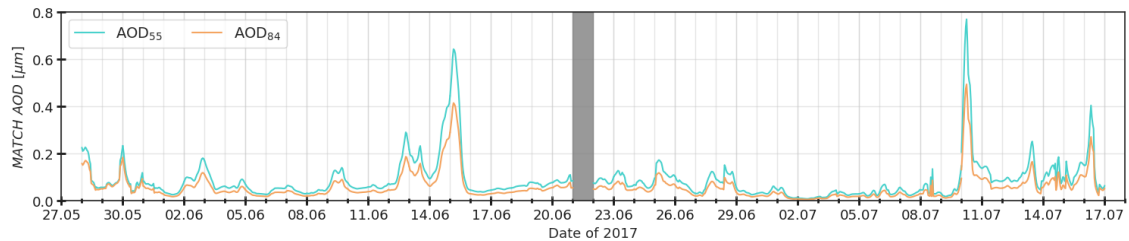


Figure C.1: Time series of AOD for PS106 based on CERES products. In teal is shown the AOD at $55 \mu\text{m}$ and in orange a $84 \mu\text{m}$.

Appendix D

Additional Observations

Sky-camera images

This appendix includes additional observations that were used to better analyse or characterize results presented in the Thesis.

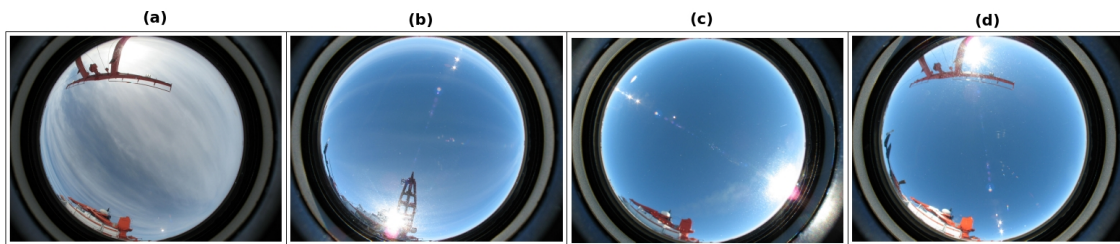


Figure D.1: Sky-camera photographs for 2 July 2017 04:00:08Z (a), for 2 July 2017 12:13:33Z (b), 3 July 2017 04:14:09Z (c), and 3 July 2017 12:04:08Z (d). All times in UTC.

MODIS observations

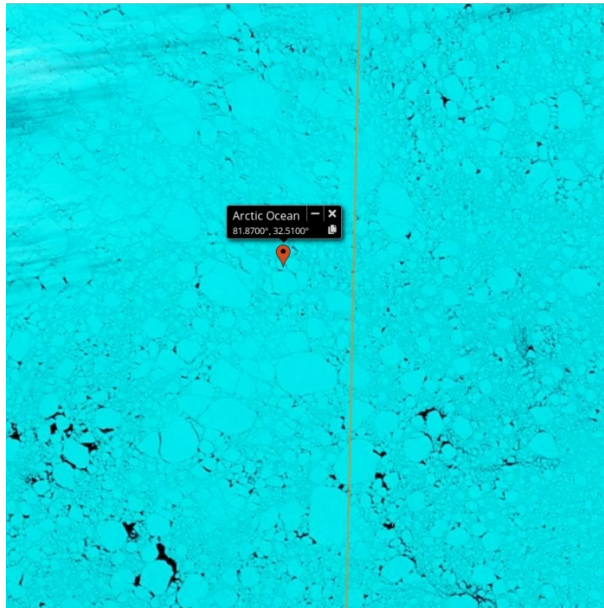


Figure D.2: Moderate Resolution Imaging Spectroradiometer (MODIS) screenshot for 3 July 2017. The red symbol indicates *Polarstern*'s location. The orange line indicates MODIS track.

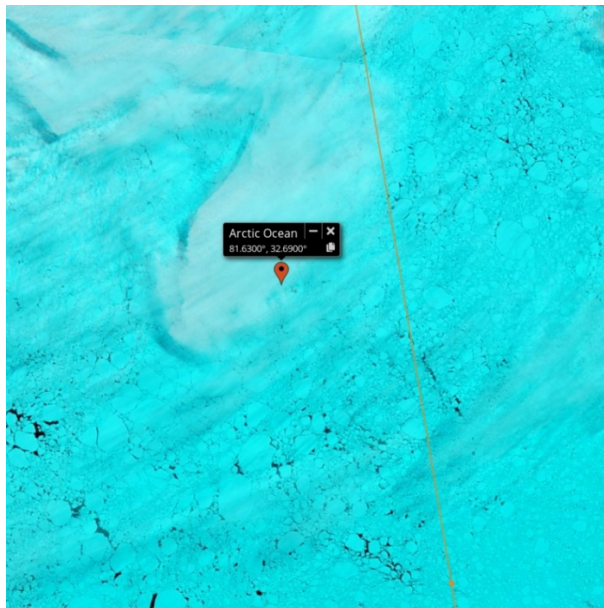


Figure D.3: Same as Fig. D.2, but for 2 July 2017.

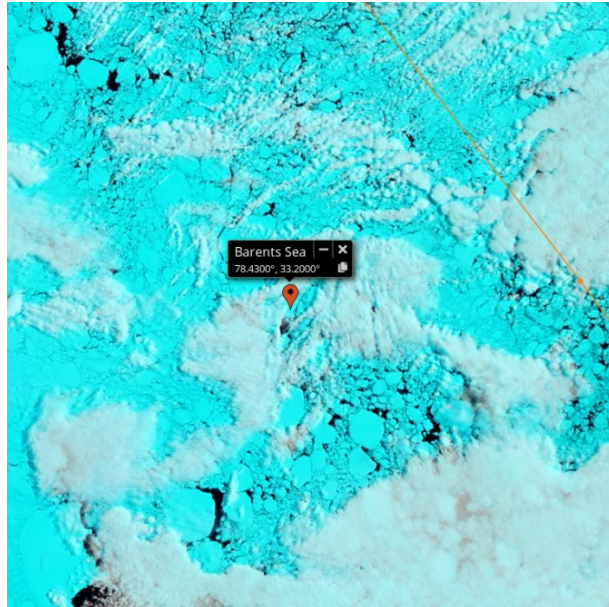


Figure D.4: Same as Fig. D.2, but for 26 June 2017.

Bibliography

- Achtert, P., O'Connor, E. J., Brooks, I. M., Sotiropoulou, G., Shupe, M. D., Pospichal, B., Brooks, B. J., and Tjernström, M.: Properties of Arctic liquid and mixed-phase clouds from shipborne Cloudnet observations during ACSE 2014. In: *Atmospheric Chemistry and Physics* 20.23, 2020, pp. 14983–15002. DOI: [10.5194/acp-20-14983-2020](https://doi.org/10.5194/acp-20-14983-2020).
- Alcaraz, M., Felipe, J., Grote, U., Arashkevich, E., and Nikishina, A.: Life in a warming ocean: thermal thresholds and metabolic balance of arctic zooplankton. In: *Journal of Plankton Research* 36.1, 2013, pp. 3–10. DOI: [10.1093/plankt/fbt111](https://doi.org/10.1093/plankt/fbt111).
- Anderson, G., Clough, S., Kneizys, F., Chetwynd, J., and Shettle, E.: AFGL Atmospheric Constituent Profiles (0.120 km). In: 1986, p. 46.
- Anstey, J. A. and Shepherd, T. G.: High-latitude influence of the quasi-biennial oscillation. In: *Quarterly Journal of the Royal Meteorological Society* 140.678, 2014, pp. 1–21.
- Arrhenius, S.: XXXI. On the influence of carbonic acid in the air upon the temperature of the ground. In: *The London, Edinburgh, and Dublin Philosophical Magazine and Journal of Science* 41.251, 1896, pp. 237–276. DOI: [10.1080/14786449608620846](https://doi.org/10.1080/14786449608620846).
- Bahramvash Shams, S. et al.: Variations in the vertical profile of ozone at four high-latitude Arctic sites from 2005 to 2017. In: *Atmospheric Chemistry and Physics* 19.15, 2019, pp. 9733–9751. DOI: [10.5194/acp-19-9733-2019](https://doi.org/10.5194/acp-19-9733-2019).
- Ballinger, T. J., Overland, J. E., Wang, M., Bhatt, U. S., Hanna, E., Hanssen-Bauer, I., Kim, S. -J., Thoman, R. L., and Walsh, J. E.: Surface Air Temperature. en-US. DOI: [10.25923/gcw8-2z06](https://doi.org/10.25923/gcw8-2z06).
- Barker, H. W. et al.: Assessing 1D Atmospheric Solar Radiative Transfer Models: Interpretation and Handling of Unresolved Clouds. In: *Journal Climate* 16.16, 2003, pp. 2676–2699. DOI: [10.1175/1520-0442\(2003\)016<2676:ADASRT>2.0.CO;2](https://doi.org/10.1175/1520-0442(2003)016<2676:ADASRT>2.0.CO;2).
- Barlakas, V., Deneke, H., and Macke, A.: The sub-adiabatic model as a concept for evaluating the representation and radiative effects of low-level clouds in a high-resolution atmospheric model. In: *Atmospheric Chemistry and Physics* 20.1, 2020, pp. 303–322. DOI: [10.5194/acp-20-303-2020](https://doi.org/10.5194/acp-20-303-2020).

- Barrientos-Velasco, C., Deneke, H., Griesche, H., Seifert, P., Engelmann, R., and Macke, A.: Spatiotemporal variability of solar radiation introduced by clouds over Arctic sea ice. In: *Atmospheric Measurement Techniques* 13.4, 2020, pp. 1757–1775. DOI: [10.5194/amt-13-1757-2020](https://doi.org/10.5194/amt-13-1757-2020).
- Barrientos-Velasco, C., Deneke, H., Hünnerbein, A., Griesche, H. J., Seifert, P., and Macke, A.: Radiative closure and cloud effects on the radiation budget based on satellite and ship-borne observations during the Arctic summer research cruise PS106. In: *Atmospheric Chemistry and Physics Discussions* 2022, 2022, pp. 1–71. DOI: [10.5194/acp-2021-1004](https://doi.org/10.5194/acp-2021-1004).
- Barrientos-Velasco, C., Deneke, H., and Macke, A.: Spatial and temporal variability of broadband solar irradiance during POLARSTERN cruise PS106/1 Ice Floe Camp (June 4th-16th 2017). data set. 2018. DOI: [10.1594/PANGAEA.896710](https://doi.org/10.1594/PANGAEA.896710).
- Barrientos-Velasco, C., Deneke, H., and Hünnerbein, A.: Radiative transfer simulations for the Arctic research expedition PS106. 2021. DOI: [10.5281/zenodo.5725382](https://doi.org/10.5281/zenodo.5725382).
- Bartlett, J. S., Ciotti, Á. M., Davis, R. F., and Cullen, J. J.: The spectral effects of clouds on solar irradiance. In: *Journal of Geophysical Research: Oceans* 103.C13, 1998, pp. 31017–31031. DOI: [10.1029/1998JC900002](https://doi.org/10.1029/1998JC900002).
- Bergeron, T.: On the physics of cloud and precipitation: mémoire présenté à L'Association de Météorologie de L'UGGI, Lisbonne, September 1933. Imprimerie Paul Dupont, 1935.
- Bitz, C. M., Gent, P. R., Woodgate, R. A., Holland, M. M., and Lindsay, R.: The Influence of Sea Ice on Ocean Heat Uptake in Response to Increasing CO₂. In: *Journal of Climate* 19.11, 2006, pp. 2437–2450. DOI: [10.1175/JCLI3756.1](https://doi.org/10.1175/JCLI3756.1).
- Bitz, C. and Roe, G.: A mechanism for the high rate of sea ice thinning in the Arctic Ocean. In: *Journal Climate* 17.18, 2004, pp. 3623–3632.
- Block, K., Schneider, F. A., Mülmenstädt, J., Salzmann, M., and Quaas, J.: Climate models disagree on the sign of total radiative feedback in the Arctic. In: *Tellus A: Dynamic Meteorology and Oceanography* 72.1, 2020, pp. 1–14. DOI: [10.1080/16000870.2019.1696139](https://doi.org/10.1080/16000870.2019.1696139).
- Boccolari, M. and Parmiggiani, F.: Trends and variability of cloud fraction cover in the Arctic, 1982–2009. In: *Theoretical and Applied Climatology* 132.3, 2018, pp. 739–749.
- Bodas-Salcedo, A., Andrews, T., Karmalkar, A. V., and Ringer, M. A.: Cloud liquid water path and radiative feedbacks over the Southern Ocean. In: *Geophysical Research Letters* 43.20, 2016, pp. 10, 938–10, 946. DOI: <https://doi.org/10.1002/2016GL070770>.

- Bony, S. et al.: How Well Do We Understand and Evaluate Climate Change Feedback Processes? In: *Journal Climate* 19.15, 2006, pp. 3445–3482. DOI: [10.1175/JCLI3819.1](https://doi.org/10.1175/JCLI3819.1).
- Box, J. E., Colgan, W. T., Wouters, B., Burgess, D. O., O’Neel, S., Thomson, L. I., and Mernild, S. H.: Global sea-level contribution from Arctic land ice: 1971-2017. In: *Environmental Research Letters* 13.12, 2018. DOI: [10.1088/1748-9326/aaf2ed](https://doi.org/10.1088/1748-9326/aaf2ed).
- Broeke, M. van den, As, D. van, Reijmer, C., and Wal, R. van de.: Assessing and Improving the Quality of Unattended Radiation Observations in Antarctica. In: *Journal of Atmospheric and Oceanic Technology* 21.9, 2004, pp. 1417–1431. DOI: [10.1175/1520-0426\(2004\)021<1417:AAITQO>2.0.CO;2](https://doi.org/10.1175/1520-0426(2004)021<1417:AAITQO>2.0.CO;2).
- Burek, K. A., Gulland, F. M. D., and O’Hara, T. M.: Effects of climate change on Arctic marine mammal health. In: *Ecological Applications* 18.sp2, 2008, S126–S134. DOI: [10.1890/06-0553.1](https://doi.org/10.1890/06-0553.1).
- Byrne, R. N., Somerville, R. C. J., and Subařilar, B.: Broken-Cloud Enhancement of Solar Radiation Absorption. In: *Journal of Atmospheric Sciences* 53.6, 1996, pp. 878–886. DOI: [10.1175/1520-0469\(1996\)053<0878:BCEOSR>2.0.CO;2](https://doi.org/10.1175/1520-0469(1996)053<0878:BCEOSR>2.0.CO;2).
- CERES-Guide.: CERES Terra/Aqua Edition4A SYN1deg Computed Fluxes - Accuracy and Validation. Last access: July 27, 2021. 2021.
- Data Quality Summary (4/8/2021). Last access: July 27, 2021. 2021.
- Cesana, G. and Storelmo, T.: Improving climate projections by understanding how cloud phase affects radiation. In: *Journal of Geophysical Research: Atmospheres* 122.8, 2017, pp. 4594–4599. DOI: [10.1002/2017JD026927](https://doi.org/10.1002/2017JD026927).
- Chan, M. A. and Comiso, J. C.: Arctic Cloud Characteristics as Derived from MODIS, CALIPSO, and CloudSat. In: *Journal Climate* 26.10, 2013, pp. 3285–3306. DOI: [10.1175/JCLI-D-12-00204.1](https://doi.org/10.1175/JCLI-D-12-00204.1).
- Cloud features detected by MODIS but not by CloudSat and CALIOP. In: *Geophysical Research Letters* 38.24, 2011. DOI: [10.1029/2011GL050063](https://doi.org/10.1029/2011GL050063).
- Chen, Y., Sun-Mack, S., Arduini, R., and Minnis, P.: Clear-sky and surface narrow-band albedo variations derived from VIRS and MODIS data. In: 12th Conference on Cloud Physics, and 12th Conference on Atmospheric Radiation, 2006.
- Choi, Y.-S., Hwang, J., Ok, J., Park, D.-S. R., Su, H., Jiang, J. H., Huang, L., and Limpasuvan, T.: Effect of Arctic clouds on the ice-albedo feedback in midsummer. In: *International Journal of Climatology* 40.10, 2020, pp. 4707–4714.
- Christensen, M. W., Behrangi, A., L’ecuyer, T. S., Wood, N. B., Lebsock, M. D., and Stephens, G. L.: Arctic Observation and Reanalysis Integrated System: A New Data Product for Validation and Climate Study. In: *Bulletin of the American*

- Meteorological Society 97.6, 2016, pp. 907–916. DOI: [10.1175/BAMS-D-14-00273.1](https://doi.org/10.1175/BAMS-D-14-00273.1).
- Clough, S., Shephard, M., Mlawer, E., Delamere, J., Iacono, M., Cady-Pereira, K., Boukabara, S., and Brown, P.: Atmospheric radiative transfer modeling: a summary of the AER codes. In: *Journal of Quantitative Spectroscopy and Radiative Transfer* 91.2, 2005, pp. 233–244. DOI: [10.1016/j.jqsrt.2004.05.058](https://doi.org/10.1016/j.jqsrt.2004.05.058).
- Cohen, J. et al.: Recent Arctic amplification and extreme mid-latitude weather. In: *Nature geoscience* 7.9, 2014, pp. 627–637.
- Collins, W. D., Rasch, P. J., Eaton, B. E., Khattatov, B. V., Lamarque, J.-F., and Zender, C. S.: Simulating aerosols using a chemical transport model with assimilation of satellite aerosol retrievals: Methodology for INDOEX. In: *Journal of Geophysical Research: Atmospheres* 106.D7, 2001, pp. 7313–7336. DOI: [10.1029/2000JD900507](https://doi.org/10.1029/2000JD900507).
- Cox, C. J., Walden, V. P., Rowe, P. M., and Shupe, M. D.: Humidity trends imply increased sensitivity to clouds in a warming Arctic. In: *Nature communications* 6.1, 2015, pp. 1–8.
- Crewell and Löhnert.: Accuracy of cloud liquid water path from ground-based microwave radiometry 2. Sensor accuracy and synergy. In: *Radio Science* 38.3, 2003. DOI: [10.1029/2002RS002634](https://doi.org/10.1029/2002RS002634).
- Crook, J. A., Forster, P. M., and Stuber, N.: Spatial patterns of modeled climate feedback and contributions to temperature response and polar amplification. In: *Journal Climate* 24.14, 2011, pp. 3575–3592.
- Curry, J. A., Schramm, J. L., and Ebert, E. E.: Sea Ice-Albedo Climate Feedback Mechanism. In: *Journal Climate* 8.2, 1995, pp. 240–247. DOI: [10.1175/1520-0442\(1995\)008<0240:SIACFM>2.0.CO;2](https://doi.org/10.1175/1520-0442(1995)008<0240:SIACFM>2.0.CO;2).
- Curry, J. A., Schramm, J. L., Rossow, W. B., and Randall, D.: Overview of Arctic Cloud and Radiation Characteristics. In: *Journal Climate* 9.8, 1996, pp. 1731–1764. DOI: [10.1175/1520-0442\(1996\)009<1731:00ACAR>2.0.CO;2](https://doi.org/10.1175/1520-0442(1996)009<1731:00ACAR>2.0.CO;2).
- de Boer, G., Collins, W. D., Menon, S., and Long, C. N.: Using surface remote sensors to derive radiative characteristics of Mixed-Phase Clouds: an example from M-PACE. In: *Atmospheric Chemistry and Physics* 11.23, 2011, pp. 11937–11949. DOI: [10.5194/acp-11-11937-2011](https://doi.org/10.5194/acp-11-11937-2011).
- de Boer, G., Eloranta, E. W., and Shupe, M. D.: Arctic Mixed-Phase Stratiform Cloud Properties from Multiple Years of Surface-Based Measurements at Two High-Latitude Locations. In: *Journal of the Atmospheric Sciences* 66.9, 2009, pp. 2874–2887. DOI: [10.1175/2009JAS3029.1](https://doi.org/10.1175/2009JAS3029.1).
- Delamere, J. S., Clough, S. A., Payne, V. H., Mlawer, E. J., Turner, D. D., and Gamache, R. R.: A far-infrared radiative closure study in the Arctic: Application

- to water vapor. In: *Journal of Geophysical Research: Atmospheres* 115.D17, 2010. DOI: [10.1029/2009JD012968](https://doi.org/10.1029/2009JD012968).
- Delanoë, J., Protat, A., Bouniol, D., Heymsfield, A., Bansemmer, A., and Brown, P.: The Characterization of Ice Cloud Properties from Doppler Radar Measurements. In: *Journal of Applied Meteorology and Climatology* 46.10, 2007, pp. 1682–1698. DOI: [10.1175/JAM2543.1](https://doi.org/10.1175/JAM2543.1).
- Deneke, H. M., Knap, W. H., and Simmer, C.: Multiresolution analysis of the temporal variance and correlation of transmittance and reflectance of an atmospheric column. In: *Journal of Geophysical Research: Atmospheres* 114.D17, 2009. DOI: [10.1029/2008JD011680](https://doi.org/10.1029/2008JD011680).
- Deshler, T., Stübi, R., Schmidlin, F. J., Mercer, J. L., Smit, H. G. J., Johnson, B. J., Kivi, R., and Nardi, B.: Methods to homogenize electrochemical concentration cell (ECC) ozonesonde measurements across changes in sensing solution concentration or ozonesonde manufacturer. In: *Atmospheric Measurement Techniques* 10.6, 2017, pp. 2021–2043. DOI: [10.5194/amt-10-2021-2017](https://doi.org/10.5194/amt-10-2021-2017).
- Di Biagio, C., Sarra, A. di, Eriksen, P., Ascanius, S. E., Muscari, G., and Holben, B.: Effect of surface albedo, water vapour, and atmospheric aerosols on the cloud-free shortwave radiative budget in the Arctic. In: *Climate dynamics* 39.3-4, 2012, pp. 953–969.
- Dolinar, E. K., Dong, X., Xi, B., Jiang, J. H., and Loeb, N. G.: A clear-sky radiation closure study using a one-dimensional radiative transfer model and collocated satellite-surface-reanalysis data sets. In: *Journal of Geophysical Research: Atmospheres* 121.22, 2016, pp. 13, 698–13, 714. DOI: [10.1002/2016JD025823](https://doi.org/10.1002/2016JD025823).
- Dong, X., Mace, G. G., Minnis, P., and Young, D. F.: Arctic stratus cloud properties and their effect on the surface radiation budget: Selected cases from FIRE ACE. In: *Journal of Geophysical Research: Atmospheres* 106.D14, 2001, pp. 15297–15312. DOI: <https://doi.org/10.1029/2000JD900404>.
- Dong, X., Xi, B., Crosby, K., Long, C. N., Stone, R. S., and Shupe, M. D.: A 10 year climatology of Arctic cloud fraction and radiative forcing at Barrow, Alaska. In: *Journal of Geophysical Research: Atmospheres* 115.D17, 2010. DOI: [10.1029/2009JD013489](https://doi.org/10.1029/2009JD013489).
- Dong, X., Xi, B., Qiu, S., Minnis, P., Sun-Mack, S., and Rose, F.: A radiation closure study of Arctic stratus cloud microphysical properties using the collocated satellite-surface data and Fu-Liou radiative transfer model. In: *Journal of Geophysical Research: Atmospheres* 121.17, 2016, pp. 10, 175–10, 198. DOI: [10.1002/2016JD025255](https://doi.org/10.1002/2016JD025255).
- Dong, X., Zib, B., Xi, B., Deng, Y., Zhang, X., Lin, B., and Long, C.: Critical Mechanisms for the Formation of Extreme Arctic Sea-Ice Extent in the Summers of 2007 and 1996. In: *Climate Dynamics* 43, 2013. DOI: [10.1007/s00382-013-1920-8](https://doi.org/10.1007/s00382-013-1920-8).

- Doyle, J. G., Lesins, G., Thackray, C. P., Perro, C., Nott, G. J., Duck, T. J., Damoah, R., and Drummond, J. R.: Water vapor intrusions into the High Arctic during winter. In: *Geophysical Research Letters* 38.12, 2011. DOI: [10.1029/2011GL047493](https://doi.org/10.1029/2011GL047493).
- Dutra, E., Balsamo, G., Viterbo, P., Miranda, P. M. A., Beljaars, A., Schär, C., and Elder, K.: An Improved Snow Scheme for the ECMWF Land Surface Model: Description and Offline Validation. In: *Journal of Hydrometeorology* 11.4, 2010, pp. 899–916. DOI: [10.1175/2010JHM1249.1](https://doi.org/10.1175/2010JHM1249.1).
- Eastman, R. and Warren, S. G.: Interannual Variations of Arctic Cloud Types in Relation to Sea Ice. In: *Journal Climate* 23.15, 2010, pp. 4216–4232. DOI: [10.1175/2010JCLI3492.1](https://doi.org/10.1175/2010JCLI3492.1).
- Ebell, K., Nomokonova, T., Maturilli, M., and Ritter, C.: Radiative Effect of Clouds at Ny-Ålesund, Svalbard, as Inferred from Ground-Based Remote Sensing Observations. In: *Journal of Applied Meteorology and Climatology* 59.1, 2020, pp. 3–22. DOI: [10.1175/JAMC-D-19-0080.1](https://doi.org/10.1175/JAMC-D-19-0080.1).
- Egerer, U., Ehrlich, A., Gottschalk, M., Griesche, H., Neggers, R. A. J., Siebert, H., and Wendisch, M.: Case study of a humidity layer above Arctic stratocumulus and potential turbulent coupling with the cloud top. In: *Atmospheric Chemistry and Physics* 21.8, 2021, pp. 6347–6364. DOI: [10.5194/acp-21-6347-2021](https://doi.org/10.5194/acp-21-6347-2021).
- Ehrlich, A. et al.: A comprehensive in situ and remote sensing data set from the Arctic CLOUD Observations Using airborne measurements during polar Day (ACLOUD) campaign. In: *Earth System Science Data* 11.4, 2019, pp. 1853–1881. DOI: [10.5194/essd-11-1853-2019](https://doi.org/10.5194/essd-11-1853-2019).
- Engelmann, R. et al.: The automated multiwavelength Raman polarization and water-vapor lidar Polly^{XT}: the neXT generation. In: *Atmospheric Measurement Techniques* 9.4, 2016, pp. 1767–1784. DOI: [10.5194/amt-9-1767-2016](https://doi.org/10.5194/amt-9-1767-2016).
- England, M. R., Eisenman, I., Lutsko, N. J., and Wagner, T. J. W.: The Recent Emergence of Arctic Amplification. In: *Geophysical Research Letters* 48.15, 2021. e2021GL094086 2021GL094086, e2021GL094086. DOI: <https://doi.org/10.1029/2021GL094086>.
- Findeisen, W., Volken, E., Giesche, A. M., and Brönnimann, S.: Colloidal meteorological processes in the formation of precipitation. In: *Meteorologische Zeitschrift* 24.4, 2015, pp. 443–454.
- Francis, J. A., Hunter, E., Key, J. R., and Wang, X.: Clues to variability in Arctic minimum sea ice extent. In: *Geophysical Research Letters* 32.21, 2005. DOI: [10.1029/2005GL024376](https://doi.org/10.1029/2005GL024376).
- Francis, J. A. and Skific, N.: Evidence linking rapid Arctic warming to mid-latitude weather patterns. In: *Philosophical Transactions of the Royal Society A: Mathematical, Physical and Engineering Sciences* 373.2045, 2015, p. 20140170. DOI: [10.1098/rsta.2014.0170](https://doi.org/10.1098/rsta.2014.0170).

- Francis, J. A., Chan, W., Leathers, D. J., Miller, J. R., and Veron, D. E.: Winter Northern Hemisphere weather patterns remember summer Arctic sea-ice extent. In: *Geophysical Research Letters* 36.7, 2009. DOI: <https://doi.org/10.1029/2009GL037274>.
- Frisch, A. S., Feingold, G., Fairall, C. W., Uttal, T., and Snider, J. B.: On cloud radar and microwave radiometer measurements of stratus cloud liquid water profiles. In: *Journal of Geophysical Research: Atmospheres* 103.D18, 1998, pp. 23195–23197. DOI: [10.1029/98JD01827](https://doi.org/10.1029/98JD01827).
- Frisch, S., Shupe, M., Djalalova, I., Feingold, G., and Poellot, M.: The Retrieval of Stratus Cloud Droplet Effective Radius with Cloud Radars. In: *Journal of Atmospheric and Oceanic Technology* 19.6, 2002, pp. 835–842. DOI: [10.1175/1520-0426\(2002\)019<0835:TROSCD>2.0.CO;2](https://doi.org/10.1175/1520-0426(2002)019<0835:TROSCD>2.0.CO;2).
- Fu, Q. and Liou, K. N.: On the Correlated k-Distribution Method for Radiative Transfer in Nonhomogeneous Atmospheres. In: *Journal of the Atmospheric Sciences* 49.22, 1992, pp. 2139–2156. DOI: [10.1175/1520-0469\(1992\)049<2139:OTCDMF>2.0.CO;2](https://doi.org/10.1175/1520-0469(1992)049<2139:OTCDMF>2.0.CO;2).
- Garrett, K. J., Yang, P., Nasiri, S. L., Yost, C. R., and Baum, B. A.: Influence of Cloud-Top Height and Geometric Thickness on a MODIS Infrared-Based Ice Cloud Retrieval. In: *Journal of Applied Meteorology and Climatology* 48.4, 2009, pp. 818–832. DOI: [10.1175/2008JAMC1915.1](https://doi.org/10.1175/2008JAMC1915.1).
- Garrett, T. J., Radke, L. F., and Hobbs, P. V.: Aerosol Effects on Cloud Emissivity and Surface Longwave Heating in the Arctic. In: *Journal of the Atmospheric Sciences* 59.3, 2002, pp. 769–778. DOI: [10.1175/1520-0469\(2002\)059<0769:AEOCEA>2.0.CO;2](https://doi.org/10.1175/1520-0469(2002)059<0769:AEOCEA>2.0.CO;2).
- Goosse, H. et al.: Quantifying climate feedbacks in polar regions. In: *Nature Communications* 9.1, 2018, p. 1919. DOI: [10.1038/s41467-018-04173-0](https://doi.org/10.1038/s41467-018-04173-0).
- Graversen, R. G., Mauritsen, T., Drijfhout, S., Tjernström, M., and Mårtensson, S.: Warm winds from the Pacific caused extensive Arctic sea-ice melt in summer 2007. In: *Climate Dynamics* 36.11-12, 2011, pp. 2103–2112. DOI: [10.1007/s00382-010-0809-z](https://doi.org/10.1007/s00382-010-0809-z).
- Grenfell, T. C. and Warren, S. G.: Representation of a nonspherical ice particle by a collection of independent spheres for scattering and absorption of radiation. In: *Journal of Geophysical Research: Atmospheres* 104.D24, 1999, pp. 31697–31709. DOI: [10.1029/1999JD900496](https://doi.org/10.1029/1999JD900496).
- Griesche, H. J. et al.: Application of the shipborne remote sensing supersite OCEANET for profiling of Arctic aerosols and clouds during *Polarstern* cruise PS106. In: *Atmospheric Measurement Techniques* 13.10, 2020, pp. 5335–5358. DOI: [10.5194/amt-13-5335-2020](https://doi.org/10.5194/amt-13-5335-2020).
- Gröbner, J., Reda, I., Wacker, S., Nyeki, S., Behrens, K., and Gorman, J.: A new absolute reference for atmospheric longwave irradiance measurements with trace-

- ability to SI units. In: *Journal of Geophysical Research: Atmospheres* 119.12, 2014, pp. 7083–7090. DOI: [10.1002/2014JD021630](https://doi.org/10.1002/2014JD021630).
- Gröbner, J. and Wacker, S.: Pyrgeometer Calibration Procedure at the PMOD/WRC-IRS. In: World Meteorological Organization, 2015.
- Gupta, S. K., Kratz, D. P., Stackhouse Paul W., J., Wilber, A. C., Zhang, T., and Sothcott, V. E.: Improvement of Surface Longwave Flux Algorithms Used in CERES Processing. In: *Journal of Applied Meteorology and Climatology* 49.7, 2010, pp. 1579–1589. DOI: [10.1175/2010JAMC2463.1](https://doi.org/10.1175/2010JAMC2463.1).
- Hanschmann, T., Deneke, H., Roebeling, R., and Macke, A.: Evaluation of the short-wave cloud radiative effect over the ocean by use of ship and satellite observations. In: *Atmospheric Chemistry and Physics* 12.24, 2012, pp. 12243–12253. DOI: [10.5194/acp-12-12243-2012](https://doi.org/10.5194/acp-12-12243-2012).
- Hansell, R. I. C., Malcolm, J. R., Welch, H., Jefferies, R. L., and Scott, P. A.: Atmospheric Change and Biodiversity in the Arctic. In: *Environmental Monitoring and Assessment* 49.2, 1998, pp. 303–325. DOI: [10.1023/A:1005807212017](https://doi.org/10.1023/A:1005807212017).
- He, M., Hu, Y., N., C., D., W., J, H., and K., S.: High cloud coverage over melted areas dominates the impact of clouds on the albedo feedback in the Arctic. In: *Scientific Reports* 9, 2019. DOI: [10.1038/s41598-019-44155-w](https://doi.org/10.1038/s41598-019-44155-w).
- Hersbach, H. et al.: The ERA5 global reanalysis. In: *Quarterly Journal of the Royal Meteorological Society* 146.730, 2020, pp. 1999–2049. DOI: [10.1002/qj.3803](https://doi.org/10.1002/qj.3803).
- Hogan, R. and Connor, E.: Facilitating cloud radar and lidar algorithms: the Cloudnet Instrument Synergy/Target Categorization product. In: 2004.
- Hogan, R., Mittermaier, M. P., and Illingworth, A. J.: The Retrieval of Ice Water Content from Radar Reflectivity Factor and Temperature and Its Use in Evaluating a Mesoscale Model. In: *Journal of Applied Meteorology and Climatology* 45.2, 2006, pp. 301–317. DOI: [10.1175/JAM2340.1](https://doi.org/10.1175/JAM2340.1).
- Hori, M. et al.: In-situ measured spectral directional emissivity of snow and ice in the 8–14 μm atmospheric window. In: *Remote Sensing of Environment* 100.4, 2006, pp. 486–502. DOI: [10.1016/j.rse.2005.11.001](https://doi.org/10.1016/j.rse.2005.11.001).
- Hu, Y. X. and Stamnes, K.: An Accurate Parameterization of the Radiative Properties of Water Clouds Suitable for Use in Climate Models. In: *Journal Climate* 6.4, 1993, pp. 728–742. DOI: [10.1175/1520-0442\(1993\)006<0728:AAPOTR>2.0.CO;2](https://doi.org/10.1175/1520-0442(1993)006<0728:AAPOTR>2.0.CO;2).
- Huang, Y., Dong, X., Xi, B., Dolinar, E. K., Stanfield, R. E., and Qiu, S.: Quantifying the Uncertainties of Reanalyzed Arctic Cloud and Radiation Properties Using Satellite Surface Observations. In: *Journal Climate* 30.19, 2017, pp. 8007–8029. DOI: [10.1175/JCLI-D-16-0722.1](https://doi.org/10.1175/JCLI-D-16-0722.1).
- Illingworth, A. J. et al.: Cloudnet. In: *Bulletin of the American Meteorological Society* 88.6, 2007, pp. 883–898. DOI: [10.1175/BAMS-88-6-883](https://doi.org/10.1175/BAMS-88-6-883).

- Intrieri, J. M., Fairall, C. W., Shupe, M. D., Persson, P. O. G., Andreas, E. L., Guest, P. S., and Moritz, R. E.: An annual cycle of Arctic surface cloud forcing at SHEBA. In: *Journal of Geophysical Research: Oceans* 107.C10, 2002, SHE 13-1-SHE 13–14. DOI: [10.1029/2000JC000439](https://doi.org/10.1029/2000JC000439).
- Intrieri, J. M., Shupe, M. D., Uttal, T., and McCarty, B. J.: An annual cycle of Arctic cloud characteristics observed by radar and lidar at SHEBA. In: *Journal of Geophysical Research: Oceans* 107.C10, 2002, SHE 5-1-SHE 5–15. DOI: [10.1029/2000JC000423](https://doi.org/10.1029/2000JC000423).
- IPCC.: *Climate Change 2021: The Physical Science Basis. Contribution of Working Group I to the Sixth Assessment Report of the Intergovernmental Panel on Climate Change*. Cambridge, United Kingdom and New York, NY, USA: Cambridge University Press, 2021.
- Jahangir, E., Libois, Q., Couvreur, F., Vié, B., and Saint-Martin, D.: Uncertainty of SW Cloud Radiative Effect in Atmospheric Models Due to the Parameterization of Liquid Cloud Optical Properties. In: *Journal of Advances in Modeling Earth Systems* 13.12, 2021. e2021MS002742 2021MS002742, e2021MS002742. DOI: <https://doi.org/10.1029/2021MS002742>.
- Johannessen, O. M. et al.: Arctic climate change: observed and modelled temperature and sea-ice variability. In: *Tellus A: Dynamic Meteorology and Oceanography* 56.4, 2004, pp. 328–341. DOI: [10.3402/tellusa.v56i4.14418](https://doi.org/10.3402/tellusa.v56i4.14418).
- Kalisch, J. and Macke, A.: Radiative budget and cloud radiative effect over the Atlantic from ship-based observations. In: *Atmospheric Measurement Techniques* 5.10, 2012, pp. 2391–2401. DOI: [10.5194/amt-5-2391-2012](https://doi.org/10.5194/amt-5-2391-2012).
- Kanitz, T., Ansmann, A., Engelmann, R., and Althausen, D.: North-south cross sections of the vertical aerosol distribution over the Atlantic Ocean from multiwavelength Raman/polarization lidar during Polarstern cruises. In: *Journal of Geophysical Research: Atmospheres* 118.6, 2013, pp. 2643–2655. DOI: [10.1002/jgrd.50273](https://doi.org/10.1002/jgrd.50273).
- Kashiwase, H., Ohshima, K., Nihashi, S., and Eicken, H.: Evidence for ice-ocean albedo feedback in the Arctic Ocean shifting to a seasonal ice zone. In: *Scientific Reports* 7, 2017. DOI: [10.1038/s41598-017-08467-z](https://doi.org/10.1038/s41598-017-08467-z).
- Kato, S. et al.: Surface Irradiances of Edition 4.0 Clouds and the Earth’s Radiant Energy System (CERES) Energy Balanced and Filled (EBAF) Data Product. In: *Journal Climate* 31.11, 2018, pp. 4501–4527. DOI: [10.1175/JCLI-D-17-0523.1](https://doi.org/10.1175/JCLI-D-17-0523.1).
- Kay, J. E. and L’Ecuyer, T.: Observational constraints on Arctic Ocean clouds and radiative fluxes during the early 21st century. In: *Journal of Geophysical Research: Atmospheres* 118.13, 2013, pp. 7219–7236. DOI: [10.1002/jgrd.50489](https://doi.org/10.1002/jgrd.50489).
- Kay, J. E., L’Ecuyer, T., Chepfer, H., Loeb, N., Morrison, A., and Cesana, G.: Recent Advances in Arctic Cloud and Climate Research. In: *Current Climate Change Reports* 2.4, 2016, pp. 159–169. DOI: [10.1007/s40641-016-0051-9](https://doi.org/10.1007/s40641-016-0051-9).

- Kay, J. E., L'Ecuyer, T., Gettelman, A., Stephens, G., and O'Dell, C.: The contribution of cloud and radiation anomalies to the 2007 Arctic sea ice extent minimum. In: *Geophysical Research Letters - GEOPHYS RES LETT* 35, 2008. DOI: [10.1029/2008GL033451](https://doi.org/10.1029/2008GL033451).
- Kay, J. E., Raeder, K., Gettelman, A., and Anderson, J.: The Boundary Layer Response to Recent Arctic Sea Ice Loss and Implications for High-Latitude Climate Feedbacks. In: *Journal Climate* 24.2, 2011, pp. 428–447. DOI: [10.1175/2010JCLI3651.1](https://doi.org/10.1175/2010JCLI3651.1).
- Key, J.: Streamer user's guide. In: *Tech. Rep.*, 1996, pp. 96–01, 85.
- Knudsen, E. M. et al.: Meteorological conditions during the ACLOUD/PASCAL field campaign near Svalbard in early summer 2017. In: *Atmospheric Chemistry and Physics* 18.24, 2018, pp. 17995–18022. DOI: [10.5194/acp-18-17995-2018](https://doi.org/10.5194/acp-18-17995-2018).
- Kopp, G. and Lean, J. L.: A new, lower value of total solar irradiance: Evidence and climate significance. In: *Geophysical Research Letters* 38.1, 2011. DOI: [10.1029/2010GL045777](https://doi.org/10.1029/2010GL045777).
- Lanconelli, C., Busetto, M., Dutton, E. G., König-Langlo, G., Maturilli, M., Sieger, R., Vitale, V., and Yamanouchi, T.: Polar baseline surface radiation measurements during the International Polar Year 2007–2009. In: *Earth System Science Data* 3.1, 2011, pp. 1–8. DOI: [10.5194/essd-3-1-2011](https://doi.org/10.5194/essd-3-1-2011).
- Light, B., Grenfell, T. C., and Perovich, D. K.: Transmission and absorption of solar radiation by Arctic sea ice during the melt season. In: *Journal of Geophysical Research: Oceans* 113.C3, 2008. DOI: [10.1029/2006JC003977](https://doi.org/10.1029/2006JC003977).
- Loeb, N. and Wielicki, B.: SATELLITES AND SATELLITE REMOTE SENSING Earth's Radiation Budget. In: *Encyclopedia of Atmospheric Sciences*, 2015, pp. 67–76. DOI: [10.1016/b978-0-12-382225-3.00349-2](https://doi.org/10.1016/b978-0-12-382225-3.00349-2).
- Loeb, N. G. et al.: Clouds and the Earth's Radiant Energy System (CERES) Energy Balanced and Filled (EBAF) Top-of-Atmosphere (TOA) Edition-4.0 Data Product. In: *Journal of Climate* 31.2, 2018, pp. 895–918. DOI: [10.1175/JCLI-D-17-0208.1](https://doi.org/10.1175/JCLI-D-17-0208.1).
- Lohmann, G. M. and Monahan, A. H.: Effects of temporal averaging on short-term irradiance variability under mixed sky conditions. In: *Atmospheric Measurement Techniques* 11.5, 2018, pp. 3131–3144. DOI: [10.5194/amt-11-3131-2018](https://doi.org/10.5194/amt-11-3131-2018).
- Lohmann, G. M., Monahan, A. H., and Heinemann, D.: Local short-term variability in solar irradiance. In: *Atmospheric Chemistry and Physics* 16.10, 2016, pp. 6365–6379. DOI: [10.5194/acp-16-6365-2016](https://doi.org/10.5194/acp-16-6365-2016).
- Löhnert, U. and Crewell, S.: Accuracy of cloud liquid water path from ground-based microwave radiometry 1. Dependency on cloud model statistics. In: *Radio Science* 38.3, 2003. DOI: [10.1029/2002RS002654](https://doi.org/10.1029/2002RS002654).

- Mace, G. G., Benson, S., and Kato, S.: Cloud radiative forcing at the Atmospheric Radiation Measurement Program Climate Research Facility: 2. Vertical redistribution of radiant energy by clouds. In: *Journal of Geophysical Research: Atmospheres* 111.D11, 2006. DOI: [10.1029/2005JD005922](https://doi.org/10.1029/2005JD005922).
- Macke, A.: The Expedition of the Research Vessel “Polarstern” to the Antarctic in 2008 (ANT-XXIV/4). In: *Berichte zur Polar- und Meeresforschung – Reports on Polar and Marine Research*, 591, 2009.
- Macke, A. and Flores, H.: The Expeditions PS106/1 and 2 of the Research Vessel POLARSTERN to the Arctic Ocean in 2017. In: *Berichte zur Polar und Meeresforschung* 714, 2018. DOI: [10.2312/BzPM_0714_2017](https://doi.org/10.2312/BzPM_0714_2017).
- Macke, A. et al.: The HD(CP)² Observational Prototype Experiment (HOPE) – an overview. In: *Atmospheric Chemistry and Physics* 17.7, 2017, pp. 4887–4914. DOI: [10.5194/acp-17-4887-2017](https://doi.org/10.5194/acp-17-4887-2017).
- Macke, A., Francis, P. N., McFarquhar, G. M., and Kinne, S.: The Role of Ice Particle Shapes and Size Distributions in the Single Scattering Properties of Cirrus Clouds. In: *Journal of the Atmospheric Sciences* 55.17, 1998, pp. 2874–2883. DOI: [10.1175/1520-0469\(1998\)055<2874:TR0IPS>2.0.CO;2](https://doi.org/10.1175/1520-0469(1998)055<2874:TR0IPS>2.0.CO;2).
- Madhavan, B. L., Deneke, H., Witthuhn, J., and Macke, A.: Multiresolution analysis of the spatiotemporal variability in global radiation observed by a dense network of 99 pyranometers. In: *Atmospheric Chemistry and Physics* 17.5, 2017, pp. 3317–3338. DOI: [10.5194/acp-17-3317-2017](https://doi.org/10.5194/acp-17-3317-2017).
- Madhavan, B. L., Kalisch, J., and Macke, A.: Shortwave surface radiation network for observing small-scale cloud inhomogeneity fields. In: *Atmospheric Measurement Techniques* 9.3, 2016, pp. 1153–1166. DOI: [10.5194/amt-9-1153-2016](https://doi.org/10.5194/amt-9-1153-2016).
- Manabe, S. and Stouffer, R. J.: Sensitivity of a global climate model to an increase of CO₂ concentration in the atmosphere. In: *Journal of Geophysical Research: Oceans* 85.C10, 1980, pp. 5529–5554. DOI: [10.1029/JC085iC10p05529](https://doi.org/10.1029/JC085iC10p05529).
- Manabe, S. and Wetherald, R. T.: The Effects of Doubling the CO₂ Concentration on the climate of a General Circulation Model. In: *Journal of Atmospheric Sciences* 32.1, 1975, pp. 3–15. DOI: [10.1175/1520-0469\(1975\)032<0003:TEODTC>2.0.CO;2](https://doi.org/10.1175/1520-0469(1975)032<0003:TEODTC>2.0.CO;2).
- Marchand, R., Ackerman, T., Westwater, E. R., Clough, S. A., Cady-Pereira, K., and Liljegren, J. C.: An assessment of microwave absorption models and retrievals of cloud liquid water using clear-sky data. In: *Journal of Geophysical Research: Atmospheres* 108.D24, 2003. DOI: [10.1029/2003JD003843](https://doi.org/10.1029/2003JD003843).
- Markowicz, K., Lisok, J., and Xian, P.: Simulation of long-term direct aerosol radiative forcing over the arctic within the framework of the iAREA project. In: *Atmospheric Environment* 244, 2021, p. 117882.

- Marshak, A. and Davis, A.: 3D radiative transfer in cloudy atmospheres. Springer Science & Business Media, 2005.
- Maturilli and Ebell.: Twenty-five years of cloud base height measurements by ceilometer in Ny-Ålesund, Svalbard. In: *Earth System Science Data* 10.3, 2018, pp. 1451–1456. DOI: [10.5194/essd-10-1451-2018](https://doi.org/10.5194/essd-10-1451-2018).
- McArthur, L. J. B.: Baseline Surface Radiation Network (BSRN). Manual. 2005. DOI: [10.1594/PANGAEA.900442](https://doi.org/10.1594/PANGAEA.900442).
- Meredith, M. et al.: Polar Regions. In: *IPCC Special Report on the Ocean and Cryosphere in a Changing Climate*. [H.-O. Pörtner, D.C. Roberts, V. Masson-Delmotte, P. Zhai, M. Tignor, E. Poloczanska, K. Mintenbeck, A. Alegría, M. Nicolai, A. Okem, J. Petzold, B. Rama, N.M. Weyer (eds.)]In press., 2019.
- Miller, G. H., Alley, R. B., Brigham-Grette, J., Fitzpatrick, J. J., Polyak, L., Serreze, M. C., and White, J. W.: Arctic amplification: can the past constrain the future? In: *Quaternary Science Reviews* 29.15-16, 2010, pp. 1779–1790.
- Miller, N. B., Shupe, M. D., Cox, C. J., Walden, V. P., Turner, D. D., and Steffen, K.: Cloud Radiative Forcing at Summit, Greenland. In: *Journal Climate* 28.15, 2015, pp. 6267–6280. DOI: [10.1175/JCLI-D-15-0076.1](https://doi.org/10.1175/JCLI-D-15-0076.1).
- Minnett, P. J.: The Influence of Solar Zenith Angle and Cloud Type on Cloud Radiative Forcing at the Surface in the Arctic. In: *Journal Climate* 12.1, 1999, pp. 147–158. DOI: [10.1175/1520-0442\(1999\)012<0147:TIOSZA>2.0.CO;2](https://doi.org/10.1175/1520-0442(1999)012<0147:TIOSZA>2.0.CO;2).
- Minnis, P. et al.: CERES MODIS Cloud Product Retrievals for Edition 4–Part I: Algorithm Changes. In: *IEEE Transactions on Geoscience and Remote Sensing*, 2020, pp. 1–37.
- Minnis, P., Sun-Mack, S., Smith Jr, W. L., Hong, G., and Chen, Y.: Advances in neural network detection and retrieval of multilayer clouds for CERES using multispectral satellite data. In: *Remote Sensing of Clouds and the Atmosphere XXIV*. Vol. 11152. International Society for Optics and Photonics. 2019, p. 1115202.
- Mlawer, E. J., Taubman, S. J., Brown, P. D., Iacono, M. J., and Clough, S. A.: Radiative transfer for inhomogeneous atmospheres: RRTM, a validated correlated-k model for the longwave. In: *Journal of Geophysical Research: Atmospheres* 102.D14, 1997, pp. 16663–16682. DOI: [10.1029/97JD00237](https://doi.org/10.1029/97JD00237).
- Morrison, A. L., Kay, J. E., Chepfer, H., Guzman, R., and Yettella, V.: Isolating the Liquid Cloud Response to Recent Arctic Sea Ice Variability Using Spaceborne Lidar Observations. In: *Journal of Geophysical Research: Atmospheres* 123.1, 2018, pp. 473–490. DOI: <https://doi.org/10.1002/2017JD027248>.
- Morrison, H., Boer, G. de, Feingold, G., Harrington, J., Shupe, M. D., and Sulia, K.: Resilience of persistent Arctic mixed-phase clouds. In: *Nature Geoscience* 5, 2012. DOI: [10.1038/ngeo1332](https://doi.org/10.1038/ngeo1332).

- Nann, S. and Riordan, C.: Solar Spectral Irradiance under Clear and Cloudy Skies: Measurements and a Semiempirical Model. In: *Journal of Applied Meteorology and Climatology* 30.4, 1991, pp. 447–462. DOI: [10.1175/1520-0450\(1991\)030<0447:SSIUCA>2.0.CO;2](https://doi.org/10.1175/1520-0450(1991)030<0447:SSIUCA>2.0.CO;2).
- Neggers, R. A. J., Chylik, J., Egerer, U., Griesche, H., Schemann, V., Seifert, P., Siebert, H., and Macke, A.: Local and Remote Controls on Arctic Mixed-Layer Evolution. In: *Journal of Advances in Modeling Earth Systems* 11.7, 2019, pp. 2214–2237. DOI: <https://doi.org/10.1029/2019MS001671>.
- Nicolaus, M., Katlein, C., Maslanik, J., and Hendricks, S.: Changes in Arctic sea ice result in increasing light transmittance and absorption. In: *Geophysical Research Letters* 39.24, 2012. DOI: [10.1029/2012GL053738](https://doi.org/10.1029/2012GL053738).
- Nomokonova, T., Ebell, K., Löhnert, U., Maturilli, M., and Ritter, C.: The influence of water vapor anomalies on clouds and their radiative effect at Ny-Ålesund. In: *Atmospheric Chemistry and Physics* 20.8, 2020, pp. 5157–5173. DOI: [10.5194/acp-20-5157-2020](https://doi.org/10.5194/acp-20-5157-2020).
- Nomokonova, T., Ebell, K., Löhnert, U., Maturilli, M., Ritter, C., and O’Connor, E.: Statistics on clouds and their relation to thermodynamic conditions at Ny-Ålesund using ground-based sensor synergy. In: *Atmospheric Chemistry and Physics* 19.6, 2019, pp. 4105–4126. DOI: [10.5194/acp-19-4105-2019](https://doi.org/10.5194/acp-19-4105-2019).
- Nussbaumer, E. A. and Pinker, R. T.: The role of shortwave radiation in the 2007 Arctic sea ice anomaly. In: *Geophysical Research Letters* 39.15, 2012. DOI: [10.1029/2012GL052415](https://doi.org/10.1029/2012GL052415).
- NWS CPC, A. index.: Arctic Oscillation index from the National Weather Service - Climate Prediction Center at NOAA. Last access: May 30. 2021.
- Olsen, M. S. et al.: The Changing Arctic Cryosphere and Likely Consequences: An Overview. In: *AMBIO* 40.1, 2011, pp. 111–118. DOI: [10.1007/s13280-011-0220-y](https://doi.org/10.1007/s13280-011-0220-y).
- Overland, J., Francis, J. A., Hall, R., Hanna, E., Kim, S.-J., and Vihma, T.: The melting Arctic and midlatitude weather patterns: Are they connected? In: *Journal Climate* 28.20, 2015, pp. 7917–7932.
- Palm, S. P., Strey, S. T., Spinhirne, J., and Markus, T.: Influence of Arctic sea ice extent on polar cloud fraction and vertical structure and implications for regional climate. In: *Journal of Geophysical Research: Atmospheres* 115.D21, 2010. DOI: [10.1029/2010JD013900](https://doi.org/10.1029/2010JD013900).
- Percival, D. P.: On estimation of the wavelet variance. In: *Biometrika* 82.3, 1995, pp. 619–631. DOI: [10.1093/biomet/82.3.619](https://doi.org/10.1093/biomet/82.3.619).
- Perovich, D. K.: Sunlight, clouds, sea ice, albedo, and the radiative budget: the umbrella versus the blanket. In: *The Cryosphere* 12.6, 2018, pp. 2159–2165. DOI: [10.5194/tc-12-2159-2018](https://doi.org/10.5194/tc-12-2159-2018).

- Petty, G. W.: A first course in atmospheric radiation. 2nd ed. Madison, Wis: Sundog Pub, 2006.
- Pinker, R. T., Niu, X., and Ma, Y.: Solar heating of the Arctic Ocean in the context of ice-albedo feedback. In: *Journal of Geophysical Research: Oceans* 119.12, 2014, pp. 8395–8409. DOI: [10.1002/2014JC010232](https://doi.org/10.1002/2014JC010232).
- Pithan, F. and Mauritsen, T.: Arctic amplification dominated by temperature feedbacks in contemporary climate models. In: *Nature Geoscience* 7.3, 2014, pp. 181–184. DOI: [10.1038/ngeo2071](https://doi.org/10.1038/ngeo2071).
- Polyakov, I. V. et al.: Arctic Ocean Warming Contributes to Reduced Polar Ice Cap. In: *Journal of Physical Oceanography* 40.12, 2010, pp. 2743–2756. DOI: [10.1175/2010JP04339.1](https://doi.org/10.1175/2010JP04339.1).
- Previdi, M., Smith, K. L., and Polvani, L. M.: Arctic amplification of climate change: a review of underlying mechanisms. In: *Environmental Research Letters* 16.9, 2021, p. 093003. DOI: [10.1088/1748-9326/ac1c29](https://doi.org/10.1088/1748-9326/ac1c29).
- Proshutinsky, A., Pavlov, V., and Bourke, R. H.: Sea level rise in the Arctic Ocean. In: *Geophysical Research Letters* 28.11, 2001, pp. 2237–2240. DOI: [10.1029/2000GL012760](https://doi.org/10.1029/2000GL012760).
- Randel, W. J. and Wu, F.: Cooling of the Arctic and Antarctic polar stratospheres due to ozone depletion. In: *Journal of Climate* 12.5, 1999, pp. 1467–1479.
- Rastak, N. et al.: Seasonal variation of aerosol water uptake and its impact on the direct radiative effect at Ny-Ålesund, Svalbard. In: *Atmospheric Chemistry and Physics* 14.14, 2014, pp. 7445–7460. DOI: [10.5194/acp-14-7445-2014](https://doi.org/10.5194/acp-14-7445-2014).
- Rigor, I. G., Wallace, J. M., and Colony, R. L.: Response of Sea Ice to the Arctic Oscillation. In: *Journal Climate* 15.18, 2002, pp. 2648–2663. DOI: [10.1175/1520-0442\(2002\)015<2648:ROSITT>2.0.CO;2](https://doi.org/10.1175/1520-0442(2002)015<2648:ROSITT>2.0.CO;2).
- Riihelä, A., Key, J. R., Meirink, J. F., Kuipers Munneke, P., Palo, T., and Karlsson, K.-G.: An intercomparison and validation of satellite-based surface radiative energy flux estimates over the Arctic. In: *Journal of Geophysical Research: Atmospheres* 122.9, 2017, pp. 4829–4848. DOI: [10.1002/2016JD026443](https://doi.org/10.1002/2016JD026443).
- Rinke, A. et al.: Trends of vertically integrated water vapor over the Arctic during 1979–2016: Consistent moistening all over? In: *Journal of Climate* 32.18, 2019, pp. 6097–6116.
- Rose, F. G., Rutan, D. A., Charlock, T., Smith, G. L., and Kato, S.: An Algorithm for the Constraining of Radiative Transfer Calculations to CERES-Observed Broadband Top-of-Atmosphere Irradiance. In: *Journal of Atmospheric and Oceanic Technology* 30.6, 2013, pp. 1091–1106. DOI: [10.1175/JTECH-D-12-00058.1](https://doi.org/10.1175/JTECH-D-12-00058.1).

- Rozwadowska, A. and Cahalan, R. F.: Plane-parallel biases computed from inhomogeneous Arctic clouds and sea ice. In: *Journal of Geophysical Research: Atmospheres* 107.D19, 2002, AAC 8-1-AAC 8–17. DOI: [10.1029/2002JD002092](https://doi.org/10.1029/2002JD002092).
- Rutan, D. A., Kato, S., Doelling, D. R., Rose, F. G., Nguyen, L. T., Caldwell, T. E., and Loeb, N. G.: CERES Synoptic Product: Methodology and Validation of Surface Radiant Flux. In: *Journal of Atmospheric and Oceanic Technology* 32.6, 2015, pp. 1121–1143. DOI: [10.1175/JTECH-D-14-00165.1](https://doi.org/10.1175/JTECH-D-14-00165.1).
- Saloranta, T. M.: Modeling the evolution of snow, snow ice and ice in the Baltic Sea. In: *Tellus A* 52.1, 2000, pp. 93–108. DOI: [10.1034/j.1600-0870.2000.520107.x](https://doi.org/10.1034/j.1600-0870.2000.520107.x).
- Salzmann, M.: The polar amplification asymmetry: role of Antarctic surface height. In: *Earth System Dynamics* 8.2, 2017, pp. 323–336. DOI: [10.5194/esd-8-323-2017](https://doi.org/10.5194/esd-8-323-2017).
- Schade, N., Macke, A., Sandmann, H., and Stick, C.: Enhanced solar global irradiance during cloudy sky conditions. In: *Meteorologische Zeitschrift* 16, 2007, pp. 295–303. DOI: [10.1127/0941-2948/2007/0206](https://doi.org/10.1127/0941-2948/2007/0206).
- Scheirer, R. and Macke, A.: Cloud inhomogeneity and broadband solar fluxes. In: *Journal of Geophysical Research: Atmospheres* 108.D19, 2003. DOI: <https://doi.org/10.1029/2002JD003321>.
- Schmidt, I. K., Jonasson, S., Shaver, G. R., Michelsen, A., and Nordin, A.: Mineralization and distribution of nutrients in plants and microbes in four arctic ecosystems: Responses to warming. In: *Plant and Soil* 242.1, 2002, pp. 93–106. DOI: [10.1023/A:1019642007929](https://doi.org/10.1023/A:1019642007929).
- Schuster, A.: Radiation through a foggy atmosphere. In: *The astrophysical journal* 21, 1905, p. 1.
- Schuur et al.: Climate change and the permafrost carbon feedback. In: *Nature* 520.7546, 2015, pp. 171–179. DOI: [10.1038/nature14338](https://doi.org/10.1038/nature14338).
- Schweiger, A. J., Lindsay, R. W., Vavrus, S., and Francis, J. A.: Relationships between Arctic Sea Ice and Clouds during Autumn. In: *Journal Climate* 21.18, 2008, pp. 4799–4810. DOI: [10.1175/2008JCLI2156.1](https://doi.org/10.1175/2008JCLI2156.1).
- Screen, J. A. and Simmonds, I.: The central role of diminishing sea ice in recent Arctic temperature amplification. In: *Nature* 464.D18, 2010. DOI: [10.1038/nature09051](https://doi.org/10.1038/nature09051).
- Sedlar, J. and Devasthale, A.: Clear-sky thermodynamic and radiative anomalies over a sea ice sensitive region of the Arctic. In: *Journal of Geophysical Research Atmospheres* 117.19, 2012, pp. 1–11. DOI: [10.1029/2012JD017754](https://doi.org/10.1029/2012JD017754).
- Sedlar, J. et al.: A transitioning Arctic surface energy budget: The impacts of solar zenith angle, surface albedo and cloud radiative forcing. In: *Climate Dynamics*, v.11 (2010) 37, 2010. DOI: [10.1007/s00382-010-0937-5](https://doi.org/10.1007/s00382-010-0937-5).

- Serreze, M. C. and Barry, R. G.: Processes and impacts of Arctic amplification: A research synthesis. In: *Global and Planetary Change* 77.1, 2011, pp. 85–96. DOI: [10.1016/j.gloplacha.2011.03.004](https://doi.org/10.1016/j.gloplacha.2011.03.004).
- Serreze, M. C. and Francis, J. A.: The Arctic Amplification Debate. In: *Climate Change* 76, 2006, pp. 241–264. DOI: [10.1007/s10584-005-9017-y](https://doi.org/10.1007/s10584-005-9017-y).
- Serreze, M. C., Holland, M. M., and Stroeve, J.: Perspectives on the Arctic’s Shrinking Sea-Ice Cover. In: *Science* 315.5818, 2007, pp. 1533–1536. DOI: [10.1126/science.1139426](https://doi.org/10.1126/science.1139426).
- Shakhova, N. et al.: Ebullition and storm-induced methane release from the East Siberian Arctic Shelf. In: *Nature Geoscience* 7.1, 2014, pp. 64–70.
- Shupe, M. D.: Clouds at Arctic Atmospheric Observatories. Part II: Thermodynamic Phase Characteristics. In: *Journal of Applied Meteorology and Climatology* 50.3, 2011, pp. 645–661. DOI: [10.1175/2010JAMC2468.1](https://doi.org/10.1175/2010JAMC2468.1).
- Shupe, M. D. and Intrieri, J. M.: Cloud Radiative Forcing of the Arctic Surface: The Influence of Cloud Properties, Surface Albedo, and Solar Zenith Angle. In: *Journal Climate* 17.3, 2004, pp. 616–628. DOI: [10.1175/1520-0442\(2004\)017<0616:CRFOTA>2.0.CO;2](https://doi.org/10.1175/1520-0442(2004)017<0616:CRFOTA>2.0.CO;2).
- Shupe, M. D., Matrosov, S. Y., and Uttal, T.: Arctic Mixed-Phase Cloud Properties Derived from Surface-Based Sensors at SHEBA. In: *Journal of the Atmospheric Sciences* 63.2, 2006, pp. 697–711. DOI: [10.1175/JAS3659.1](https://doi.org/10.1175/JAS3659.1).
- Shupe, M. D., Turner, D. D., Zwink, A., Thieman, M. M., Mlawer, E. J., and Shippert, T.: Deriving Arctic Cloud Microphysics at Barrow, Alaska: Algorithms, Results, and Radiative Closure. In: *Journal of Applied Meteorology and Climatology* 54.7, 2015, pp. 1675–1689. DOI: [10.1175/JAMC-D-15-0054.1](https://doi.org/10.1175/JAMC-D-15-0054.1).
- Shupe, M. D., Uttal, T., and Matrosov, S. Y.: Arctic Cloud Microphysics Retrievals from Surface-Based Remote Sensors at SHEBA. In: *Journal of Applied Meteorology* 44.10, 2005, pp. 1544–1562. DOI: [10.1175/JAM2297.1](https://doi.org/10.1175/JAM2297.1).
- Shupe, M. D., Walden, V. P., Eloranta, E., Uttal, T., Campbell, J. R., Starkweather, S. M., and Shiobara, M.: Clouds at Arctic Atmospheric Observatories. Part I: Occurrence and Macrophysical Properties. In: *Journal of Applied Meteorology and Climatology* 50.3, 2011, pp. 626–644. DOI: [10.1175/2010JAMC2467.1](https://doi.org/10.1175/2010JAMC2467.1).
- Shupe, M. D. et al.: Overview of the MOSAiC expedition—Atmosphere. In: *Elementa: Science of the Anthropocene* 10.1, 2022. 00060. DOI: [10.1525/elementa.2021.00060](https://doi.org/10.1525/elementa.2021.00060).
- Slagstad, D., Ellingsen, I., and Wassmann, P.: Evaluating primary and secondary production in an Arctic Ocean void of summer sea ice: An experimental simulation approach. In: *Progress in Oceanography* 90, 2011, pp. 117–131. DOI: [10.1016/j.pocean.2011.02.009](https://doi.org/10.1016/j.pocean.2011.02.009).

- Soden, B. J., Held, I. M., Colman, R., Shell, K. M., Kiehl, J. T., and Shields, C. A.: Quantifying Climate Feedbacks Using Radiative Kernels. In: *Journal Climate* 21.14, 2008, pp. 3504–3520. DOI: [10.1175/2007JCLI2110.1](https://doi.org/10.1175/2007JCLI2110.1).
- Sotiropoulou, G. et al.: Atmospheric Conditions during the Arctic Clouds in Summer Experiment (ACSE): Contrasting Open Water and Sea Ice Surfaces during Melt and Freeze-Up Seasons. In: *Journal Climate* 29.24, 2016, pp. 8721–8744. DOI: [10.1175/JCLI-D-16-0211.1](https://doi.org/10.1175/JCLI-D-16-0211.1).
- Stapf, J., Ehrlich, A., Jäkel, E., Lüpkes, C., and Wendisch, M.: Reassessment of shortwave surface cloud radiative forcing in the Arctic: consideration of surface-albedo–cloud interactions. In: *Atmospheric Chemistry and Physics* 20.16, 2020, pp. 9895–9914. DOI: [10.5194/acp-20-9895-2020](https://doi.org/10.5194/acp-20-9895-2020).
- Reassessment of the common concept to derive the surface cloud radiative forcing in the Arctic: Consideration of surface albedo – cloud interactions. In: *Atmospheric Chemistry and Physics Discussions* 2019, 2019, pp. 1–24. DOI: [10.5194/acp-2019-534](https://doi.org/10.5194/acp-2019-534).
- Stapf, J., Ehrlich, A., Lüpkes, C., and Wendisch, M.: Radiative energy budget and cloud radiative forcing in the daytime marginal sea ice zone during Arctic spring and summer. In: *Atmospheric Chemistry and Physics Discussions* 2021, 2021, pp. 1–43. DOI: [10.5194/acp-2021-279](https://doi.org/10.5194/acp-2021-279).
- Stroeve, J., Serreze, M., Drobot, S., Gearheard, S., Holland, M., Maslanik, J., Meier, W., and Scambos, T.: Arctic Sea Ice Extent Plummet in 2007. In: *Eos, Transactions American Geophysical Union* 89.2, 2008, pp. 13–14. DOI: [10.1029/2008E0020001](https://doi.org/10.1029/2008E0020001).
- Stuecker, M. F. et al.: Polar amplification dominated by local forcing and feedbacks. In: *Nat. Climate Change* 8, 2018, pp. 1076–1081. DOI: [10.1038/s41558-018-0339-y](https://doi.org/10.1038/s41558-018-0339-y).
- Sun-Mack, S., Chen, Y., Arduini, R., and Minnis, P.: Clear-sky narrowband albedo variations derived from VIRS and MODIS data. In: *13th Conference on Satellite Meteorology and Oceanography*, 2006, p. 6.
- Tan, I. and Storelvmo, T.: Evidence of Strong Contributions From Mixed-Phase Clouds to Arctic Climate Change. In: *Geophysical Research Letters* 46.5, 2019, pp. 2894–2902. DOI: [10.1029/2018GL081871](https://doi.org/10.1029/2018GL081871).
- Taylor, P. C., Cai, M., Hu, A., Meehl, J., Washington, W., and Zhang, G. J.: A Decomposition of Feedback Contributions to Polar Warming Amplification. In: *Journal of Climate* 26.18, 2013, pp. 7023–7043. DOI: [10.1175/JCLI-D-12-00696.1](https://doi.org/10.1175/JCLI-D-12-00696.1).
- Taylor, P. C. et al.: Process Drivers, Inter-Model Spread, and the Path Forward: A Review of Amplified Arctic Warming. In: *Frontiers in Earth Science* 9, 2022. DOI: [10.3389/feart.2021.758361](https://doi.org/10.3389/feart.2021.758361).

- Thompson, D. W. J. and Wallace, J. M.: The Arctic oscillation signature in the wintertime geopotential height and temperature fields. In: *Geophysical Research Letters* 25.9, 1998, pp. 1297–1300. DOI: [10.1029/98GL00950](https://doi.org/10.1029/98GL00950).
- Tjernström, M. and Graversen, R. G.: The vertical structure of the lower Arctic troposphere analysed from observations and the ERA-40 reanalysis. In: *Quarterly Journal of the Royal Meteorological Society* 135.639, 2009, pp. 431–443. DOI: [10.1002/qj.380](https://doi.org/10.1002/qj.380).
- Tjernström, M., Shupe, M. D., Brooks, I. M., Achtert, P., Prytherch, J., and Sedlar, J.: Arctic Summer Airmass Transformation, Surface Inversions, and the Surface Energy Budget. In: *Journal Climate* 32.3, 2019, pp. 769–789. DOI: [10.1175/JCLI-D-18-0216.1](https://doi.org/10.1175/JCLI-D-18-0216.1).
- Tjernström, M. et al.: The Arctic Summer Cloud Ocean Study (ASCOS): overview and experimental design. In: *Atmospheric Chemistry and Physics* 14.6, 2014, pp. 2823–2869. DOI: [10.5194/acp-14-2823-2014](https://doi.org/10.5194/acp-14-2823-2014).
- Tjernström, M. et al.: Warm-air advection, air mass transformation and fog causes rapid ice melt. In: *Geophysical Research Letters* 42.13, 2015, pp. 5594–5602. DOI: [10.1002/2015GL064373](https://doi.org/10.1002/2015GL064373).
- Trepte, Q. Z. et al.: Global cloud detection for CERES Edition 4 using Terra and Aqua MODIS data. In: *IEEE Trans. Geosci. Remote Sens.* 57.11, 2019, pp. 9410–9449. DOI: [10.1109/TGRS.2019.2926620](https://doi.org/10.1109/TGRS.2019.2926620).
- Turetsky, M. R. et al.: Permafrost collapse is accelerating carbon release. 2019.
- Turner, D.: Improved ground-based liquid water path retrievals using a combined infrared and microwave approach. In: *Journal of Geophysical Research: Atmospheres* 112.D15, 2007.
- Unidata.: Integrated Data Viewer (IDV) version 3.1 [software]. Boulder, CO: UCAR/Unidata. 2012.
- Uttal, T. et al.: Surface Heat Budget of the Arctic Ocean. In: *Bulletin of the American Meteorological Society* 83.2, 2002, pp. 255–276. DOI: [10.1175/1520-0477\(2002\)083<0255:SHBOTA>2.3.CO;2](https://doi.org/10.1175/1520-0477(2002)083<0255:SHBOTA>2.3.CO;2).
- Vassel, M., Ickes, L., Maturilli, M., and Hoose, C.: Classification of Arctic multilayer clouds using radiosonde and radar data in Svalbard. In: *Atmospheric Chemistry and Physics* 19.7, 2019, pp. 5111–5126. DOI: [10.5194/acp-19-5111-2019](https://doi.org/10.5194/acp-19-5111-2019).
- Vial, J., Dufresne, J.-L., and Bony, S.: On the interpretation of inter-model spread in CMIP5 climate sensitivity estimates. In: *Climate Dynamics* 41.11, 2013, pp. 3339–3362.
- Viceto, C., Gorodetskaya, I. V., Rinke, A., Maturilli, M., Rocha, A., and Crewell, S.: Atmospheric rivers and associated precipitation patterns during the ACLOUD/PASCAL campaigns near Svalbard (May–June 2017): case studies using observations, re-

- analyses, and a regional climate model. In: *Atmospheric Chemistry and Physics Discussions* 2021, 2021, pp. 1–36. DOI: [10.5194/acp-2021-609](https://doi.org/10.5194/acp-2021-609).
- Vihma, T.: Effects of Arctic Sea Ice Decline on Weather and Climate: A Review. Vol. 35. 5. 2014, pp. 1175–1214. DOI: [10.1007/s10712-014-9284-0](https://doi.org/10.1007/s10712-014-9284-0).
- Viúdez-Mora, A., Costa-Surós, M., Calbó, J., and González, J. A.: Modeling atmospheric longwave radiation at the surface during overcast skies: The role of cloud base height. In: *Journal of Geophysical Research: Atmospheres* 120.1, 2015, pp. 199–214. DOI: [10.1002/2014JD022310](https://doi.org/10.1002/2014JD022310).
- Walsh, J. E., Chapman, W. L., and Portis, D. H.: Arctic Cloud Fraction and Radiative Fluxes in Atmospheric Reanalyses. In: *Journal Climate* 22.9, 2009, pp. 2316–2334. DOI: [10.1175/2008JCLI2213.1](https://doi.org/10.1175/2008JCLI2213.1).
- Wang, W., Zender, C. S., As, D. van, and Miller, N. B.: Spatial Distribution of Melt Season Cloud Radiative Effects Over Greenland: Evaluating Satellite Observations, Reanalyses, and Model Simulations Against In Situ Measurements. In: *Journal of Geophysical Research: Atmospheres* 124.1, 2019, pp. 57–71. DOI: [10.1029/2018JD028919](https://doi.org/10.1029/2018JD028919).
- Wendisch, M. and Yang, P.: Theory of Atmospheric Radiative Transfer - A Comprehensive Introduction. In: 2012.
- Wendisch, M. et al.: The Arctic Cloud Puzzle: Using ACLOUD/PASCAL Multiplatform Observations to Unravel the Role of Clouds and Aerosol Particles in Arctic Amplification. In: *Bulletin of the American Meteorological Society* 100.5, 2019, pp. 841–871. DOI: [10.1175/BAMS-D-18-0072.1](https://doi.org/10.1175/BAMS-D-18-0072.1).
- Wendisch, M. et al.: Understanding causes and effects of rapid warming in the Arctic. In: *Eos* 98, 2017.
- Wendler, G., Moore, B., Hartmann, B., Stuefer, M., and Flint, R.: Effects of multiple reflection and albedo on the net radiation in the pack ice zones of Antarctica. In: *Journal of Geophysical Research: Atmospheres* 109.D6, 2004. DOI: [10.1029/2003JD003927](https://doi.org/10.1029/2003JD003927).
- Wilber, A. C., Kratz, D. P., and Gupta, S. K.: Surface emissivity maps for use in satellite retrievals of longwave radiation, NASA/TP-1999-209362. August. 1999, p. 35.
- Wild, M., Folini, D., Schär, C., Loeb, N., Dutton, E., and König-Langlo, G.: The global energy balance from a surface perspective. In: *Climate Dynamics*, 2013. DOI: [10.1007/s00382-012-1569-8](https://doi.org/10.1007/s00382-012-1569-8).
- Winton, M.: Amplified Arctic climate change: What does surface albedo feedback have to do with it? In: *Geophysical Research Letters* 33.3, 2006. DOI: [10.1029/2005GL025244](https://doi.org/10.1029/2005GL025244).

- Wiscombe, W. J., Welch, R. M., and Hall, W. D.: The Effects of Very Large Drops on Cloud Absorption. Part I: Parcel Models. In: *Journal of Atmospheric Sciences* 41.8, 1984, pp. 1336–1355. DOI: [10.1175/1520-0469\(1984\)041<1336:TEOVLD>2.0.CO;2](https://doi.org/10.1175/1520-0469(1984)041<1336:TEOVLD>2.0.CO;2).
- Witthuhn, J., Hünerbein, A., Filipitsch, F., Wacker, S., Meilinger, S., and Deneke, H.: Aerosol properties and aerosol–radiation interactions in clear-sky conditions over Germany. In: *Atmospheric Chemistry and Physics* 21.19, 2021, pp. 14591–14630. DOI: [10.5194/acp-21-14591-2021](https://doi.org/10.5194/acp-21-14591-2021).
- WMO.: Measurement of radiation, chapter 7, in: *Guide to Meteorological Instruments and Methods of Observations*, Tech. Rep., World Meteorological Organization, WMO, Geneva, Switzerland, 2008. 2008.
- Wood, R. and Hartmann, D. L.: Spatial Variability of Liquid Water Path in Marine Low Cloud: The Importance of Mesoscale Cellular Convection. In: *Journal Climate* 19.9, 2006, pp. 1748–1764. DOI: [10.1175/JCLI3702.1](https://doi.org/10.1175/JCLI3702.1).
- Wyser, K. et al.: An evaluation of Arctic cloud and radiation processes during the SHEBA year: simulation results from eight Arctic regional climate models. In: *Climate Dynamics* 30.2, 2008, pp. 203–223.
- Yost, C. R., Minnis, P., Sun-Mack, S., Chen, Y., and Smith, W. L.: CERES MODIS Cloud Product Retrievals for Edition 4–Part II: Comparisons to CloudSat and CALIPSO. In: *IEEE Transactions on Geoscience and Remote Sensing*, 2020, pp. 1–30.
- Young, D. F., Minnis, P., Doelling, D. R., Gibson, G. G., and Wong, T.: Temporal Interpolation Methods for the Clouds and the Earth’s Radiant Energy System (CERES) Experiment. In: *Journal of Applied Meteorology* 37.6, 1998, pp. 572–590. DOI: [10.1175/1520-0450\(1998\)037<0572:TIMFTC>2.0.CO;2](https://doi.org/10.1175/1520-0450(1998)037<0572:TIMFTC>2.0.CO;2).
- Yu, H. et al.: A review of measurement-based assessments of the aerosol direct radiative effect and forcing. In: *Atmospheric Chemistry and Physics* 6.3, 2006, pp. 613–666. DOI: [10.5194/acp-6-613-2006](https://doi.org/10.5194/acp-6-613-2006).
- Yung, Y. L.: An introduction to atmospheric radiation. By K. N. Liou. Academic Press. Second edition, 2002. pp. xiv+583. ISBN 0 12 451451 0. In: *Quarterly Journal of the Royal Meteorological Society* 129.590, 2003, pp. 1741–1741. DOI: [10.1256/003590003102695746](https://doi.org/10.1256/003590003102695746).
- Zelinka, M. D., Klein, S. A., and Hartmann, D. L.: Computing and Partitioning Cloud Feedbacks Using Cloud Property Histograms. Part I: Cloud Radiative Kernels. In: *Journal of Climate* 25.11, 2012, pp. 3715–3735. DOI: [10.1175/JCLI-D-11-00248.1](https://doi.org/10.1175/JCLI-D-11-00248.1).
- Zelinka, M. D., Myers, T. A., McCoy, D. T., Po-Chedley, S., Caldwell, P. M., Ceppi, P., Klein, S. A., and Taylor, K. E.: Causes of Higher Climate Sensitivity in CMIP6 Models. In: *Geophysical Research Letters* 47.1, 2020. e2019GL085782

10.1029/2019GL085782, e2019GL085782. DOI: <https://doi.org/10.1029/2019GL085782>.

Zhang, J., Lindsay, R., Steele, M., and Schweiger, A.: What drove the dramatic retreat of arctic sea ice during summer 2007? In: *Geophysical Research Letters* 35.11, 2008. DOI: [10.1029/2008GL034005](https://doi.org/10.1029/2008GL034005).

Zhao, C. and Garrett, T. J.: Effects of Arctic haze on surface cloud radiative forcing. In: *Geophysical Research Letters* 42.2, 2015, pp. 557–564. DOI: [10.1002/2014GL062015](https://doi.org/10.1002/2014GL062015).

Zhao, W., Peng, Y., Wang, B., and Li, J.: Cloud Longwave Scattering Effect and Its Impact on Climate Simulation. In: *Atmosphere* 9.4, 2018. DOI: [10.3390/atmos9040153](https://doi.org/10.3390/atmos9040153).

List of Abbreviations

(AC)³ ArctiC Amplification: Climate Relevant Atmospheric and SurfaCe Processes and Feedback Mechanisms

LLS low-level stratus

MODIS Moderate Resolution Imaging Spectroradiometer

MOSAic Multidisciplinary drifting Observatory for the Study of Arctic Climate

SOL-D downward solar flux

SOL-U upward solar flux

TIR-D downward thermal infrared flux

TIR-U upward thermal infrared flux

ACLOUD Arctic Cloud Observations Using Airborne Measurements during Polar Day

ACSE Arctic Clouds in Summer Experiment

AO Arctic oscillation index

AOD aerosol optical depth

ArORIS Arctic Observation and Reanalysis Integrated System

ATg atmospheric global transmittance

BSRN Baseline Surface Radiation Network

CBH cloud base height

CERES Clouds and the Earth's Radiant Energy System

CF cloud fraction

CGT cloud geometrical thickness

CM SAF Climate Monitoring Satellite Application Facility

CRE Cloud Radiative Effect

EM electromagnetic

EOF Empirical Orthogonal Function

FD flux difference

GHI global horizontal irradiance

IASI Infrared Atmospheric Sounding Interferometer

IR Infrared

LBLRTM Line-by-Line Radiative Transfer Model

LF liquid fraction

LH Latent Heat

MATCH Model of Atmospheric Transport and Chemistry

NOAA National Oceanic and Atmospheric Administration

PASCAL Physical Feedbacks of Arctic Boundary Layer, Sea Ice, Cloud and Aerosol

Pyrnet Pyranometer Network

RC radiative closure

RMSE root-mean-square error

RRTMG rapid radiative transfer model for general circulations application

RTE Radiative Transfer Equation

SD Standard Deviation

SFC surface

SH Sensible Heat

SHEBA Surface Heat Energy Budget of the Arctic

SiPCA Survival of Polar Cod in a Changing Arctic Ocean

Skt skin temperature

SOL Solar

SST sea surface temperature

SZA solar zenith angle

TIR Thermal Infrared

TOA Top Of the Atmosphere

TROPOS Leibniz Institute for Tropospheric Research

WBF Wegener-Bergeron-Findeisen

WMO World Meteorological Organization

WSD Wavelet power Spectral Density

List of Symbols

α	Surface albedo
\bar{b}	Backscatter function
β_{abs}	Absorption coefficient
β_{ext}	Extinction coefficient
β_{sca}	Scattering coefficient
λ	Wavelength
\mathcal{P}	Phase function
μ	Cosine of solar zenith angle
Ω	Solid angle
$\hat{\Omega}$	Unit vector describing direction of incident
ϕ	Solar azimuth angle
Φ_λ	Radiant energy flux
ρ_I	Density of ice water
ρ_w	Density of liquid water
τ	Optical depth
Θ	Scattering angle
θ	Solar zenith angle
$\tilde{\omega}$	Single scattering albedo
$\tilde{\nu}$	Frequency
A	Area element
AT_g	Transmittance
c	Speed of light in a vacuum inertial frame
C_{abs}	Absorption cross-section
C_{ext}	Extinction cross-section

C_{sca}	Scattering cross-section
D_e	Ice crystal size
E	Energy budget
E_{rad}	Radiant energy
F_{\odot}	Solar flux density in the direction of the incident beam
F_{λ}	Energy flux density
h	Planck's constant
I	Intensity of radiation
J	Source function
k_B	Boltzmann's constant
m	Index of refraction
Q	Cloud water path
Q_I	Ice water path
q_I	Ice water content
Q_L	Liquid water path
q_L	Liquid water content
$r_{E,I}$	Ice crystal effective radius
$r_{E,L}$	Liquid droplet effective radius
S_0	Extraterrestrial irradiance at the TOA
T_{λ}	Spectral transmittance
x	Size parameter

List of Figures

1.1	Monthly mean cloud fraction for different cloud types at (a) Barrow also known as Utqiagvik, (b) SHEBA, and (c) Eureka. The solid black line indicates cloud fraction, ice-only (solid blue), liquid-only (solid red), liquid precipitation including drizzle and rain (solid orange), mixed-phase cloud fraction (solid light green), and mixed-phase column fraction (solid dark green). Also included are the occurrence fractions of ice in any type of cloud (dashed blue), liquid in any type of cloud (dashed red), and multiple, distinct layers of liquid water in any type of cloud (dashed orange). Annual average occurrence fractions for each phase type are indicated at the right. Figure obtained from Shupe et al. 2011.	4
1.2	Diagram of the annual energy budget for the Arctic (70-82°N). The solar (SW) and thermal infrared (LW) flux are shown in yellow and pink, respectively. The orange arrow indicates the heat transport to the Arctic. The Squiggly and broken upward arrows denote the sensible heat (SH; H_s) and latent heat (LH; H_l), correspondingly. All fluxes are expressed in W m^{-2} . The Figure is obtained from Christensen et al. 2016.	6
1.3	Series of September Arctic sea ice extent anomaly with high- and low-ice years shown (top), and the time series of autumn low cloud cover anomaly showing cloud anomalies during high- and low-ice years (bottom). Figure obtained from Eastman and Warren 2010	7
1.4	Cruise track of the PS106 Polarstern expedition is shown on a polar stereographic map of the Arctic. The red line shows the track for the first leg (PS106/1, also denoted as PASCAL), the black line indicates the position for the ice floe camp during PASCAL, and the blue line shows the cruise track for the second leg (PS106/2, also denoted as SiPCA). The upper left box zooms in the ice floe camp drift. Green dots indicate the start of PASCAL and SiPCA legs, and the beginning and end of the ice floe camp. Orange dots depict the location of several case studies discussed in chapter 7. Figure adapted from Barrientos-Velasco et al. 2022.	9
2.1	Geometry of the definition of radiance.	12
2.2	Scattering regimes for atmospheric particles, where $x = \alpha = 2\pi \cdot r/\lambda$. Figure obtained from Petty 2006.	16

- 2.3 Single scattering albedo ($\tilde{\omega}$) and co-albedo (defined as $1-\tilde{\omega}$) as a function of wavelength for water and ice particles of several sizes. Panels **(a)** and **(c)** depicts the $\tilde{\omega}$ over the visible [$0.4 \mu m < \lambda < 0.7 \mu m$], near IR [$0.7 \mu m < \lambda < 4 \mu m$] and TIR range [$4 \mu m < \lambda < 50 \mu m$]. Panels **(b)** and **(d)** shows the scattering co-albedo for the solar band. Figure obtained from Petty 2006. 20
- 2.4 Broadband solar albedo of water and ice water clouds as a function of the liquid (Q_L) and ice water path (Q_I) and the mean effective water droplet radius (a_e ; here referred as $r_{E,L}$) and hexagonal ice crystals size (D_e ; here referred as $r_{E,I}$) for the solar spectrum [$0.2-5 \mu m$]. Figure obtained from Yung 2003 21
- 3.1 Characteristics of Pyrnet set up in the Arctic. Panel **(a)** shows a photograph of a pyranometer station on the ice floe. Panel **(b)** shows the map of the pyranometer stations. Red circles show the location on 11 June 2017, at 14:50Z, while the red star marks the position of Polarstern, and the turquoise hexagon marks the approximate position of a melt-pond. Note that the latitude and longitude axes have been inverted for easier comparison with panel (c). Panel **(c)** edited photograph of the ice floe showing the approximate location of several stations (red circles) and Polarstern (red star). Photographed by Svenja Kohnemann. Figure adapted from Barrientos-Velasco et al. 2020. 26
- 3.2 Quality flags for the pyranometer sensors. The pyranometer station number is shown on the y-axis and the date on the x-axis. Each square is divided into two triangles: the upper one shows the levelling flag, and the lower triangle the cleanliness status. Green is used for well-levelled and clean stations, while yellow denotes partially levelled stations or the presence of liquid droplets on the domes, while red is used for not levelled stations or iced domes. Figure from Barrientos-Velasco et al. 2020. 29
- 3.3 Surface conditions during PS106. Panel **(a)** shows one hour resolution time series of snow cover (%) obtained from CERES. Panel **(b)** shows time series of surface albedo based on CERES (red line) and ERA5 (blue line). Panel **(c)** shows time series of near-surface temperature based on Polarstern observations at 10 m.a.s.l (orange line), based on radiosondes at 10 m.a.s.l (green line), and skin temperature from ERA5 (blue line), CERES (red line) and mean values obtained from Pyrnet (light blue line). The bottom bar indicates an approximation of the surface conditions during PS106. Dark blue indicates open ocean, yellow suggests marginal sea ice zone, and mostly sea ice is shown in teal. Figure modified from Barrientos-Velasco et al. 2022. 34
- 3.4 Panel **(a)** shows the time series of near surface wind speed (ms^{-1}) and direction obtained from Polarstern observations. Panel **(b)** shows the AO index reported by the NOAA. 35

3.5	Time-height indicator plot of atmospheric profiles obtained from ERA5 along the PS106 cruise track. Panel (a) shows the atmospheric temperature anomaly (δT_a), panel (b) shows specific humidity anomalies. In (c) and (d) , the mean profiles of atmospheric temperature and specific humidity, respectively, are shown. The blue and orange lines correspond to ERA5, radiosondes, and the Sub-Arctic Summer standard atmosphere [Anderson et al. 1986] is displayed in black. The grey-shaded area indicates the minimum and maximum while, while the rose-shaded area shows the interquartile range of ERA5 vertical profiles. Figure from Barrientos-Velasco et al. 2022.	36
3.6	Cloud fraction (CF) observed along the PS106 cruise track. Panel (a) shows the vertically resolved mean CF based on Cloudnet observations at hourly resolution. Data gaps are indicated in grey. Panel (b) shows daily mean CF based on Cloudnet plus detection of low-level stratus clouds (LLS) introduced by Griesche et al. 2020 (red) and CERES (blue). Source: Barrientos-Velasco et al. 2022.	37
3.7	Daily and overall relative frequency of occurrence (RFO) of various cloud characteristics. Panel (a) shows the RFO of clear-sky, single-level clouds, and multilayer clouds. Panel (b) shows the RFO of the thermodynamic phase of single-layer clouds, differentiating periods of ice clouds, liquid clouds, mixed-phase clouds of type 1 or 2, precipitation (PPT), and clear-sky. Data gaps are marked in grey in all panels. Panel (c) is the RFO of various quality flags indicating optimum conditions (OC), low-level stratus (LLS), PPT and simultaneous occurrence of LLS and PPT. Figure obtained from Barrientos-Velasco et al. 2022.	38
3.8	Macrophysical properties of clouds during PS106. Panel (a) shows box plot time series of cloud top. Panel (b) similar to (a) , but for the cloud base. At the end of each panel is shown the box plot for the entire time series. The limits of the box indicate the 25th and 75th percentile of the interquartile range, the line inside the box denotes the median, minimum and maximum values are given by the vertical line of each box. The outliers are presented as diamonds.	39
3.9	Cloud microphysics during PS106 based on Cloudnet data. Panel (a) shows the frequency of occurrence of liquid water path (Q_L), (b) shows the distribution of the liquid effective radius ($r_{E,L}$) based on Cloudnet (in black) and a modified ($r_{E,L,mod}$) version where all values lower than $2.5 \mu\text{m}$ are changed to $2.5 \mu\text{m}$ (in red). Panel (c) shows the frequency of occurrence of the ice water path (Q_I), and panel (d) shows the distribution of ice effective radius ($r_{E,I}$). On the top of each panel the total number of observations are indicated.	40
4.1	Comparison between the upward solar (SOL-U) flux and the SZA at the surface (SFC; panel a), and at the top-of-the-atmosphere (TOA; panel b) of the base simulation (black) and the variation of ± 0.08 surface albedo of the base simulation.	46

4.2	Comparison of solar (SOL) flux and the solar zenith angle (SZA) for different values of liquid (Q_L ; dashed line) and ice water path (Q_I ; solid line). Panels (a) and (c) show the downward flux at the surface (SFC), and panels (b) and (d) show the upward flux at the top-of-the-atmosphere (TOA).	53
4.3	Comparison between the solar flux (SOL) and the solar zenith angle (SZA) for different values of liquid ($r_{E,L}$; dashed line) and ice effective radius ($r_{E,I}$; solid line). Panel (a) shows the downward flux SOL-D at the surface (SFC), and panel (b) shows the upward flux (SOL-U) at the top-of-the-atmosphere TOA.	55
4.4	Comparison between the solar flux (SOL) and the solar zenith angle (SZA) for several single-layer mixed-phase clouds with different liquid fractions. The upper row shows the downward flux at the surface (SFC) and the lower row shows the upward flux at the top-of-the-atmosphere (TOA). Panels (a) and (e) show the comparison for a surface albedo (α) of 0.2, panels (b) and (f) for a α of 0.4, panels (c) and (g) for a α of 0.65, and (d) and (h) for a α of 0.8.	56
4.5	Mean values of the net cloud radiative effect (CRE) for a single-layer cloud at the surface (SFC) for several surface albedo and the liquid fraction (LF) values.	57
5.1	(a) Time series of atmospheric global transmittance (ATg) derived from pyranometer network. In blue is shown the mean and in red the median. (b) Time series of the inter-station standard deviation of ATg. Shaded grey area indicate minimum and maximum values in (a) and (b) . Source: Barrientos-Velasco et al. 2020.	64
5.2	Histograms of atmospheric global transmittance (ATg) for (a) overcast, (b) multilayer, (c) broken cloud, (d) thin cloud and (e) cloudless sky conditions. Source: Barrientos-Velasco et al. 2020.	64
5.3	Overview of the cloudless case: (a) shows the time series of atmospheric global transmittance (ATg), and the green-shaded background marks the cloudless period (June 10, 2017, 11:10Z - 15:43Z). (b) Histogram of global transmittance for cloudless conditions. (c) Photograph from the all-sky camera at 13:51:44Z. (d) Time series of the inter-station standard deviation (SD) of ATg based on all functional stations. (e) Map of the stations showing the temporal SD for individual stations, while the red star marks the position of Polarstern. Panel (f) shows the wind rose for the selected period. Source: Barrientos-Velasco et al. 2020.	65
5.4	Overview of overcast case: Same as Fig. 5.3, but for 6 June 2017, 00:00Z - 23:59Z. All-sky camera photograph taken at 13:41:54Z. Source: Barrientos-Velasco et al. 2020.	66
5.5	Station map showing the average atmospheric global transmittance for the overcast case (June 6, 2017, 00:00Z - 23:59Z). The red star marks the position of Polarstern. Source: Barrientos-Velasco et al. 2020.	66

5.6	Overview of thin cloud case: the same as Fig. 5.3 but for 9 June 2017, 16:36-18:08Z. (c) Photograph taken at 17:29:28Z. Source: Barrientos-Velasco et al. 2020.	67
5.7	Overview of multilayer case: Same as Fig. 5.3, but for June 13, 2017, 00:00Z - 19:15Z. All-sky camera photograph taken at 10:09:35Z. Source: Barrientos-Velasco et al. 2020.	68
5.8	Time series of 1-minute averaged temperature for all stations on June 13, 2017. Source: Barrientos-Velasco et al. 2020.	68
5.9	Overview of broken cloud case: Same as Fig. 5.3, but for June 8, 2017, 08:55Z - 19:00Z. All-sky camera photograph taken at 12:41:14Z. Source: Barrientos-Velasco et al. 2020.	69
5.10	All-sky camera photographs for (a) June 7, and (b) June 8, taken at different times throughout the day. Source: Barrientos-Velasco et al. 2020.	70
5.11	Wavelet-based power spectral density (WSD) of the station-averaged ATg (filled circles) and averaged WSD from the individual stations (empty circles), for 3-hour periods (15:00Z-18:00Z) with broken clouds (8 June 2017), multilayer (13 June 2017) and overcast (6 June 2017) conditions. The dashed horizontal line denotes the measurement uncertainty of the pyranometer. Source: Barrientos-Velasco et al. 2020.	72
5.12	Wavelet-based power spectral density (WSD) of the station-averaged ATg (filled circles) and average WSD from the individual stations (empty circles) for 3-hour periods (15:00Z-18:00Z) of broken clouds on June 7 (circles) and June 8 (squares). Solid lines indicate the linear regression for the time period selected, and the dashed horizontal line corresponds to the measurement uncertainty of the pyranometer. Source: Barrientos-Velasco et al. 2020.	73
6.1	Time series of the flux difference of downward surface radiative fluxes between CERES and T-CARS for pristine (P), clear-sky conditions (CS), all-sky (AS), and cloudy without aerosols (NA). Panel (a) shows the difference of the TIR-D CERES (CS-P) and CERES (AS-NA). Panel (b) shows the same as (a), but the downward SOL (SOL-D) flux. Panel (c) shows the TIR-D differences between T-CARS and CERES P, and T-CARS minus CERES CS. Panel (d) shows the same as (c), but for the SOL-D. The histograms of each left-hand side panel are shown on the right. The TIR-D and SOL-D fluxes are shown in red and blue, respectively. Source: Barrientos-Velasco et al. 2022.	78
6.2	Histograms of flux difference (FD) of simulations minus observations for downward TIR (TIR-D) flux (panels a and c) and the downward SOL (SOL-D) flux (panels b and d) for clear-sky (CS) conditions. Panels a and b show T-CARS comparison, where the filled histograms show the filtered data by excluding the moments where the observations were compromised. Panes c and d show the comparison of CERES for All-sky (green), clear-sky (red) and pristine simulations (blue) for the same filtered time steps as in T-CARS. Source: Barrientos-Velasco et al. 2022.	80

- 6.3 Time series of TIR-D **(a)** and SOL-D **(b)** during PS106. In panel (a) and (b), observations are shown in solid black lines, CERES all-sky (AS) products in the solid green line, and clear-sky (CS) in the dashed green line, clear-sky T-CARS simulation is shown in the dashed blue line. The distribution of the time series shown in panel (a) and (b) are shown in panel **(c)** and **(d)**, respectively. Source: Barrientos-Velasco et al. 2022. 81
- 6.4 Scatter plots comparing the CERES fluxes and ship-based radiative flux observations (Obs.) for the downward TIR (a) and SOL (b) fluxes. The black line represents the best linear fit. The resulting fit equation and the square of the Pearson correlation coefficient (R^2) are shown in each panel. Source: Barrientos-Velasco et al. 2022. 82
- 7.1 Overview of radiative fluxes for the 3 July 2017 case. Panel **(a)** shows the time series of the Cloudnet target classification and the CERES-based cloud boundaries (dashed black lines). Panel **(b)** and **(c)** show the time series of the SOL fluxes and TIR fluxes, respectively at 10-minutes resolution. In both panels (b and c), the down-looking arrow indicates (\downarrow) the downward fluxes at the surface (SFC), and the up-looking arrow (\uparrow) shows the upward fluxes at the top of the atmosphere (TOA). Panels **(d)** and **(e)** show histograms of the difference of T-CARS/CERES SOL-D and TIR-D fluxes and observations at the surface, respectively. Panels **(f)** and **(g)** show histograms of the difference of T-CATS and CERES SOL-U and TIR-U fluxes at the TOA, respectively. The number of 10-minute data points contributing to the histogram in panel (d) is 44, while it is 55 for panels (e)-(g). Pale-rose shading indicates periods when the ship's superstructures obstructed the ship-borne flux observations. Light-blue background indicates the period of clear-sky considered for the analysis. Source: Barrientos-Velasco et al. 2022. 85
- 7.2 Overview of radiative fluxes for the 2 July 2017 case. Panel (a) shows the time series of the Cloudnet target classification and the CERES-based cloud boundaries (dashed black lines). Panel (b) and (c) show the time series of the SOL fluxes and TIR fluxes, respectively at 10-minutes resolution. In both panels (b and c), the down-looking arrow indicates (\downarrow) the downward fluxes at the surface (SFC), and the up-looking arrow (\uparrow) shows the upward fluxes at the top of the atmosphere (TOA). Panels (d) and (e) show histograms of the difference of T-CARS/CERES SOL-D and TIR-D fluxes and observations at the surface, respectively. Panels (f) and (g) show histograms of the difference of T-CATS and CERES SOL-U and TIR-U fluxes at the TOA, respectively. The number of 10-minute data points contributing to the histogram in panel (d) is 44, while it is 55 for panels (e)-(g). Pale-rose shading indicates periods when the ship's superstructures obstructed the ship-borne flux observations. Light-blue background indicates the period of clear-sky considered for the analysis. Source: Barrientos-Velasco et al. 2022. 87

7.3	Time series of 10-minutes resolution cloud microphysics properties and CRE between CERES and Cloudnet for 2 July 2017 case. Panel (a) shows the comparison between CERES and Cloudnet of liquid water path (Q_L ; blue) and ice water path (Q_I ; red). Panel (b) shows the liquid effective radii ($r_{E,L}$; blue) and the ice effective radii ($r_{E,I}$; red). Panel (c) shows the cloud radiative effect (CRE) at the surface (SFC; solid lines) and the top of the atmosphere (TOA; dashed lines) from T-CARS (brown) and CERES (green). Source: Barrientos-Velasco et al. 2022.	88
7.4	Same as Figure 7.2, but for 26 June 2017. Pale-orange shaded background indicate lidar attenuation. Source: Barrientos-Velasco et al. 2022.	89
7.5	Same as Figure 7.3, but for 26 June 2017. Pale-orange shaded background indicate lidar attenuation. Source: Barrientos-Velasco et al. 2022.	89
8.1	Time series of hourly TIR (a) , SOL (b) , and NET (c) CRE for PS106 expedition at the SFC (solid line) and at the TOA (dashed line). Source: Barrientos-Velasco et al. 2022.	92
8.2	Scatter plots comparing the CRE_{SFC} with several parameters. Panel (a) shows the comparison with cloud fraction (CF). Panel (b) shows the comparison of surface albedo (α). Panels (c) and (d) show the comparison between the liquid water path (Q_L) at low surface albedo (< 0.4) and high surface albedo (> 0.4). All scatter plots are colour coded with the values of the solar zenith angle (SZA). Source: Barrientos-Velasco et al. 2022.	94
8.3	Maps of several time-averaged CERES data sets for the Arctic (70° to 90° N) and the time period of the PS106 expedition. Panel (a) shows the mean surface albedo, (b) the top of the atmosphere (TOA) albedo, and (c) the mean cloud fraction (CF). Panels (d), (e), and (f) show the CRE for the SOL, TIR, and net spectral regions, respectively, at the surface (SFC), while panels (g), (h), and (i) present the same at the TOA. An orthographic projection is used, and the PS106 cruise track is indicated in magenta. Source: Barrientos-Velasco et al. 2022.	95
8.4	Radiation budget for PS106 cruise (a) and the entire Arctic region for the PS196 period (b) . Mean values for the SW (SOL, yellow) and LW (TIR, red) are shown in $W\ m^{-2}$. Values in parentheses show the radiation budget during cloudless conditions. Source: Barrientos-Velasco et al. 2022	99
A.1	Microphysical properties of single-layer and multilayer cloud conditions during PS106. Panels (a) and (c) show the frequency of occurrence of liquid (Q_L) and ice (Q_I) water path, respectively. Panels (b) and (d) show the distribution of the frequency of occurrence of ice and liquid effective radius. In orange is depicted all single-layer cases, and in green the multilayer cases.	109
A.2	Same as Fig. A.1, but for single-layer liquid (in blue), ice (in grey), mixed-phase type 1 (in green), type 2 (in orange) cloud conditions.	110

B.1	Mean values of the net cloud radiative effect (CRE) for a single-layer liquid and ice cloud at the surface (SFC) and at the top of the atmosphere (TOA) for several values of cloud water path (Q).	111
B.2	Mean values of the net cloud radiative effect (CRE) for a single-layer liquid and ice cloud at the surface (SFC) and at the top of the atmosphere (TOA) for several values of effective radius (r_E).	112
B.3	Mean values of the net cloud radiative effect (CRE) for single-layer mixed-phase clouds at the top of the atmosphere (TOA) for several values of surface albedo.	112
B.4	Mean values of the net cloud radiative effect (CRE) for a single-layer liquid and ice cloud at the surface (SFC) and at the top of the atmosphere (TOA) for several values of cloud base height (CBH).	113
B.5	Mean values of the net cloud radiative effect (CRE) for a single-layer liquid and ice cloud at the surface (SFC) and at the top of the atmosphere (TOA) for several values of cloud geometrical thickness (CGT).	113
C.1	Time series of AOD for PS106 based on CERES products. In teal is shown the AOD at $55 \mu\text{m}$ and in orange a $84 \mu\text{m}$	114
D.1	Sky-camera photographs for 2 July 2017 04:00:08Z (a), for 2 July 2017 12:13:33Z (b), 3 July 2017 04:14:09Z (c), and 3 July 2017 12:04:08Z (d). All times in UTC.	115
D.2	Moderate Resolution Imaging Spectroradiometer (MODIS) screenshot for 3 July 2017. The red symbol indicates <i>Polarstern</i> 's location. The orange line indicates MODIS track.	116
D.3	Same as Fig. D.2, but for 2 July 2017.	116
D.4	Same as Fig. D.2, but for 26 June 2017.	117

List of Tables

3.1	Main components and specifications of a pyranometer station	27
3.2	The table summarizes the instruments, main assumptions, limitations (Limit.) and references used in Cloudnet to derive the liquid and ice water content (q), and ice and liquid effective radius (r_E). The abbreviation MWR stands for microwave radiometer, CDD for cloud-droplet distribution, IPSD for ice-particle size distribtuion, PPT for precipitation, and Exp for exponential.	31
3.3	T-CARS input parameters	43
4.1	Variation of several atmospheric and surface parameters for clear-sky simulations. The table indicates the mean upward and downward SOL and TIR flux differences between the perturbed simulations minus the idealized base atmosphere simulation. All values indicate surface fluxes in $W m^{-2}$	48
4.2	Variation of several atmospheric parameters. The table indicates the mean upward SOL, TIR, and net flux differences at the top-of-the-atmosphere (TOA) of clear-sky perturbed simulations minus the simulated idealized atmosphere. Values in $W m^{-2}$	49
4.3	The table indicates the mean upward SOL, TIR, and net flux differences at the top-of-the-atmosphere (TOA) of clear-sky perturbed simulations minus idealized atmosphere simulation. Values in $W m^{-2}$	49
4.4	Description of constant and variable parameters for the sensitivity analysis of a single-layer cloudy sky.	51
4.5	Mean TIR and SOL flux results from the sensitivity analysis of water path (Q) for a single-layer liquid and ice clouds. The downward and upward mean fluxes are calculated at the surface (SFC) and top-of-the-atmosphere (TOA), respectively.	52
4.6	Mean TIR and SOL flux values of the sensitivity analysis of effective radii (r_E) for liquid and ice clouds. The downward and upward mean fluxes are calculated at the surface (SFC) and top-of-the-atmosphere (TOA), respectively.	54
4.7	Mean TIR and SOL flux values of the sensitivity analysis of cloud base height (CBH) for liquid and ice clouds. The downward and upward mean fluxes are calculated at the surface (SFC) and top-of-the-atmosphere (TOA), respectively.	58

4.8	Mean TIR and SOL fluxes of the sensitivity analysis of cloud geometrical thickness (CGT) for liquid and ice clouds. The downward and upward mean fluxes are calculated at the surface (SFC) and top-of-the-atmosphere (TOA), respectively.	59
4.9	Ranking of parameters that affect the SOL and TIR fluxes at the SFC and TOA for clear-sky conditions. The value of 1 is given to the parameter that affects the most, and 5 to the parameter that affects the least each flux. In bold are marked the parameters that need the most attention. Symbol ‘-’ indicates no effect.	60
4.10	Ranking of parameters that affect the SOL and TIR fluxes at the SFC and TOA for cloudy conditions. The value of 1 is given to the parameter that affects the most, and 5 to the parameter that affects the least each flux. In bold are marked the parameters that need the most attention.	60
5.1	Mean values of: Ambient temperature T_a [K], atmospheric global transmittance AT_g [-] for case studies (C) and all period (P). All based on the pyranometer network. Source: Barrientos-Velasco et al. 2020.	71
8.1	Cloud radiative effect (CRE) based on CERES for PS106 cruise and Arctic region. Source: Barrientos-Velasco et al. 2022.	93
8.2	Summary of literature comparison of range CRE_{SFC} from different studies. Values in parenthesis indicate the mean for the entire study. Source: Barrientos-Velasco et al. 2022.	97
8.3	Radiation budget for PS106 for all-sky (AS) and a cloudless-sky (CS) based on CERES. Values represent mean and standard deviation (in parentheses) from 28 May to 20 June, 22 June to 16 July 2017. Source: Barrientos-Velasco et al. 2022.	101

Acknowledgement

I would like to take the opportunity to thank several people who supported me over the past years, whose guidance and encouragement made my PhD journey unforgettable.

I would like to acknowledge and give my deepest thanks to my supervisors, Hartwig Deneke, Anja Hühnerbein and Andreas Macke, for their constant support and fruitful discussion throughout this thesis. Their guidance and advice carried me through all the stages of writing my thesis. They also motivated me to investigate my research topic from different angles and overcome unexpected challenges.

I would also like to express my warm appreciation to Patric Seifert and Hannes J. Griesche for all the work invested in our discussions and the feedback I received from them over the past years. Their opinions were always of high importance and part of the foundation of my thesis.

Moreover, I am very thankful to Jonas Witthuhn for his support and good suggestions during different stages of my PhD work. I am also very grateful to Vasileios Barlakas for all the help I received from him when I arrived in Leipzig and his friendship.

I would like to thank Fabian Senf, Rico Hengst, Sebastian Bley, Vasileios Tzallas, Stephan Lenk, and Daniel Merk. Each of them supported me and were part of a very enjoyable and pleasant working group. I learnt something new from each one of them.

I would like to thank the TROPOS and (AC)³ communities who allowed me to experience an enjoyable working environment that fostered new friendships and scientific connections that were crucial for the development of this thesis.

I would like to express my immense gratitude to my brothers for their constant support during different stages in my life. I thank my dear mom and dad, who have sacrificed so much for me that all my accomplished goals will always be dedicated to them.

Last but not least, I would like to thank my friends and express my innermost gratitude to Dattaraj P. Mahale, whose unconditional support and caring has always inspired and pushed me further in any situation. I thank him for always believing in me and being my core support.